NORTHWESTERN UNIVERSITY

Geomechanical Modeling of Inception and Propagation of Compaction Bands in Porous Rocks

A DISSERTATION

SUBMITTED TO THE GRADUATE SCHOOL
IN PARTIAL FULFILLMENT OF THE REQUIREMENTS

for the degree

DOCTOR OF PHILOSOPHY

Field of Civil and Environmental Engineering

By

Ghassan Shahin

EVANSTON, ILLINOIS

June 2020

ABSTRACT

Geomechanical Modeling of Inception and Propagation of Compaction Bands in Porous Rocks

Ghassan Shahin

The term *compaction band* identifies a rich variety of structural features of the Earth's crust that affect formations of sedimentary rocks. The most common definition for compaction band often found in the literature describes them as narrow planar zones of concentrated porosity reduction, which may involve limited to none shear offset between adjacent rock volumes. These structures occur through spatio-temporal processes in media characterized by intrinsic heterogeneity which have so far eluded complete understanding. Examples include their emergence in geological settings characterized by very different tectonic regimes, and thus characterized by different subsurface stress fields and background tectonic strain. The outcomes of such variability are concentrated compaction zones with different thickness, length and spacing.

This thesis investigated compaction banding in porous rocks by means of analytical and computational geomechanics. In this context, constitutive laws based on a standard strain-hardening plasticity and involving tunable hardening and softening variables were used to reproduce the phenomenology of selected porous rocks. The model is augmented by incorporating rate effects to capture the inherent viscosity of these materials and their long-term inelastic deformability. This work led to the calibration and the assessment of the performance against data for two porous rocks, a siliciclastic sandstone and a carbonate rock, displaying a distinct hardening behavior and very different compaction band patterns. Compaction banding is simulated as a form of material instability of porous viscoplastic solids. For this purpose, the controllability theory and the mathematical tools for nonlinear differential systems are employed to develop criteria for identifying the time of incipient instability. The importance of material heterogeneity in the context of compaction localization analysis was examined on the bases of synthesized and real porosity maps connected from computerized tomography images to finite element models through a novel mapping scheme based on the concept of representative elementary volume. The analysis focused on the role played by the spatial heterogeneity in generating delayed compaction bands, determining the zones where the localized compaction nucleates, and controlling the extent of its propagation. This role is further quantified in the presence of interfering factors, specifically frictional boundaries, that could induce heterogeneous stress fields, and the bias that they could generate in the context of assessing the compaction banding characteristics. This thesis also involves numerical analyses of field-scale problems, where theoretical models are used to elucidate the interactions taking place between layers of sandstone prone to compaction localization and bounding elastic layers in multi-strata systems. Various scenarios and combinations of geological processes and tectonic settings are tested to understand the conditions promoting the coexistence of various modes of compaction banding in natural formations.

The analyses of delayed compaction bands based on viscoplastic idealization revealed that pulses of overstress correspond to stages of inception and propagation of new compaction bands. Intimate relations between the spatial patterns of deformation bands and the temporal dynamics of deformation are demonstrated. While homogeneous compaction develops with decaying rates of accumulation, localized compaction occurs through stages of accelerating deformation. Spatial variations in the local yielding resistance provide hotspots for inelastic deformation, eventually generating delayed compaction bands under moderated levels of loading. Furthermore, the spatial heterogeneity is shown to play a predominant role in determining the location at which compaction banding nucleates and the extent of its propagation. In frictionless specimens, the onset of compaction localization is promoted in zones characterized by higher porosity (i.e., lower strength). Yet, this role is critically affected by the existence of interfering conditions, such as frictional boundaries in laboratory testings which were found to nearly eliminate the impact of material heterogeneities, such that compaction localization is forced to occur at the specimen boundaries. Furthermore, the analyses revealed the existence of an intermediate range of platen-specimen friction coefficient which favors the emergence of a transitional regime of strain localization at which material heterogeneity and boundary effects concurrently control the compaction banding patterns. The analyses show marked dependence of the three zones on the degree of heterogeneity, showing that increasing values of boundary friction are necessary to offset the effect of material weaknesses in strongly heterogeneous samples. Furthermore, it was found that the effects of boundary friction can be strong enough to bias the identification of compaction banding characteristics. Field-scale simulations show that the nucleation and propagation of compaction bands in sandstone formation in multi-strata systems are influenced by the contrast elasticity of the bounding layers. As a result of Poisson effects, stiffer bounding layers promote higher mean stress and lower deviatoric stresses, eventually shifting the point of intersection of the stress path with the yield surface, and hence the angle of compaction localization. It is also shown that the sequential growth of compaction bands induces deviations in the field of local stress responses leading to varying types of compaction band along rock formations. The coexistence of various types of band, however, is generated by a rich loading history, suggesting that, contrary to some hypotheses, the sequencing of compaction band formation may not be contemporaneous. These findings feature the importance of geomechanical

modeling when performed in conjunction with strain localization analyses in providing a useful guidance to explain the origin of natural formations and reduce the uncertainty involved in the geological reconstruction of field observations.

Acknowledgments

I would like to thank my advisor, **Giuseppe Buscarnera**, for the time he has dedicated to supporting me, especially the generous advice and the sweet interactions throughout the journey. Thanks particularly for your patience with my impetuosity. Working with you was truly enjoyable (which I really need to function!), I am in awe of your way of approaching mentorship of students. I would next like to extend my thanks to my co-advisor, **Cino Viggiani**. Thank you for everything, notably your consistent support and constant attention. You are responsible for much of my personal and professional development; not everyone is blessed with such a great and endearing *Godfather*! Many thanks as well to **John Rudnicki**. You gave me much of your time with patience and interest in my work. I learned much from you, but perhaps the most important thing is your method of non-judgmentally accepting and answering questions. Thanks also to **Ferdinando Marinelli** for the constructive co-mentorship and the fruitful discussions we had in the first years of my training, in addition to **Mehmet Cil** and **Athanasios Papazoglou** for the fruitful work we have done together. I would then like to extend a special thank you to **Richard Finno** and **James Hambleton** for serving as committee members, thanks for your time and feedback. Finally, I am grateful to **Melissa Koelling** for her help with administrative issues and for the friendly and kind vibe she spreads in the Department.

A special thank you to the staff of The International Office, especially to **Emlyn Torres** and **Ravi Shankar**, for their support and assistance with my immigration issues along the

journey, especially upon the issuance of the travel-ban executive order. This work could not have been possible without the unconditional and astonishing support of the staff at ADA-Grenoble, especially **Fanny Braud**, the **Préfecture de l'Isère**, the **Ministry of Interior in France**, especially **Mr. Olivier Massuelle**, and The General Consulate of France in Chicago, and especially the Consul **Rodolphe Le Dref**. All of your roles in resolving the issues of my refugee paperwork were vital to the completion of this doctoral degree.

Finally, thanks would not be complete if I did not acknowledge Northwestern University for giving me the most beautiful years I have ever experienced so far, and for giving me the opportunity to meet amazing people and make lifelong friends, including (alphabetically ordered!) **Adel, Alec, Alexandre, Alexis, April, Asma, Aymeric, Emma, Gabrielle, Jordan, Julia, Mathilde, Matthias, Mia, Roman, Servane, Stephane, Thomas, and Valentine**.

Table of Contents

List of Tables

List of Figures

CHAPTER 1

Introduction

1.1. Motivation and Objectives

The rapid growth of our hydrocarbon-based economy has raised enormous pressure on the development of increasingly aggressive subsurface geo-technologies, as well as major challenges to guarantee a safe and sustainable supply of fossil fuels, while minimizing the negative impacts of greenhouse gases on the Earth's climate. Increasing the efficiency of hydrocarbons recovery and the geologic storage of carbon dioxide represent possible strategies to address these challenges, which yet require major technological developments and scientific breakthroughs. In fact, developing adequate solutions cannot be accomplished unless the mechanics of underground reservoirs is fully understood. In this regard, the role of geomechanics is pivotal to elucidate the key factors involved in the spatially-heterogeneous, multi-scale deformation processes of porous rocks, i.e. some of the basic building block of geological reservoirs (Fig. 1.1).

High-porosity rocks are among the most interesting materials of the shallow crust. One of the most remarkable features of these materials is their marked pressure-sensitivity, which allows them to transition from a brittle-like response characterized by fracture and dilative slip to a plastic behavior displaying pore collapse, macroscopic hardening, and homogeneous deformation [*Wong and Baud*, 2012]. What makes the behavior of porous rocks even more subtle is the existence of intermediate patterns of behavior between these end-members (Fig.

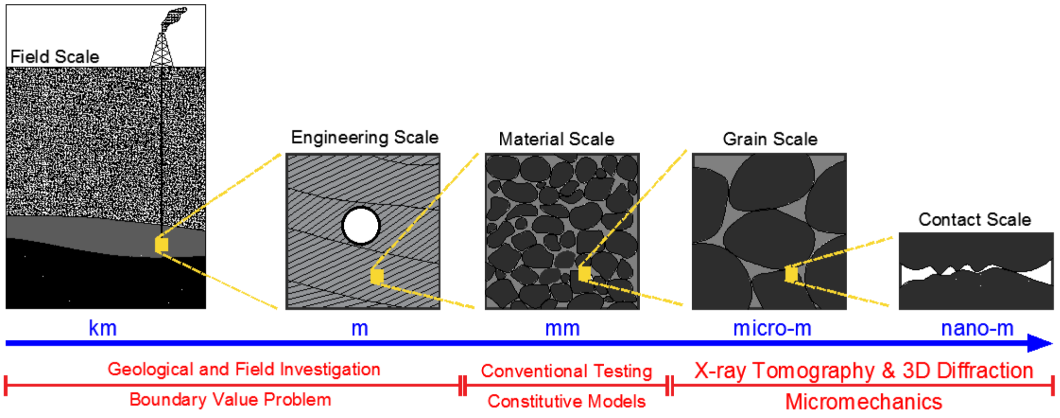

Figure 1.1. Illustration of the multiscale nature of the geomechanics problems involved in energy technology, spanning from intergranular contacts (i.e., micrometer or sub-micrometer scale) up to the field-scale (i.e., order of several km), summarizing the experimental and modeling strategies of each scale.

1.2). In fact, porous rocks are known to exhibit elusive forms of failure referred to as *compaction banding* [*Olsson*, 1999]. This mode of deformation localization leads to narrow zones of intense material destructuration that develop sub-perpendicular to the main compressive stress [*Holcomb et al.*, 2007; *Wong and Baud*, 2012]. Aside from porous rock, compaction banding was documented in a variety of natural and artificial materials including metal foams [*Bastawros et al.*, 2000; *Park and Nutt*, 2001], polycarbonate honeycombs [*Papka and Kyriakides*, 1998], gasbeton [*Castellanza et al.*, 2009], and more recently in snow [*Barraclough et al.*, 2017].

Understanding this form of transition from homogeneous to heterogeneous compaction is a major challenge for modern geomechanics, as it affects numerous geotechnologies and geophysical processes including the gradual activation of faults [*Cruz-Atienza et al.*, 2018; *Deng et al.*, 2015a; *Fortin et al.*, 2006], the short- and long-term quality of hydrocarbon reservoirs [*Hettema et al.*, 2002], aquifer production [*Deng et al.*, 2015a; *Sternlof et al.*, 2006], and the stability of target formations for CO_2 sequestration [*Wawersik et al.*, 2001] and nuclear

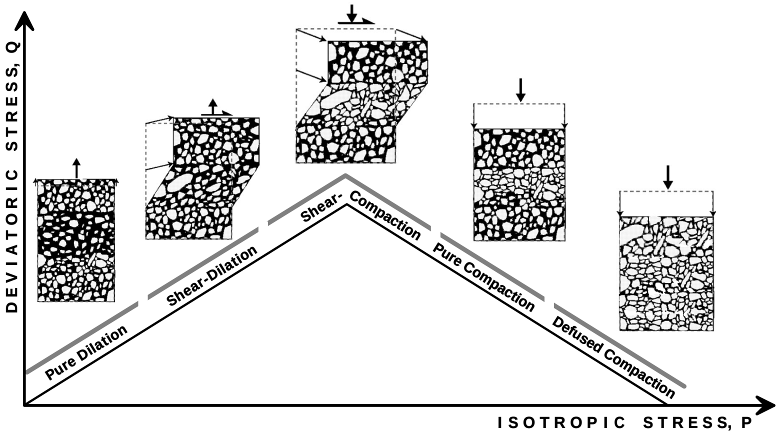

Figure 1.2. Deformation band spectrum (inspired by *Fossen et al.* [2007a]).

wastes disposal [*Rass et al.*, 2017; *Torabi et al.*, 2015]. Research on compaction bands has provided evidence of non-negligible deterioration in local and regional hydraulic conductivity (Fig. 1.3), and therefore accounting for them in the context of reservoirs permeability assessment has become crucial for an accurate prediction of productivity and cost-efficiency. This thesis contributes to the effort that has been devoted to establish a robust mechanistic interpretation of compaction bands, with a focus on the heterogeneous spatio-temporal processes that lead to their emergence and propagation at both the laboratory and field scale.

1.2. Structure of the Thesis

This thesis is organized in seven chapters and five appendices. **Chapter 2** provides a review of the state of the art on compaction banding, detailing field and laboratory evidence, permeability implications, patterns of propagation, and the theories and constitutive models used for their investigation. **Chapter 3** presents a mechanics-based theory for the interpretation of material instability in viscoplastic solids and its use for the formation of

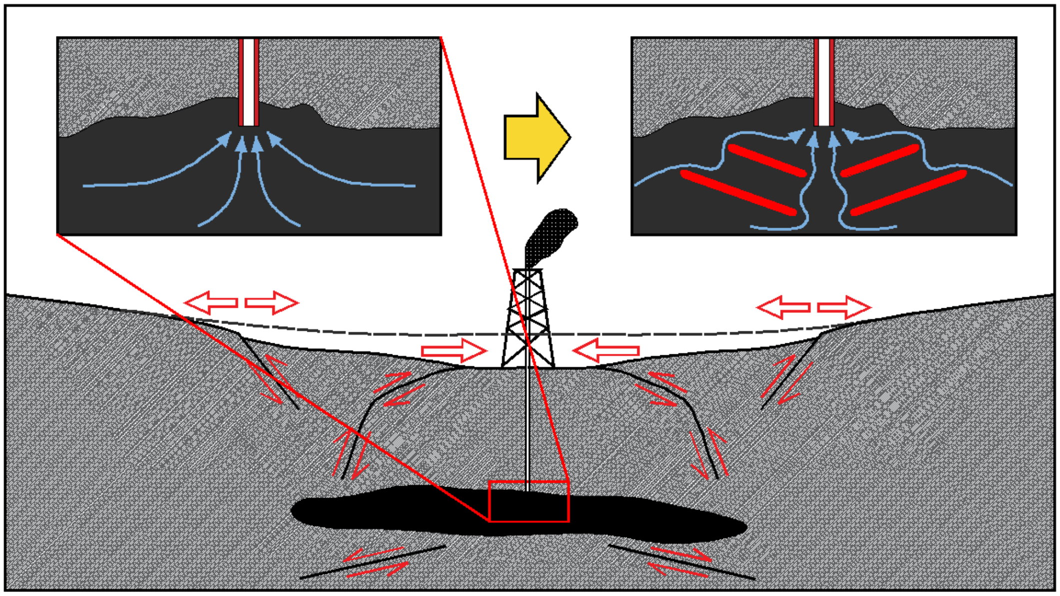

Figure 1.3. Schematic illustration of the impacts of compaction bands on the conductivity of hydrocarbon reservoirs.

closed-form stability indices characterizing the onset of compaction banding over time. The chapter further presents a theoretical analysis of the role of the spatial heterogeneity of material properties in generating delayed compaction banding, and its influence on the rate of compaction creep. **Chapter 4** examines the role of material heterogeneity in the determination of the zones of first nucleation of strain localization. The study is based on a rich dataset available for a high-porosity limestone from central Europe characterized through mechanical testing aided by concurrent x-ray tomography scanning. Material behavior is reproduced through a strain-hardening plasticity with multiple internal variables, whose calibration and validation are reported in the context of the chapter. **Chapter 5** inspects a possible role of boundary effects on the triggering of compaction localization, as well as on the determination of the extension of the compaction banding domain in the stress space. It also inspects the relative role of boundary effects such as friction and material heterogeneity, and the role played by boundary effects in introducing a bias over the characterization of compaction banding domain is also inspected. The analyses provided in this chapter rely on previous calibration of two porous rocks for which available evidence in the lab shows very different modes of compaction localization, one characterized by tabular, discrete bands, and the other by a propagating compaction front. **Chapter 6** discusses the numerical modeling of field-scale problems relevant to compaction bands, including sandstone layers inter-bedded between elastic layers, and the geological factors leading to the emergence of compaction bands with various modes of strain localization. The chapter tackles these geological-scale problems from a mechanics standpoint by interpreting the emergence of compaction bands and their geometrical characteristics in light of inelastic constitutive modeling and strain localization theory. **Chapter 7** provides conclusions and research perspectives.

CHAPTER 2

State of the Art

Compaction banding occurs at stress conditions typical of cap plasticity [*Baud et al.*, 2004; *Charalampidou et al.*, 2011; *Fortin et al.*, 2006; *Holcomb and Olsson*, 2003; *Olsson et al.*, 2002; *Tembe et al.*, 2008] and is characterized by the appearance of zones with concentrated porosity loss that spread until covering the whole sample [*Olsson and Holcomb*, 2000; *Olsson*, 2001]. As a result, deformation in the compaction banding regime involves considerable porosity loss [*Aydin et al.*, 2006] and may lead to a deviatoric stress plateau during the propagation of compaction fronts (Fig. 2.1), followed by stages of re-hardening [*Wong et al.*, 1997].

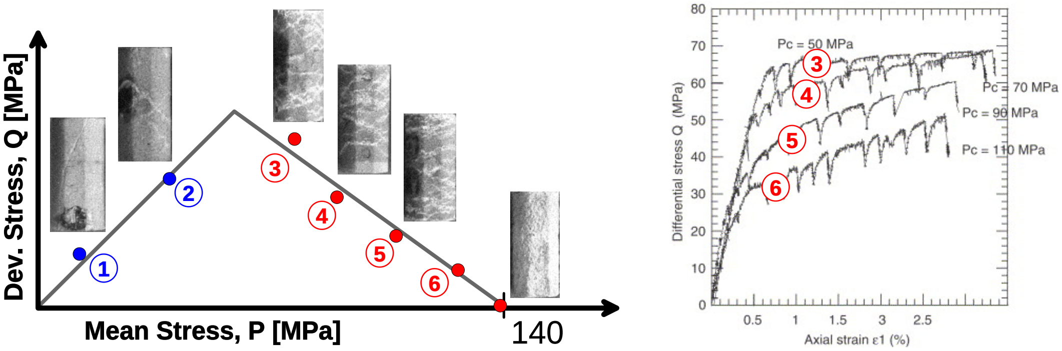

Figure 2.1. Illustration of mechanical characteristics typical of compaction banding, showing that yielding occurs in the cap regime (left), associated with flat to modest hardening post-yielding plateau (right) (data and sub-figures after [*Fortin et al.*, 2005]).

2.1. Field and Laboratory Evidence

Compaction bands were first documented in the United States, in south-central Utah [*Mollema and Antonellini*, 1996], and southeastern Nevada [*Hill*, 1989; *Sternlof et al.*, 2004, 2005, 2006]. Pictures from these locations are presented in Fig. 2.2 and 2.3. Similar structures were also found at numerous locations worldwide, including France [*Ballas et al.*, 2013; *Klimczak et al.*, 2011; *Saillet and Wibberley*, 2010], Germany [*Soliva et al.*, 2016], the United Kingdom [*Griffiths et al.*, 2018], New Zealand [*Nicol et al.*, 2013], and the Middle East [*Gajst et al.*, 2018]. Compaction bands in such locations were found in sandstone outcrops, Few cases in carbonate rocks were further documented including Italy [*Cilona et al.*, 2012; *Micarelli et al.*, 2006; *Rustichelli et al.*, 2012; *Tondi et al.*, 2006], Spain [*Robert et al.*, 2018; *Tavani et al.*, 2018], Austria [*Baud et al.*, 2017; *Rath et al.*, 2011], Malta [*Rotevatn et al.*, 2016]. The rarity of these structures in carbonate formations may be attributed to the reactive nature of such rocks, which specifically favours chemo-mechanical processes (e.g., dissolution and cementation) associated with development of compaction bands [*Cilona et al.*, 2012]. Rare cases of compaction bands in volcaniclastic rocks and chalks were reported from Taiwan [*Soliva et al.*, 2016] and Norway [*Wennberg et al.*, 2013]. The study of chalks constituted a particularly intriguing contribution as it not only documented compaction bands in this class of rocks, but also provided for the first time evidence of strain localization in samples collected from the subsurface, specifically from wells in the hydrocarbons field of Oseberg, in the Norwegian part of the North Sea (Fig. 2.4). More recently, evidence of compaction bands in hydrocarbon sandstone reservoirs has been made available based on samples collected from oil wells in the Holstein Field, in the Gulf of Mexico, USA (Fig. 2.5).

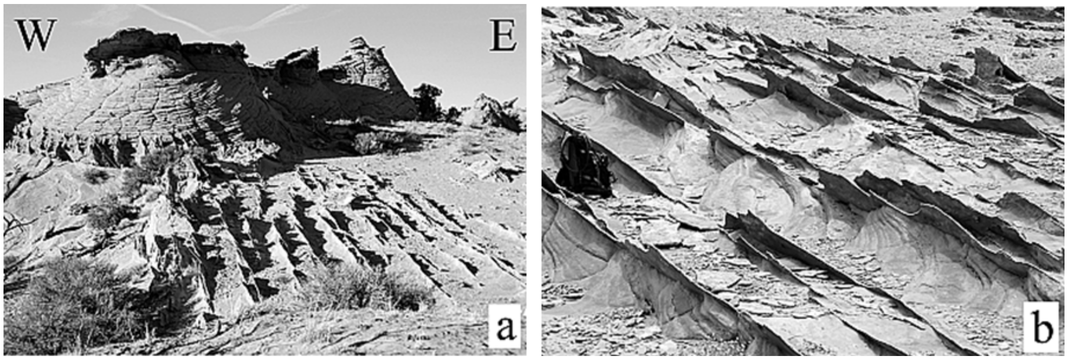

Figure 2.2. Outcrop expression of compaction bands exposed as resistant formation in Utah (after *Schultz* [2009]).

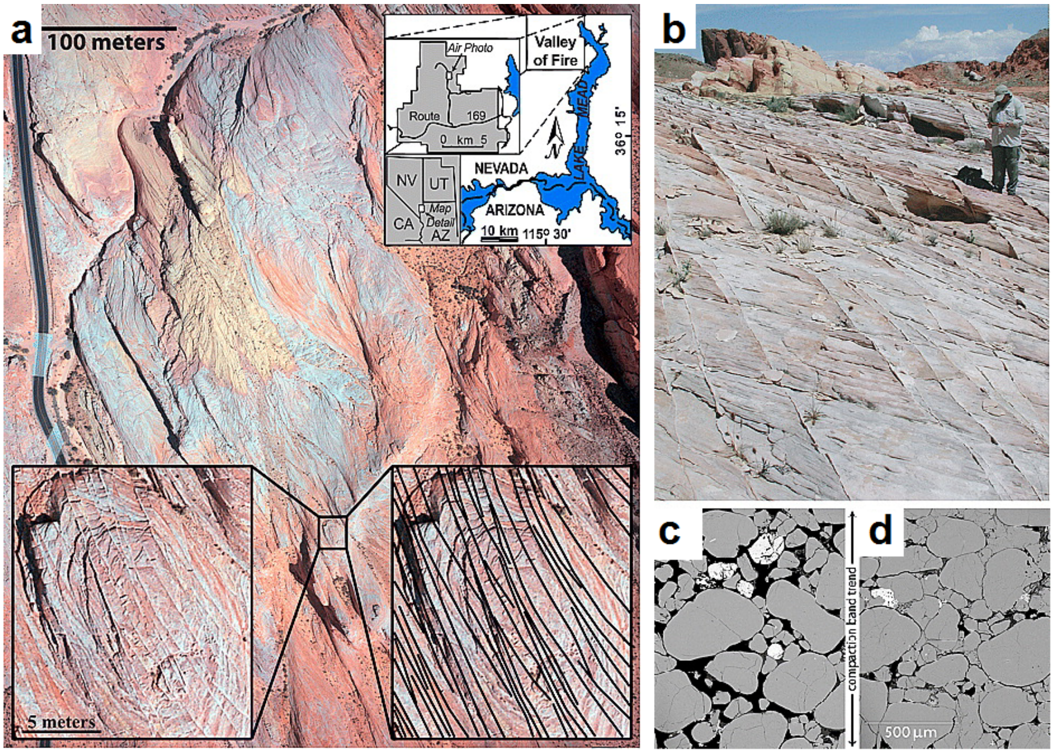

Figure 2.3. Compaction bands in the Aztec Sandstone in the Valley of Fire State Park of southeastern Nevada. (a) Aerial photograph showing an outcrop area. Individual, cm thick compaction bands cropping out as distinct fins over an area of more than 150,000 m^2. (b) A typical outcrop pattern of subparallel compaction bands. Compositional backscatter electron images of the sandstone (c) just outside and (d) inside a compaction band (after *Sternlof et al.* [2006]).

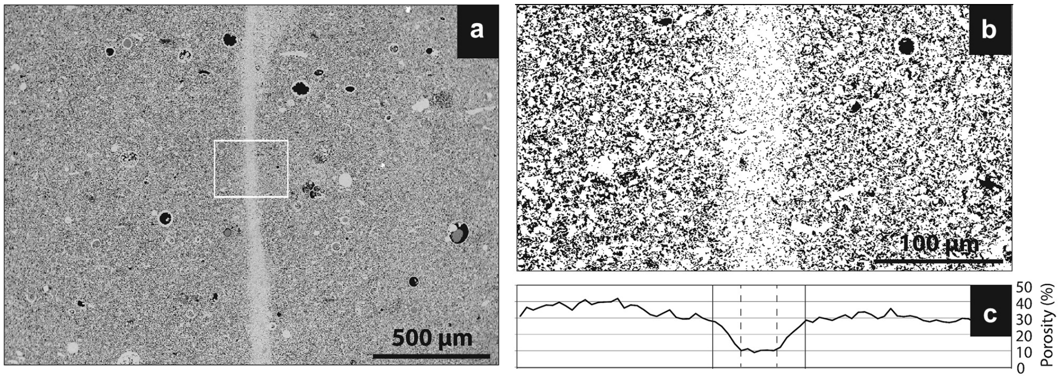

Figure 2.4. Compaction bands in the Shetland Chalk in the Oseberg Field. (a) Backscattered Electron image of a subsurface sample collected from an operation well. The white box indicates the area shown in (b). (c) Porosity profile across the deformation band, calculated from the binarized image in (b) using a sampling window parallel to the deformation band of 10 pixels (edited from *Wennberg et al.* [2013]).

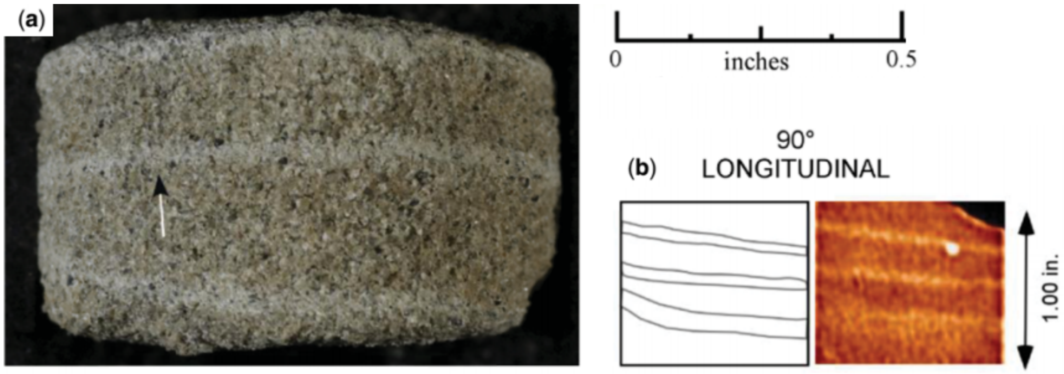

Figure 2.5. Compaction bands in sandstone cores from wells in the Holstein Field, Gulf of Mexico, USA. (b) Core plug with horizontal deformation bands, and (b) sketch based on the CT scan (edited from *Wilkins et al.* [2019]).

The most common type of compaction bands found in the field are compactive shear bands, i.e. structures involving an amount of compaction clearly smaller than shear component. Less common are shear-enhanced compaction bands that involve comparable amounts of shear and compaction. Pure compaction bands seem to be the least common with the only two sites where they are well described are Buckskin Gulch in Utah [*Mollema and*

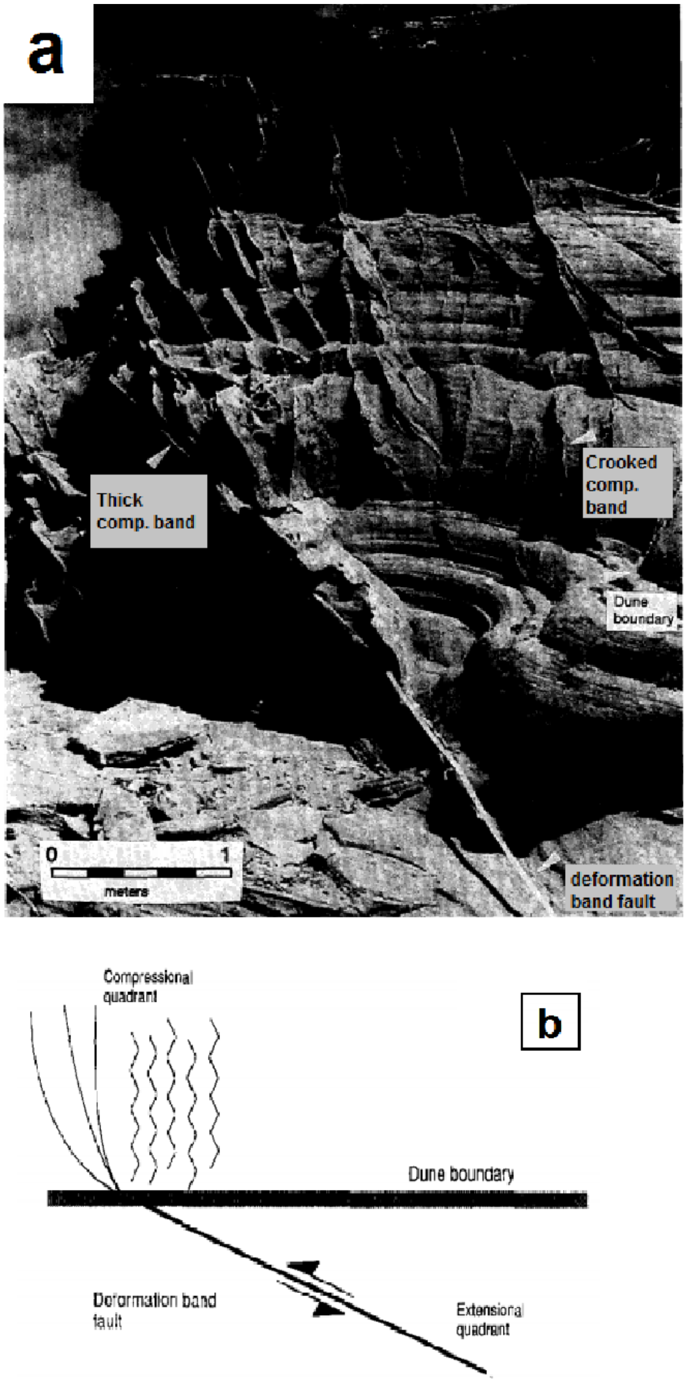

Figure 2.6. Compaction bands in Navajo Sandstone, east Kaibab monocline, Utah. (a) Picture showing compaction bands observed in the compressional quadrant at the tip of a deformation band fault. (b) Mechanical model of the system in (a) (after *Mollema and Antonellini* [1996]).

Antonellini, 1996] and the Valley of Fire State Park area in Nevada [*Sternlof et al.*, 2004]. Despite their infrequent appearance in the field, pure compaction bands were successfully reproduced in physical experiments on sandstones [*Baud et al.*, 2004; *Olsson*, 1999; *Townend et al.*, 2008] and carbonates [*Baud et al.*, 2015; *Baxevanis et al.*, 2006]. Therefore, the reasons of their scarcity in nature remains an open question [*Fossen et al.*, 2011].

Compaction bands appear in the field either as primary structures or subsidiary structures to other primary mechanisms. Examples of the former include compaction bands arrays in the Valley of Fire State Park, southeastern Nevada (Fig. 2.3) and the Buckskin Gulch in Utah (Fig. 2.2). On the other hand, the subsidiary structures are typically found in the close proximity of faults, such as those seen, for example, in the compressional quadrant at the tip of a deformation band fault in east Kaibab monocline, Utah (Fig. 2.6). Other examples of subsidiary compaction bands include those that were seen in the proximity of the Bartlett Fault in Utah (Fig. 2.7), a normal faulting regime. Such arrays are considered a key mechanism in the off-fault damage accumulation during the stages of deformation preceding faulting, especially in high-porosity sandstones [*Shipton and Cowie*, 2003]. Faulting, in fact, is thought to emerge as a result of the transition from strain hardening associated with compaction bands development to localised strain softening as a slip-surface develops (Fig. 2.8).

Various forms of compaction bands may develop in the same formation, such as those that were found in the Buckskin Gulch (Fig. 2.9). Pure compaction bands occur as subvertical structures, These structures were found bisecting conjugate sets of shear-enhanced compaction bands. The shear-enhanced compaction bands commonly form two oppositely dipping sets that mutually cross-cut each other [*Schultz and Siddharthan*, 2005]. Such systems carry numerous questions about their causation, sequentiality, whether one of them

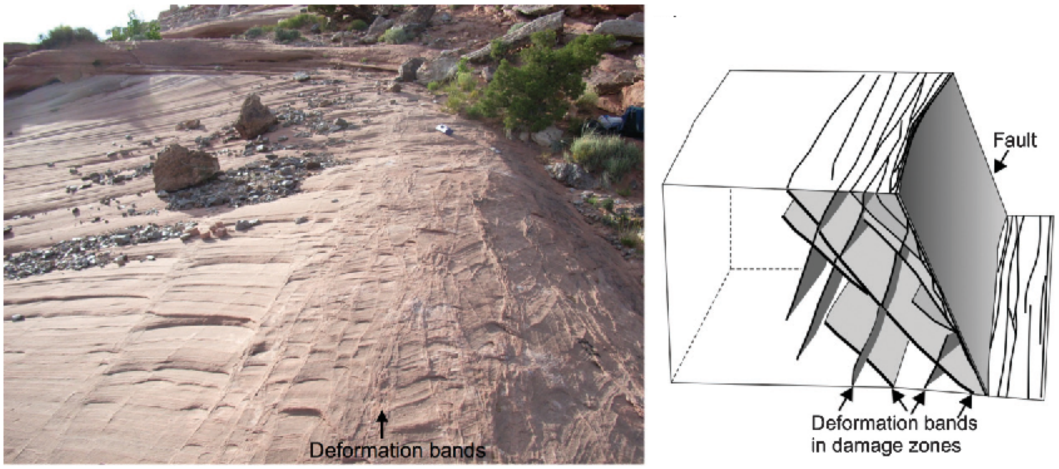

Figure 2.7. Illustration of typical deformation-band fault damage zones in porous sandstones. (a) Fault damage zone of Bartlett Fault, Utah. (b) Schematic illustration of the typical conjugate arrangement of deformation bands in the damage zone around a simple fault (modified from *Fossen and Bale* [2007]).

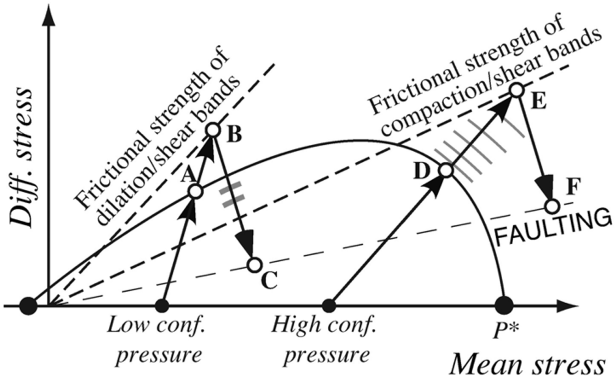

Figure 2.8. Conceptual model of faulting activation following compaction banding. Stress paths AC are for dilatant shear bands, and DF for compactional shear bands. Loading in the compaction regime of hardening rocks leads to expansion in the yield surfaces, showing an activation of faulting by engaging the frictional mechanism (adapted from [*Schultz and Siddharthan*, 2005]).

leads to the other, and the possible geological conditions promoting their emergence. Despite the existence of many theories, much speculation is involved and a robust mechanistic interpretation has not yet been established.

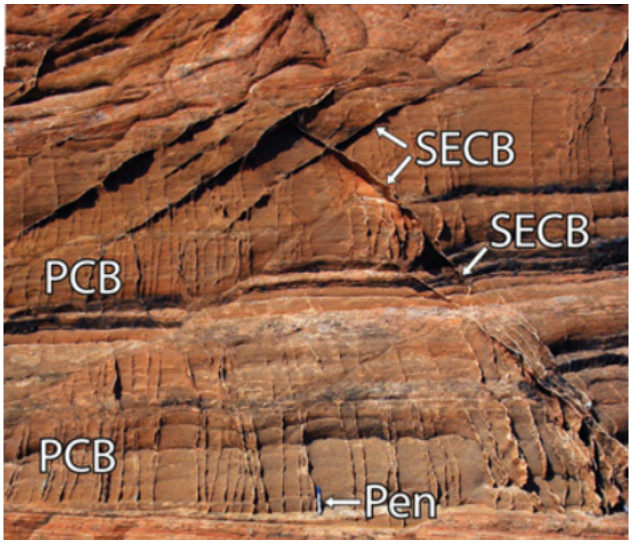

Figure 2.9. Sets of pure compaction bands (PCB) overprinted by shear-enhanced compaction bands (SECB) (adapted from [*Fossen et al.*, 2011]).

Apart from the external factors, the microstrucural factors promoting compaction banding were inspected in petrophysical and geomechanical studies. Most of these studies centered attention on porosity, grain size, and cement content and showed that compaction bands are common in high porosity rocks with a relatively uniform grain size distribution [*Cheung et al.*, 2012; *Fossen and Bale*, 2007; *Katsman et al.*, 2005; *Schultz and Siddharthan*, 2005; *Wang et al.*, 2008]. This trend was found insensitive to the mean grain size [*Cheung et al.*, 2012]. The grain size, however, was found to influence the persistent band thickness (Fig. 2.10). Studies conducted on Leitha limestones brought up intriguing observations, showing that the development of compaction bands occured in some of the less cemented samples, while more cemented end-members failed by cataclastic flow in the compaction regime (i.e., they reached a deviatoric stress plateau through a stage of homogeneous plastic compaction) [*Baud et al.*, 2017].

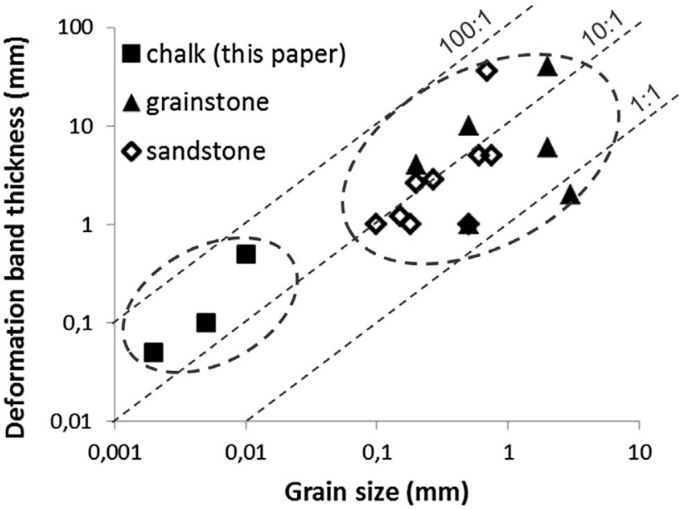

Figure 2.10. Deformation band thickness vs. grain size for chalk, carbonate grainstone and sandstone (after [*Wennberg et al.*, 2013]).

A range of inter-related grain-scale mechanisms, including pore collapse [*Aydin et al.*, 2006], cement debonding [*Wong and Baud*, 2012], grain crushing [*Haimson and Klaetsch*, 2007], sub-critical cracking [*Atkinson*, 1984], and intergranular pressure solution creep [*Croize et al.*, 2013; *Schutjens*, 1991] formed the bases for interpreting the inelastic processes accumulated inside compaction bands. Combinations of these mechanisms appear a nominal characteristic of porous rocks prone to compaction banding. Pore collapse, however, is the most persistent mechanism. Grain crushing and shattering, by contrast, may be absent. For example, in a study conducted on specimens of St. Peter sandstone with different porosity [*Haimson and Klaetsch*, 2007], compaction bands in lower-porosity samples involved heavily crushed grains, while higher-porosity samples developed compaction bands with negligible grain crushing (Fig. 2.11).

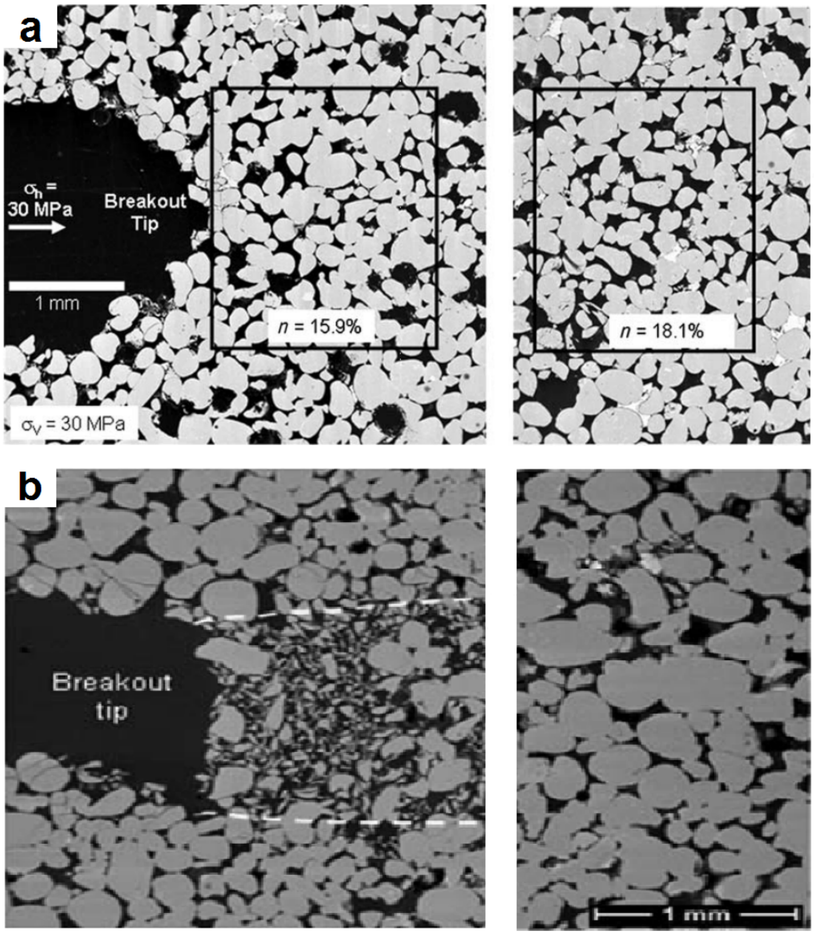

Figure 2.11. Backscattered electron images of the area ahead of the breakout tip in laboratory simulations of borehole stability problem conducted on St. Peter sandstone with intact porosity (a) 18.1% and (b) 12.0% (the intact rock is shown on the right-hand side). The images reveal compaction localization with a zone of porosity collapse with almost intact grains in the high-porosity sample, whereas porosity collapse is blended with grain crushing and shattering in the lower porosity sample (adapted from [*Haimson and Klaetsch*, 2007]).

2.2. Implications for Subsurface Fluid Flow

The pore collapse and solid destructuration render compaction bands structures with detectable deterioration of the hydraulic properties [*Baud et al.*, 2012; *Vajdova et al.*, 2004]. The decay in permeability could be as acute as many orders of magnitude (e.g., Fig. 2.12).

Compaction bands in the Aztec Sandstone, for example, display one order of magnitude permeability reduction [*Aydin and Ahmadov*, 2009], while in other locations, such as the Buckskin Gulch bands in Utah and the Eisenstadt-Sopron Basin on the border between Austria and Hungary showed greater loss in permeability, up to 4 orders of magnitude [*Fossen et al.*, 2011; *Rath et al.*, 2011].

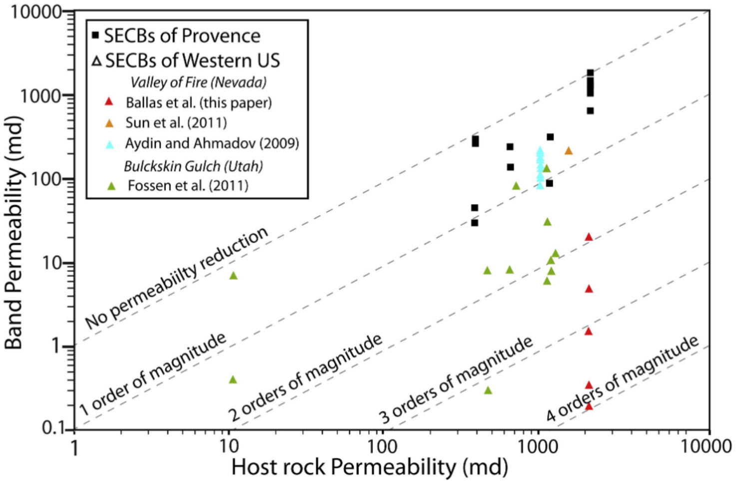

Figure 2.12. Plot of compaction band permeability vs. the host rock permeability. (after *Ballas et al.* [2013]).

The precise causes of the high contrasts in permeability deterioration is not yet fully understood. It is widely accepted, however, that pore collapse and grain crushing are among the most influential factors. Studies based on data synthesized from field and laboratory examples connected the permeability loss primarily to the intensity of grain-crushing [*Ballas et al.*, 2015]. Specifically, higher permeability reduction was found in cataclasite and ultracataclasite bands (e.g. [*Torabi and Fossen*, 2009]), which are typically found in association with normal-faults and at modest (1-3 km) burial depths [*Fossen et al.*, 2007b]. Such conditions are inferred to promote shear-enhanced compaction banding and compactive shear banding.

Inspections of the rock lithologies suggested that the properties of the host-material constitute a second-order factor with high porosity, coarse grain-size and good grain-sorting that were linked to resulting compaction bands with greater permeability variation. The elimination of connected pore space and increased tortuosities due to the porosity decrease are the major factors contributing to the permeability reduction [*Sun et al.*, 2011]. The influence of such local conductivity loss on regional flow and transport characteristics was examined through numerical studies [*Sternlof et al.*, 2006]. These studies pointed out possibilities of aggravation in the pressure gradient required to drive flow through bands arrays up to three times, subsequently leading to more than 50% decay in production efficiency. More recent studies conducted based on sandstone simulations showed that in order for the band to exert influence over reservoirs conductivity, its permeability contrast with reference to the host rock has to exceed 3 orders of magnitude [*Zuluaga et al.*, 2016]. Further studies conducted with reference to carbonate outcrops demonstrated that such a thresholds is dependent on the host-rock permeability [*Rotevatn et al.*, 2017]. Specifically, low-permeability host rocks are more sensitive to the presence of deformation bands compared to host rocks with higher permeability. Such studies have further identified a set of geometrical factors that are relevant to conductivity, including the configuration and connectivity of deformation bands and their mean thickness, and most importantly flaw direction with respect to the alignment of compaction bands.

In this context, compaction banding studies have to address one of the fundamental questions regarding the effects of the mechanical anisotropy of porous rocks on strain localization[*Cilona et al.*, 2014]. The directional disturbance that anisotropy introduces over the stress-strain relationship could inhibit the emergence of compaction bands in specific directions, while promoting them in other directions [*Louis et al.*, 2009]. It could also affect

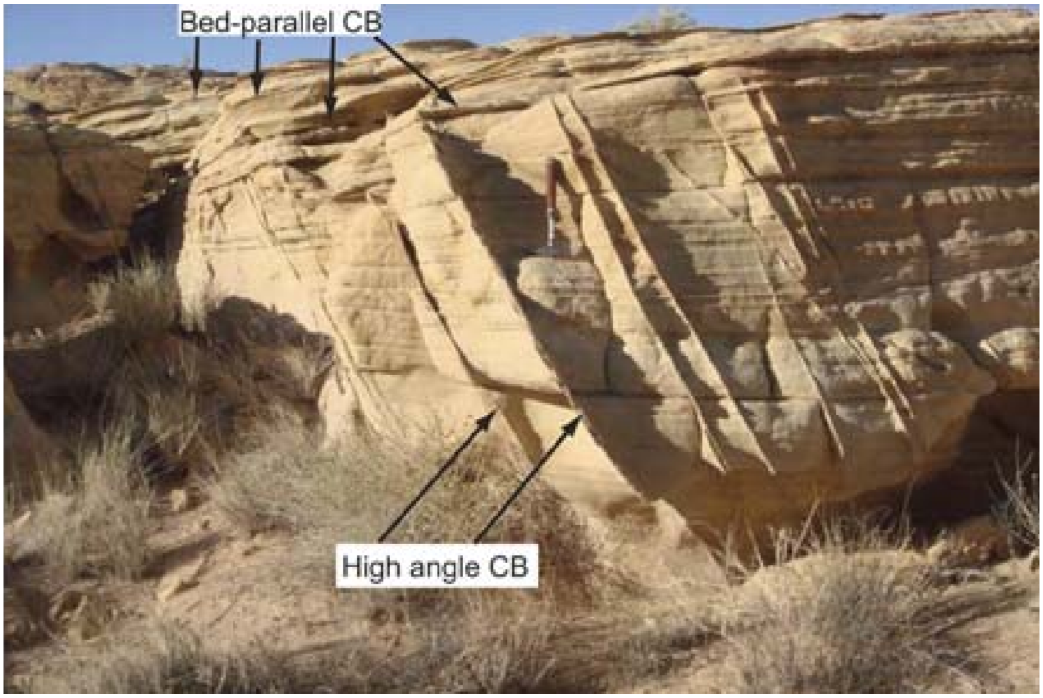

Figure 2.13. Photographs showing examples of various geological structures and their overprinting patterns in the Aztec Sandstone exposed in the Valley of Fire State Park, Nevada. High-angle and bed-parallel compaction bands in cross-section view (after *Zhou et al.* [2014]).

the geometry of the band and its inclination [*Tembe et al.*, 2008] and subsequently be central to the directional permeability of the rock reservoirs [*Baud et al.*, 2012]. Such effects were unequivocally reported from the Aztec Sandstone in Nevada, USA, where the depositional architecture took a marked control over the formation and orientation of compaction localization, resulting in low-angle bed-parallel bands [*Deng and Aydin*, 2012; *Deng et al.*, 2015a,b; *Zhou et al.*, 2014].

2.3. Patterns of Formation and Propagation

By making reference again to the geometrical factors influencing conductivity, field surveys pointed out various forms of compaction-band dispositions, including discrete-band arrays (Fig. 2.2 & 2.3) and band clusters (Fig. 2.14). Band arrays involve multiple bands at almost constant spacing. Band clusters, in contrast, appear as a thick structure of compacted rock with a thickness that could be as big as two orders of magnitude of the thickness of discrete bands. Band clusters are less frequent than band arrays and typically detected in geological systems that involve large deformation (Fig. 2.15). Such variety of dispositions could be explained on the basis of the propagation patterns observed through laboratory studies which have often reported forms of discrete bands growth (Fig. 2.16-a) and thickening bands (Fig. 2.16-b).

Figure 2.14. Deformation-band cluster in the Entrada Sandstone, San Rafael Desert, Utah (after [*Fossen and Bale*, 2007]).

Despite being frequently observed, the precise causes of these various propagation patterns continue to be elusive. Theoretical and numerical studies suggested that hardening

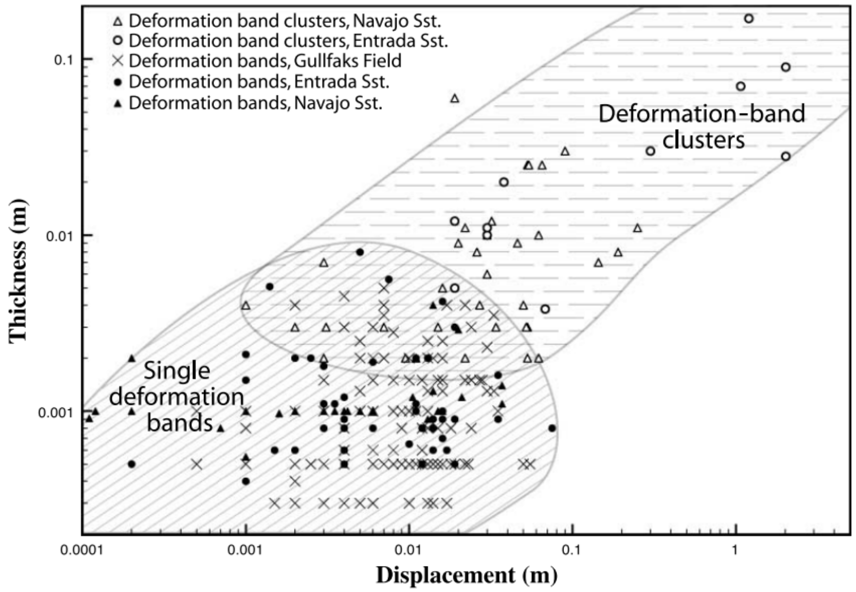

Figure 2.15. Thickness-displacement data for deformation bands (single bands and clusters) (after [*Fossen and Bale*, 2007]).

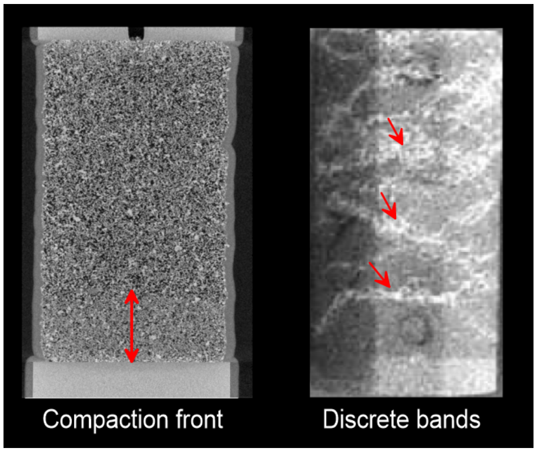

Figure 2.16. Patterns of compaction band propagation: band growing in thickness indicated by a red double-headed arrow (left) and thin bands spread across the specimen indicated by red arrows (right) (source: Ref.s [*Fortin et al.*, 2005; *Tsopela*, 2014])

characteristics take major control over the form of compaction propagation. Specifically, materials with strain hardening properties tend to display compaction banding in form of discrete bands, while materials with softening characteristics tend to compact with thickening bands [*Chemenda*, 2009]. Another theory for interpreting the discrete bands involved viscoplastic analyses explaining discrete bands as the outcome of periodic stress singularities [*Veveakis and Regenauer-Lieb*, 2015; *Veveakis et al.*, 2014]. Although such theory of stress singularities suggests that media with a first-order dissipating mechanism do not develop discrete bands, recent numerical and constitutive models provide contradictory evidence [*Das and Buscarnera*, 2014]. Substantial questions remain surrounding propagation patterns. It is not yet understood whether band thickening and discrete banding are truly different forms of compaction band propagation or simply band thickening is a sub-process that occurs inside a thicker discrete band. The role of material heterogeneity in the context of activating several thickening bands, eventually appearing as discrete bands, has not yet been addressed. This is to say, despite the effort that has been done on this topic, much work has to be done to reach a satisfactory interpretation of propagation patters.

Questions of such kind are corroborated by experimental evidence illustrating the intimate connections between material heterogeneity and compaction propagation. In a study of Bleurswiller sandstone, samples displayed discrete bands propagation (Fig. 2.16-a) over a wide range of confinements [*Baud et al.*, 2015; *Fortin et al.*, 2006]. Early studies [*Fortin et al.*, 2006] attributed the onset of these bands to failure in porosity clusters, whereas more recent studies [*Baud et al.*, 2015] suggested that the poorly sorted granular systems associated with these clusters render them inhibitors of band propagation. More recent studies on Leitha limestone aided by microstructural monitoring provided evidence of major pore collapses in conjugation with compaction localization [*Huang et al.*, 2019]. At variance with these studies, evidence of compaction front propagation from the specimen ends towards its center was very often reported in laboratory simulations (Fig. 2.16-b), and was attributed to the frictional interactions between the specimen and the apparatus platens [*Baud et al.*, 2004; *Castellanza et al.*, 2009; *DiGiovanni et al.*, 2007; *Klein et al.*, 2001; *Valdes et al.*, 2012; *Wong et al.*, 2001]. Such influence of boundary friction of the mode of compaction localization has never been verified. The duality of propagation patterns, however, could indicate a complex interplay between the possible triggering factors, i.e., boundary friction and material heterogeneity. This laboratory-scale problem exemplifies questions of the same kind emerging at larger scale of observation, specifically at the field scale, where more complex boundary conditions and more subtle field heterogeneity are involved.

The rich datasets available about the spatial patterns of compaction bands formation and propagation was recently expanded by laboratory studies focused on their temporal evolution under constant-traction [*Heap et al.*, 2015]. Specifically, transient stages of accelerated deformation have been observed in conjunction with the initiation and propagation of compaction zones during creep tests conducted on samples of Bleurswiller sandstone, a porous rock known to exhibit compaction localization [*Fortin et al.*, 2005]. The samples were subjected to a constant stresses, at and below the level of the inferred yielding threshold, and left to creep over time, revealing growth of compaction zones. Most notably, distinct patterns of temporal evolution of the axial deformation were found (Fig. 2.17), with trends of decaying or growing deformation rate which were assessed as *stable* and *unstable*, respectively. Despite the intriguing implications of these findings in terms of long-term prediction of crustal deformations and reservoir quality deterioration, the literature offers limited tools to explain them and replicate their patterns through computational analyses.

2.4. Analytical Theories and Constitutive Modeling

Theories explaining compaction banding appeared following the work of *Olsson* [1999], who used instability considerations to explain some features of the stress-strain responses obtained through compaction experiments on Castlegate Sandstone. A robust theoretical interpretation of compaction banding, however, was established by *Issen and Rudnicki* [2000], where the constitutive instability formalism of dilating shear bands [*Rudnicki and Rice*, 1975] was shown to encompass also compaction localization for a range of material parameters typical of highly-porous rocks. The *strain localization theory* represents the main reference to identify the conditions at which bifurcated solutions emerge leading to narrow deformation bands. This criterion was combined with elastoplasticity by *Chambon* [1986], suggesting that the criterion of bifurcation can be written as follows:

$$A(\theta) = det[n_j(\theta)(C^{ep}_{ijkl})n_l(\theta)] \leq 0 \tag{2.1}$$

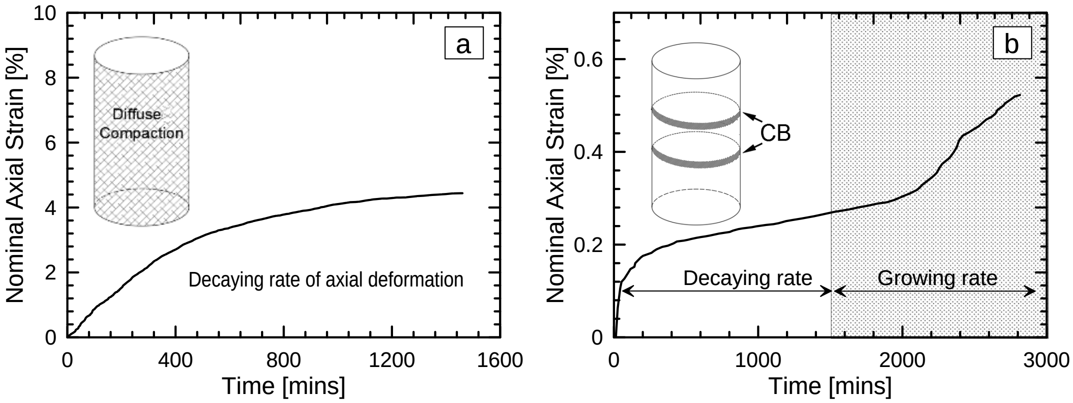

Figure 2.17. Creep test on Bleurswiller sandstone showing the development of time-dependent compaction with distinct patterns of (a) decaying axial deformation rate associated with diffuse (non-localized) compaction, and (b) stages of growing axial deformation rate (hatched zone) associated with the emergence of discrete compaction bands (data after *Heap et al.* [2015]).

Where θ is the angle of a unit vector, n_j, normal to the band, identified with respect to Cartesian coordinate, and C^{ep}_{jjkl} is a fourth-order elastoplastic constitutive tensor. The expression above enables the computation of a *localization profile* for a given stress state, i.e. a representation of the determinant of the acoustic tensor $A(\theta)$ as a function of the band angle θ, thus identifying the states with potentials for strain localization.

The same condition of instability was obtained by *Buscarnera and Nova* [2011] using the so-called "controllability theory", which inspects the ability of a material to sustain incremental perturbations enforced through combinations of stress and/or strain increments [*Imposimato and Nova*, 1998]. In this approach, the uniqueness of the elastoplastic response is examined for a purely compactive mode of localized deformation. The strain jump associated with a compaction band involves a discontinuity of the axial strains and radial stresses (Fig. 2.18). By assuming that the stress-strain response of the material inside and outside the band is represented by the same constitutive tensor, the mechanical response inside the band can be expressed, as follows:

$$\begin{Bmatrix} \Delta\dot{\sigma}_1 \\ \Delta\dot{\sigma}_2 \\ \Delta\dot{\sigma}_3 \end{Bmatrix} = \begin{bmatrix} D_{11} & D_{12} & D_{13} \\ D_{21} & D_{22} & D_{23} \\ D_{31} & D_{32} & D_{33} \end{bmatrix} \begin{Bmatrix} \Delta\dot{\varepsilon}_1 \\ \Delta\dot{\varepsilon}_2 \\ \Delta\dot{\varepsilon}_3 \end{Bmatrix} \tag{2.2}$$

where Δ represents a jump of stress and/or strain measures across the band, and D_{ij} indicates the component of the constitutive tensor. Equilibrium conditions require the continuity of the stresses acting normal to the band (i.e., $\Delta\dot{\sigma}_1 = 0$). Similarly, compatibility requires the continuity of the strain rate components in the plane of the discontinuity (i.e., $\Delta\dot{\varepsilon}_2 = \Delta\dot{\varepsilon}_3 = 0$). These conditions can be expressed by collecting the strain increments controlled by compatibility in a vector, $\Delta\dot{\varepsilon}_\beta = [\Delta\dot{\varepsilon}_2\ \Delta\dot{\varepsilon}_3]^T$, while its work-conjugate counterparts are

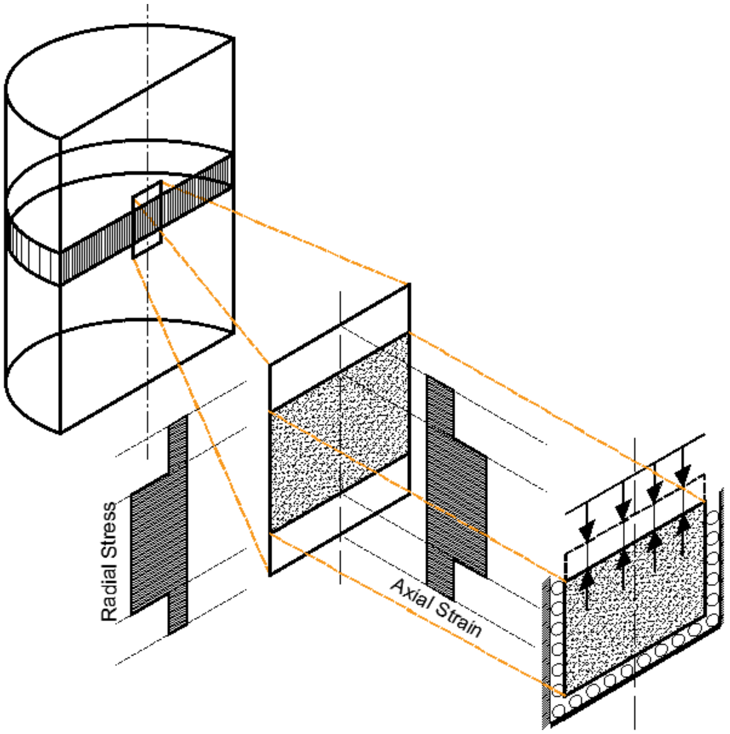

Figure 2.18. Schematic illustration of the kinematic and static conditions associated with compaction banding, showing strain jumps in the axial deformation, and discontinuities in the radial stresses between inside and outside the band.

collected in the stress vector $\Delta\dot{\sigma}_\beta = [\Delta\dot{\sigma}_2 \; \Delta\dot{\sigma}_3]^T$. Rearranging these controls, it follows:

$$\begin{Bmatrix} \Delta\dot{\sigma}_1 = 0 \\ \Delta\dot{\varepsilon}_\beta = 0 \end{Bmatrix} = \begin{bmatrix} D_{11} - D_{1\beta}D_{\beta\beta}^{-1}D_{\beta 1} & D_{1\beta}D_{\beta\beta}^{-1} \\ -D_{\beta\beta}^{-1}D_{\beta 1} & D_{\beta\beta}^{-1} \end{bmatrix} \begin{Bmatrix} \Delta\dot{\varepsilon}_1 \\ \Delta\dot{\varepsilon}_\beta \end{Bmatrix} = \mathbf{X} \begin{Bmatrix} \Delta\dot{\varepsilon}_1 \\ \Delta\dot{\varepsilon}_\beta \end{Bmatrix} \tag{2.3}$$

where $D_{1\beta}$, $D_{\beta\beta}^{-1}$, $D_{\beta 1}$ are partitions of the constitutive matrix. Singularities of the control matrix, $\mathbf{X}$, allow for nontrivial solutions for the axial strain jump and hence for localized compaction. The determinant of $\mathbf{X}$ can be expressed as follows [*Zhang*, 2006]:

$$det\mathbf{X} = det(D_{11})det(D_{\beta\beta}^{-1}) \tag{2.4}$$

which boils down to the condition $det(D_{11}) \leq 0$, which coincides with the compaction localization criterion obtained through the bifurcation theory [*Rudnicki*, 2002].

These two approaches to material instability analyses offer a platform for interpreting instability conditions, especially in rate-independent elastoplastic idealizations [*Chambon*, 1986; *Nova et al.*, 2003]. In this context, the literature offers numerous constitutive models developed for the purpose of reproducing the mechanics of high-porosity rocks. Sophisticated constitutive laws were very often required, as geomaterials display elusive tendencies to dilate or contract depending on the loading path [*Menéndez et al.*, 1996; *Wong and Baud*, 2012; *Wong et al.*, 1997]. This rich variety of deformation responses derives from the competition between numerous inelastic processes, which leads to either softening or hardening depending on the dominant mechanism [*Bésuelle*, 2001; *Bésuelle and Rudnicki*, 2004]. Typical strategies used to replicate the behavior of porous rocks include cap plasticity [*DiMaggio and Sandler*, 1971; *Fossum et al.*, 2000; *Grueschow and Rudnicki*, 2005; *Rudnicki*, 2004] and critical state plasticity [*Carroll*, 1991; *Cuss et al.*, 2003; *Wood*, 1990]. Despite being able to replicate yielding conditions, this class of models often lacked the ability to simultaneously inspect the deformation response and the formation of compaction bands [*Issen and Rudnicki*, 2000; *Issen*, 2002]. In this context, improvements were proposed by Challa and Issen [*Challa and Issen*, 2004] who used multiple yield surfaces to capture this variability. The approach was proved effective in capturing the onset and inclination of the compaction band, yet clear evidence on rheological characteristics has never been demonstrated.

At variance with this class of models, the literature involves sophisticated models that account for the rich mechanisms active in the brittle-ductile transition regime. Models specifically based on the Breakage Mechanics theory [*Das et al.*, 2011] connected internal variables to their underlying micromechanics, thus were particularly useful to illustrate the significance of the grain size distribution and pore collapse on the formation of compaction bands. In the same direction of research, multi-scale modeling approaches, specifically FEMxDEM, were also used to explain the micromechanics associated with compaction banding[*Wu et al.*, 2020]. These studies showed that the phenomenological signatures of compaction banding can be obtained even in the absence of grain crushing.

The strain-hardening elasto-plasticity model adopted in the current study aims to accurately reproduce pre- and post-localization deformations, while enabling the representation of pressure-dependent strain localization patterns. The model was developed in a series of contributions by Nova and coworkers [*Gens and Nova*, 1993; *Lagioia and Nova*, 1995; *Nova et al.*, 2003], and has been selected by virtue of its proven success in capturing the inception and development of plastic compaction under different stress paths and for a variety of boundary conditions [*Arroyo et al.*, 2005; *Buscarnera and Laverack*, 2014; *Das and Buscarnera*, 2014]. The structure of the model is inspired by classical critical state plasticity laws such as Cam clay [*Wood*, 1990], in which a single yield surface evolves homothetically upon plastic deformation is used. The expression proposed by *Lagioia et al.* [1996], was used to describe both the yield surface and the plastic potential, as follows:

$$\left.\begin{matrix} f \\ \\ g \end{matrix}\right\} = \left(A_h^{K_{1h}/C_h} \cdot B_h^{-K_{2h}/C_h}\right) P^\star - P_c^\star = 0 \tag{2.5a}$$

$$A_h = 1 + \frac{\eta^\star}{K_{1h} M_h} \tag{2.5b}$$

$$B_h = 1 + \frac{\eta^\star}{K_{2h} M_h} \tag{2.5c}$$

$$C_h = (1 - \mu_h)(K_{1h} - K_{2h}) \tag{2.5d}$$

$$d = \frac{\dot{\epsilon}_v^p}{\dot{\epsilon}_d^p} = \frac{\partial g/\partial p}{\partial g/\partial q} = \mu_g(M_g - \eta^\star)(\frac{\alpha_g M_g}{\eta^\star} + 1) \tag{2.6}$$

with the functions $K_{1h,2h}$ defined as:

$$K_{1h/2h} = \frac{\mu_h\,(1-\alpha_h)}{2\,(1-\mu_h)}\left(1 \pm \sqrt{1 - \frac{4\alpha_h\,(1-\mu_h)}{\mu_h\,(1-\alpha_h)^2}}\right). \tag{2.7}$$

p and q represent the mean and deviator stresses, respectively, while $\eta^\star$ is the corresponding stress ratio, defined as follows:

$$p = \frac{1}{3}\sigma_{ij}\delta_{ij} \quad q = \sqrt{\frac{3}{2}s_{ij}s_{ij}} \quad \eta^\star = \frac{q}{p+P_t} \tag{2.8}$$

in which $s_{ij} = \sigma_{ij} - p\delta_{ij}$, δ_{ij} is the Kronecker delta. Under axisymmetric compression, p and q are be specified as following:

$$p = \frac{\sigma_1 + 2\sigma_3}{3} \quad q = \sigma_1 - \sigma_3, \tag{2.9}$$

with σ_3 the minimum principal stress. The variable $P_c^\star$ represents the hydrostatic yield stress and is defined through an additive combination of the hardening variables P_s and P_m (i.e., $P_c^\star = P_s + P_m + P_t$ where P_t indicates the tensile strength and is equal to $P_t = kP_m$). The former variable incorporates the contribution of the skeleton packing, while P_m mimicks the inter-granular cementation. The shape of the two surfaces in Eqs. (C.9) is controlled by the shape parameters, M_h, μ_h, and α_h, for which the subscript h makes reference to either the yield surface ($h \equiv f$) or the plastic potential ($h \equiv g$). These expressions provide considerable flexibility to fit experimental data, in that distinct sets of shape parameters can be used to adjust the degree of non-associativity and the shape of the elastic domain. The evolution of the hardening variables (i.e., P_s and P_m) is governed by the following rules:

$$\dot{P}_s = \frac{P_s}{B_p}\dot{\varepsilon}_v^p \tag{2.10}$$

$$\dot{P}_m = -\rho_m P_m(|\dot{\varepsilon}_v^p| + \xi_m \dot{\varepsilon}_s^p), \tag{2.11}$$

where B_p, ρ_m and ξ_m are material parameters. P_s reproduces mechanisms associated with porosity changes (thus incorporating hardening in compacting geomaterials and softening in dilative geomaterials). By contrast, P_m introduces softening mechanisms due to both volumetric and deviatoric plastic strain. The interplay between these variables leads to a homothetical contraction/expansion of the yield surface, which affects the accuracy with which localization processes and post-localization deformation are captured. This constitutive law can be used in its original rate-independent form, according to which the plastic strains are obtained through a standard consistency condition, as follows:

$$\dot{\varepsilon}_{ij}^p = \Lambda \frac{\partial g}{\partial \sigma_{ij}} \tag{2.12}$$

with Λ being a non-negative plastic multiplier. However, a simple adaptation of the model to viscoplastic form allows the simulation of rate-dependency and creep. For this purpose, the inelastic strain rate in Eq. (12) can be replaced by the viscoplastic strain rate, $\dot{\varepsilon}_{ij}^{vp}$, which is computed through a viscous nucleus function Φ which depends on the violation of the plastic constraints (i.e., on the distance between the stress state lies outside the elastic domain and the yield surface, often referred to as overstress):

$$\dot{\varepsilon}_{ij}^{vp} = \Phi(f)\left[\frac{\partial g}{\partial \sigma_{ij}}\right]. \tag{2.13}$$

$$\Phi(f) = \mu \left[\frac{\langle f \rangle}{P_{co}} \right] \tag{2.14}$$

where P_{co} is the initial hydrostatic yielding stress, the symbol $\langle \bullet \rangle$ indicates the McCauley brackets and μ is a fluidity parameter (i.e., the inverse of viscosity). Isotropic linear elasticity is here employed to compute the increment of the stress state $\dot{\sigma}_{ij}$ through the standard relation:

$$\dot{\sigma}_{ij} = D^e_{ijkl} \dot{\varepsilon_{kl}}^e \tag{2.15}$$

where ε^e_{kl} is the elastic strain tensor, and D^e_{ijkl} is the isotropic linear elastic tensor.

2.5. Thesis Goals

The research presented in this thesis addresses some open questions that are singled out here below, while the following chapters illustrate the work that has been conducted to achieve that.

- Is it possible to establish a unified theoretical framework to identify both the time-dependent and time-independent unstable compaction?
- How do the spatial heterogeneity and boundary conditions interact to affect the nucleation and propagation of compaction bands?
- Can geomechanical models explain the coexistence of different forms of compaction bands and identify whether their emergence is contemporaneous of not?

CHAPTER 3

Viscoplastic Interpretation of Compaction Localization*

Compaction localization is usually interpreted through the bifurcation theory, based on which critical values of hardening modulus associated with the vanishing of the acoustic tensor can be defined at the onset of compaction bands [*Issen and Rudnicki*, 2000]. These methods, however, are applicable for elastoplastic constitutive laws, which are notoriously unable to reproduce time-dependent features. Viscoplastic constitutive laws are used as alternatives to simulate the rate- and time-dependence of the rock behavior, and as a regularization strategy to suppress the ill-posedness associated with full-field strain localization analyses. In such cases, however, localization analyses cannot be conducted through the same techniques developed for rate-independent plastic models, in that a tangent constitutive tensor between stress and strain increments is no longer defined [*Needleman*, 1988].

In this chapter, these limitations are circumvented by providing an interpretation of stable and unstable compaction creep which reflects the temporal dynamics underlying the viscoplastic rock behavior, but at the same time it is also consistent with the standard indices used to differentiate homogeneous and localized compaction. Specifically, reference is made to the mathematical formalism introduced by *Pisanò and di Prisco* [2016] to identify instabilities in viscoplastic solids. According to this approach, the delayed deformation of

---

*The content of this chapter is published in:

- Shahin, G., Marinelli, F., and Buscarnera, G. (2019). Viscoplastic interpretation of localized compaction creep in porous rock. Journal of Geophysical Research: Solid Earth, 124(10), 10180-10196.
- Shahin, G. and Buscarnera, G. (2019, August). Numerical simulation of localized compaction creep in heterogeneous porous rock. In 53rd US Rock Mechanics/Geomechanics Symposium. American Rock Mechanics Association.

a viscoplastic material can be expressed in terms of multiple ordinary differential equations (ODEs), each associated with a stress/strain variable describing the evolution of the current state. From a mathematical standpoint, this methodology bears resemblance with the study of Lyapunov stability in multi-variable dynamic systems [*Hale and Koçak*, 2012]. From a geomechanical standpoint, it is an effective platform to cope with kinematics constraints due to the presence of pore fluids, as recently shown for the liquefaction of loose granular solids at variable degrees of saturation [*Marinelli and Buscarnera*, 2018; *Marinelli et al.*, 2017]. Hereafter, it will be shown how this formalism can be generalized to compaction creep in porous rocks, especially for problems characterized by a marked potential for compaction localization.

3.1. Stability Criteria for Viscoplastic Solids

The time-dependent behavior of porous rocks is modeled through the overstress approach proposed by the pioneering work of Perzyna [*Perzyna*, 1966], which has been successfully used to reproduce the rate-dependent characteristics of a wide range of granular solids, [*di Prisco et al.*, 2000; *Lazari et al.*, 2018; *Tommasi et al.*, 2000; *Yin et al.*, 2010]. Under suitable conditions, such constitutive framework can suppress the ill-posedness associated with strain localization and restore the uniqueness of the field equations [*Needleman*, 1988]. However, material instability can still be found in the form of sharp variations in the temporal evolution of the material response. In this context, *Oka et al.* [1994] formulated a strategy to detect the onset of instabilities by showing that the inception of accelerating trend of behavior during creep (i.e., an unstable response) can be identified by rearranging the constitutive equations into an ODE. More recently, *Pisanò and di Prisco* [2016] generalized this idea to multidimensional systems characterized by a wider set of kinematic constraints, thus providing a direct link between the inception of accelerating response and the instability indices derived through controllability analyses [*Buscarnera et al.*, 2011; *Imposimato and Nova*, 1998; *Nova*, 1994].

According to this approach, the constitutive response can be reformulated as follows:

$$\dot{X} = \mathbf{A}X + F \tag{3.1}$$

where X and $\dot{X}$ are the rate and the acceleration of the selected response variables, respectively. $\mathbf{A}$ is a constitutive operator governing the evolution of the system, and F is a forcing term associated with the imposed controls. It can be readily shown that, during stages of creep, the external forcing vanishes and the spontaneous evolution of the system in proximity of a given stress state is uniquely controlled by the local characteristics of $\mathbf{A}$, which can be inspected by studying the corresponding set of eigenvalues. Specifically, negative eigenvalues indicate local exponential decay of the response variables (i.e., a response characterized by a stable trend of behavior), while positive eigenvalues indicate an incipient accelerating growth of the same variables (i.e., unstable response).

Time-dependent compaction localization can also be studied through this formalism, which yet requires the development of consistent instability criteria. As a result, Eq. 3.1 is a useful tool to accomplish this goal, provided that the local static/kinematic conditions active within a deformation band formation can be defined. This is simple for pure compaction bands, in that they involve a local strain jump characterized by uniaxial deformation (i.e., orthogonal to the band and characterized by lack of lateral extension/contraction [*Issen and Rudnicki*, 2000]). These conditions resemble the kinematic constraints applied during oedometric (radially constrained) compression [*Arroyo et al.*, 2005; *Buscarnera and Laverack*, 2014] and can be readily inspected at a material-point level by considering axisymmetric stress conditions. Specifically, a potential compaction band during creep would involve a constant axial stress (i.e., $\dot{\sigma}_a = 0$), as well as a constrained radial strain (i.e., $\dot{\epsilon}_r = 0$) as controlled variables (Fig. 2.18). For this multi-variable system, the kinematics of the strain jump in the active zone of localized compaction can be described through a system of ODE compatible with Eq.3.1 in which the axial strain and the radial stress define the vector of the response variable X (i.e., $X = \dot{\epsilon}_a\ ,\ \dot{\sigma}_r$). As a result, the underlying system of ODEs governing this particular uniaxial deformation process can be written as follows:

$$\begin{Bmatrix} \ddot{\varepsilon}_a \\ \\ 2\ddot{\sigma}_r \end{Bmatrix} = \begin{bmatrix} -\dfrac{\partial \Phi}{\partial f} H_{CB} & \dfrac{\nu}{1-\nu}\Phi\dfrac{\partial^2 g}{\partial \sigma_r^2} + \Phi\dfrac{\partial^2 g}{\partial \sigma_a \partial \sigma_r} \\ \\ 0 & -\dfrac{\partial \Phi}{\partial f} H_{CB} - \dfrac{2E}{(1-\nu)}\Phi\dfrac{\partial^2 g}{\partial \sigma_r^2} \end{bmatrix} \begin{Bmatrix} \dot{\varepsilon}_a \\ \\ 2\dot{\sigma}_r \end{Bmatrix} + \mathbf{F} \tag{3.2}$$

where E and ν indicate the Young's modulus and Poisson's ratio, respectively, while H_{CB} represents the instability index for the selected controlled conditions, defined as:

$$H_{CB} = H - H_{\chi} + \frac{H_{\sigma\varepsilon}}{\Phi}. \tag{3.3}$$

Where $H_{\sigma\varepsilon}$ is a term dependent on the loading rate, H is the hardening modulus and H_{χ} represents the controllability index derived by *Buscarnera and Laverack* [2014] in the framework of rate-independent plasticity by enforcing the kinematic conditions typical of a pure compaction band:

$$H_{\chi} = -\frac{\partial g}{\partial \sigma_r}\frac{E}{2(1-\nu)}\frac{\partial f}{\partial \sigma_r}. \tag{3.4}$$

The derivations leading to this system of ODEs are provided in Appendix A. It is worth remarking that, in case of creep, the ODEs described in Eq. 3.2 can be rewritten in a compact form (i.e., $\dot{X} = \mathbf{A}X$) resulting from the lack of forcing (i.e., $F_\varepsilon \equiv 0$ and $F_\sigma \equiv 0$, as well as $H_{\sigma\varepsilon}$=0). As a result, due to the lack of coupling between the response variables, $\dot{\epsilon}_a$ and $\dot{\sigma}_r$, the local stability of the system can be evaluated by tracking the sign of the eigenvalues of $\mathbf{A}$, which correspond to the diagonal terms:

$$\lambda(\mathbf{A}) \rightarrow \begin{cases} \lambda_{\varepsilon_a} = -\dfrac{\partial \Phi}{\partial f} H_{CB} \\ \lambda_{\sigma_r} = \lambda_{\varepsilon_a} - \dfrac{2E}{(1-\nu)} \Phi \dfrac{\partial^2 g}{\partial \sigma_r^2} \end{cases} \tag{3.5}$$

The process is locally stable if both eigenvalues are *negative* [*Pisanò and di Prisco*, 2016], thus implying that the response variables exhibit a decaying trend of behavior. By contrast, if at least one of the two eigenvalues is non-negative, the process can be regarded as unstable, in that it exhibits an accelerated evolution of the corresponding response variable. Furthermore, by observing Eq. 3.5, it can be noticed that when the stress state implies $\lambda_{\varepsilon_a} \geq 0$, the eigenvalue λ_{σ_r}, related with the radial stress is either positive or could be negative depending on the magnitude of its second term. This result indicates that the evaluation of λ_{ε_a} is sufficient to assess the stability of the stress state.

3.2. Constitutive Modeling of Bleurswiller Sandstone

The material selected for this study is the Bleurswiller sandstone, a porous rock known to develop compaction bands over a wide range of confinements [*Fortin et al.*, 2005], and recently studied by *Heap et al.* [2015] through triaxial creep experiments. In this context, *Marinelli and Buscarnera* [2015] proposed the use of a constitutive model based on prior contributions by Nova and coworkers [*Lagioia and Nova*, 1995; *Nova et al.*, 2003] and discussed in (Section 2.4).

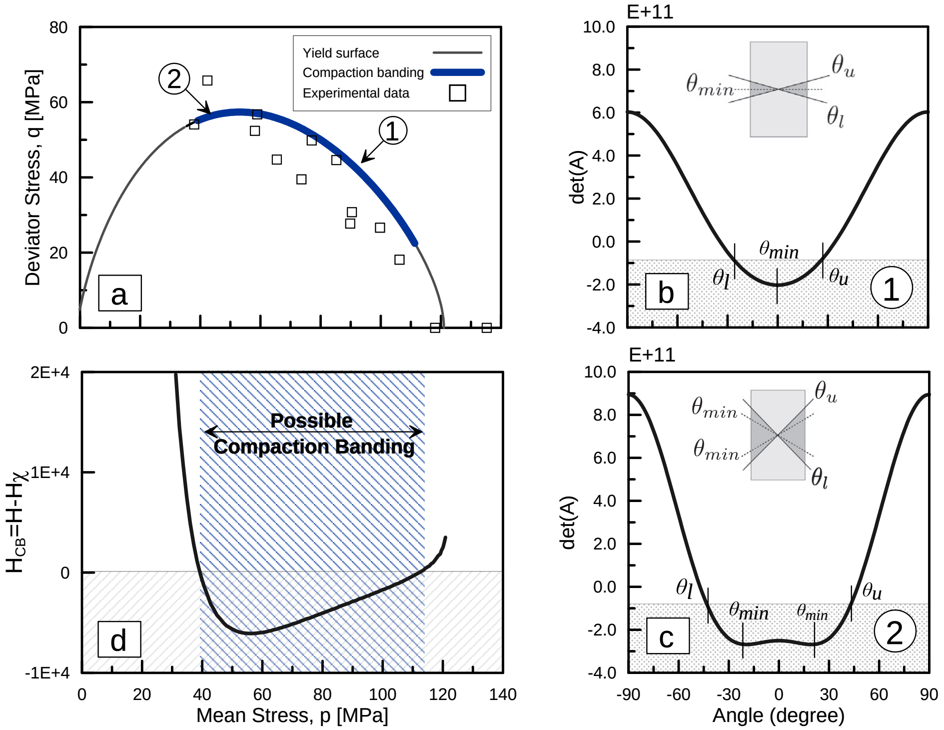

Figure 3.1. Compaction band analysis for Bleurswiller sandstone. (a) Yield surface and measured yielding points at which compaction band was detected; the thick line indicates the predicted domain of localized compaction. (b-c) Localization profile at two different stress states (marked as 1 and 2 in (a)), showing the evolution of the acoustic tensor determinant as a function of the band angle. (d) Computed instability index showing compatibility with predictions based on the bifurcation theory.

The calibration procedure conducted by *Marinelli and Buscarnera* [2015] for the Bleurswiller sandstone(Table 3.1) was based on the experimental data reported by *Fortin et al.* [2005]. Such procedure relied on the strain localization theory, thus identifying the conditions at material point level that are conductive of bifurcated solutions. An example of this strategy is illustrated in Fig. 3.1 in which the stress states predicting localized compaction in the form of horizontal bands (i.e., $\theta_{min} = 0$) are plotted at initial yielding with a solid blue line, thus identifying the so-called *localization domain*. In particular, a transition from pure

Table 3.1. Constitutive parameters and internal variables for Bleurswiller sandstone calibrated by *Marinelli and Buscarnera* [2015].

	Definition	
K [MPa]	Bulk modulus	9100
G [MPa]	Shear modulus	6000
ρ_m	Parameter governing volumetric destructuration	3.0
ξ_m	Parameter governing deviatoric destructuration	2.0
B_p	Isotropic plastic compressibility	0.026
μ_f	Shape parameter of yield surface	1.01
α_f	Shape parameter of yield surface	0.11
M_f	Shape parameter of yield surface	1.06
μ_g	Shape parameter of plastic potential	1.55
α_g	Shape parameter of plastic potential	1.2
M_g	Shape parameter of plastic potential	1.75
κ	Expansion of yield surface in the tensile stress domain	0.01
μ [MPa.s]	Fluidity factor	5.0E-4
P_{so} [MPa]	Initial size of the elastic domain (cohesionless medium)	15
P_{mo} [MPa]	Lithification-induced expansion of the initial elastic domain	106

compaction bands (i.e., $\theta_{min} = 0$) and shear-enhanced compaction bands (i.e., $\theta_{min} > 0$) can be seen in Fig. 3.1c, thus emphasizing the possible coexistence of different strain localization mechanisms. From Fig. 3.1a it is readily apparent that the bifurcation conditions are satisfied over a wide range of confinements spanning from 40 to 112 MPa, consistently with the experimental evidence reported in Fig. 3.1a (i.e., data points showing stress states at which compaction localization was observed). These results, here obtained by employing the localization theory [*Rudnicki and Rice*, 1975], can be recovered also by using controllability indices [*Imposimato and Nova*, 1998; *Nova*, 1994] adapted for the control conditions characterizing the kinematics of a compaction band. Specifically, as shown by *Buscarnera and Laverack* [2014], it is possible to make reference to the index $H_{CB} = H - H_{\chi}$ associated with pure compaction bands (Fig. 3.1d).

The performance of the model is further illustrated with reference to a set of simulated triaxial compression tests. Fig. 3.2 shows the predicted response under 40-, 60-, 80-, and 100-MPa confinement pressure. The comparison against corresponding measurements illustrates a satisfactory agreement between model simulations and experimental data. As a result,

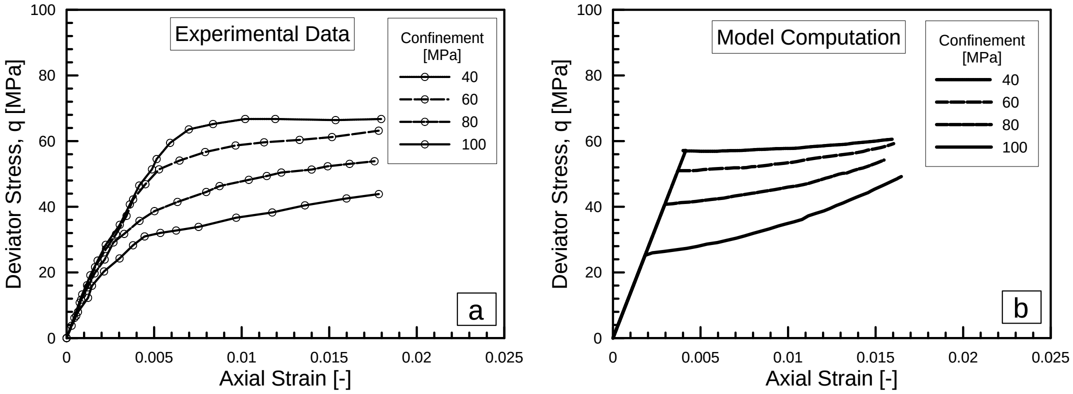

Figure 3.2. Comparison between (a) experiments and (b) material point simulations of triaxial compression on Bleurswiller sandstone specimens (data after *Fortin et al.* [2005]).

this constitutive law will be used in the following to discuss the temporal development of compaction bands in light of a viscoplastic enhancement of the constitutive equations.

3.3. Interpretation of Compaction Creep

To illustrate the connection between the phenomenology of compaction creep and concepts of viscoplastic instability, a particular stress path has been computed at the material point level. Such path consists of two stages: *i)* a triaxial compression used to bring the stress state in the proximity of the initial yield surface, *ii)* a creep stage performed to analyze the evolution of the strain over time, in which the control conditions were switched to radially-constrained deformation in order to replicate the kinematics of compaction bands.

Two values of initial confinement have been selected as end-members of creep compression, namely $P_1 = 80$ MPa (at which the creep phase starts from a stress state within the localization domain) and $P_2 = 115$ MPa (at which the creep phase starts from a stress state outside the localization domain). The results of the analyses are illustrated in Fig. 3.3 which are here explained in light of the theory presented in Section 3.1.

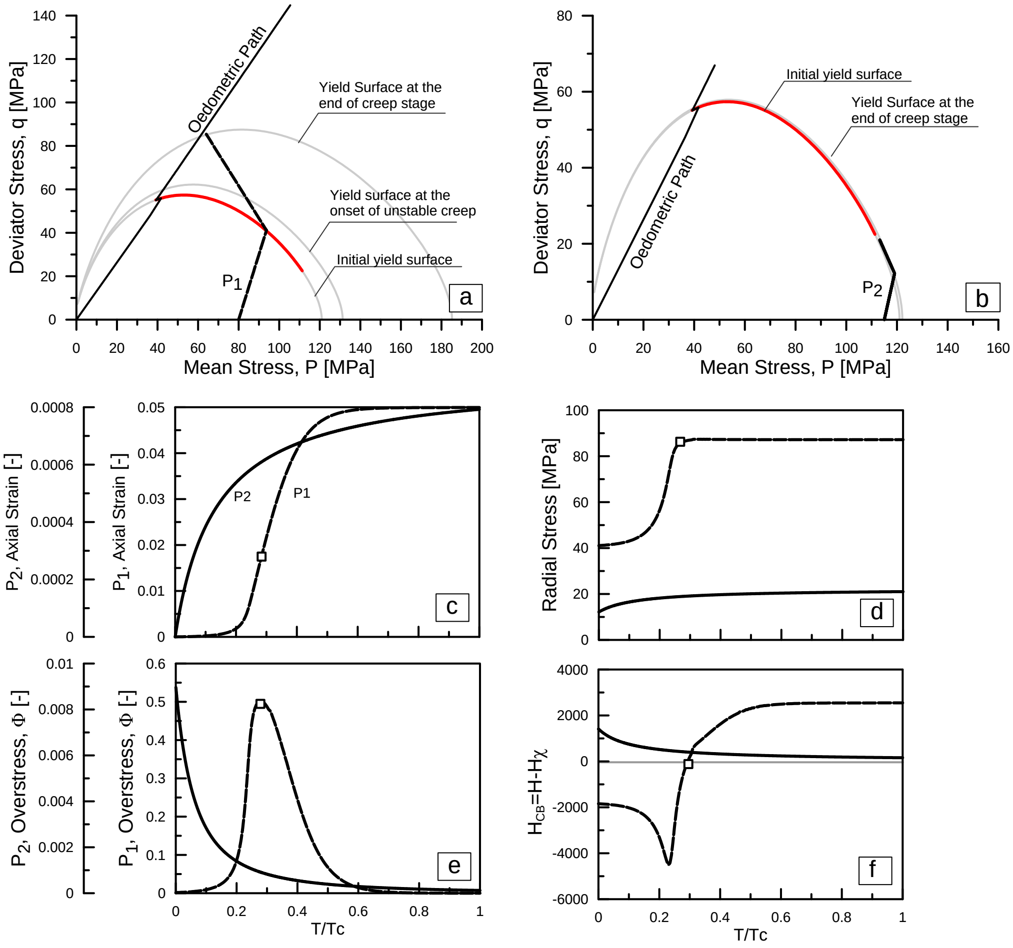

Figure 3.3. Material point analyses of constant-stress axisymmetric test preceded by triaxial loading. (a) Path P_1 with initial confinement of 80 MPa, intersecting with the yield surface inside the compaction localization domain predicted based on the theory of Bifurcation. (b) Path P_2 with initial confinement of 115 MPa, intersecting with the yield surface outside the localization zone. (c) Axial strain evolution during creep stage for both paths. The first path displays a transition from accelerated to decelerated axial strain rate (the point of transition is marked by a hollow square); the second path displays a decay pattern over the entire simulation. (d) Evolution of deviatoric stress. (e) Mobilized overstress (P_1 exhibits a peak, whereas P_2 displays an overall decaying trend). (f) Variation of the instability index H_{CB} for both paths, where the first path is associated with initially negative value indicating unstable response. The second path displays positive index indicating stable response. T indicates the current creep time, while Tc is the total creep time.

It can be seen that, in both cases, the creep stage involved an expansion of the yield surface, with a stress path typical of constant axial-stress deformation. A close look at the simulation of 80 MPa reveals that the evolution of the stress state and the expansion of the yield surface display detectable differences in terms of the rate of evolution. Specifically, upon setting the material under oedometric conditions the stress response evolves rapidly. The expansion of the yield surface appears to develop at a markedly lower rate. When the stress response reaches what appears as a stabilization state, the accumulated deformation is around half the total required deformation necessary to diminish the accumulated overstress. To further elucidate these dynamics, the evolution of the axial strain is depicted in Fig. 3.3c, plotted as a function of the normalized time (i.e., the ratio between the actual elapsed time and the whole duration of the creep simulation). It can be seen that distinct patterns of strain evolution are associated with these stress paths. The strain response associated with P_1 can be characterized by an initially growing rate of evolution, followed by stages of deceleration. At variance, the strain response associated with P_2 is characterized by a decaying trend of evolution throughout. Similar patterns of evolution can be seen in the radial stress responses (Fig. 3.3d), where P_1 is accompanied with an initially accelerating stress response followed by stages of deceleration, whereas P_2 evolves with a decelerating form along the entire path.

As mentioned above, the adopted viscoplastic model allows the stress state to lay outside the yield surface. This violation controls the magnitude of the overstress, Φ, and in turn the viscoplastic strain rate. As a result, the temporal dynamics of creep (i.e., whether the strain accelerates or decelerates) depends on the relative movement of the stress state and yield surface, which are in turn controlled by the static/kinematic constraints (i.e., the strain jump) and the hardening characteristics of the material. Fig. 3.3e presents the evolution of the overstress for the two stress paths. It can be seen that P_1 is associated with a simultaneous pulse of overstress with a peak that coincides with the point of transition from the domain of instability to the domain of stability (Fig. 3.3f). At variance, the overstress evolves with a decaying trend in P_2, where the instability index indicates stable states throughout (Fig. 3.3f). The white marker indicates the point of transition from accelerating to decelerating growth rate in the axial strain, revealing that the stages of instability, spontaneous mobilization of overstress pulses, acceleration in the radial stress, and the accelerated growth in the axial strain are nearly synchronized.

On the ground of this analysis, the domain of instability in the stress space can be identified through numerical integration. Along triaxial probes, the local instability is evaluated by tracking the sign of the instability index along the path. The domain of instability is displayed along with the stress paths, P_1 and P_2, in Fig. 3.4b. It can be noticed that the point of intersection between P_1 and the yield surface occurs within the zone of instability, followed by stress growth that stabilizes at the boundaries of the instability domain. By contrast, the intersection between P_2 and the yield surface and its entire evolution locates outside the instability domain.

.

3.4. Finite Element Simulation of a Creep Test

Material-point analyses describe idealized homogeneous processes which should be regarded only as approximations of real experiments. Hereafter, a numerical simulation based on the Finite Element (FE) method is used to illustrate the spatio-temporal richness of localized compaction creep, as well as to explain the full-field behavior of rock samples in light of the viscoplastic theory discussed previously.

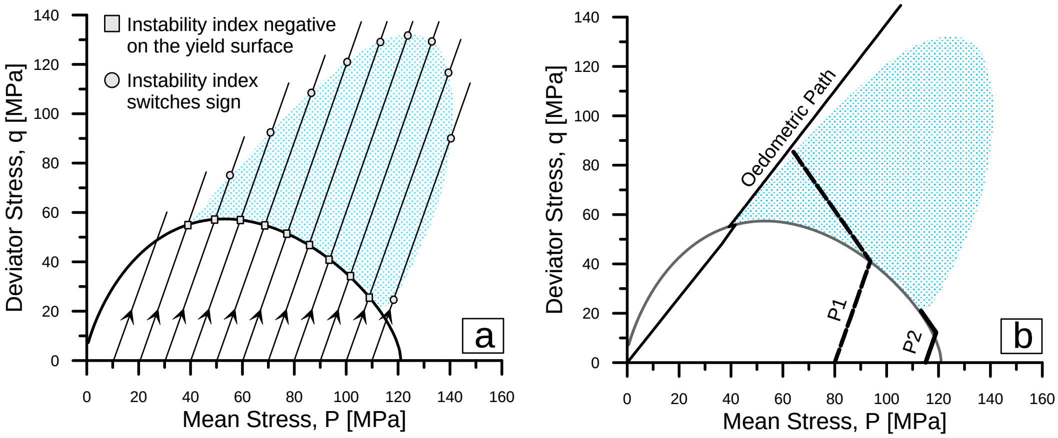

Figure 3.4. Identification of stress states of unstable creep. (a) Stress paths used to identify unstable states (shaded region). Triaxial probes at various confinement pressures are integrated and the state is marked unstable if the corresponding index is negative. (b) Depiction of the location of the stress paths P_1 and P_2 with respect to the detected instability zone. Path P_1 crosses the yield surface within the unstable zone, whereas path P_2 is always located outside the shaded area.

The numerical test is conducted with reference to a cylindrical specimen with aspect ratio height/diameter = 2. The purpose of the analysis is to replicate the testing procedure discussed by *Heap et al.* [2015] in a controlled numerical setting. The specimen is discretized by a finite element mesh consisting of more than 75,000 4-node tetrahedral linear elements. A single element is assigned 98% of the hydrostatic yielding pressure prescribed throughout the rest of the domain. This weak element promotes the triggering of strain localization by altering the homogeneity of deformation field. The boundary conditions set at the base of the specimen include fixed vertical displacements and a node with no horizontal translation to prevent rigid body motion. The numerical specimen is subjected to two-step loading paths consisting of a displacement-controlled shearing followed by force-controlled creep. An initial confinement pressure (here 80 MPa) is imposed by applying on each boundary a normal

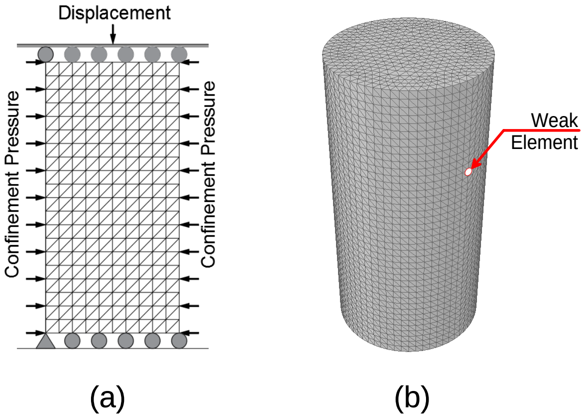

Figure 3.5. Illustration of the finite element model used for triaxial test simulations. (a) Specimen section showing the finite element mesh and the boundary conditions; (b) Location of the weak element in a 3D cylindrical sample.

pressure in equilibrium with an equivalent internal stress state. The radial pressure is then kept constant and the nodes at the top boundary are translated vertically during triaxial shearing, and then subjected to constant traction during creep. The imposed axial strain rate during the shearing stage is set to $1.0E-5\ s^{-1}$, in agreement with the experiments here used as a reference. Once the desired stress level is attained, the traction at the top boundary is kept constant and the specimen is left to creep over time. A schematic illustration of the FE model and its boundary conditions are illustrated in Fig. 3.5.

The response of the specimen is inspected from two standpoints. First, the averaged vertical traction at the base (i.e., the reaction provided by the specimen to the imposed axial deformation) is reported along with the response computed based on displacement-controlled simulation in Fig. 3.6a. The vertical displacement at the top boundary is reported as a function of time in Fig. 3.6b (continuous line). It can be seen that the numerical specimen has reproduced essential features of the physical experiment of *Heap et al.* [2015] (see also to Fig. 2.17), specifically exhibiting three stages of deformation: initially a decaying trend of evolution followed by stages of acceleration and then deceleration in creep deformation.

The evolution of the strain field that accompanies these forms of deformation response is illustrated in Fig. 3.6d, which shows the volumetric plastic strain field at various deformation intervals, noted by Ci where $i = 1 - 6$. It can be seen that the specimen exhibits a propagation of discrete bands which spread sequentially across the domain, starting from the second interval C_2 and span up to $C4$. Afterwards, compaction propagates in the form of a band thickening from the compacted zones at $C4$ until the entire specimen is compacted. By comparing the strain field evolution with its counterpart obtained from compression loading (Fig. 3.6c-Li where $i = 1 - 6$.), it can be readily seen that the propagation patterns are comparable, in that both cases display similar forms of discrete bands propagation followed by thickening bands. These predictions are also in part corroborated by experimental observations based on maps of acoustic emission measurements documented by *Heap et al.* [2015], which reported the location of active compaction banding by identifying multiple discrete bands that formed across the specimen during the initial stages of compaction propagation. Although the resolution of the measurements does not provide conclusive evidence for the presence of a subsequent stage of band thickening, other tests conducted by *Fortin et al.* [2009] on the same sandstone suggest a more wide spread emission zone adjacent to discrete bands, which may be consistent with the band thickening process predicted by the numerical model.

Despite the similarities between the imposed-deformation simulation and the traction-fixed simulation, some important differences can be seen. For example, the emergence of a well-defined compaction band required a larger deformation interval in the displacement-controlled simulation. The first band can be seen after considerable interval of deformation

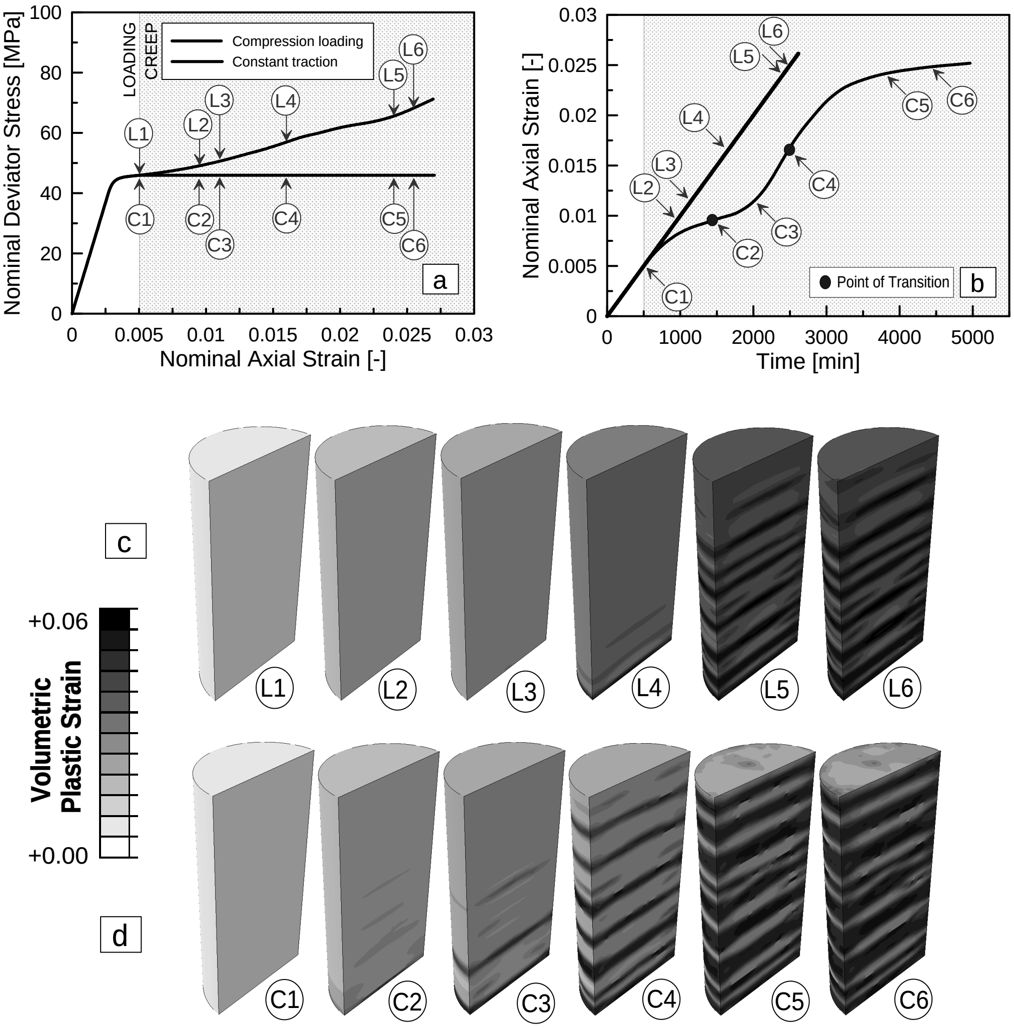

Figure 3.6. Finite element simulation of constant-stress test shown compared against a simulation of imposed deformation at constant strain rate. (a) Response of the specimen for constant-traction and constant-deformation-rate simulations. (b) Temporal evolution of vertical deformation normalized by the specimen height. The shadowed domain in a and b indicates the creep stage. (c) The cumulative volumetric plastic strain field of the constant-strain-rate simulation (indicated by the letter L in subfigure (a)). (d) The cumulative volumetric plastic strain field of the constant-traction test simulation shown at several intervals (indicated by the letter C in subfigure (a)). A comparison of the strain fields, in c and d, reveals that in both cases compaction propagates initially in a series of discrete bands, followed by a propagation in the form of band thickening.

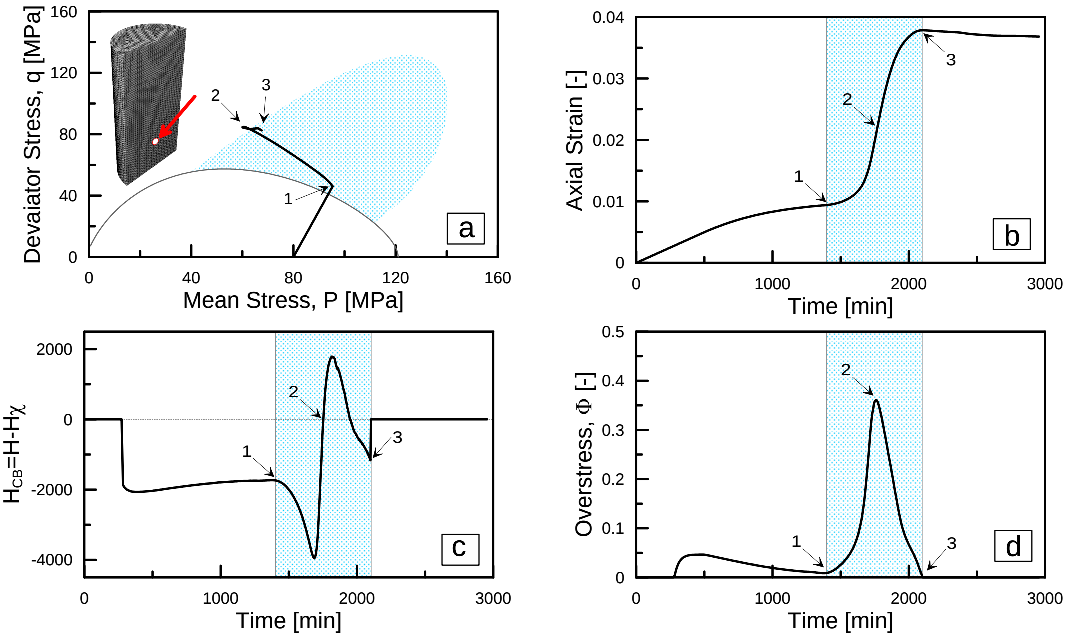

Figure 3.7. Gauss point computations extracted from a finite element simulation of a triaxial-creep test. (a) The stress path is shown together with the yield surface and instability zone, where the path violates the yield surface at point 1, and progresses in a quasi-axisymmetric path to point 2. The stress state remains then almost unaltered up to point 3. (b) Temporal evolution of the axial strain. (c) Temporal evolution of the instability index H_{CB}. (d) Temporal evolution of the viscous nucleus Φ.

($L4$), while the first band in the creep simulation can be detected at $C2$. Differences can also be seen in terms of the global deformation response (Fig. 3.6b). Specifically, variations in the temporal evolution of deformation develop starting from the early stages of the phase of creep. At, for instant, an axial strain of 0.0175 the delay in deformation is about 1000 minutes, while this delay exacerbates up to about 2000 minutes by the end of the simulation (at $L6/C6$).

Although a one-to-one causal connection between globally unstable behavior and local material instabilities is not possible, the index of locally unstable compaction response defined in Section 3.1 can be used here as a diagnostic tool to explain from a qualitative standpoint the numerical results. For this purpose, Gauss point computations at a randomly selected element is reported in Fig. 3.7. The evolution of the stress state is shown in Fig. 3.7a plotted along with the zone of instability. It can be seen that the local stress path resembles those known to be typical of constant axial-stress compression (i.e., $q/p = \pm 2/3$), and limited by the boundaries of the instability zone. When the stress state reaches the outer boundary of the instability zone, (i.e., at point (2)), stress evolution changes direction, thus marking the deactivation of a previously active strain localization zone. Kinematically, when viscoplasticity initiates at point (1), the local response exhibits an acceleration in the axial strain (Fig. 3.7b), which continues across the entire stage between (1) and (2). This unstable response is related to a negative sign of $(H - H_\chi)$ (i.e. positive instability index) as can be seen in Fig. 3.7c, and is associated with a spontaneous increase in the overstress, which has a peak at the end of this stage (Fig. 3.7c). Between (2) and (3) the stress state remains almost unaltered, yet significant accumulation of axial strain develops, reflecting the activation of delayed deformation inside the compaction zone. Later, the overstress diminishes, indicating that after (3) there is no longer accumulation of plastic strain. This analysis illustrates that the insights gained from the local viscoplastic interpretation share numerous features with the spatially heterogeneous dynamics of time-dependent compaction instability resulting from the finite element analyses.

To further inspect the simulations, a number of elements at the central axis and along the height of the specimen were selected, and the associated evolution of the axial strain, overstress ratio, and $H - H_\chi$ are reported in Fig. 3.8. The point at which the instability

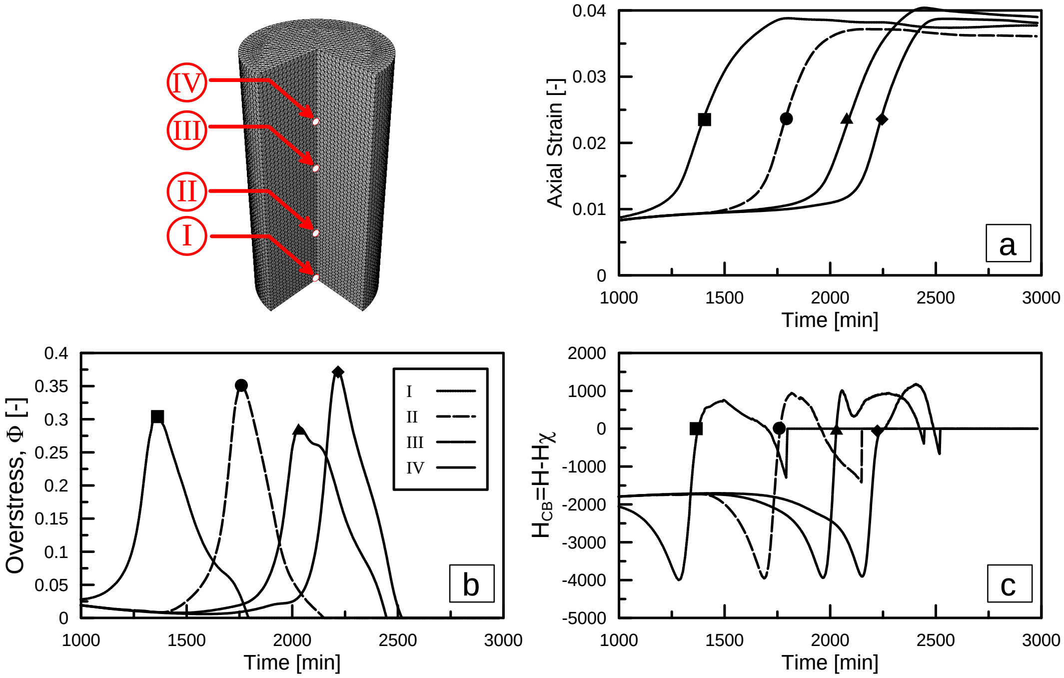

Figure 3.8. Temporal evolution during the simulated creep test of (a) axial strain, (b) overstress, and (c) instability index H_{CB} at Gauss points located along the axis of the specimen. H_{CB}=0 is marked on all plots to show that the proposed instability index is capable of identifying the conditions of unstable creep response.

index switches sign (i.e., $H - H_\chi = 0$) is marked in all plots. Although the use of this index in the context of a boundary value problems should be regarded as an approximation, in that it is affected by potential shifts in local stress paths and cycles of unloading-reloading, this result suggests that heterogeneous delayed compaction localization can be interpreted as a time-dependent instability of the axial strain response. It can also be seen that the point of transition from an unstable response to a stable response appears to be correspond with peaks of overstress (i.e., a spike of viscoplastic strain rate). This result can be corroborated by inspecting the spatial field of incremental variables. For example, Fig. 3.9 shows the

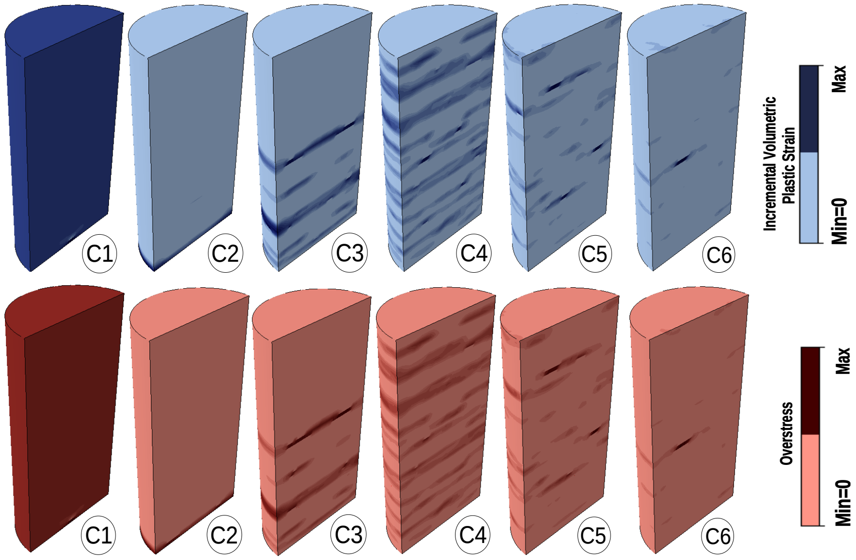

Figure 3.9. Full-field data from a constant-traction test simulation. (Upper) Incremental volumetric plastic strain field confirming the activation of new discrete bands in the first three intervals followed by propagation of the already activated zones. (Lower) Overstress field at the same intervals confirming coincidence of overstress peaks with the active strain field.

simultaneous fields of the incremental volumetric strain and the overstress, confirming once again that the active zones of compaction are associated with zones of high overstress.

3.5. Simulation of a Relaxation Test

While the previous section focused on conditions mimicking recent laboratory tests, hereafter the model is employed to predict compaction band growth under boundary conditions not yet explored in experimental settings. Specifically, tests conducted at constant axial deformation (also referred to as relaxation tests) have been simulated to assess changes in the spatio-temporal dynamic of localized compaction. Such conditions are relevant for a variety of underground activities such as hydrocarbon reservoirs depletion [*Pijnenburg et al.*, 2018]. In addition, they may provide useful insights to explore boundary conditions relevant

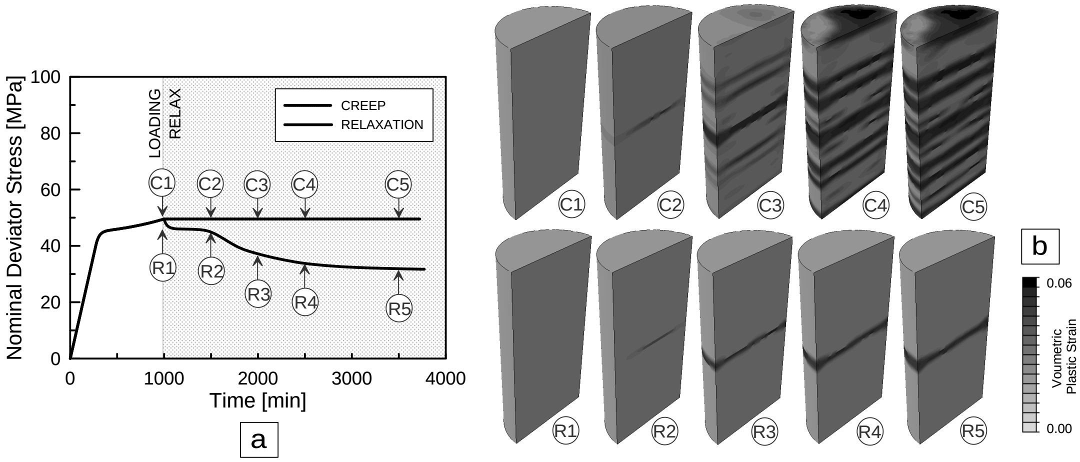

Figure 3.10. Full-Field simulations of relaxation test compared with a creep test simulation. (a) Axial force evolution reported as a function of time. (b) Volumetric plastic strain field taken at the temporal intervals marked in (a).

for geophysical processes but rarely tested in conjunction with viscoplastic behavior. This additional set of simulations is based on the same specimen geometry discussed in previous sections. To facilitate visualization, the location of the weak element is placed at the middle of the specimen. The specimen is first subjected to a given confinement pressure and then sheared by lowering the upper boundary at a constant rate (equivalent to nominal axial strain of 1.0%) while maintaining the lateral stress constant. The shearing stage has been defined such that viscoplastic deformation is initiated. The vertical velocity of the upper boundary is then set to zero and the specimen is left to relax. In order to compare the outcome of fixed-displacement simulations with those of constant-traction conditions, the same simulation has been repeated by replacing the relaxation stage by a creep phase characterized by the same (constant) nominal axial stress attained prior to the start of the relaxation path.

Fig. 3.10a displays the mechanical responses associated with the relaxation test, where it can be seen that the specimen exhibited sequential stages of axial stress loss. The first of such stages occurs right at the beginning of relaxation ($R1 \rightarrow R2$) and results in a 10% loss of axial force carried by the specimen. Afterwards, an additional stage of stress loss is obtained, resulting in an overall 40% decay of the sustained axial force. Both stages of axial force decay are characterized by an initial sharp relaxation, followed by stabilizing stress conditions. Fig. 3.10b shows snapshots of the volumetric strain field at various time intervals along the relaxation/creep phase, from which it can be seen that both conditions lead to compaction localization. While compaction localization during relaxation results into a single band growing at the middle of the specimen (i.e., exactly in correspondence of the weak zone), constant-traction conditions lead to multiple bands scattered throughout the sample volume. Such patterns are consistent with those shown in the previous section, thus emphasizing that creep simulations are not significantly affected by the location of the weak element. These results indicate that the fixed boundaries inherent with relaxation conditions promote the formation of isolated deformation structures in proximity of existing flaws, as well as that the resulting force decay is sufficient to shield much of the sample volume from inelasticity. By making reference to the axial stress loss, it can be noticed that the first phase corresponds to the initial lateral growth of the band ($R1 \rightarrow R2$), while the second phase of axial force decay corresponds to a stage of band thickening ($R2 \rightarrow R5$). These features indicate that creep and relaxation tests display similar key stages of compaction band growth. In addition, they suggest that creep may be suitable to study features such as band spacing, while relaxation may be convenient to identify the geometric characteristics of a single band and isolate a dominant weakness zone.

3.6. Creep Simulations based on Heterogeneous Specimens

The use of homogeneous specimens with weak elements to simulate rock specimens is a simplification of the real full-field experiments. This idealization implies that geomaterials are treated homogeneous, but because this class of materials rarely satisfies this idealization, full field analyses have to account for their inherent heterogeneity. In the laboratory, two levels of heterogeneity are perceived. At the microscopic level, rock compaction involves complex micro-structural mechanisms including cement debonding, intergranular slipping, and grain crushing [*Wong and Baud*, 2012]. These processes are mainly governed by microstructural heterogeneity and microcracking, thus explaining the tendencies of porous rocks to deform under constant loads as an outcome of a spontaneous subcritical fractures growth driven by stress concentrations at the extremities of existing cracks. At higher scale of observation, i.e., the mesoscale, material heterogeneity is identified by the fluctuation of material properties (such as porosity and strength) around the overall averaged value (see App B). While subcritical fracture may explain the role of the microstructural heterogeneities on creep behavior, the role of the mesoscale heterogeneities is still under-explored, as readily apparent from the not yet fully understood role of the spatial fluctuation of material properties on triggering strain localization [*Borja et al.*, 2013; *Shahin et al.*, 2016]. This section explores the complex links between microstructural heterogeneity, rock constitutive behavior and delayed strain localization.

For this purpose, numerical simulations based on the finite element method are used hereafter to simulate unstable creep in heterogeneous specimens of Bleuswiller sandstone. This qualitative study is based on porosity fields generated through random processes characterized by a normal distribution with different values of standard deviation. The specimens are generated by first identifying a unique random process characterized by a normal distribution with mean/standard deviation=0/1. A single realization (R) is generated (Fig. 3.11a) and then is rescaled by choosing specific values of standard deviation. Each realization is then shifted by centering it around a mean value of 1, and then multiplied by the averaged value of the porosity (i.e., ϕ_o= 0.24). Fig. 3.11b depicts a set of random porosity fields associated with three different levels of standard deviation (i.e., STD= 0.1%, 0.5% and 1.5%).

The features of the constitutive model used in this study require conversion procedures to integrate the porosity field in the numerical analyses. In this context, a rule is proposed in Appendix B and here is adopted. According to this rule, data set with a normal distribution of porosity converts into a log-normal distribution of yielding thresholds, as can be seen in Fig. 3.11c. Fig. 3.11d shows the heterogeneous simulations with porosity fields of STD=0.1%, 0.5% and 1.5% displayed with the associated field of P_{so} and denoted by S_{01}, S_{05} and S_{15}, respectively.

Each numerical specimen has been tested with three different levels of creep stress (i.e., 40-, 42-, and 44-MPa). These levels were chosen to be lower than the yielding stress (45.9 MPa) characterized through triaxial compression-loading on homogeneous specimens (i.e., the tests are conducted in the apparent linear stage, see Fig. 3.12). The response of the specimen is inspected with reference to the vertical displacement at the top boundary normalized by the initial height of the specimen ”nominal axial strain” (NAS) is reported as a function of time.

The obtained results are reported in Fig. 3.13 , where it can be seen that under both levels of stress (i.e., 42- and 44-MPa), all specimens have displayed creep deformation associated with stages of deceleration and acceleration similar to those observed in previous sections. Most notably, the simulations reveal a significant role of the heterogeneity on creep behavior,

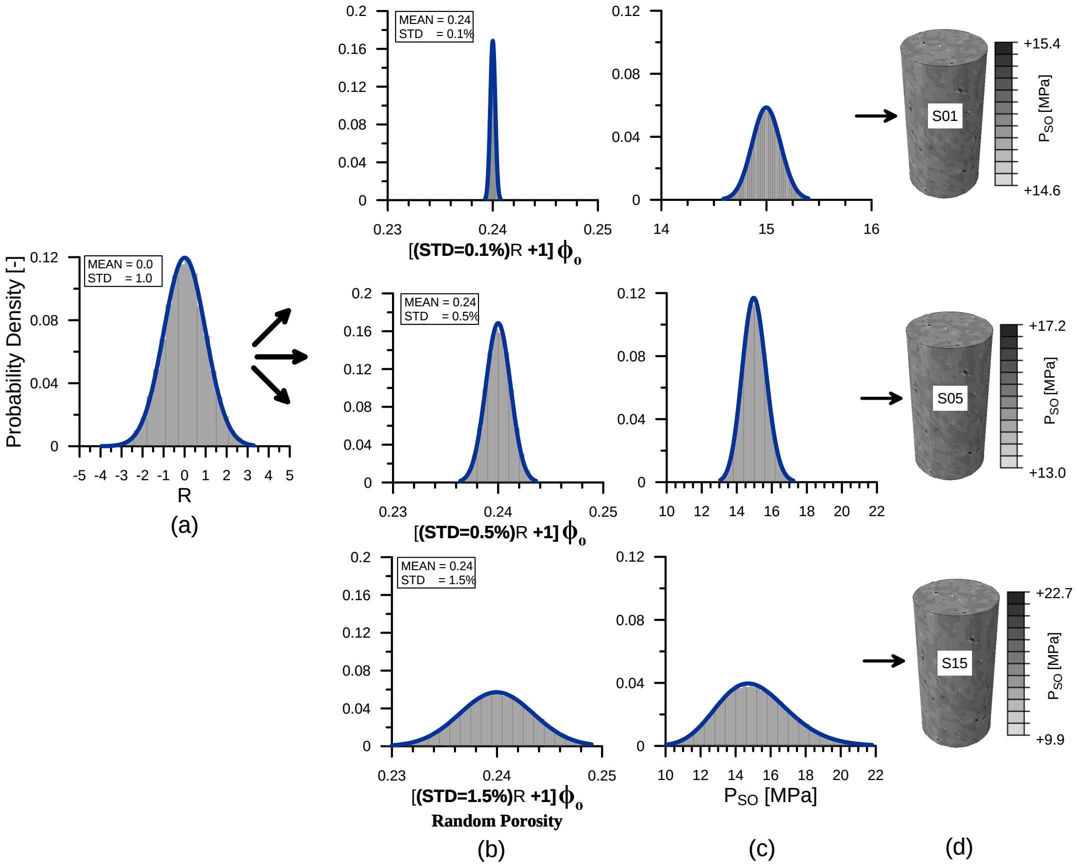

Figure 3.11. Generating numerical specimens with random porosity fields. (a) A unique realization of normally distributed data with mean= 0 and standard deviation=1. (b) Scaling the random field to the desired standard deviation (i.e., 0.1%, 0.5%, 1.5%) and then shifting to the desired mean value (i.e., $\phi_0 = 0.26$). (c) Converting the porosity field to model-specific parameter (i.e., P_{so}). (d) FEM simulation after embedding the random porosity field.

in that the heterogeneity has allowed the specimen to display inelastic behavior at stress levels below the nominal threshold. By making reference to these results again, it can be noticed that the rate of deformation appears to be connected with the intensity of heterogeneity. The rate of deformation associated with the specimen of the modest heterogeneity (STD= 0.1%) appears to be the lowest among the other specimens with a stronger heterogeneity. For example, the delay between the specimens of the strongest and modest heterogeneity is

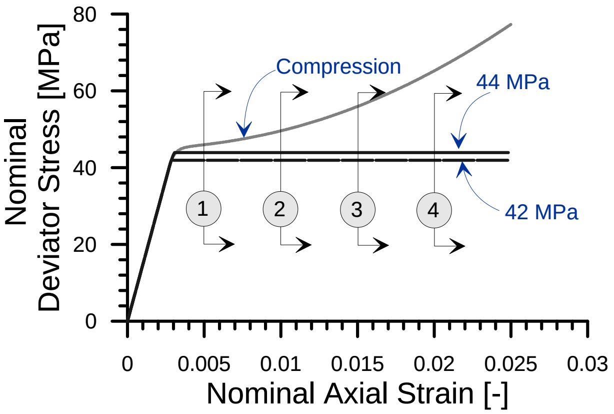

Figure 3.12. Stress-strain response associated with constant-traction test simulation, showing two levels of traction intensities (i.e., 42 and 44 MPa) presented along with the response of compression-loading test simulation on homogeneous specimen.

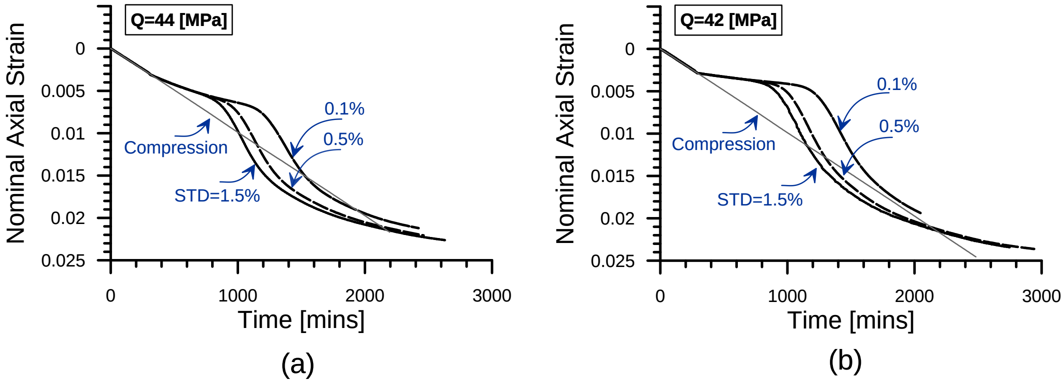

Figure 3.13. Deformation response of three different heterogeneous specimens with various values of standard deviation (i.e., STD=0.1%, 0.5% and 1.5%). The specimens are simulated under constant-traction. (a) Response under traction of 44 MPa. (b) Response under traction of 42 MPa.

about 400 minutes at 0.015 axial strain. Despite the differences in the rate of deformation, all specimens tend to stabilize around the same level of total compaction (i.e., close to 0.022 axial strain) after an elapsed time interval of 3000 minutes.

The simulations reveal also an important role of the stress level on the rate of deformation. A comparison between the specimen's behavior under different levels of constant-traction (i.e., 40-, 42-, and 44-MPa) is presented in Fig. 3.14.

First, it can be seen that under 40 MPa traction, all specimens display no deformation responses over time. In contrast, the specimens exhibited a clear tendency to accumulate creep deformation at higher levels of traction. The rate of deformation appears dependent on the intensity of traction. Specifically, the specimens under higher levels of traction displayed a tendency to accumulate deformation at higher rates. By making reference to the subset Fig. 3.14a where the results associated with S_{01}, it can be seen that after an elapsed time of 1000 minutes, the specimen under 44 MPa has accumulated a total deformation of NAS=0.65%, while under 42 MPa it has accumulated 33% less deformation (NAS=0.4%).

Fig. 3.14 also presents the strain fields associated with these simulations, inspected at the same deformation intervals (i.e., 0.5, 1.0, 1.5, and 2.0 axial strain). It can be seen that all specimens have undergone compaction localization. The activation of the bands appears to occur instantaneously, as can be seen in the first interval of all simulations. The bands that were activated at this stage accumulate further deformation over time as can be seen at the second interval. Compaction then propagates in a form of band thickening (third and fourth intervals). In this context, it can be observed that neither the intensity of stresses nor the intensity of heterogeneity has affected the pattern of propagation.

3.7. Conclusions

This chapter discussed a mathematical approach based on nonlinear dynamics and viscoplasticity to interpret the evolution of delayed compaction bands during stages of creep.

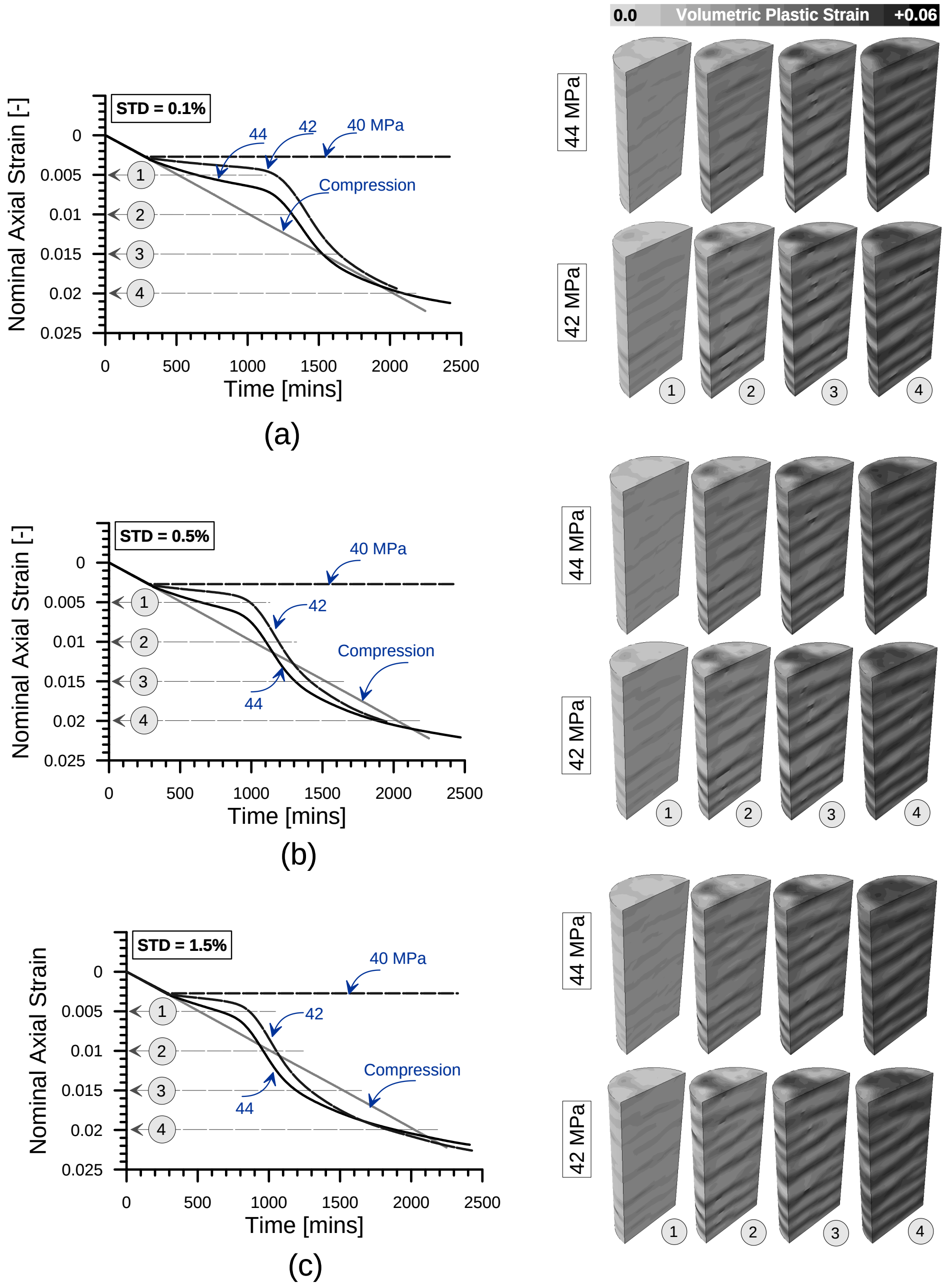

Figure 3.14. Constant-traction test simulation on heterogeneous specimens under different levels of stress. The heterogeneous specimens include different values of STD: (a) 0.1%, (b) 0.5%, and (c) 1.5%. The deformation responses are reported in the left-hand side, while the associated evolution of the volumetric plastic strain field is depicted on the right-hand side.

For this purpose, the constitutive equations have been recast in the form of an ODE specific for the kinematic control conditions associated with the strain jump within an active compaction band. In particular, an instability index connected with the eigenvalues of the constitutive operators governing the temporal dynamics during localized compaction creep was derived and used to detect the transition from stable to unstable deformation in material point simulations. The acceleration of response variables in the simulated deformation was shown to be caused by a pulse of overstress related with the coordinated evolution of stress state and yield surface. This framework was shown to be a useful tool to explain the emergence and propagation of compaction bands in full-field analyses of compaction creep based on finite element simulations. An intimate relation between the spatial patterns of compaction and their temporal progression was found, revealing that the pulses of overstress and viscoplastic strain rate concentrate at discrete locations. These spatial patterns were accompanied by a global response characterized by an accelerating stage of deformation followed by a stage of decaying axial deformation rate. While the accelerating stage was found to correspond to the formation of multiple compaction bands, the decelerating stage indicated the homogeneous development of stable compaction throughout the specimen, with no remaining pulses of overstress and localized strain acceleration.

The second part of the chapter explored the role of the spatial heterogeneity on the emergence of delayed compaction banding and the temporal evolution of global subsidence under creep. For this purpose, heterogeneous specimens were generated by adopting a single realization that is scaled up with respect to its standard deviation to obtain different intensities of material property variation. The specimens were tested under different levels of constant-traction, all lower than the nominal yielding stress known from homogeneous simulations. It was found that the fluctuation in material properties enabled the specimen to display inelastic deformation under stress levels lower than those associated with nominal yielding. The intensity of the spatial heterogeneity was found to play an important role on the rate of deformation accumulation, in that specimens with greater intensity of heterogeneity tended to display higher rates of creep deformation. The stress level was found to also affect the rate of the response, in that lower levels of constant traction were accompanied by lower rates of compaction. These results emphasize the importance of accounting for material heterogeneity in localization analyses and provide tools and concepts to study the interplay between delayed deformation and material spatial variability.

CHAPTER 4

Effects of Spatial Heterogeneity on Compaction Propagation*

Modern experimental geomechanics offers an unprecedented access to characterize local material properties through non-invasive techniques such as x-ray computed tomography [*Alshibli and Hasan*, 2008; *Desrues and Viggiani*, 2004]. The use of these technologies in conjunction with mechanical testing has enabled the examination of the material response across length scales by tracking the evolution of the microstructure along with the the global response [*Desrues et al.*, 1996; *Hall et al.*, 2010]. These technologies were recently applied to examine compaction banding in Maastricht Tuffeau [*Papazoglou et al.*, 2017, 2019], a limestone from central Europe susceptible to compaction banding [*Baxevanis et al.*, 2006]. Compaction bands propagating from the specimen ends were observed. Along with mechanical data, the initial and evolving porosity maps were collected.

The rich dataset collected through such experiments offers a unique opportunity to investigate the role of material heterogeneity in triggering compaction localization. In this context, a mapping strategy that allows for integrating x-ray micro-tomography measurements in continuum-based numerical analyses has to be established. To this end, numerous

---

*The content of this chapter is published in:

- Papazoglou, A., Shahin, G., Marinelli, F., Dano, C., Buscarnera, G., and Viggiani, G. (2017, May). Localized Compaction in Maastricht Tuffeau: Experiments and Modeling. In International Workshop on Bifurcation and Degradation in Geomaterials (pp. 481-488). Springer, Cham.
- Shahin, G., Papazoglou, A., Marinelli, F., and Buscarnera, G. (2019). Simulation of localized compaction in Maastricht Tuffeau based on evidence from X-ray tomography. International Journal of Rock Mechanics and Mining Sciences, 121, 104039.
- Shahin, G., Viggiani, G. , and Buscarnera, G. (In review). Simulating spatial heterogeneity through a CT-FE mapping scheme discloses boundary effects on emerging compaction bands. International Journal of Solids and Structures.

questions have to be addressed beforehand. For example, the scale gap between rock samples and the numerical models (the FE simulations) raises questions about how the microscale discrete observables can be inferred to macroscopic continuum quantities, and the size of material volume necessary for the inference. Mapping local measurements further requires the identification of the attributes most relevant to the mechanical properties (e.g., porosity, cement, and/or grain size distribution). In fact, dealing with a multi-phase material (such as cemented granular materials) further increases the complexity of the problem, in that the size of the material volume suitable to map local properties may vary from one phase to another. Dedicated studies are required to understand how the heterogeneities emerging form different phases (i.e., porosity, cement, and grains) interact among each other and across the specimen. The study presented in this chapter considers first-order heterogeneities based on the initial porosity, where the alteration/concentration in stress and strain spaces caused by material porosity can be argued to play a major factor in activating heterogeneous deformation mechanisms.

4.1. Tomography to Finite Element Mapping Scheme

Incorporating spatial heterogeneities in numerical analyses has been an active topic of research. For example, *Gudehus and Nübel* [2004] projected the FE mesh onto optical images of sand specimens, so that the averaged value over the material volume encapsulated by each FE is assigned to the corresponding integration points. The same strategy was utilized by *Borja et al.* [2013] on CT-images of sand specimens. Although the method succeeded in capturing effects of spatial heterogeneity, it may lead to potential inconsistencies between the characteristic scale of the material and the length of the discretization (e.g., mesh refinement may generate elements with size comparable or even smaller than individual grains/pores).

In other contexts, material heterogeneities were reproduced by relying on the concept of image-based (data-driven) modeling, in which data sets provided by imaging methods allow the characterization of an underlying random field and the generation of corresponding equivalent computational domains [*Chen et al.*, 2012; *Kim and Santamarina*, 2006]. This approach implies the determination of a correlation function that is used in combination with statistical reconstruction to reproduce equivalent realizations [*Andrade et al.*, 2008; *Chen et al.*, 2012]. Despite its success in preserving the statistical characteristics, this approach leads to the loss of the original fields, thus hindering spatial accuracy.

In this work, a mapping scheme to connect CT measurements and FE simulation (hence, referred to as CT-FE scheme) is discussed. The focal point of this proposed scheme is to produce a numerical replica of the physical specimen while preserving a realistic depiction of material heterogeneity at the continuum scale. For this purpose, the concept of representative elementary volume (REV) is used to homogenize discrete measurements and transfer them into continuum quantities applicable for integration in numerical models [*Drugan and Willis*, 1996; *Hill*, 1963]. This is, in fact, motivated by an extensive application of the REV concept to study the mechanics and physics of heterogeneous media, where it was applied for obtaining a homogenized continuum from materials with inherently random microscopic architecture. The REV is defined by considering the smallest volume of material at which the fluctuations of average physical quantities stabilize [*Ando*, 2013; *Matheron*, 1989]. See also Appendix D. Examples of its application include the determination of effective properties of composite material such as effective elasticity [*Castañeda*, 2002; *Hashin and Shtrikman*, 1963]. In such cases, the medium is postulated to extend to infinity and therefore the REV provides *"asymptotic"* estimates [*Hassani and Hinton*, 1998]. Problems of homogenization were also addressed by using the idealization of the microstructure based on evidence from tomography scans. In that case, the notion of REV was used to conduct statistical inference of macroscopic quantities from microscopic observables by identifying material volumes that are sufficiently large to be statistically representative [*Bruchon et al.*, 2013a] (see also Appendix D). This implies that sampling volumes must include a sufficient number of microscopic heterogeneities (e.g. grains, cement, fluid, pores) in order to generate stable estimates of the statistics of the whole domain [*Andrade et al.*, 2012; *Desrues et al.*, 1996; *Hall et al.*, 2010; *Kanit et al.*, 2003]. The size of the volume, however, has to remain small enough to be considered as a volume element in terms of continuum mechanics [*Bonet and Wood*, 1997]. The relation between continuum level, elementary volume and microscale is governed by the principle of scale separation. This principle states that the scale of the microstructure fluctuation, l, must be much smaller than the size of the representative volume, L, which in turn has to be much smaller than the characteristic fluctuation length of the macroscopic deformation field, D:

$$l \ll L \ll D \tag{4.1}$$

Continuum mechanics focuses on the homogeneous scale, D, with the elementary volume behavior, L, characterized through constitutive relations. Recently, this paradigm was enriched by the emergence of multiscale frameworks that incorporated refined microstructural simulations serving as material models. This is inspired by the pioneering work of *Tadmor et al.* [1996], who proposed a quasi-continuum method by making use of the so-called CauchyBorn rule to obtain an energy density function from molecular dynamics computations. Later, *Liu and McVeigh* [2008] proposed a virtual power domain decomposition to do concurrent and hierarchical simulations in solids with heterogeneities at multiple scales. Aggregation of discontinuities across scales has came through double continua (FE^2) multiscale methods [*Belytschko et al.*, 2008; *Van den Eijnden et al.*, 2016], and discontinuum-continuum (discrete elements method × finite element method) multiscale schemes [*Andrade et al.*, 2011; *Guo and Zhao*, 2014; *Meier et al.*, 2008; *Miehe et al.*, 2010; *Nitka et al.*, 2011; *Shahin et al.*, 2016]. Pivotal to this class of models is the REV concept that made it possible to bridge the gap between the different length scales.

In this work the fundamental concept of REV is employed to obtain a robust connection between experimental data and numerical analyses. Upon idealization of the physical specimen by a finite element model, integration points are assigned state quantities and/or material properties directly from the in-situ measurements. Typically, a unified value is assigned to all Gauss points, that is the averaged value recovered from the physical specimen with the assumption of homogeneous material. The proposed mapping scheme suggests the determination of selected state variables and material properties for each integration point directly from the CT-image. The conceptualization of the proposed scheme is illustrated in Fig. 4.1a. First, the coordinates of the integration point (Fig. 4.1b) are projected onto the CT-image (Fig. 4.1c) where each integration point is associated with a material subdomain (Fig. 4.1d). The subdomain is defined by the size of the REV identified particularly for the property of interest [*Gitman*, 2006; *Kanit et al.*, 2003]. This size may be determined statistically [*Matheron*, 1989], by combining basic morphological tools with stereological and image analyses techniques in order to describe the geometrical dispersion across the specimen domain (see e.g., [*Bruchon et al.*, 2013a]). More details about the statistical procedure to define the representative elementary volume based on digital images are provided in Appendix D, with reference to a particular case of microscopic heterogeneity caused by reactive-transport. Microscopic observables are finally averaged over the REV domain and the homogenized value is assigned to the corresponding integration point.

This scheme will be applied to benefit from the rich dataset available with the experiments on Maastricht Tuffeau. An essential step, however, has to be first accomplished by establishing a constitutive model capable of replicating the mechanics of the limestone, a step that will be conducted throughout the next two sections.

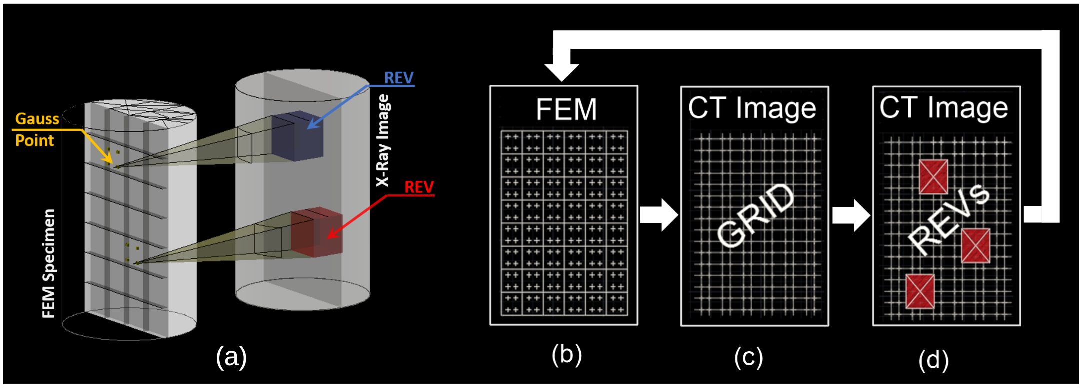

Figure 4.1. Illustration of REV-based mapping scheme connecting x-ray in-situ measurements to finite element analyses. (a) Conceptual schematic displaying the identification of state variables of two Gauss points from the CT-image. Mapping is conducted by (b) extracting Gauss points coordinates, (c) detecting the coordinate on the binarized CT-image, (d) identifying the sub-volume (the REV) for each Gauss point, over which the observable of interest is homogenized. The homogenized value is then assigned to the corresponding Gauss point in the FE mesh.

4.2. Constitutive Modeling of Maastricht Tuffeau

The strain-hardening model discussed in Chapter 2 is here retained to replicate the mechanical behavior of Maastricht Tuffeau. While available measurements of the limestone reveal non-negligible anisotropy [*Papazoglou et al.*, 2019], the following analysis is conducted under the assumption of isotropy for simplicity. While further analyses of the effects of anisotropy on comapction localization characteristics can be conducted with reference to the model developments and calibration presented in Appendix C. The model calibration has been conducted following the two-step procedure discussed by *Das and Buscarnera* [2014]; *Marinelli and Buscarnera* [2015]. First, the mechanical measurements are used to tune a preliminary set of parameters which is subsequently augmented through the bifurcation theory on the basis of evidence of strain localization (Sec. 2.4).

4.2.1. Parameter Calibration based on Global Measurements

The yield surface is calibrated based on data-points recovered from the triaxial-compression and the isotropic-compression tests. The yielding points detected through such experiments are located in the $p - q$ stress space. The mathematical expression of the yield surface is tuned by adjusting the shape parameters, M_f, μ_f, and α_f, as shown in Fig. 4.2a. The shape parameters associated with the plastic potential, i.e., M_g, μ_g, and α_g, are defined on the basis of the underlying stress-dilatancy relationship (Eq. 2.6). This function defines the ratio of volumetric and deviatoric plastic strains computed for a given imposed stress level. These ratios can be reported in the $\eta^\star - d$ space, as shown in Fig. 4.2b, and used to calibrate the plastic potential. This procedure relies on global measurements taken in the post-yielding regime (i.e., where the specimen exhibits a structural response with heterogeneous deformation patterns). Data-points, however, are expressed in the form of a normalized strain ratio, thus are regarded as representative of the material behavior inside the active zone and the first-order insight it provides on the expected plastic flow characteristics will be later assessed through full-field analyses.

The internal variables, P_{so} and P_{mo}, and the hardening parameter associated with volumetric straining, B_p, are calibrated with reference to the isotropic compression behavior.

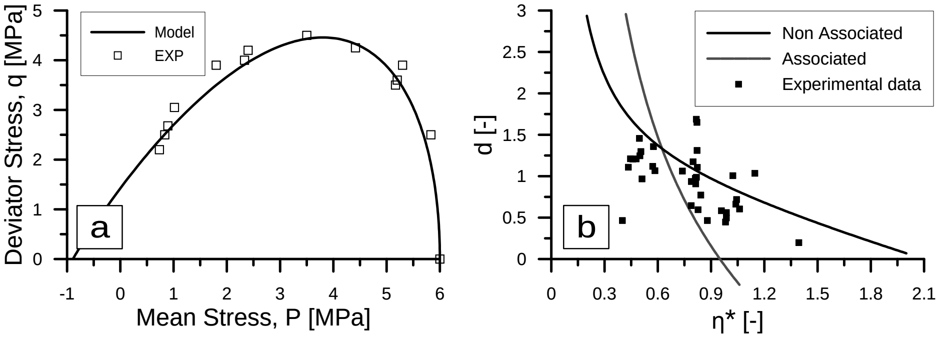

Figure 4.2. Calibration of the shape-parameters of the yield surface and plastic potential from (a) the initial yield points and (b) relation between dilatancy and stress-ratio obtained from triaxial compression data.

The first stress point at which the volumetric deformation changes drastically is considered the hydrostatic yielding point, P_{co} (where $P_{co} = P_{so} + P_{mo}$). The ratio P_{so}/P_{mo} controls the compressibility of the material, i.e., the magnitude of volumetric deformation that separates the point of first yielding and the point at which material displays re-hardening. This set of parameters can be readily calibrated from the hydrostatic compression curve, Fig. 4.3a. The material compressibility during the phase of re-hardening, where inter-particle bonds have been fully destructured, is governed by B_p. As a result, this constant regulates the porosity hardening emerging upon volumetric deformation in a completely reconstituted material. Thus, B_p is calibrated on the grounds of the experimental dataset obtained from hydrostatic compression on destructured material (Fig. 4.3b).

It can be noted that the model overestimates the compressibility in the plastic regime. In fact, as it will be shown in the subsequent sections, higher volumetric softening was necessary to augment the porosity loss during shearing and match the elongation of the deviator stress plateau exhibited by the limestone during triaxial compression. The final set of isotropic compression parameters was, in fact, a compromise aimed at obtaining a

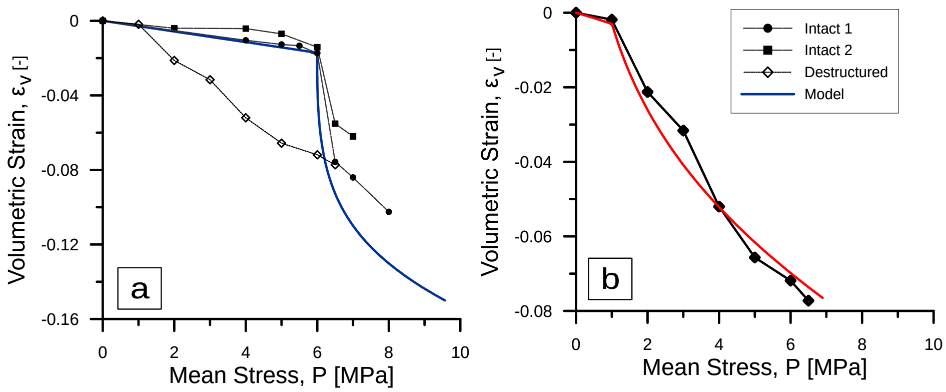

Figure 4.3. Isotropic compression tests used to calibrate the compressibility parameters (i.e., B_p, ρ_m, and the ratio P_{so}/P_{mo}): (a) is the intact sample and (b) the destructured material.

reasonable match with the measurements, while prioritizing the model performance in the compaction localization regime.

4.2.2. Calibration based on Strain Localization Analyses

The data used in the calibration above were derived from global measurements of specimens deformed in localization regime. During this phase, strain localization promotes a transition from homogeneous to heterogeneous deformation fields. Measurements performed in the localization regime might have considerable deviations from the material point behavior, thus not being able to solely provide reliable information for model calibration. To overcome this obstacle, enhancements are possible by using evidence about the onset and pressure-dependence of strain localization modes, as recently proposed by *Marinelli and Buscarnera* [2015]. This procedure is based on the modes of strain localization predicted by the model for a given set of parameters, which can be optimized in order to match the evidence of pressure-dependent compaction banding. With reference to the model used in this work, ξ_m,

ρ_m, and M_g were used for such optimization. By controlling these parameters, the material rheology, as well as the strain localization characteristics, can be successfully captured.

Strain localization analyses (Sec.2.4) have been conducted for this purpose. An illustration of these analyses is reported in Fig. 4.4, where the localization profile is computed for triaxial stress paths at varying confinements. This plot depicts the pressure dependence of the strain localization potential of the selected material. In particular, a transition from the development of conjugate shear-enhanced compaction bands at lower confinements (i.e., state I, II, III) to the potential formation of pure compaction bands at high pressure (i.e., state IV) is readily apparent. Locating these results in the stress space provides information about the strain localization modes predicted by the model for varying stress conditions (see upper-left chart in Fig. 4.4). The transition between these two end-members takes place smoothly, thus providing opportunities to calibrate the relevant model parameters by adjusting their values to cover the entire range of expected strain localization. As shown by *Marinelli and Buscarnera* [2015], the extent and characteristics of strain localization domain are strongly dependent on the softening parameters and the degree of non-associativity. Thus, the calibration of these parameters is tuned based on information from tomographic imaging. In particular, full-field measurements enabled the distinction between stress states resulting into pure compaction bands from those associated with shear-enhanced compaction bands. As a result, the optimization of the model parameters in light of these findings resulted into model computations able to reflect the evidence (see data points in Fig. 4.4a). Finally, the zone of instability determined on the basis of viscoplastic instability indices (Chapter 3) is presented in Fig. 4.5, where it can be noticed that the results are quite comparable with those obtained through the localization analyses (for the cases of $\theta = 0$), as the model here is again used within the quasi-rate-independent restrictions.

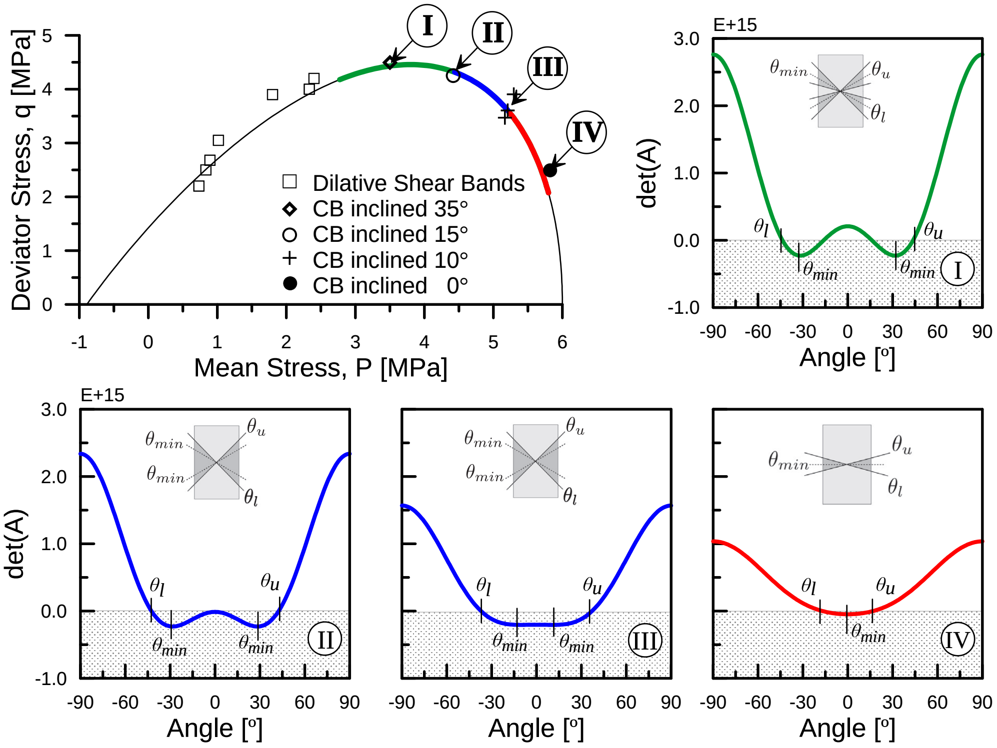

Figure 4.4. Strain localization characteristics of Maastricht Tuffeau predicted with the selected constitutive model. The localization domain in stress space is superposed to the yield surface (thick line) and the associated inclination of the deformation band predicted by a bifurcation analysis. The theory defines different modes of strain localization. Zone 1 (green line), implies two distinct cones of localization, each with a non-zero preferable angle of localization. Zone 2 (blue line), involves a single cone of localization potential with two non-zero preferential angles of strain localization. Both zones represent shear-enhanced compaction bands. By contrast, Zone 3 (red line) involves a single cone of expected strain localization with a unique angle of preferential band formation which is perpendicular to the maximum principal stress (pure compaction band). The localization profiles at the points I, II, III, and IV are presented with the same color convention. This points represent the intersection point of triaxial paths under 2.0, 3.0, 4.0, and 5.0 MPa confinement, thus providing information about the predicted localization model.

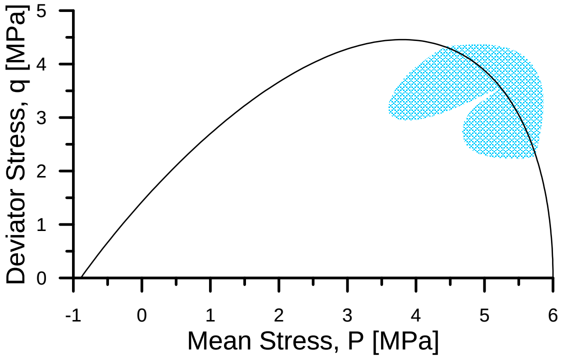

Figure 4.5. Instability zone of Maastricht Tuffeau provided by the lower-bound calibration set (analyses conducted through the viscoplastic instability indices discussed in Chapter 3.)

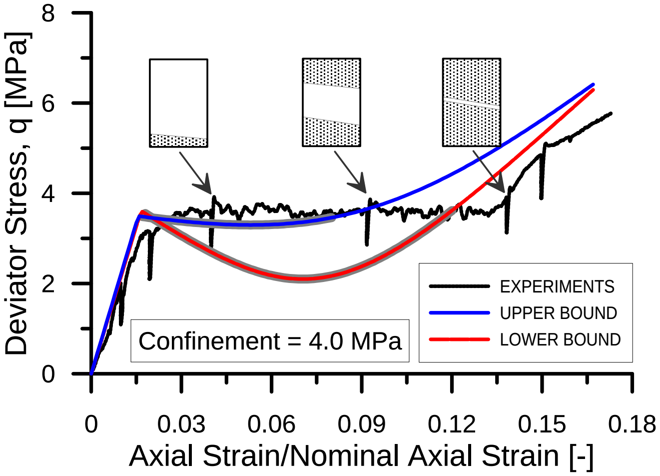

Figure 4.6. Comparison of material point analyses conducted on the basis of two different sets of model parameters (upper bound and lower bound calibration). The upper bound calibration matches the post-yielding stress plateau and the re-hardening process, while the lower bound computations exploit the large drop in the post-yielding resistance to ensure that the deformation regime of active localized compaction matches the measurements (i.e., the strain level at which the stress goes back to pre-yielding values corresponds to the extent of the strain plateau). The measured zone of compaction propagation is depicted on the measured response.

4.2.3. Upper and lower bounds calibration

Material point analyses based on the proposed model parameters are reported in Fig. 4.6, along with experimental measurements displaying the transition from localized to delocalized compaction. The analysis replicated triaxial compression under 4.0 MPa, and was based (as can be seen in the figure) on two different sets of model parameters, here called *upper* and *lower bounds*. As can be seen, with the upper bound model focus was placed on the representation of the strength throughout the post-yielding plateau, which was possible only for a localization domain limited to the proximity of 4.0 MPa. At variance, with the lower bound calibration focus was given to the deformation behavior, the localization potential, and the rate of compaction band propagation over a wider range of confinements (i.e., from 2.0- to 5.0-MPa). Achieving this goal, however, has required the use of marked strain softening to prevent early delocalization (see at this reference the finite element simulations discussed in the next sections). This trade off between different macroscopic signatures of the limestone behavior implied a remarkable drop in resistance along the post-yielding response for the case of the lower bound calibration. A possible source of such mismatch is the use of linear elasticity for high-porosity rocks, which was suggested to lead to inaccuracies in the simulation of the post-yielding response [*Dewers et al.*, 2014, 2017]. Another source of mismatch is the development of plasticity within the yield surface, which may or may not be accompanied by simultaneous changes in stiffness properties. These shortcomings could in principle can be addressed through a variety of strategies, such as bounding surface plasticity [*Dafalias*, 1986] coupled with damage or elasto-plastic coupling [*Maier and Hueckel*, 1979]. Other strategies may include adjusting the competition between P_s and P_m embedded in the hardening rule by adopting more flexible formalisms. These factors may be considered

Table 4.1. Constitutive parameters and internal variables for Maastricht Tuffeau, including the upper and the lower bound calibrations.

	Definition	Lower Bound	Upper Bound
K [MPa]	Bulk modulus	350	350
G [MPa]	Shear modulus	78	80
ρ_m	Parameter governing volumetric destructuration	0.45	0.7
ξ_m	Parameter governing deviatoric destructuration	12.5	2
B_p	Isotropic plastic compressibility	0.03	0.034
μ_f	Shape parameter of the yield surface	1.01	1.01
α_f	Shape parameter of the yield surface	2.0	2.0
M_f	Shape parameter of the yield surface	0.95	0.88
μ_g	Shape parameter of the plastic potential	0.6	0.65
α_g	Shape parameter of the plastic potential	0.15	0.15
M_g	Shape parameter of the plastic potential	2.1	2.1
κ	Expansion of the yield surface in the tensile stress domain	0.15	0.20
P_{so} [MPa]	Initial size of the elastic domain (cohesionless medium)	0.06	0.09
P_{mo} [MPa]	Lithification-induced expansion of the initial elastic domain	5.94	5.91

in the context of future developments of the model. The work presented in the rest of this chapter, however, is based only on the set of parameters associated with the lower bound calibration.

4.3. Simulation based on Non-heterogeneous Specimens

4.3.1. Regularization of Strain Localization

The use of conventional continuum models in full-field simulations affected by strain localization are typically hampered by the lack of objective results and pathological mesh dependence. To address this problem, continuum models can be enriched with an internal length scale reflecting the material microstructure. Usual choices made for this purpose include second gradient continua [*De Borst and Mühlhaus*, 1992], nonlocal models [*Bažant and Jirásek*, 2002; *Liu et al.*, 2016], and rate-dependent models [*Perzyna*, 1966]. Here, the viscoplastic version of the strain hardening model discussed in Section. 2.4 is employed under the constraints of quasi-rate-independent conditions, i.e. allowing minimal changes in the viscoplastic responses with respect to the equivalent plastic material.

In the laboratory, Maastricht Tuffeau was tested under quasi-static conditions by imposing a nominal axial strain rate $d\epsilon_a/dt \leq$ 1.0E-5 MPa.s, in which dt is the time increment during which a loading step is imposed. The use of viscoplasticity for regularization purposes has been achieved by pursuing a quasi-rate-independent behavior, i.e. by introducing minimal deviations between the regularized material behavior and the underlying rate-independent calibration discussed in the previous section. The range of viscosity that guarantees quasi-rate-independent response has been identified through a sensitivity analysis of the model performance during triaxial compression tests at two confinements (2.0MPa and 4.0MPa), through which the viscosity was varied from 1.0E-2 to 1.0E+5 MPa.s. The results are reported in Fig. 4.7 a and b, respectively. The inset shows the variation of the computed deviatoric stress at $\epsilon_a = 0.03$ as a function of viscosity. It can be readily seen that in both cases a viscosity threshold of 1000 MPa.s can be identified (shaded area within the inset) below which the model displays a stable stress response and therefore a limited role of the rate-dependent effects introduced by the viscoplastic extension.

4.3.2. Simulations of Triaxial Compression

The proposed calibration has been validated through finite element simulations of specimens treated as boundary value problems. The assessment of the performance of the simulations was focused on various features of the macroscopic response, such as post-yielding deformation behavior (i.e., elongation of the plateau), as well as the geometrical characteristics of the persistent bands, the portion of specimen across which compaction propagates, and the dependence of these features on the confinement pressure. The same finite element model and boundary conditions depicted in (Fig. 3.5) for the simulation of triaxial compression have been adopted.

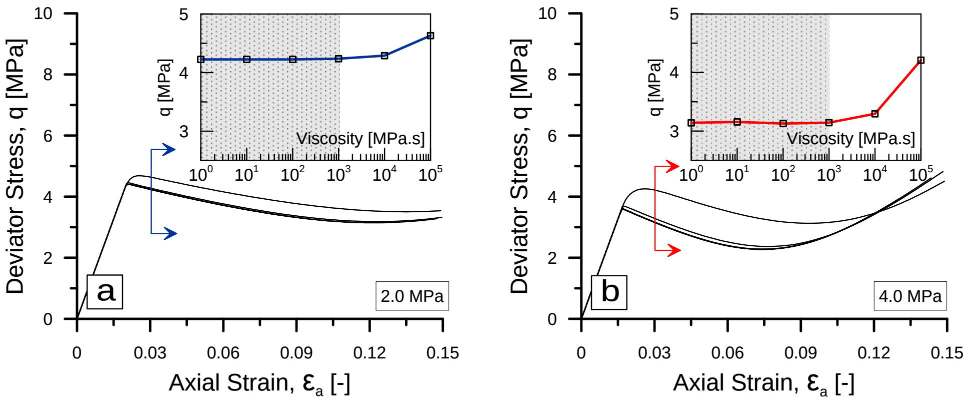

Figure 4.7. Sensitivity analysis of viscosity effects on the material-point response at different confinements: (a) 2.0 MPa and (b) 4.0 MPa. The inset shows the value of deviatoric stress computed for each value of viscosity at a fixed strain level (3.0%). Simulations conducted with a strain rate of $\dot{\epsilon}_a = d\epsilon_a/dt \leq$ 1.0E-5 $/s$, and viscosity varying from 1.0 to 10.0E+5 MPa.s.

An essential step before proceeding with finite element analyses is to tune the parameters that control the thickness of the band and identify an optimal finite element mesh. Although the precise determination of the band thickness heavily depends on the frequency with which CT scans are conducted, thus representing a major challenge, an indirect estimate of the thickness of successively formed compaction zones can be gained from the inspection of DIC measurements associated with relatively small strain increments. From a modeling standpoint, the thickness of the band is controlled through viscosity, which is here constrained by the quasi-rate-independent threshold (i.e., $\omega = 1000\ MPa.s$). The value of ω has therefore been defined with the goal to match the size of the compacted zone detected by the kinematic field upon the application of 2% global deformation (Fig. 4.8a). In this context, Fig. 4.8b shows the thickness of the compacted zone for the same value of viscosity for three different meshes. It can be seen that the thickness of the band becomes almost unaffected between the second and the third (finer) mesh. Fig. 4.8c reports the computed responses up to 5%

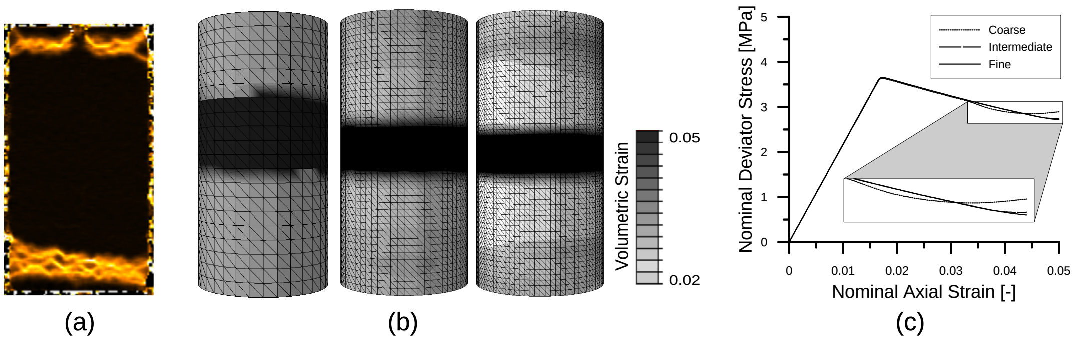

Figure 4.8. Assessment of mesh-sensitivity and thickness of the simulated compaction zone. (a) A vertical slice of 3D volumetric strain field obtained through DIC for incremental loading of 2% axial strain in a triaxial compression test performed at 4 MPa confinement. (b) the volumetric strain field resulting from finite element analyses with different mesh size, corresponding to more than 12000, 75,000, and 170000 elements, respectively. The comparison shows that the FE simulations capture satisfactorily the thickness of the compaction zone with $\omega = 650$ MPa.s. Furthermore, they confirm the successful regularization of the computations by suppressing mesh dependence, as is readily apparent from the nearly identical global responses computed for the three simulations (c).

nominal axial strain (at which the strain field in (b) is illustrated). It can be readily noticed that solutions are mesh-independent for the last two simulations which provide nearly identical responses. The good agreement between the simulations confirms the effectiveness of a viscosity factor of $\omega = 650$ MPa.s in replicating the measurements of spatially propagating compaction, as well as in suppressing mesh-dependence of the solutions.

Based on this optimal value of viscosity, four triaxial compression simulations were conducted under 2.0-, 3.0-, 4.0-, and 5.0-MPa confining pressure. Results are reported in Fig. 4.9, where the deviator stress is plotted as a function of the normalized vertical displacement. It can be seen that, in all cases, yielding was triggered at stress levels comparable to the physical specimens. The simulations, however, tend to display more softening, with a sharp drop of resistance shortly after yielding, after which a stress plateau is achieved for a sustained amount of axial deformation. This tendency is more pronounced at higher confinements. As mentioned previously, the lower bound calibration adopted in this simulations has focused on deformation characteristics, thus this tendency can be attributed to the exponential expression of the hardening laws, which requires a steeper loss of strength to guarantee a quantitatively accurate length of the deformation plateau. Despite their limitations, the choice of the hardening parameters can be considered satisfactory to capture the volume change taking place during plastic compaction (i.e., something which is directly associated with the extension of the deformation plateau).

The advantages of this choice become more readily apparent by comparing the responses obtain with the upper bound and the lower bound calibrations. This comparison is illustrated in Fig. 4.10, with reference to the experiment conducted at 4.0 MPa. It is readily apparent that, although the upper bound calibration satisfactorily replicated the reaction force provided by the specimen, it severely underestimates the nominal axial deformation during which localized compaction is active (i.e., the simulated response transitions to homogeneous compaction approximately half-way along the deviatoric stress plateau measured in the experiment). This shortcoming is not present in the lower bound calibration, which accurately predicts the transition from localized compaction to homogeneous re-hardening. It can therefore be concluded that the former set of parameters (upper bound calibration) is preferable if the focus is on force calculation, while the latter (lower bound calibration) is the optimal choice if the goal of the analyses is to replicate the propagation of compaction zones at similar deformation levels.

This point is further highlighted in Fig. 4.11, which displays the volumetric deformation as a function of the axial deformation obtained with the upper and lower bounds along with the experimental measurements. It can be readily seen that the FE analyses have been

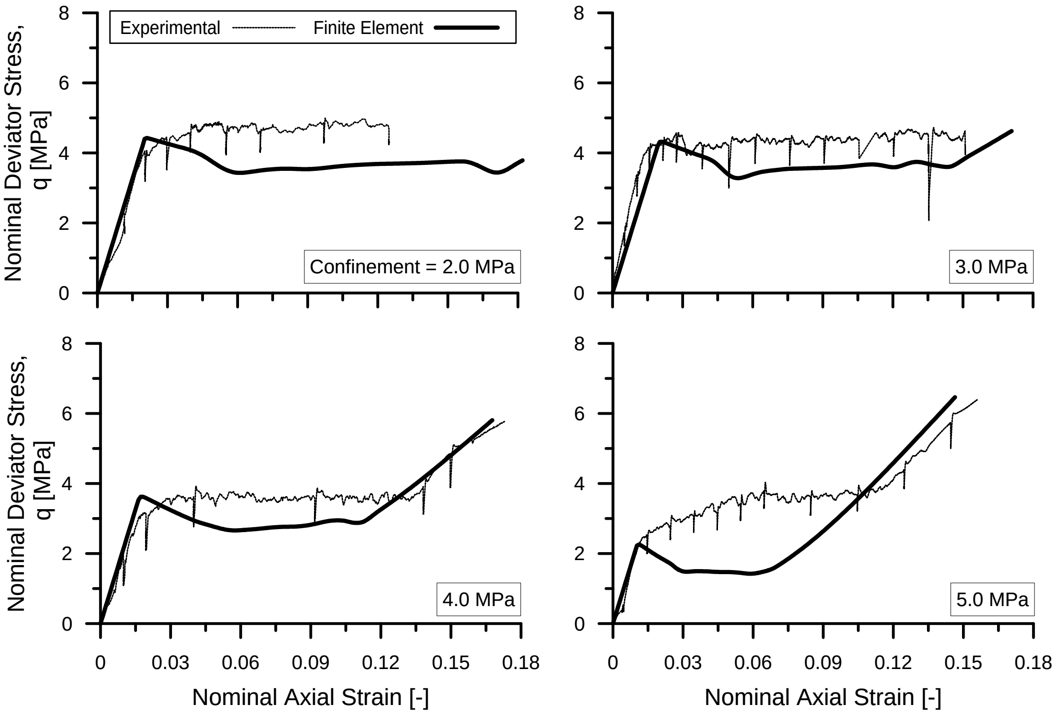

Figure 4.9. Comparison between finite element simulations and measurements of deformation tests on samples of Maastricht Tuffeau at varying confinement pressures.

capable of reproducing with a marked accuracy the overall deformation characteristics. The range of compaction propagation as a function of the axial strain is displayed through solid symbols, emphasising again the satisfactory match with the measurements obtained with the lower bound calibration.

A closer inspection on the strain field predicted by the lower bound calibration is shown in Fig. 4.12, along with the experimental counterparts obtained through DIC. This comparison indicates remarkable agreement in terms of the inclination of the the compaction band. Specifically, simulations under 2.0-, 3.0-, 4.0-, and 5.0-MPa displayed compaction bands at, respectively, an angle of 35°, 20°, 12°, and 0°, which match satisfactorily with the laboratory

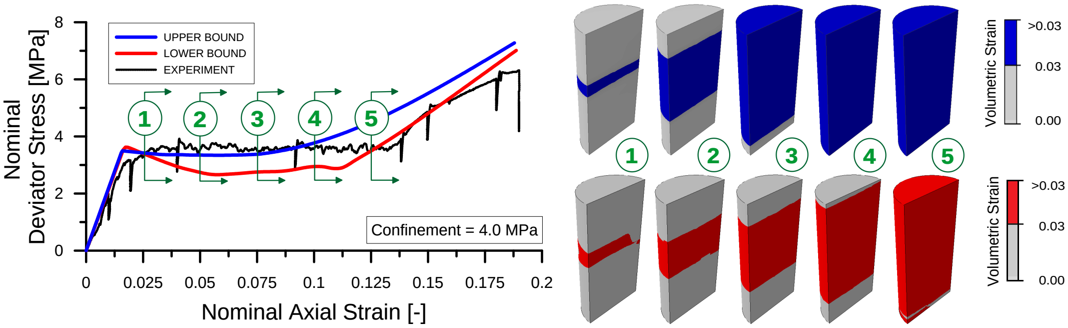

Figure 4.10. Comparison between the full-field responses computed with an upper-bound and lower-bound calibration. The propagation of compaction zone is illustrated at various intervals throughout the deformation process. This comparison illustrates the advantages and disadvantages of each set of model parameters, in that, the upper-bound calibration reproduces satisfactorily the stress levels, while the lower-bound calibration results in a better performance in replicating the compaction propagation pattern.

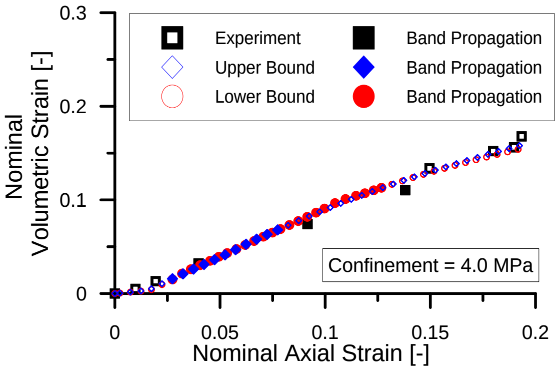

Figure 4.11. Volumetric deformation associated with the upper bound and lower bound calibration compared with experimental measurements. The solid symbols indicate the range of compaction propagation.

specimens (measured angles of 35°, 15°, 10°, and 0°, respectively). It is worth mentioning that these results are also consistent with the predicted angles obtained from the bifurcation analysis reported in Section 4.2.2, which predicted higher localization potential (i.e., minimum acoustic tensor determinant for each localization profile) at 32°, 28°, 11°, and 0°. This

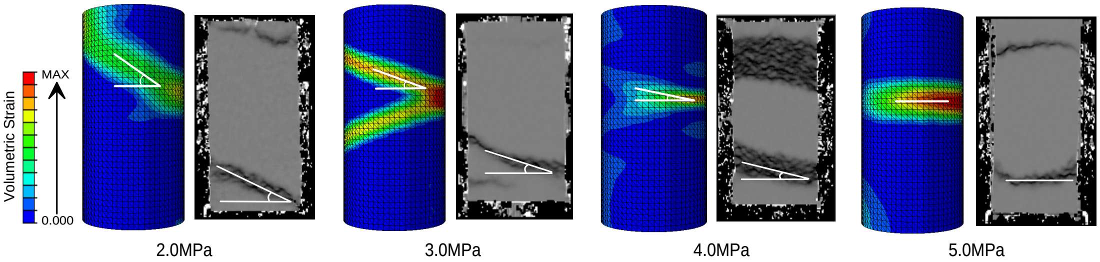

Figure 4.12. Comparison between finite element simulations and DIC computations for laboratory tests on samples of Maastricht Tuffeau deformed under triaxial compression conditions at various confinement pressures. The comparison was conducted with reference to the incremental volumetric strain field at the inception of localization.

comparison confirms the adequacy of the calibration in replicating the pressure-dependent mechanisms of compaction localization.

The model is then examined for its ability to replicate the rate at which compaction propagates across the specimen as a function of the global deformation. For this purpose, a compression has been conducted between the simulations and the experiments on the basis of the volumetric strain field and the evolving porosity maps (Fig. 4.13). The comparison was conducted at various deformation intervals indicated on the stress-strain curves. For instance, Fig. 4.13a, shows the comparison for the case of 2.0 MPa, where the strain fields were presented at 6.8%, 9.5%, and 12.4% axial strain. Based on visual inspection, it can be readily seen that, for this case, the numerical model has adequately reproduced the portion of the specimen across which compaction has propagated (here nearly 20%, 40%, and 60% at the three intervals).

Similar conclusions can be drawn from the simulations of 3.0 and 4.0 MPa, while a less satisfactory agreement is obtained at 5.0 MPa (Fig. 4.13d). In the latter case, the simulations overestimated the extent of plastically compacted sample volume (i.e., while at 7.0% axial strain the laboratory tests displayed major compaction only over 40% of the sample volume, the numerical analyses reached almost full compaction at the same global strain level). This can be considered as an outcome of the high amount of softening incorporated into the analyses and, as previously mentioned, can be mitigated by employing augmented hardening rules with more flexible analytical expressions. Despite these limitations, the overall performance of the model can be considered satisfactory, in that it succeeds in reproducing most of the evidence measured in the laboratory, most notably the pace and spatial extent of localized compaction. Nevertheless, it is worth remarking that the analysis was unable to reproduce the exact spatial patterns of strain localization. In fact, since a weak element was used to trigger localization, the onset and propagation was always controlled by this element.

Given the important role of spatial variations in material properties on the triggering of strain localization [*Borja et al.*, 2013; *Shahin et al.*, 2016], greater benefits from microtomography measurements of initial and emerging heterogeneity should be considered in the numerical analyses.

4.4. Simulations Based on Replicas of Heterogeneous Specimens

The mapping scheme described in Section 4.1 is here applied to incorporate in-situ measurements of porosity field in the FE model. The local porosity is mapped into the FE mesh following the procedure discussed in Section 4.1, and the conversion rule discussed in App. B is employed throughout. A binarized image of the specimen is considered with an REV size of $54 \times 54 \times 54$ voxel, which is consistent with the evidence collected by *Papazoglou et al.* [2017, 2019]. Such an REV size corresponds to a cubic cell with 700 μm sides, i.e., about 5 times the median grain size (D_{50}) of Maastricht Tuffeau. Fig. 4.14a shows a numerical replica of the heterogeneous specimen based on the initial porosity map, while Fig. 4.14b

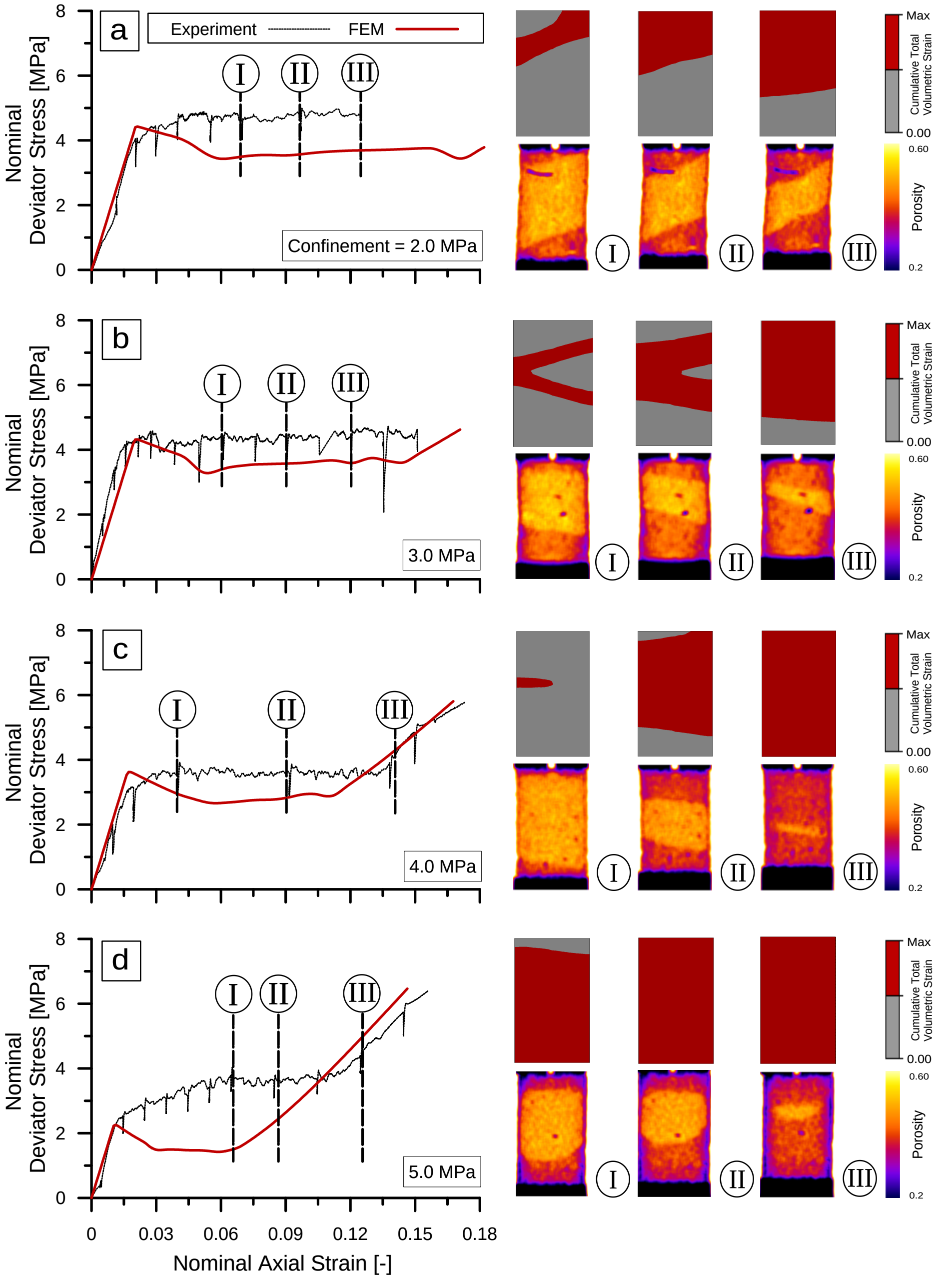

Figure 4.13. Triaxial test simulations with confinement pressures ranging from 2.0 MPa to 5.0 MPa. The propagation of compaction along the deformation process is illustrated in terms of cumulative volumetric strain field. The comparison of these results with their counterparts obtained through X-ray tomography demonstrates the capabilities of the numerical model in capturing the portion of the specimen across which compaction has propagated as a function of the imposed global deformation.

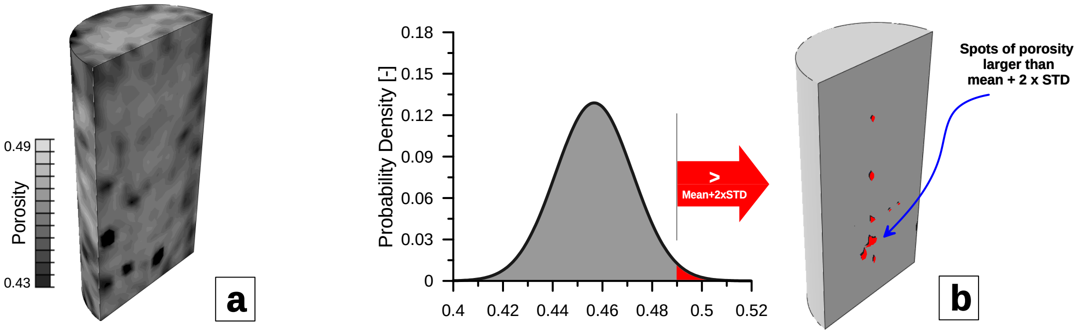

Figure 4.14. Incorporation of porosity measurements into finite element computations. (a) Porosity field characterizing the initial condition of a heterogeneous specimen. (b) Identification of areas characterized by values of porosity within the upper tail of the distribution reported by digital images (i.e., porosity spots $\geq$ 2STD, where STD is the measured standard deviation of the porosity field). The analysis indicates that hotspots of high porosity are mainly located in correspondence of the vertical axis and along the middle portion of the specimen.

highlights the locations characterized by values of porosity corresponding to the upper tail of the distribution. This numerical replica is used in triaxial compression simulation, where the same loading procedure used above in Section 3.4 for triaxial shearing has been adopted.

Fig. 4.15a shows the mechanical response of the heterogeneous specimen reported in terms of the nominal stress deviator versus the nominal axial strain. The mechanical response of the specimen based on a homogeneous simulation (with weak element) is reported in the same figure. It can be seen that the mechanical response of both simulations is characterized by a peak strength that is achieved at the same deformation interval (1.8% axial strain), followed by stages of strain softening. Both specimens display by the end of the plateau a sharp transition of deformation behavior characterized by a remarkable gain of stiffness (at around 12.0% axial strain). On the other hand, the strain fields associated with the two simulations are presented in Fig. 4.15b-c, where the onset and evolution of compaction

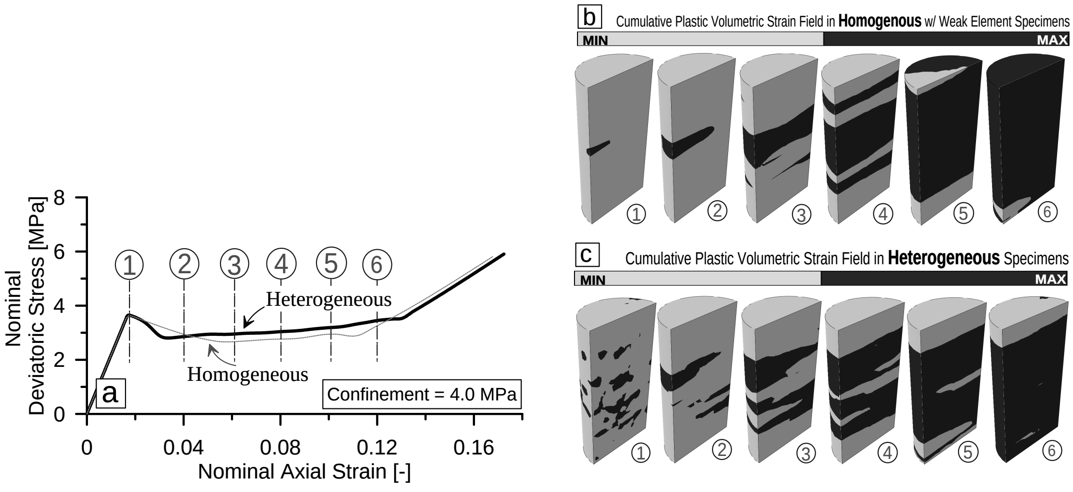

Figure 4.15. Comparison of FE triaxial test simulations under 4.0 MPa confining pressure between homogeneous specimen with weak-element and a specimen with spatial heterogeneities (porosity). (a) Global deformation response showing no significant effect of the heterogeneity on the macroscopic behavior. (b) Cumulative volumetric strain field of the homogeneous specimen showing the onset of localization at the weak element (stage 1), as well as the propagation of a compaction front towards the sample boundaries. (c) Cumulative volumetric strain field of the heterogeneous specimen showing the onset of compaction localization at several points located in the middle of the specimen (stage 1), as well as the propagation of the bands towards the specimen boundaries (stages 2-6).

bands are illustrated in terms of plastic volumetric strain reported at various deformation intervals. These intervals are marked in Fig. 4.15a with numbers from 1-6, also shown on the corresponding field illustration. In this figure, it can be seen that the simulation based on a homogeneous specimen undergoes compaction localization through the following steps: ($b1$) Strain localization is triggered by the weak element located around the mid-height of the specimen. ($b2$) The newly generated compaction band extends laterally. ($b3$) Once the band has reached the lateral boundary of the sample, the compaction zone further propagates in the axial direction through band thickening, while new bands nucleate. ($b4-6$) All active bands continue to thicken until the entire specimen is compacted. By contrast, simulations based on a heterogeneous porosity field has displayed inception of compaction localization at many locations (c1). Such results can be explained as a consequence of weaknesses corresponding with areas of higher porosity (Fig. 4.14b). The persistent bands in (c2) continue to propagate in a form of band thickening until the entire specimen is compacted (c3-c6). This comparison, however, shows that taking into account the porosity field has altered the rate of compaction propagation. Specifically, while the homogeneous simulation has undergone nearly a full compaction by (b6), the heterogeneous specimen displays a compaction of around 90% for the same deformation interval (c6).

Observations made on the global response and the evolution of the kinematic field highlight two features. First, material heterogeneity has a significant role in triggering strain localization, where it was found that material spots associated with higher porosity have played a key role in identifying the location of compaction localization onset. Although in the heterogeneous virtual specimen compaction is initiated concurrently at multiple locations, each of these active zones propagate through a mode of band thickening similar to that recovered in the homogeneous simulation. As a result, while material heterogeneity constrains the initiation of localization, the material properties encoded into the model parameters underpin a well defined mode of compaction propagation. Furthermore, the global responses in all cases were quite comparable, suggesting that global measurements cannot offer any insight on the spatial patterns of compaction localization underlying a particular force-deformation response. The strain fields computed by the two simulations should be compared with the in-situ tomography measurements illustrated in Fig. 4.13c, which reveals clear mismatches in the location of zones of active compaction localization. In fact, while in the FE analyses strain localization is triggered at the middle of the specimen, the porosity measurements show that compaction propagated from the specimen ends. This suggests that the compaction banding mode observed in the experiments cannot be explained in light of material heterogeneity alone, thus requiring other factors to be taken into consideration.

4.5. Conclusions

This chapter investigated the role of heterogeneity in material properties on the onset and propagation of compaction localization. The work relied heavily on rich measurements obtained through laboratory testing of Maastricht Tuffeau that was tested through triaxial compression at varying confinements using concurrent X-ray computed tomography and digital image correlation to track the onset and propagation of compaction localization. A mapping scheme relying on the concept of representative elementary volume was proposed and used to bridge local material measurements acquired via x-ray tomography and the numerical discretization inherent with the selected finite element formulation. In particular, each Gauss point was associated with a unique elementary volume, thus allowing the identification of material state variables directly form the physical specimen.

The mechanical behavior of the rock was reproduced through a constitutive model based on a standard strain-hardening plasticity but including viscoplasticity to mitigate pathological mesh dependence. A rich dataset including macroscopic mechanical measurements aided by tomography-based tracking of compaction propagation was used for model calibration. Triaxial compression tests were then simulated as boundary value problems, illustrating the ability of the calibrated model to capture satisfactorily a wide range of macroscopic attributes of the compaction process, such as the elongation of the post-yielding plateau, the inclination of the deformation bands and the spatial propagation of compaction across the specimen. Despite the inevitable approximations related with the use of a relatively simple constitutive law, the satisfactory agreement between numerical results and laboratory measurements point out the benefits of parameter optimization strategies accounting synergistically for global measurements and spatially-distributed deformations, especially in the presence of compaction localization processes.

The spatially distributed heterogeneity was incorporated in the finite element model based on the proposed mapping scheme. The resulting numerical replica was eventually used to conduct high-fidelity numerical analyses exploring the effects of material heterogeneity on the initiation and propagation of localized compaction.The main findings of the analyses can be summarized as follows:

(1) Compaction localization was triggered in correspondence of regions of highest porosity, which effectively served as areas of concentrated weakness.

(2) Regardless of the location of the weak spots, in all cases compaction propagated through band thickening, thus indicating that while the heterogeneity constrains the initiation of localization, the material properties encoded into the constitutive parameters underpin a well-defined mode of compaction propagation.

(3) Material heterogeneity alone was insufficient to explain the observed spatial patterns of sample compaction.

The unique combination of full-field experimental measurements and high-fidelity compaction band simulations presented in this work allowed not only to construct for the first time a virtual replica of a porous rock sample exhibiting compaction banding, but also provided insight on the processes that govern the emergence of such complex deformation structures.

CHAPTER 5

Effects of Boundary Friction on Compaction Propagation[*]

The previous chapter pointed out non-negligible effects of material heterogeneity on the triggering of strain localization, which explains similar observations reported in the literature [*Heap et al.*, 2015; *Hol et al.*, 2018; *Huang et al.*, 2019]. The literature, however, provides abundant evidence of compaction banding initiating from the specimen ends, which are often attributed to boundary effects [*Papazoglou et al.*, 2019]. It can, therefore be expected that the feedback between boundary effects and material heterogeneity is much richer than what can be displayed by using specimen-specific values of material variability. This chapter investigates the interplay between the boundary friction and material heterogeneity on the emergence of compaction localization.

5.1. Effects of Boundary Friction

The FE simulations presented in the previous chapter are here improved to incorporate the effects of frictional interaction between the specimen's ends and loading platens. For this purpose, each platen is modeled as a rigid body while the platen-specimen interaction was simulated by a Coulomb-type frictional interface. As a result, the ratio between the tangential and the normal traction at the boundaries is quantified by the friction coefficient,

---

[*] The content of this chapter is published in:

- Shahin, G., Viggiani, G., and Buscarnera, G. (submitted) Simulating spatial heterogeneity through a CT-FE mapping scheme discloses boundary effects on emerging compaction bands.
- Shahin, G., and Buscarnera, G. (submitted) Simulation of emergent compaction banding fronts caused by frictional boundaries.

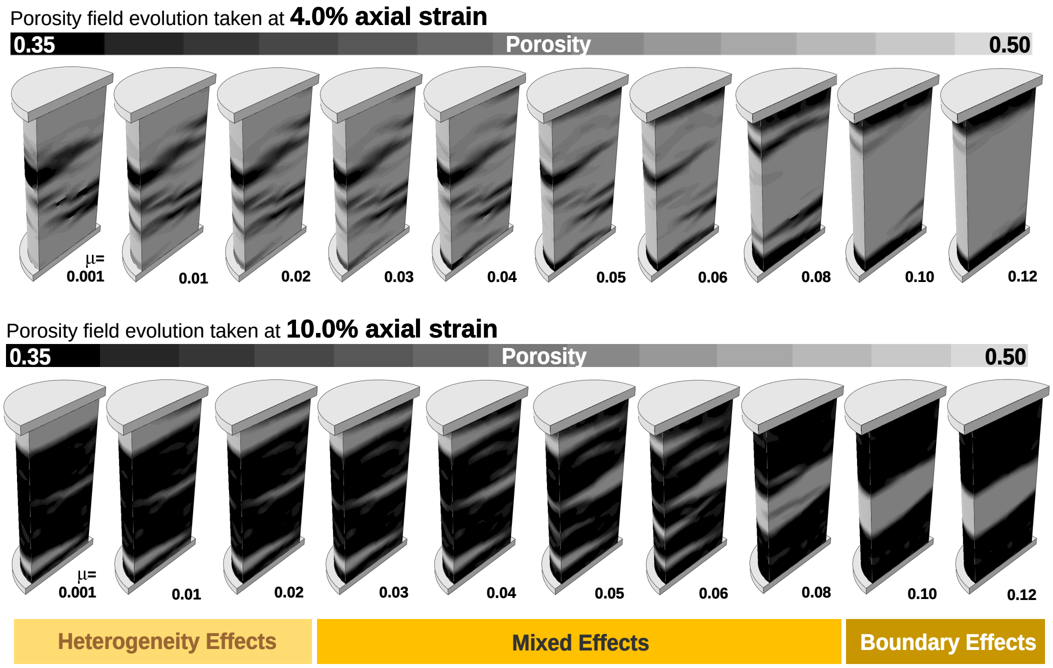

Figure 5.1. Triaxial test simulations of heterogeneous specimens with varying values of platen-specimen friction (0.0 to 0.12). Porosity field evolution illustrated at various deformation intervals, i.e. at (upper) 4.0% and (lower) 10.0% nominal axial strain, showing that in simulations based on low friction, the spatial fluctuation of the material properties dominates the triggering of compaction localization (in the middle of the specimen, the porosity is slightly larger). By contrast, in simulations based on higher values of boundary friction, the platen-specimen interface controls the onset of compaction localization. The simulations also reveal the existence of a transitional zone between these end members (between $0.03 - 0.08$), where both factors influence the initiation of compaction localization (i.e., compaction bands emerge both in the middle and at the boundaries of the specimen.)

μ. This coefficient forms the focal point in the following analysis, where the effects of its intensity on strain localization onset and propagation are explored. Specimens with boundary frictions that vary from 0 to ∞ (i.e., perfectly rough surface hindering lateral slip) have been tested with reference to triaxial compression under 4.0 MPa confining pressure.

The outcomes of this analysis are reported in Fig. 5.1 which shows the evolution of the porosity field at two different deformation intervals (i.e. 4.0% and 10.0% nominal axial strain). It can be readily seen that in the presence of low friction (0.001 → 0.02), compaction localization tends to be triggered by material heterogeneities, similar to the case of frictionless boundaries discussed in the previous section. By contrast, simulations based on higher values of boundary friction (i.e., 0.10 → 0.12) show compaction bands emerging at the specimen ends, and then propagating towards the center. These observations shed light on the role of boundary friction in triggering this mode of strain localization. Intriguingly, this analysis reveals the existence of a transition zone between these two end members (i.e., 0.03 → 0.08), where field heterogeneity and boundary friction appear to exert comparable degrees of influence by triggering compaction bands at both the spots of lower strength and near the boundaries. A close look at the specimen ends, however, reveals that as soon as compaction starts to concentrate at the boundaries because of the effect of rough interfaces, inelastic effects start being hindered in the central portion of the specimen, thus revealing a gradually declining impact of spatial heterogeneity.

The response of the simulation based on 0.10 boundary friction is compared with the response of the simulation based on frictionless boundaries in Fig. 5.2, showing that the difference in strain localization patterns does not have a noticeable impact on the global response. It is worth mentioning that these results hold also for simulations based on higher friction coefficients, up to values compatible with an ideal rough boundary (i.e., conditions preventing the relative tangential movement between the specimen and the platen).

A comparison between the numerical analysis and the laboratory measurements is presented in Fig. 5.3 reported in terms of the global deformation response and the evolution of the porosity field. The figure emphasizes a noticeable improvement in the model performance, especially in the location of compaction bands onset and their from of propagation. It can be seen that the deformation intervals of 9.0% and 14.0%, the portion of the specimen

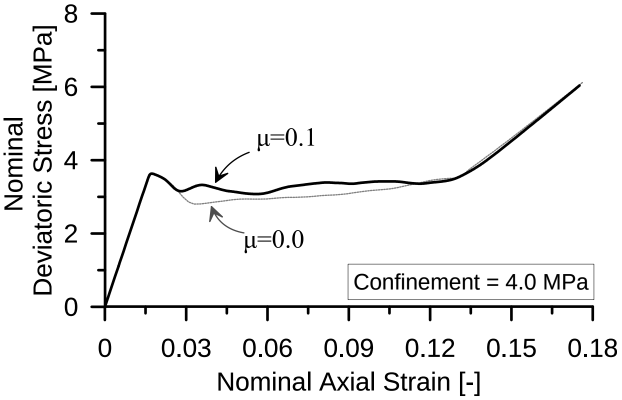

Figure 5.2. Global deformation response of triaxial test simulations conducted on finite element models with frictionless boundaries (light-gray line) and rough boundaries with μ=0.10 (dark-gray line). Compaction localization in the first was triggered by field heterogeneity, while in the second it was triggered under the influence of boundary friction. As a result, the comparison suggests that changes in the spatial pattern of localized compaction are hardly detectable from the global response.

across which compaction has propagated is consistent with the laboratory measurements (i.e., around 50% and 95%, respectively). In this figure, it can also be seen that the reduction in porosity upon compaction localization was effectively reproduced with a deterioration in the pore space from 50% to 35%. It is in fact arguable that the model with rough boundaries provides a more accurate representation of the Maastricht Tuffeau behavior, especially considering that a significant improvement of the predicted compaction localization patterns is obtained even with the use of low values of specimen-platen friction compatible with the use of lubricants [*Labuz and Bridell*, 1993].

5.2. Interplay between Boundary Friction and Material Heterogeneity

The previous section pointed out non-negligible effects of the platen-specimen interaction on the triggering of strain localization, up to the point of making the role of initial porosity

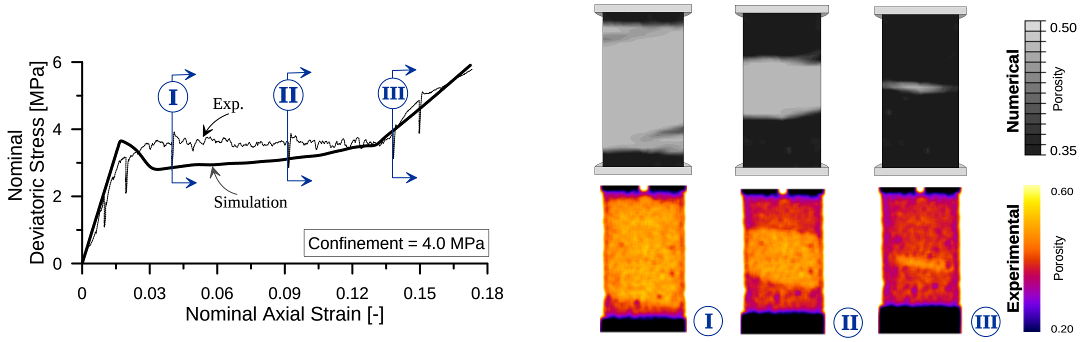

Figure 5.3. Triaxial test simulation at a confining pressure of 4.0 MPa conducted based on a numerical replica of a laboratory specimen with heterogeneous porosity field. The simulation includes a platen-specimen interface characterized by friction coefficient $\mu = 0.10$. The propagation of compaction localization along the loading path is illustrated in terms of the porosity field. Comparing these results with their experimental counterparts demonstrates the capabilities of the model in reproducing the spatial propagation of compaction as a function of the imposed deformation.

heterogeneities practically ineffective. This section aims to investigate the impact of varying degrees of sample heterogeneity in presence of rough boundaries, with the main objective to quantify their interaction. This analysis is based on quasi-synthetic porosity maps generated by benefiting from the measured one, by adjusting the standard deviation of their statistical distribution, but at the same time by preserving the spatial distribution of porosity assigned on the basis of the available digital images. As a consequence, porosity values across the specimen were first shifted to locate the mean value of the Gaussian distribution at zero. Afterwards, these values are divided by their standard deviation (here STD $= 0.02$), eventually obtaining a porosity map with zero mean value and STD$= 1.0$. This configuration forms a "*primary map*" that is then multiplied by the desired standard deviation and relocated at the targeted mean porosity value (always the same of the original one, i.e., 0.455). This procedure has been applied twice, first to generate porosity maps with reduced heterogeneity (STD= 0.005), and then with exacerbated heterogeneity (STD= 0.04).

Fig. 5.4 presents three sets of numerical experiments based on three heterogeneous specimens. For each scenario, the boundary friction coefficient increases from left to right. The specimens were tested under triaxial compression by following the same procedures discussed in the previous sections. The results are presented in terms of porosity fields taken at 4.0% nominal axial strain. In this illustration, it can be seen that the three sets of simulations display similar patterns of compaction banding at lower levels of boundary friction, in all cases characterized by a primary control of the material heterogeneity on the location of compaction band initiation. All cases have displayed a gradually increasing influence of boundary friction, such that at a given friction threshold, the role of material heterogeneity disappears. The threshold at which the effects of boundary friction becomes noticeable and the threshold at which the effects of spatial heterogeneity become negligible is found to markedly depend on the degree of spatial heterogeneity. For example, in specimens with modest heterogeneity, high-porosity hotspots constrain compaction localization only for low values of boundary frictions (i.e., $\mu \leq 0.02$), while virtual specimens with wider porosity variability exhibit a dominant effect of the heterogeneity up to values of boundary friction three times larger (i.e., up to μ=0.06). Furthermore, for specimens with modest heterogeneity, the threshold of boundary friction beyond which the role of the porosity field becomes negligible is μ=0.04, while it grows up to values five times larger (i.e., μ=0.20) in the specimen with widely distributed porosity values. These systematic numerical results confirm once again the existence of three regimes of interaction between spatial heterogeneity and boundary conditions, which are schematically depicted in Fig. 5.5.

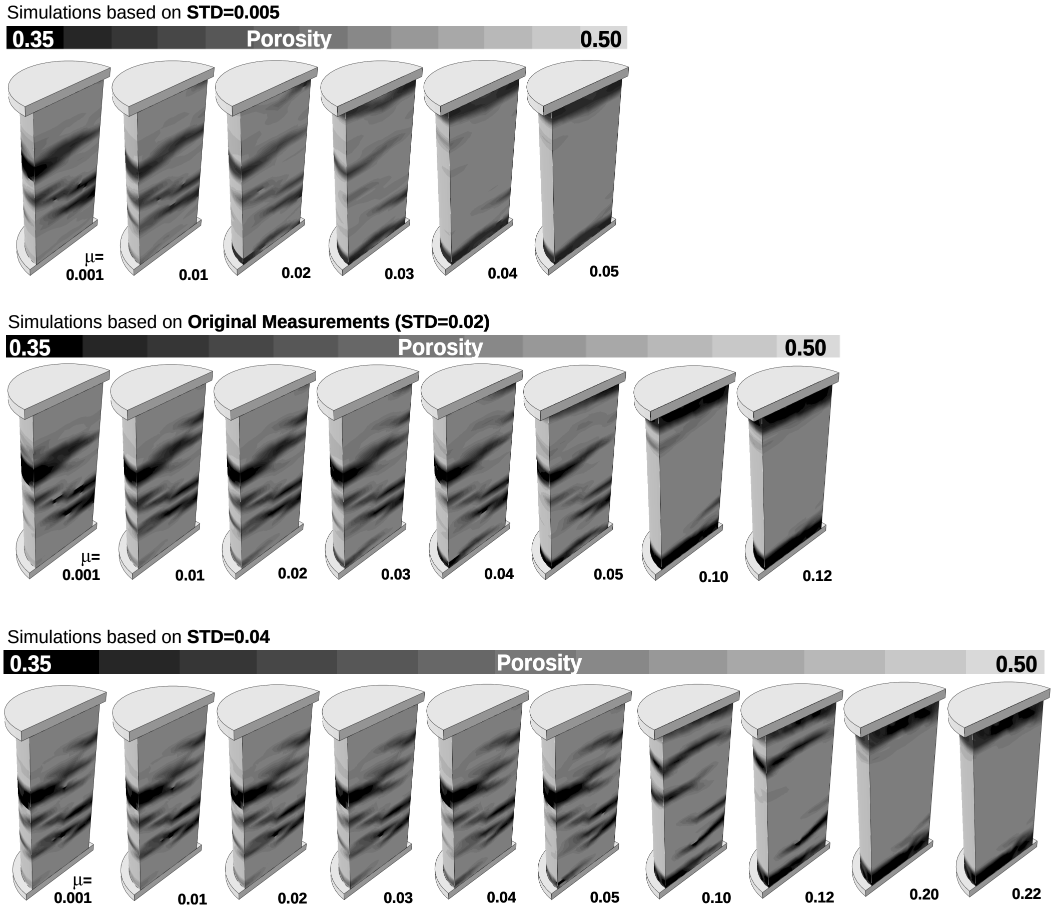

Figure 5.4. Triaxial test simulations at a confining pressure of 4.0 MPa conducted based on specimens with different degrees of spatial heterogeneity obtained by scaling the original field based on a target value of standard deviation, STD. The middle row has STD=0.02, coinciding with the degree of spatial variability detected from x-ray measurements. The upper and lower rows refer to synthetic porosity fields based on STD= 0.005 (first row) and STD= 0.04 (third row), respectively. The results show that the influence of boundary effects is mediated by the intensity of material heterogeneity.

5.3. Effects of Boundary Friction Outside the Strain Localization Domain

The findings above motivated further inspections of the boundary effects to assess if frictional interaction can influence the interpretation of global measurements even for loading paths conducted outside the domain of compaction localization. The analyses provided in

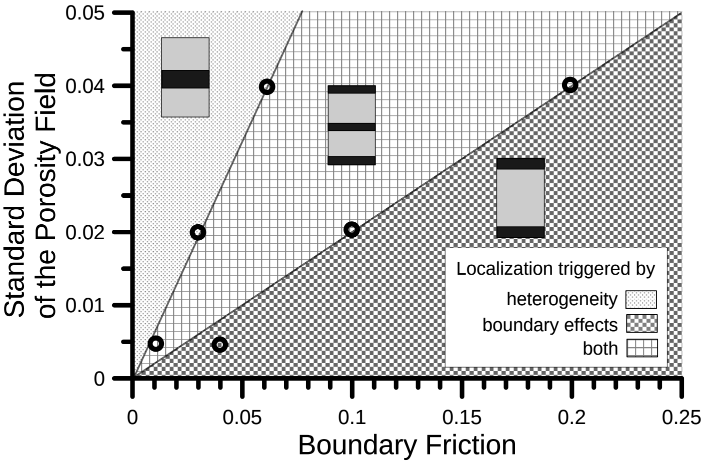

Figure 5.5. Illustration of the interplay between boundary friction intensity and heterogeneity intensity on the triggering of compaction localization, showing that the space is subdivided into three zones, namely a zone of dominant heterogeneity (upper left), a zone of dominant boundary effects (lower right), and an intermediate zone characterized by the concurrent influence of material weaknesses and boundary effects.

this chapter rely on previous calibration of two porous rocks for which available evidence in the laboratory shows very different modes of compaction localization, one characterized by tabular, discrete bands, and the other by a propagating compaction front. Appendix E emphasizes the role of material properties and specifically hardening characteristics in promoting these various modes of heterogeneous compaction and illustrates the associated stress fields.

5.3.1. Material-Point Analyses

Simulations based on homogeneous idealizations (material-point analyses) are conducted first to illustrate the response predicted by the model for loading paths imposed outside the strain localization regime. Simulations of oedometric compression and triaxial compression were conducted, following isotropic compression. The initial mean stress is chosen to enable both

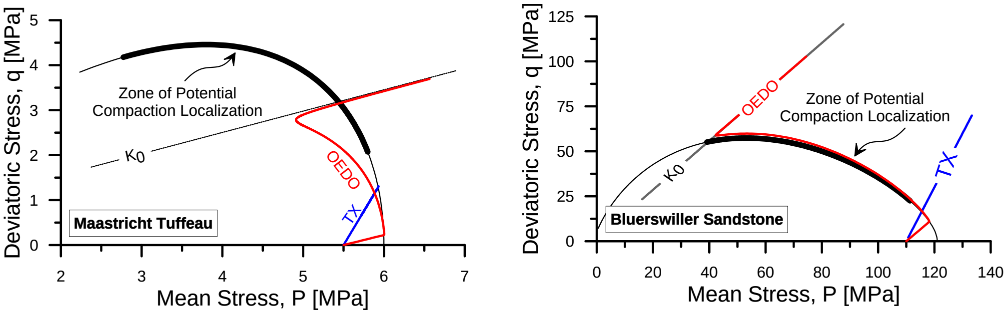

Figure 5.6. Material point simulations of triaxial (TX) and oedometric (OEDO) compression on numerical specimens of Maastricht Tuffeau (left) and Bleurswiller sandstone (right) conducted outside the strain localization regime. For illustration purposes the figure includes the K_0 line that results upon continued compression for the two materials.

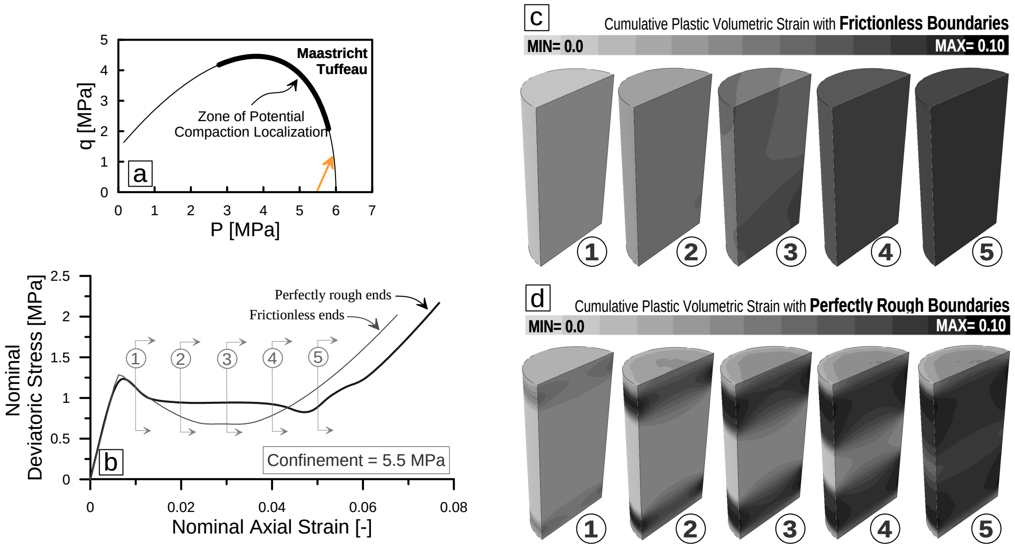

Figure 5.7. Triaxial test simulations on specimens of Maastricht Tuffeau sheared outside the domain of compaction localization. The comparison is between simulations based on frictionless boundaries and boundaries with perfect roughness. (a) The localization domain is marked by a thick solid line. (b) Deformation response resulting from both simulations. (c-d) Compaction field displayed in a form of cumulative volumetric plastic strain at various deformation intervals, also marked in (b).

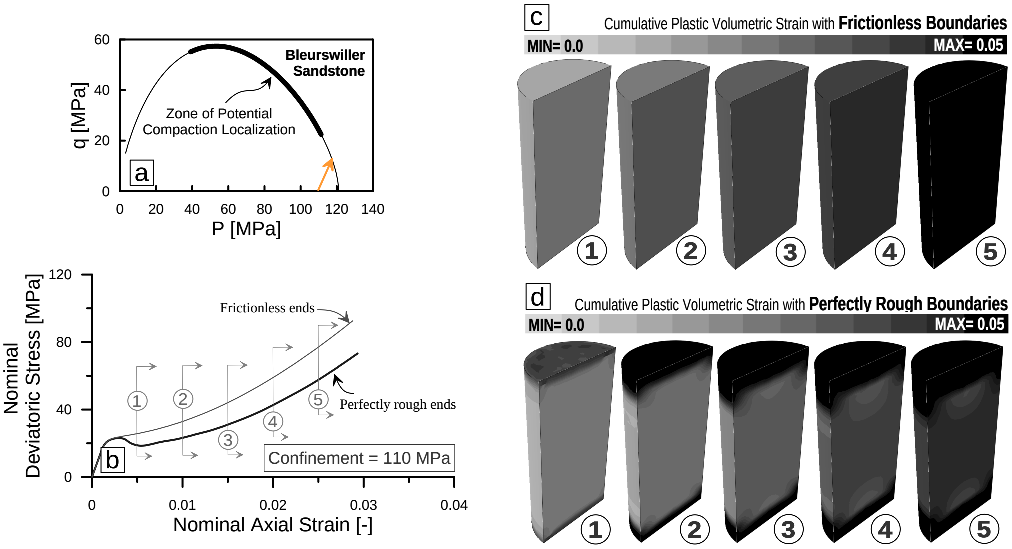

Figure 5.8. Triaxial test simulations on specimens of Bleurswiller sandstone sheared outside the domain of compaction localization. The comparison is between simulations based on frictionless boundaries and boundaries with perfect roughness. (a) The localization domain is marked by a thick solid line. (b) Deformation response resulting from both simulations. (c-d) Compaction field displayed in a form of cumulative volumetric plastic strain at various deformation intervals, also marked in (b)

paths to intersect with the yield surface outside the localization domain. Fig. 5.6 illustrates the computed response in both simulations, where it can be seen that the elastic response of both materials under oedometric conditions is characterized by a stress ratio (q/p) markedly lower than the stress ratio of the triaxial path. With softening in Maastricht Tuffeau and hardening in Bleurswiller sandstone, the oedometric path evolves in the post-yielding regime with increasing deviatoric stress, eventually converging asymptotically to the K_0 line. By contrast, the response under triaxial compression evolves with a stress path typical of a constant radial-stress path.

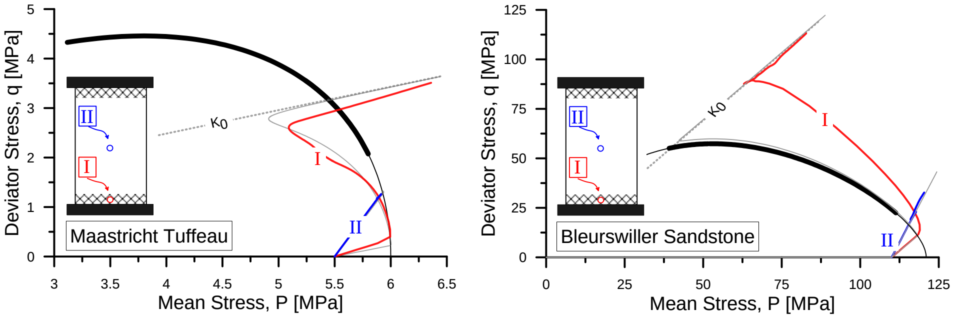

Figure 5.9. Computed stress paths at Gauss points located at the bottom and the middle of the specimen based on material models of (a) Maastricht Tuffeau and (b) Bleurswiller sandstone. The triaxial test simulation is based on perfectly rough boundaries. For comparison purposes, the dotted line indicates the stress path generated by a material point analysis characterized by a one-dimensional (oedometric) compression path.

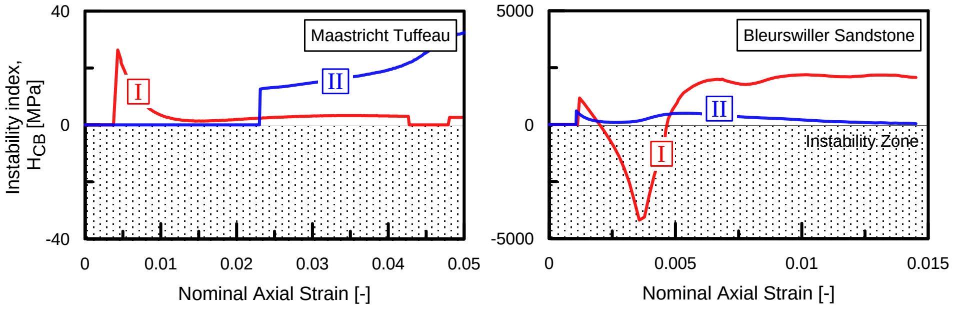

Figure 5.10. Assessment of material instability along the stress paths presented in Fig. 5.9

5.3.2. Full-field Numerical Analyses

Material-point analyses describe idealized homogeneous processes providing only an approximation of real experiments. For this purpose, virtual experiments based on the finite element method are used hereafter to conduct triaxial compression tests outside the strain localization domain.

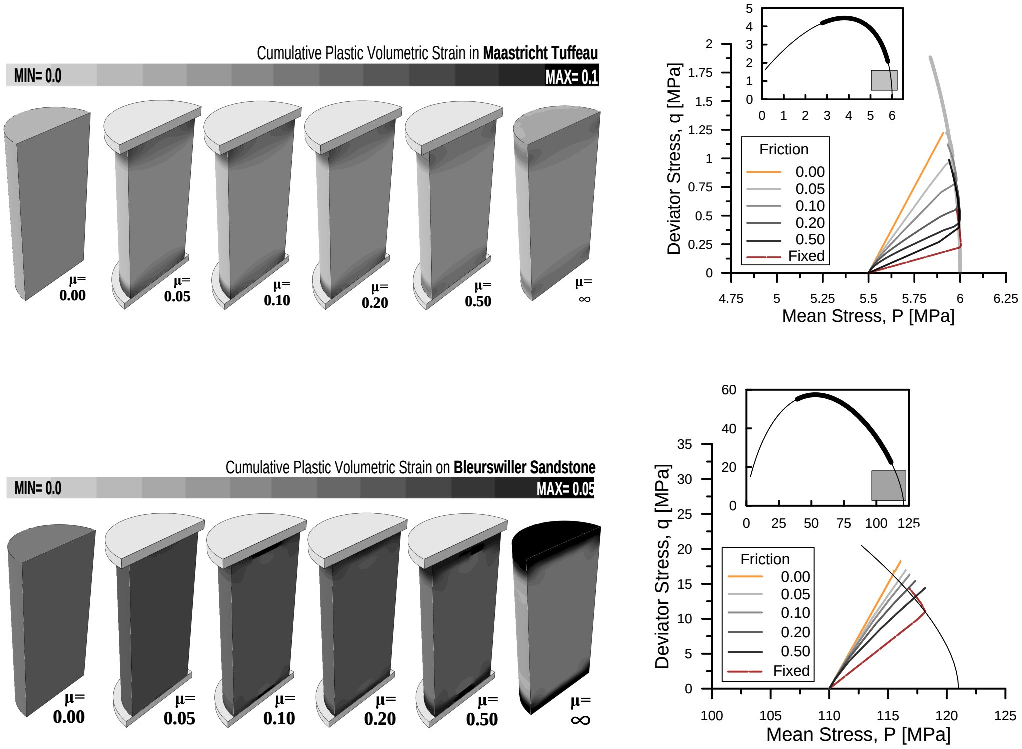

Figure 5.11. Triaxial test simulations conducted on Maastricht Tuffeau (upper) and Bleurswiller sandstone (lower) specimens including Coulomb-type frictional boundaries with friction coefficient ranging from 0.05 to 0.50, compared with simulations based on frictionless boundaries and perfectly rough boundaries. (left) Strain fields at the inception of heterogeneous compaction induced by boundary friction. (right) Computations extracted from Gauss points located at the bottom of the specimens where compaction bands emerged, showing shifting from triaxial-like to oedometic-like compression behavior as the boundary friction shifts from 0 to ∞.

Computations of the response of Maastricht Tuffeau specimens based on frictionless and perfectly rough boundaries are presented in Fig. 5.7, which shows (a) the overall stress response of the specimen intersecting with the yield surface outside the potential zone of compaction localization, and (b) the stress-strain responses associated with both boundary conditions, here reported in terms of the deviatoric stress evolution as a function of the applied axial strain. It is readily apparent that both conditions lead to a comparable deviatoric stress peak followed by stages of strain softening and eventually a marked gain of resistance. Despite these similarities, some differences can be observed. Specifically, the specimen with rough boundaries displayed a tendency to deform with an extended post-yielding plateau and relatively less softening.

The evolution of the strain field is illustrated in Fig. 5.7c-d, at various deformation intervals, also marked in (b). As expected, frictionless boundaries promoted a homogeneous strain field. By contrast, a heterogeneous deformation field emerged in simulations with rough boundaries, as compaction fronts propagated from the specimen's ends towards the center. Similar results can be obtained from corresponding simulations conducted on virtual specimens of Bleurswiller sandstone (Fig. 5.8).

To further inspect these results, the stress path associated with material points located at the center and near the boundaries are presented in Fig. 5.9. Although the specimen was globally subjected to triaxial compression, the boundary zones exhibit stress paths closely resembling oedometric compression (see Fig. 5.6 for comparison), while the central portion consistently maintains a triaxial compression path. The deviation in stresses in the vicinity of the specimen ends promotes an early engagement of the yield surface resulting in the activation of plasticity. It is, therefore apparent that the kinematic constraints imposed by the frictional boundaries impacts the ability of the material to deform laterally close to the loading platens, resulting in a response that shares similarities with one-dimensional compaction.

The heterogeneous compaction fronts emerging from the simulations are the product of concurrent factors, which include the early activation of cap plasticity due to frictional confinement, as well as the shift of the stress path towards the compaction banding domain. The nature of these factors is widely different, in that the former involves stable compaction, while the latter implies unstable pore collapse. Hence, to elucidate the origin of such fronts the simulations were further inspected with the compaction instability index proposed in Chapter 3. This index is assessed along the stress paths that are presented in Fig. 5.9 and its evolution is reported as a function of the nominal axial strain (Fig. 5.10). For both rocks, it can be seen that near the boundaries the activation of plasticity involves a stable compaction. However, the kinematic constraint causes the path to intersect the zone of compaction localization at a subsequent stage, thus facilitating a possible transition from the spreading of heterogeneous (stable) compaction to the propagation of an active instability front. Such mechanism is clearly seen in the simulations conducted with reference to Bleurswiller sandstone, for which non-normality tends to maintain a large size of the localization domain (i.e., the altered stress path and the zone of compaction localization tend to intersect upon growing deformation). By contrast, the state remains stable along the entire period of active compaction in Maastricht Tuffeau, for which softening is prevalent and the extent of the localization domain tends to shrink rapidly upon deformation [*Buscarnera and Laverack*, 2014]. Such analysis reveals that material instability is not required to promote a heterogeneous compaction front, which may emerge solely as a result of the spatially heterogeneous engagement of the plastic resources of the material.

5.3.3. Influence of the Value of Boundary Friction

The finite value of platen-specimen friction reflective of actual laboratory tests is expected to generate intermediate trends between the end-members discussed above [*Labuz and Bridell*, 1993]. The role of the platen roughness on generating heterogeneous fields is therefore assessed hereafter through parametric analyses varying the boundary friction coefficient, μ. Fig. 5.11 and Fig. 5.11 illustrate the computed responses for Maastricht Tuffeau and

Bleurswiller sandstone, respectively. Snapshots of the strain field upon yielding are reported on the left for all cases ($\mu = 0.0, 0.05, 0.10, 0.20, 0.50$, and ∞), while the stress path of material points located near the specimen boundaries is showed on the right-hand side of the figures. It is readily apparent that boundary friction caused an heterogeneous strain field in this quasi-homogeneous (with weak element) specimens regardless of the intensity of friction, and in both hardening and softening regimes (i.e., for both Bleurswiller and Tuffeau, respectively). The local stress paths associated with these simulations are characterized by a tendency to shift from a triaxial-like behavior to an oedometric-like path as the friction shifts from $0.0 \rightarrow \infty$, while the central portion of these simulations maintains a triaxial behavior regardless of the friction value. The analyses suggest that this dependence is nonlinear, in that, equal increments of friction do not lead to the same deviation in the stress path. For example, in Maastricht Tuffeau, the increase of boundary friction from $0.05 \rightarrow 0.10$ and from $0.10 \rightarrow 0.20$ was associated with the same angular shift of the stress path towards the perfectly oedometric path.

5.4. Conclusions

The unique combination of full-field experimental measurements and high-fidelity compaction band simulations presented in this work allowed not only to construct for the first time a virtual replica of a porous rock sample exhibiting compaction banding, but also provided insight on the processes that govern the emergence of such complex deformation structures. In particular, the proposed analysis of the relative influence of boundary effects and material heterogeneity exemplifies a ubiquitous problem in geotechnology and geophysics, i.e. the interplay between natural heterogeneity and pre-existing boundaries (e.g., interactions between penetrating probes and layered ground, feedbacks between reservoir faults and caprock, concurrent initiation of multiple deformation zones around a wellbore).

(1) Material heterogeneity alone was insufficient to explain the observed spatial patterns of sample compaction, thus requiring an augmented model considering the roughness of the platen-specimen interface. Such incorporation of boundary friction in conjunction with an heterogeneous porosity field allowed the predictive capability of the model to be enhanced, as well as the spatial patterns of compaction to be accurately replicated.

(2) The analyses revealed the existence of non-negligible interplay between boundary effects (here represented by platen-specimen friction) and local properties (here represented by variations of porosity). Specifically, it was found that while for low boundary friction compaction localization is triggered systematically in the regions of highest porosity, increases in boundary friction may override the influence of spatial variations, up to a degree at which its role becomes negligible and compaction banding is forced to occur at the platen-friction interface. Interestingly, the simulations also revealed an intermediate regime between the two aforementioned end members, where compaction localization is influenced by both the porosity field and boundary effects (i.e., multiple bands nucleate concurrently within the specimen and at the platen-specimen interface).

(3) Further simulations disclosed that the transition between these regimes is chiefly controlled by the degree of material variability. In other words, large fluctuations of porosity prevent the interference of boundary effects, thus favoring the onset of localization at weak, highly porous regions. By contrast, narrow distributions of

porosity facilitate compaction localization at the boundaries by rendering the role of porosity hotspots virtually negligible.

The role of boundary friction on the generation of heterogeneous compaction in specimens loaded outside the domain of strain localization was inspected. The analysis was based on two porous rocks, i.e., Maastricht Tuffeau and Bleurswiller sandstone, because they display softening and hardening behavior in the plastic cap zone, respectively, thus providing distinct end members of behavior. Virtual triaxial compression experiments showed that the specimens with boundary friction displayed heterogeneous deformation associated with spatially varying evolution of the stress paths. While the center of the specimen continued to display triaxial-like responses, the portions of the specimen near the boundaries exhibited a deformation behavior that resembles oedometric compression. This behavior can be explained in light of the ability of the boundary constraints to hinder the lateral deformation of the specimen's ends, thus justifying the deviation of the local stress paths. Heterogeneous compaction subsequently emerged as a result of heterogeneous activation of plasticity, with compaction fronts able to propagate even with locally stable conditions (i.e., material instability was not necessary to generate the fronts). A transition from heterogeneous compaction to compaction band front characterized by active unstable collapse was found possible only when the unstable domain was sustained upon deformation until it intersected the local stress path. Parametric analyses examining the effect of the boundary friction disclosed that the higher the platen roughness, the closer the local behavior is to one-dimensional (oedometric) response. Such transition, however, was found to be nonlinear with stronger shifts occurring at the lower end of the examined interval of boundary friction (i.e., for values close to those that can be expected in typical laboratory settings). These findings suggest that in laboratory experiments on porous rocks, where the specimen-platen friction is an unavoidable factor, boundary effects could bias the interpretation of the observations by producing modes of localized compaction.

Understanding the factors leading to the onset of strain localization is therefore necessary to enhance our ability to predict the initiation and fate of subsurface deformation structures for cases in which the competition of the local factors (e.e., field heterogeneity) and system effects (e.g., boundary conditions) is crucial to identify the most likely outcome. The use of the proposed CT-FE mapping scheme to assess the causes of emerging inelasticity in pressure-dependent, porous geomaterials, therefore represents a particular example of the benefits that may derive from a deeper integration of physical measurements and numerical modeling, and epitomize an approach which should in principle be extended to all length scales of interest for geophysical and geotechnical applications.

CHAPTER 6

Field-scale Simulation of Compaction Bands

Laboratory testing of compaction banding in porous rocks provides an idealized characterization of the conditions promoting their emergence under controlled settings. Such settings should be considered as approximations of the more intricate field conditions which involve the coexistence of spatially varying boundary conditions, morphological characteristics and variations in material properties. Pronounced examples of such richness can be found in the literature. For instance, compaction bands can be found in sandstone layers that are interbedded between non-localized layers with different mechanical properties (Fig. 6.1). The interplay between rock layers in stratified systems and its possible influence on compaction banding is not yet fully understood. This is apparent from recent studies by *Chemenda et al.* [2014], who, on the basis of numerical analyses, suggested that spacing between propagating discrete bands increases as the stiffness of the neighbouring elastic layers increases. These studies, however, involved numerical weaknesses (such as lack of regularization) and were based on over-simplified constitutive models, which may have limited the ability to reproduce different forms of band propagation patterns, as well as the complete pressure dependence of these strain localization phenomena.

Other instances of field intricacies include reported evidence [*Schultz*, 2011; *Schultz et al.*, 2010] of complex systems of compaction bands that involve coexisting structures with different modes of compaction localization (Fig. 6.2 and 6.3). Such complex systems were even found [*Schultz et al.*, 2010] in sandstone layers inter-bedding non-localized sandstone layers

(Fig. 6.3). Field observations indicated that the vertical structures are pure compaction bands, while the inclined ones are shear-enhanced compaction bands. In fact, the propagation of pure compaction bands was found to terminate at the borders of the sandstone layer, while shear-enhanced bands continue to invade the neighbouring layers. *Schultz et al.* [2010] suggested that *both sets of compaction bands formed contemporaneously.* However, evidence that corroborates this hypothesis have never provided. The mechanical conditions promoting their emergence and the sequence according to which they developed remain open questions, among many, surrounding such complex systems of compaction bands.

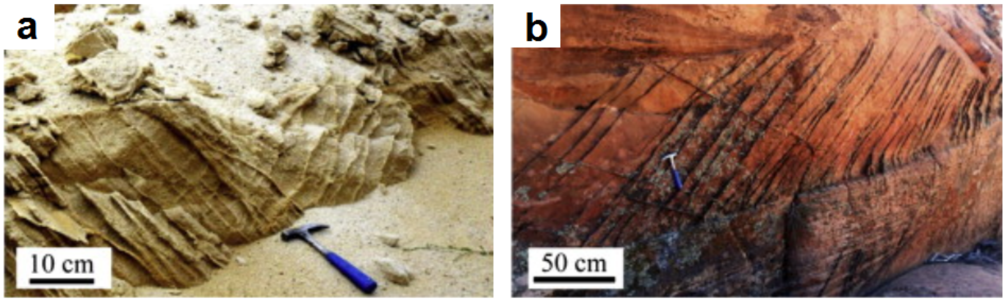

Figure 6.1. Examples of asymmetric SECBs formed under thrust-fault regime in multilayer series of sandstones. (a) Band clusters of different families in the sandstone at the Tresques quarry (Bassin du Sud-Est, Provence, France). (b) A sandstone layer inter-bedded between finer sandstones at Buckskin Gulch in Utah, USA (adapted from *Chemenda et al.* [2014]).

This chapter uses geomechanical modeling to address such questions by providing a conceptual framework of interpretation and discussing idealized numerical examples. Essential to these analyses is the selection of loading histories inspired by the locations briefly discussed above. In fact, the determination of the stress field in earth's crust has been one of the most elusive questions for structural geologist and geo-engineers. The crust typical undergoes combined effects of geological and tectonic processes (e.g., burial, tectonic deformation, and erosion) as well as local thermo-mechanical responses (e.g., creep, solids dissolution,

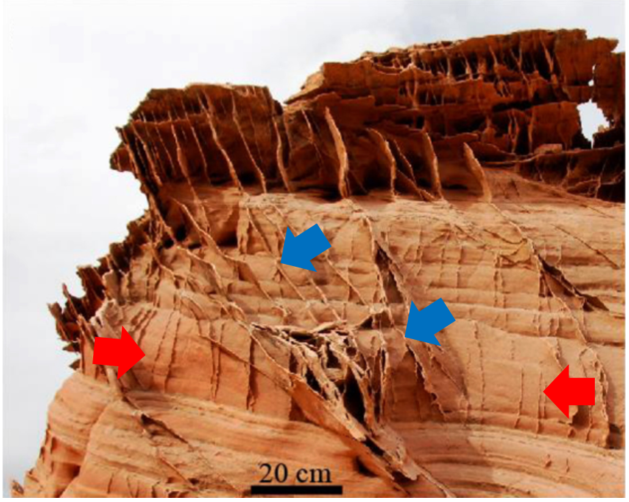

Figure 6.2. Complex systems of compaction bands involving pure compaction (red arrows) and shear-assisted compaction bands (blue arrows) in Navajo sandstone, Utah (adapted from *Chemenda and Mas* [2016])

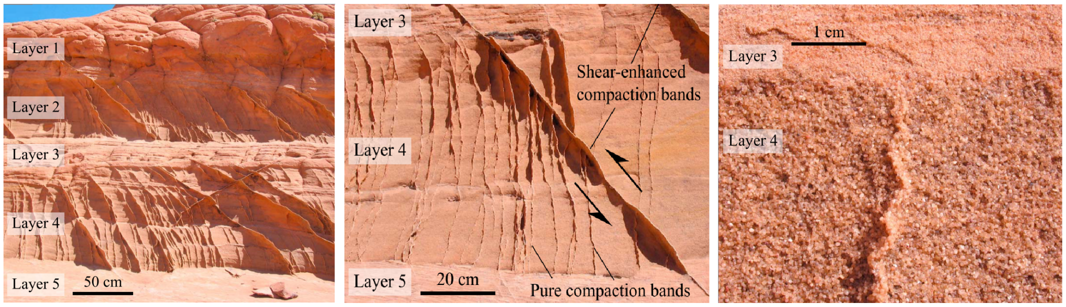

Figure 6.3. Compaction bands in the field locality in south central Utah. (a) Outcropping of the five sandstone layers. (b) Example of the coexistence of nearvertical, pure compaction bands and inclined shear enhanced compaction bands. (c) Termination of a pure compaction band along the contact between layers 3 and 4 (after *Schultz et al.* [2010]).

and thermal changes), that involve considerable uncertainties in the assessment of the stress fields [*Haimson*, 1978; *McGarr and Gay*, 1978]. Despite such uncertainties, most studies have agreed that anisotropic stress states driven by combined effects of gravitational and tectonic loads could be most representative of the stress fields [*Brace and Kohlstedt*, 1980; *Vernik and Zoback*, 1992]. Such arguments further encourage a mechanical analysis of the

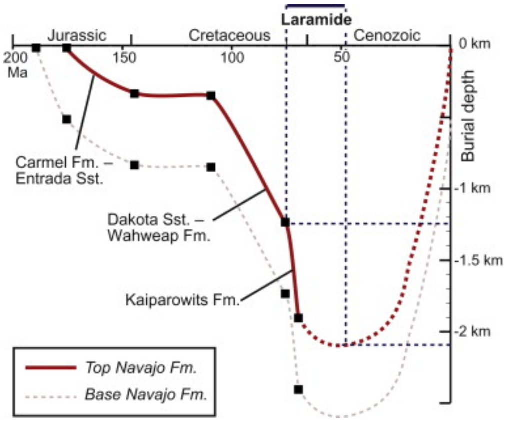

Figure 6.4. Burial graph of the Navajo Sandstone (top and base) based on stratigraphic information from the East Kaibab area (after *Fossen et al.* [2011]).

3D field-scale processes leading to compaction banding. The loading conditions used in the following numerical simulations were inspired from recent reconstruction of the geological history formulated with reference to Navajo Sandstone formation (East Kaibab area) as presented in Fig. 6.4 and illustrated by *Fossen et al.* [2011]. Specifically, combinations of burial depth increase, burial depth decrease (erosion), and tectonic contraction have been adopted.

6.1. Analysis of Compaction Banding Initiation under 3D Stress Fields

As the literature lacks experimental data about the mechanical properties of the Navajo sandstone, the following study has been based on the predictions of an elasto-plastic model of Berea Sandstone, that was calibrated on the grounds of a rich dataset provided through laboratory experimentation [*Marinelli and Buscarnera*, 2015]. This material was selected in virtue of its characteristics of strain localization as it tends to display compaction banding with various modes along a wide range of confining pressure, in connection with strain hardening in the post-yielding regime. The model parameters are summarized in Table 6.1. The performance of the model is illustrated with reference to a set of simulated triaxial

Table 6.1. Constitutive parameters and internal variables for Berea Sandstone proposed by *Marinelli and Buscarnera* [2015].

	Definition	
K [MPa]	Bulk modulus	9550
G [MPa]	Shear modulus	7000
ρ_m	Parameter governing volumetric destructuration	3.7
ξ_m	Parameter governing deviatoric destructuration	0.5
B_p	Isotropic plastic compressibility	0.03
μ_f	Shape parameter of the yield surface	1.3
α_f	Shape parameter of the yield surface	0.2
M_f	Shape parameter of the yield surface	1.02
μ_g	Shape parameter of the plastic potential	2.00
α_g	Shape parameter of the plastic potential	0.2
M_g	Shape parameter of the plastic potential	1.88
κ	Expansion of the yield surface in the tensile stress domain	0.025
P_{so} [MPa]	Initial size of the elastic domain (cohesionless medium)	80
P_{mo} [MPa]	Lithification-induced expansion of the initial elastic domain	295

compression tests. Fig. 6.5 shows the predicted response under 75-, 150-, 200-, and 300-MPa confinement pressure where the comparison illustrates a good agreement between model computations and the experimental data. For the sake of simplicity, the yield surface has been kept independent of the Lode angle. Strain localization analyses in three-invariant stress space (the mean stress, the deviatoric stress, and the Lode angle) have been conducted and the results are presented in $p-q$ space of triaxial compression plane and $p-l$ (l stands for Lode angle) space in Figure (6.6). The stress space regions associated with different compaction banding modes are depicted by using the same color convention adopted in previous chapters (green= compactive-shear bands, blue= shear-enhanced compaction bands, and red= pure compaction bands). This analysis illustrates interesting features of the domain of instability, in that it displays that the zones of potential pure-compaction localization is limited to compressive stress states (i.e., $-30 < l < 0$), while strain localization in the extension regime (i.e., $0 < l < +30$) is predicted only in the form of shear banding. Such computations are consistent with the findings of *Ma et al.* [2017].

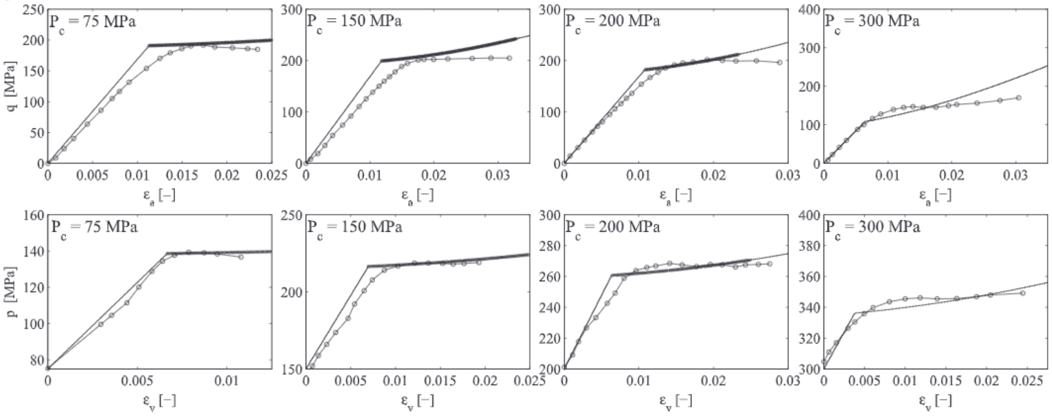

Figure 6.5. Mechanical behavior of Berea Sandstone under triaxial compression at several confining pressures. Continuous lines indicate model computations. Lines with circles indicate the experimental data (after *Marinelli and Buscarnera* [2015]).

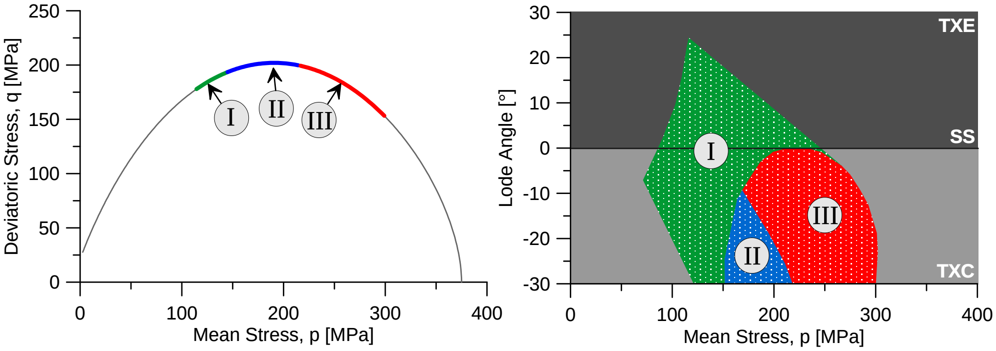

Figure 6.6. .

Strain localization characteristics of Berea Sandstone predicted with the selected constitutive model: (left) in the triaxial compression plane, and (right) the mean stress-Lode angle domain. The localization domain in stress space is superposed to the yield surface (thick line) and the associated inclination of the deformation band predicted by a bifurcation analysis. The theory defines different modes of strain localization. Zone I (green) indicates a domain of compactive shear banding. Zone II (blue) indicates a domain of shear-enhanced compaction. By contrast, Zone III (red) indicates a domain of pure compaction banding. TXC=triaxial compression, SS=simple shear, and TXE=triaxial extension.

6.2. Compaction Banding in Sandstone Bounded by Elastic Layers

This section investigates the mechanics of compaction localization in multi-layer systems by conducting finite element simulations of a sandstone layer inter-bedded between two elastic strata. The focus of this analysis is to examine the effects of the stiffness of the elastic layers on the strain localization characteristics in an elastoplastic sandstone formation. The analysis has been conducted under plane strain geometry with reference to a rectangular plate with aspect ratio height/width = 150/400. The plate has been equally divided into three horizontal layers, and discretized by a finite element mesh consisting of more than $120,000$ 4-node tetrahedral linear elements. In order to promote triggering of strain localization, a single element is assigned 98% of the hydrostatic yielding pressure prescribed throughout the rest of the domain.

An initial confining pressure (arbitrarily selected as 30 MPa) is applied by subjecting each boundary surface to a normal pressure in equilibrium with an equivalent internal stress state. The lateral deformation has been applied by translating the nodes of the right-hand face of the model in the normal direction at a rate equivalent to a strain of $1.0E-5\ /s$, while the normal velocity of the other faces is set to zero. The intermediate layer has been assigned sandstone properties, while the upper and lower layers have been assigned elastic properties with 0.2 Poisson's ratio and varying Young's modulus (0.6, 1.0, 1.2, 2.0 of the Young's modulus of the sandstone, E_b= $16,875$ MPa). A schematic illustration of the FE model and its boundary conditions are illustrated in Fig. 6.7.

The results of the analyses are reported in Fig. 6.8a-d, where the evolving deformation field in the sandstone formation (trimmed for visualization purpose) has been presented at different steps along the simulation. It can be seen that, in all cases, compaction localization

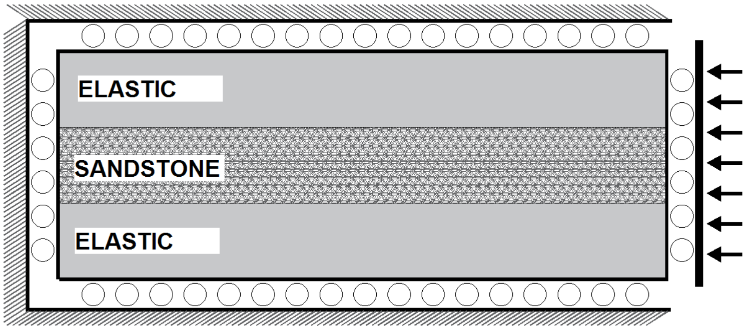

Figure 6.7. Illustration of the finite element model and boundary conditions.

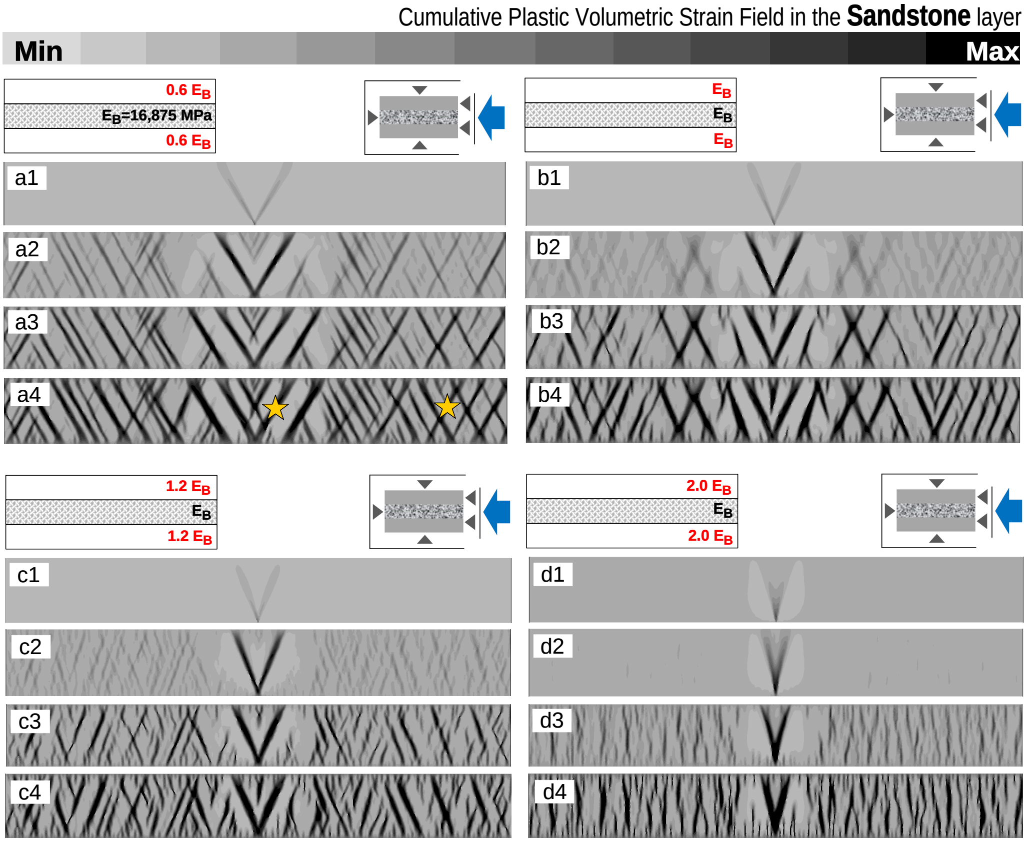

Figure 6.8. Finite element simulations of three-layers system with intermediate Berea Sandstone layer topped and bottomed by elastic layers. The elastic layers are characterized by varying Young's modulus: (a) $10,000-$, (b) $16,875-$, (c) $20,000-$, (d) $32,000-$MPa. The system is initially subjected to 30 MPa confining pressure followed by lateral contraction.

emerges first in a form of V-shape structure emanating from the location of the weak element at the bottom of the layer (e.g., $b1$). This primary structure reaches a termination at the upper end, indicating that the elastic layer has inhibited farther propagation. The simulation reveals that additional lateral contraction has been accommodated through inelastic deformation that has spread across the entire layer. As a result, a network of intersecting compaction bands grows away from the primary structure (e.g., $b2$). This network thickens as contraction continues (e.g., $b2 \rightarrow b3 \rightarrow b4$).

Despite these similarities, marked differences depending on the stiffness of the elastic layers can be readily detected. Comparison is made with reference to the case presented in (Fig. 6.8b) where the elastic layers have the same elastic properties of the sandstone. Starting from the primary structure (the V-shaped band), the geometrical attributes of the emerging bands appear to vary with the relative stiffness of the three simulated layers. Specifically, an increase in the stiffness of the elastic layers results in a decrease in the inclination of the compaction bands (reference is made to the plane orthogonal to loading direction). With $E = 0.6E_B$, the band's inclination is around 45^o. This inclination drops to around 30^o, 25^o, and 10^o for the other cases of $E = 1.0E_B$, $= 1.2E_B$, and $= 2.0E_B$. Such variation reflects a transition in the mode of strain localization.

To elucidate the causes of such variations, Fig. 6.9 shows the local responses associated with Gauss points located (a) inside the primary structure and (b) inside subsequent bands (shown by stars in (a4)). It can be readily seen that the sandstone layer has experienced loading conditions that differ depending on the elastic properties of the elastic layers. The lateral deformation of the elastic layer has induced variations in the vertical stresses as a result of Poisson's effect. Subsequently, the stress ratio, q/p, according to which the stress path evolves in the elastic stage is characterized by a tendency to decrease as the stiffness of

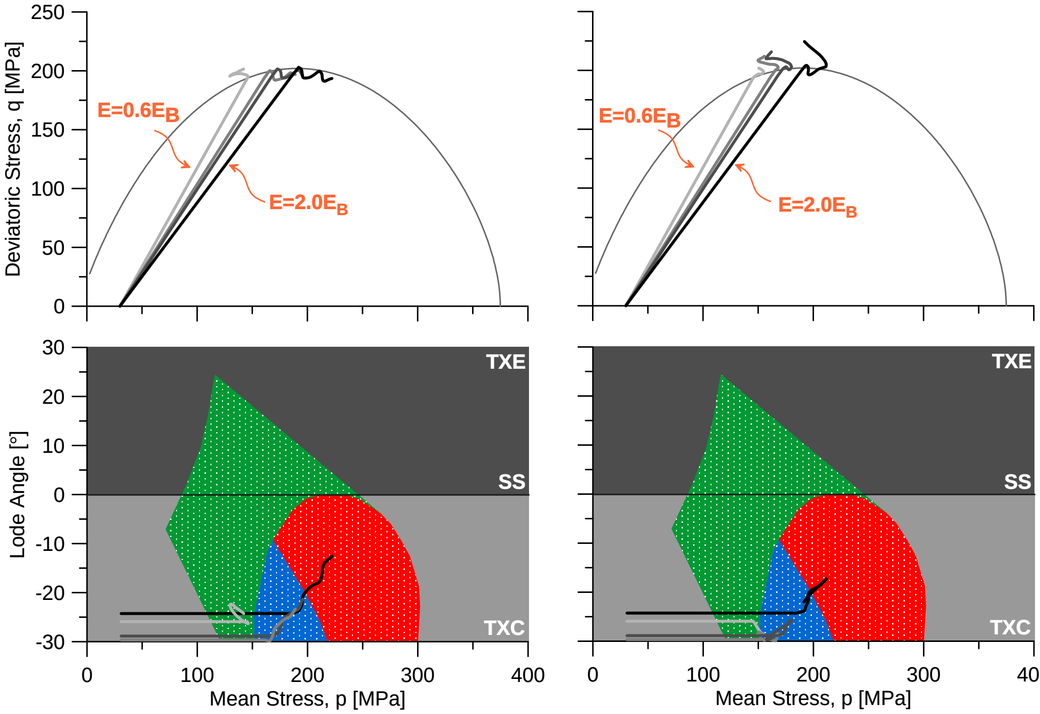

Figure 6.9. Local responses of the sandstone layer in the three-layer simulations presented in Fig. 6.8. The local responses are reported for material points located inside the emerging compaction bands: (left) first band and (right) subsequent bands.

the elastic layer increases. Lode angle varies depending on the stiffness value as well. Such deviations promote engaging the yield surface at states with varying angles of potential strain localization. For example, with a lower stiffness ($E = 0.6E_B$) the stress path intersects with the yield surface in the zone of compactive-shear banding (Fig. 6.8a), while with higher stiffness ($E = 1.2E_B$) the intersection occurs in the zone of shear-enhanced compaction (Fig. 6.8c).

This set of simulations reveals further intriguing observations. In fact, by making reference to the case presented in Fig. 6.8d, it can be noticed that the V-shape structure and the subsequent network of compaction bands are characterized by different inclination. While

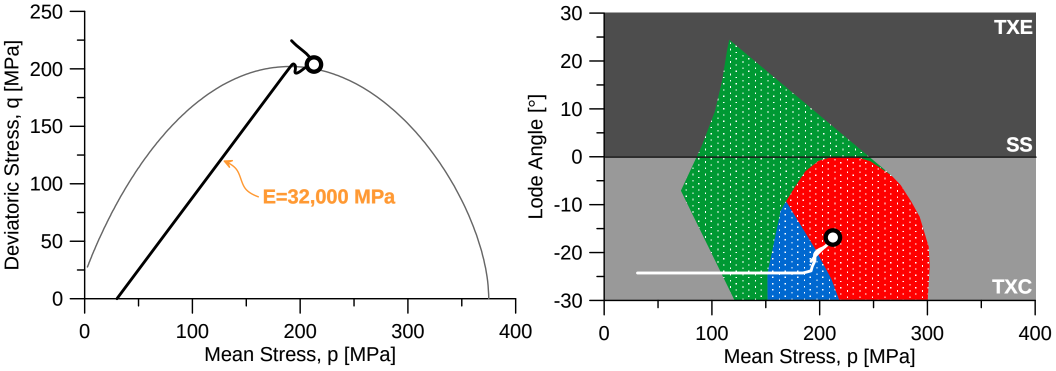

Figure 6.10. Local responses of the sandstone layer in the three-layer simulations presented in Fig. 6.8d, inside the pure-compaction bands emerging away from the first V-shaped bands.

the primary structure involves an inclination of about 10^o, the compaction bands of the network have emerged with almost a vertical alignment (0^o). This change in geometry points out transitions in the model of compaction localization from shear-enhanced compaction bands to pure compaction localization. Fig. 6.10 elucidates such transitions by showing the local responses associated with one of the pure compaction bands. It can be seen that the emergence of such mixed modes of compaction banding can be explained on the basis of the significant alteration in the stress path associated with unloading in this area during the growth of the primary bands. Specifically, the deviations in the stress paths taking place in the domain away from the zone of the primary structure promote conditions for engaging the yield surface at locations different from those associated with the primary structure. As a result, the compaction bands grow with different inclination. Here, the state associated with the activation of the second set of bands (marked by a hollow circle in Fig. 6.10) is located in the domain of pure-compaction, while the activation of the primary structure (Fig. 6.9c) occurs in the domain of shear-enhanced compaction.

6.3. Field Conditions Leading to Mixed Modes of Compaction Bands

This section examines the field conditions that could promote the emergence of complex structures of compaction bands in sandstone deposits. For this purpose, various scenarios of geological processes have been considered. The first scenario includes a sequence of an increase in the burial depth followed by an activation of tectonic contraction, while the second scenario consists of a sequence of an increase in the burial depth, followed by a decrease in the burial depth and finally an activation of tectonic contraction.

Material point analyses have first been carried out with reference to such scenarios. These sequences were implemented following a range of arbitrarily selected confining pressure (i.e., 0-, 30-, and 70-MPa). The stage of axisymmetric compression is terminated once loading brings the material into a stress state that engages the yield surface. The stage of axisymmetric extension is terminated at varying values, which reflect differences in the duration of erosion.

6.3.1. Burial-increase→Lateral-contraction

Fig. 6.11 illustrates the stress responses associated with the analyses conducted on the basis of the first scenario, along with a schematic depiction of the loading stages. As can be readily seen, the vertical compression ($1 \rightarrow 2$) under the selected range of confining pressure leads to material responses that engage the yield surface inside the domain of strain localization, specifically in the domain of shear-assisted compaction. Along this segment, material responses remain inside the triaxial compression plane. The stage of lateral compression ($2 \rightarrow 3$) results in a marked deviation in the stress response characterized by a decay in the deviatoric stress along with an increase in the mean stress. The material during this stage displays a transition from the compression to the extension regime, with a Lode angle that evolves from −30 to +30. The intersection of the stress path with the yield surface takes place at points located outside the domain of compaction localization (3), indicating that such paths do not promote vertical compaction bands.

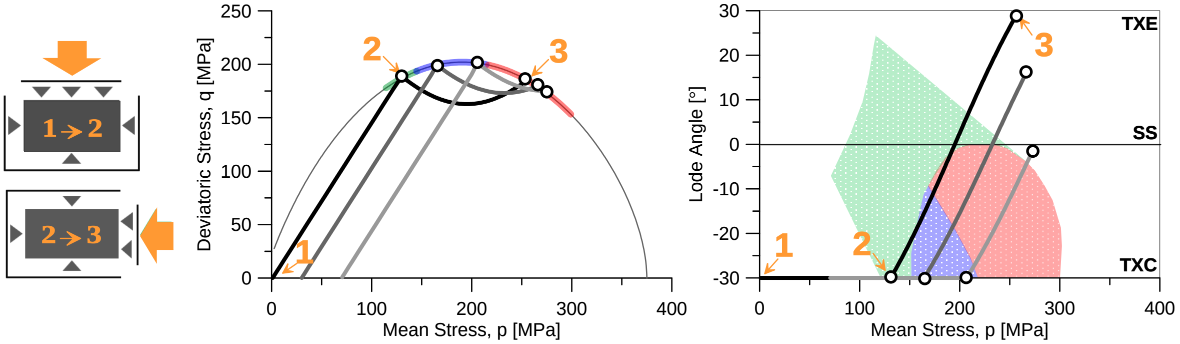

Figure 6.11. Material point analyses of the stress path emerging upon sequential application of vertical compression followed by lateral compression, all under uniaxial compression.

To demonstrate this hypothesis, a finite element simulation of the Berea Sandstone layer subjected to loading conditions similar to those applied in material point analyses has been carried out. For this purpose, a FE model similar to the one discussed in Section 6.2 has been adopted. In this model, however, the entire domain has been modeled as an elastoplastic porous rock. Fig. 6.12 illustrates the geometry of the FE model and its boundary conditions of the various loading stages. All simulations have led to similar conclusions, and here the one corresponding to a confining pressure of 70 MPa has been presented as a representative demonstration (Fig. 6.13). The evolving deformation field as a result of vertical compaction (Fig. 6.13a) indicates the growth of conjugate shear-enhanced compaction bands that nucleate from the location of the weak element ($a1$) and propagate towards the boundaries of the layer ($a2 \rightarrow a4$). The evolution of the deformation field under the effects of lateral

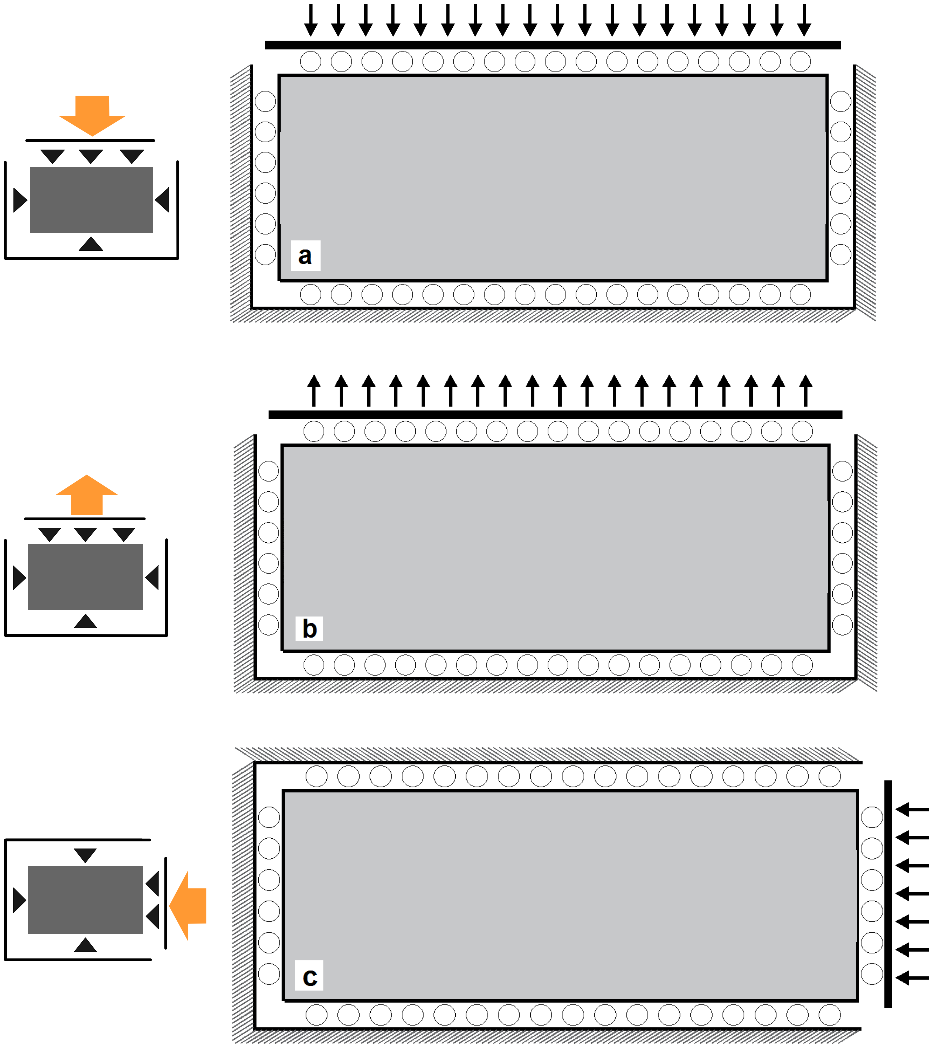

Figure 6.12. Illustration of a plane-strain finite element model of a sandstone layer with boundary conditions: (a) increase burial load, (b) decrease burial load, and (c) contractional tectonics.

contraction is presented in (Fig. 6.13b), showing that diffused deformation takes place during this stage of loading. To elucidate these observations, the local responses associated with two Gauss points located inside and outside the compaction bands (marked by stars in $b4$) are presented in Fig. 6.13c-d. The stress path evolves from 1 → 2 during the first

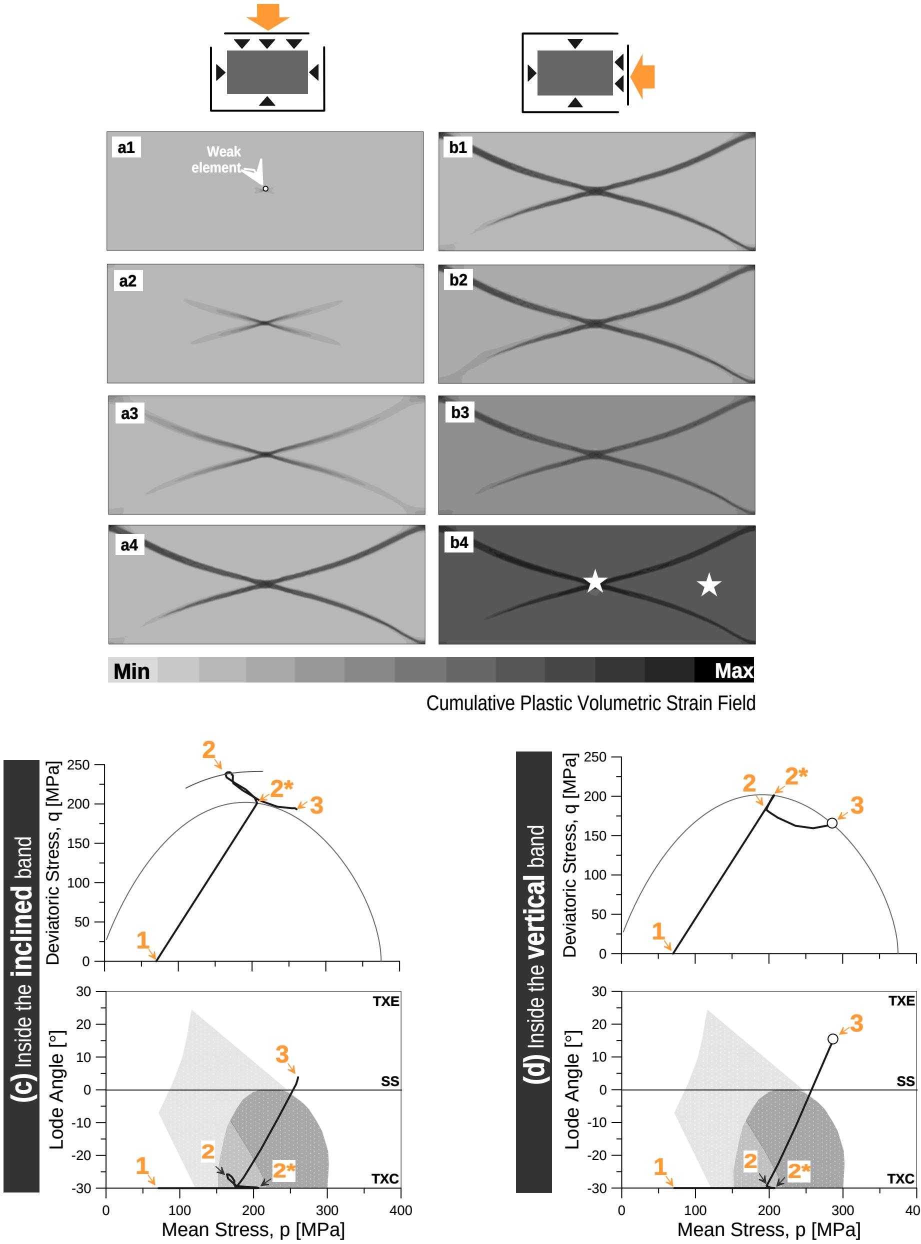

Figure 6.13. Finite element simulation of Berea Sandstone layer subjected to two stages of loading: (a) vertical loading representing an increase in the burial depth, and (b) lateral loading replicating compressive tectonics. Local responses inside the band (c) and outside the band (d).

stage of loading and involves an intersection with the yield surface at 2^*, a point associated with a potential of shear-enhanced compaction banding, which explains the emergence of the conjugate inclined bands ($2 \rightarrow 2^*$, Fig. 6.13c). Away from the active zone, the material undergoes elastic unloading ($2 \rightarrow 2^*$, Fig. 6.13d). The evolution of the stress path takes place in the plane of triaxial compression during the first stage. During the second stage, however, the stress path evolves from $2 \rightarrow 3$, displaying transitions from the compression to the extension regime with a Lode angle that evolves from -30 to $+15$. The second intersection with the yield surface takes place outside the domain of compaction localization (3, Fig. 6.13d), which explains the accommodation of deformation during this stage in a form of diffused compaction.

6.3.2. Burial-increase→Burial-decrease→Lateral-contraction

Fig. 6.14 illustrates the stress responses associated with material point analyses conducted on the basis of the second loading scenario, along with a schematic illustration of loading stages. As can be seen, the vertical compression ($1 \rightarrow 2$) under the selected range of confining pressure leads to material responses that evolve elastically and eventually engage the yield surface at points located inside the domain of shear-assisted compaction localization. The second stage (axisymmetric extension) causes a reversed evolution of the stress path with elastic unloading ($2 \rightarrow 3$). During these two segments, the material responses remain inside the plane of triaxial compression with a Lode angle equal to -30^o. The third stage of lateral compression ($3 \rightarrow 4$) results in a marked deviation in the stress response characterized by an increase in the mean stress associated with a decay and then an increase in the deviatoric stress. The stress path involves transitions from the compression to the extension regime, followed by a return to the compression regime. As can be readily seen, the point

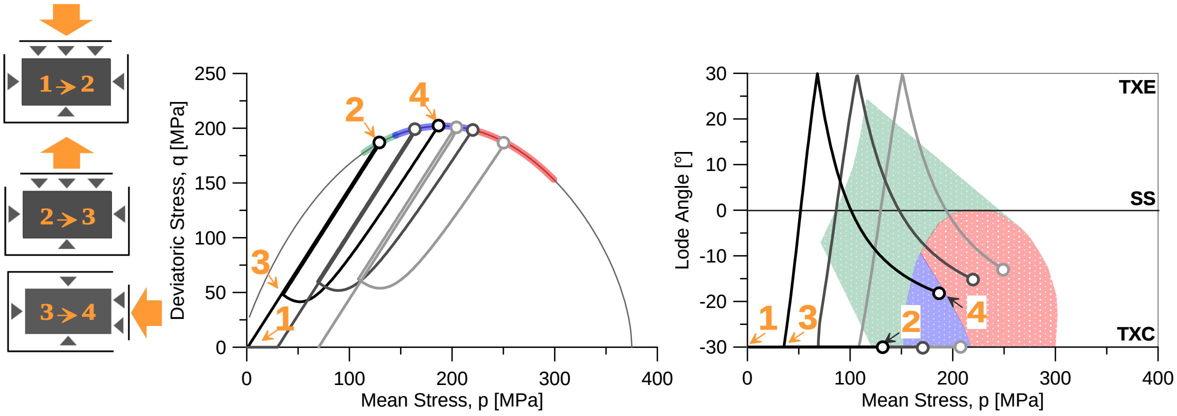

Figure 6.14. Material point analyses of the stress path emerging upon sequential application of vertical loading, vertical unloading, followed by a lateral compression, all under axisymmetric conditions.

at which the stress path engages the yield surface (4) is located, in all cases, inside the domain of compaction localization. In the simulations based on initial confining pressures of 30- and 70-MPa, these points specifically locate inside the domain of pure compaction banding, suggesting that perturbation histories similar to those applied in this set of material simulations promote the emergence of vertical compaction bands during stages of tectonic contraction.

To verify that, full field analyses based on finite element simulations with similar loading history have been conducted (Fig. 6.15). Again, the evolving deformation field under the effects of vertical compaction (Fig. 6.15a) indicates the growth of conjugate shear-enhanced compaction bands that nucleate from the location of the weak element ($a1$) and propagates towards the boundaries of the layer ($a2 \rightarrow a4$). The layer during the stage of unloading displays no variations in the deformation field ($b1 \rightarrow b4$). Intriguingly, the stage of lateral contraction has resulted into the emergence of pure compaction bands in the vertical direction

($c1 \rightarrow c2$). Compaction banding in the vertical direction propagates in form of discrete bands as loading continues ($b2 \rightarrow b4$).

The mechanical origin of these rich results can be found in the non-trivial stress path alterations, as well as how they engage plasticity and localization in multiple forms. To elaborate, the local response associated with two Gauss points located inside the inclined compaction band and inside one of the vertical compaction bands (marked by stars in $c4$) are presented in Fig. 6.15d-e. Inside the inclined band, the stress path during the burial increase evolves in the plane of triaxial compression from $1 \rightarrow 2$, intersecting with the yield surface at (2^*) within the regime of shear-enhanced compaction. The loading taking place in the zone of active compaction leads to yield-surface expansion, and accompanies unloading in the inactive zones $2^* \rightarrow 2$. Unloading takes place in the entire domain during the stage of burial depth decrease $2 \rightarrow 3$, with evolving stresses almost entirely inside the plane of triaxial compression. Transitions from triaxial compression towards the plane of triaxial extension emerge starting with the initiation of the stage of tectonic contraction (at 3). During this stage, the stress path evolves in the elastic domain and displays a return towards the compression domain where the first engagement of the yield surface takes place within the range of pure compaction localization. By making reference to Fig. 6.14, it can be noticed that material point analyses have provided robust predictions of the conditions leading to such complex compaction bands system.

6.4. Conclusions

This chapter presented numerical analyses based on finite element method of field-scale problems involving compaction banding. While the work is inspired by actual field studies, it was conducted in a general, abstract nature, in that it aims to achieve a theoretical

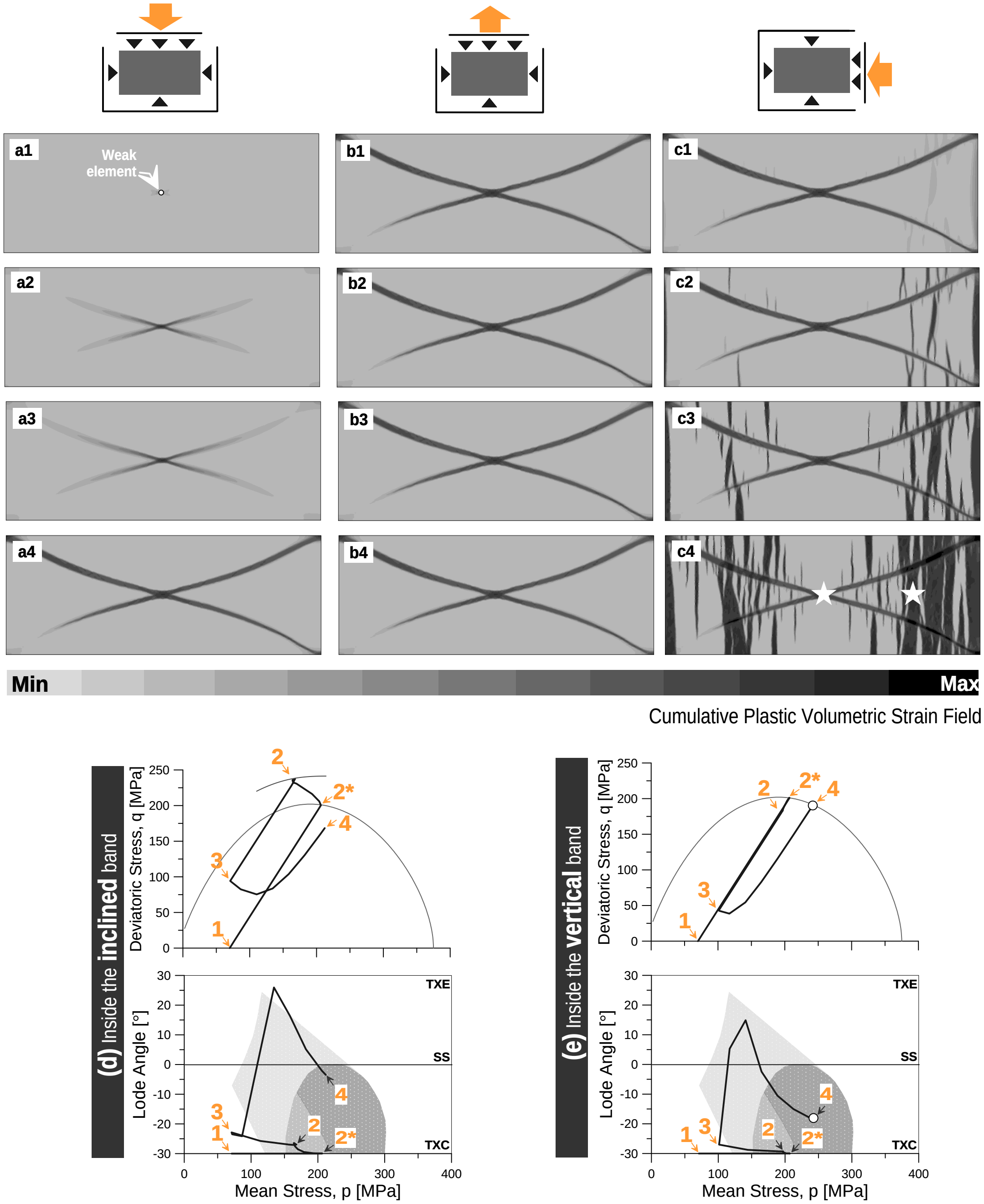

Figure 6.15. Finite element simulation of Berea Sandstone layer subjected to three stages of loading: (a) vertical loading representing an increase in the burial depth, (b) vertical unloading representing erosion effects, and (c) lateral loading replicating compressive tectonics. Local responses inside the (d) inclined band and the (e) vertical band.

explanation of the effects of stratigraphic settings and geological processes on compaction banding. The analysis was based on the predictions of a calibrated material model of Berea Sandstone, without making reference to any locations or specific field conditions. It is, however, inspired by reconstructions of geological processes and tectonic strain background based on field surveys from the location of Navajo Sandstone formation in Utah.

The work investigated possible effects of the stiffness properties of surrounding layers on the characteristics of emergent compaction bands in sandstone layers. As a result, it was based on a three-layer system with a sandstone layer inter-bedding elastic layers. The analyses revealed inception of compaction bands in two stages: a primary structure of conjugate compaction bands followed by a secondary stage of growth of a network of conjugate compaction bands across the rest of the domain. The geometrical characteristics of both the primary and the secondary structures were found to be influenced by the stiffness properties of the elastic layers. Specifically, compaction localization occured with an increasing inclination as the stiffness of the elastic layers increases. Systems with elastic layers assigned a lower stiffness displayed compaction localization in form of compactive shear bands, while systems with a higher stiffness displayed compaction localization in form of shear-enhanced compaction bands. The elastic layers were found to exert specific effects of increasing the vertical stresses when subjected to lateral contraction as a result of Poisson's effect, resulting in an increase in the mean stress and a decrease in the deviatoric stress in the sandstone layer. These changes in stress responses alter the locations at which material engages the yield surface and subsequently the angle of compaction localization.

The second part of the chapter examines the loading conditions leading to rich formations of compaction bands that involves coexisting structures of inclined and vertical alignments. For this purpose, two loading scenarios were tested. The first scenario involved a sequence of two stages of increasing burial followed by tectonic contraction. The second scenario involved a three-stage sequence of increasing burial, decreasing burial, and finally tectonic contraction. While inclined compaction bands (shear-assisted compaction bands) were seen with both scenarios, the simulations suggested that a stage of burial decrease has to take place in order for the sandstone layer to develop a second stage of strain localization in form of pure compaction bands with vertical alignments. The results showed that the rich loading history inspired by the geological reconstruction of real field locations is at the origin of the coexistence of different band types. It also shows that, contrary to some hypotheses for these fields, the sequencing of band formation may not be contemporaneous. Finally, a single weak element leads to such remarkable spatial richness and emerging heterogeneity, which is simply a function of the material properties (and the band spacing characteristics encoded in it) and the relation between geological loading path and material path/history dependence.

CHAPTER 7

Conclusions and Research Perspectives

This thesis presented a theoretical and computational research of compaction bands in porous rocks. The work was based on a strain-hardening multi-variable plasticity model augmented in viscoplastic form to replicate the rate-dependent properties of porous rocks. The study combined simulations at the scale of material points and boundary value problems (based on the finite element method) to analyse standard geomechanical tests and field scale problems. Compaction banding was simulated as a material instability. In this context, the work included theoretical developments of instability indices (derived based on the controlability theory and the mathematics of non-linear systems) for viscoplastic porous solids. Methodological developments were proposed in this work including a mapping scheme to connect numerical models and x-ray tomography measurements based on the concept of representative elementary volume. With this tool, the thesis investigated the spatio-temporal dynamics of delayed compaction bands, the role of spatial heterogeneity in various aspects of their emergence and propagation, and addressed open questions regarding geological settings and field-scale processes affecting their formation and morphological characteristics. The main conclusions deriving from this research can be listed as follows:

- The same strain-hardening plasticity/viscoplasticity model with competing hardening and softening is capable of simulating two very different modes of compaction band propagation (discrete and thickening bands), their nucleation under the effects of heterogeneity, and spontaneous growth under creep and relaxation.

- The viscoplastic idealization has allowed to establish a unified theoretical interpretation of the time-dependent and time-independent emergence of compaction bands.
- Although the spatial heterogeneity plays a role in the nucleation and propagation of compaction bands, other factors including boundary effects (here frictional boundaries) and compliant constraints (elastic bounding layers) have competing effects.
- The hypothesis of contemporaneous modes of compaction banding is not confirmed. Non-local effects and rich geological history may be necessary for the formation of rich compaction bands.
- The models and mathematical tools provided by this work can therefore contribute to predictive analyses of the short- and long-term deformation of underground formations susceptible to inelastic compaction and near-failure conditions.

Research Perspectives

The research presented in this thesis opens several opportunities to further the interpretation of compaction bands and widen the range of applications of geomechanical modeling to other geotechnical and geophysical problems:

- The framework of interpretation discussed in this work and its use in numerical analyses of delayed compaction banding can provide guidance to explain the mechanics of time-dependent compaction at laboratory and field scales. In particular, the possibility to define indices reflecting impending instability in the form of accelerating deformation can be fruitfully used to predict the occurrence of catastrophic failure after extended stages of slow deformation. While here only delayed compaction banding was discussed, this logic can in principle be extended to a variety of failure mechanisms, such as distributed damage, frictional slip, dilation and shear bands, thus potentially impacting a range of geophysical problems, simply by adapting the constitutive law for the geomechanical problem at stake. It is therefore arguable that the techniques discussed in this work can be used in the future to cope with a wide range of geophysical problems, such as the mechanics of seismogenic faults, the onset of landslides and the collapse of volcanic edifices and underground cavities.

- The analysis of the relative influence of boundary effects and material heterogeneity presented in this work exemplifies a ubiquitous problem in geotechnology and geophysics, i.e. the interplay between natural heterogeneity and pre-existing boundaries (e.g., interactions between penetrating probes and layered ground, feedbacks between reservoir faults and caprock, concurrent initiation of multiple deformation zones around a borehole). Understanding the factors leading to the onset of strain localization is therefore necessary to enhance our ability to predict initiation and fate of subsurface deformation structures for cases in which the competition of the local factors (e.e., field heterogeneity) and system effects (e.g., boundary conditions) is crucial to identify the most likely outcome. The use of the proposed CT-FE mapping scheme to assess the causes of emerging inelasticity in pressure-dependent, porous geomaterials, therefore represents a particular example of the benefits that may derive from a deeper integration of physical measurements and numerical modeling, and epitomize an approach which should in principle be extended to every length scales of interest for geophysical and geotechnical applications.
- In laboratory experiments on porous rocks, where the specimen-platen friction is an unavoidable factor, boundary effects could bias the interpretation of the observations by producing modes of heterogeneous deformation which resemble compaction

band front or that may convert into them because of stress path deviations. Experimental countermeasures and informed model calibration procedures are therefore necessary to minimize such bias and conduct more accurate predictions of soft rock compaction.

- The simulation of field-scale problems presented in this work represents an illustration of the unique opportunity that modern geomechanical theories and models offer to elucidate the origin and causes of geological structures, and reducing the uncertainty involved in the reconstructions of structural geology, and constraining the geological processes such as the burial history and stress configuration at the time of formation. Following the same line of thoughts may be useful in elucidating other field scale problems such as the emergence of compaction bands under extensional tectonics. It could also be useful in examining the hypothesis about the emergence of compaction bands near faults and verify whether they proceed or accompany the activation of faulting.
- The material models extensively used in this thesis offer an opportunity to examine engineering problems with material of a predominant softening and materials of a predominant hardening, such as borehole breakout and compaction banding in underground reservoirs. For example, available laboratory studies which reported deformation bands emanating from model boreholes may offer useful platforms to examine whether these bands are originated by unstable deformation or are simply the outcomes of heterogeneous plasticity. The models can also help illustrating the effects of the growth of compaction bands in subsurface strata on the local and regional stress field and understand their implications on the surrounding environment and land subsidence.

- Recent experimental studies have quantified the relaxation behavior of Maastricht Tuffeau [*Sari*, 2019]. This study presented limited analyses of relaxation test for Bleurswiller sandstone, which may provide preliminary indications of that the strain-hardening model calibrated in this thesis for the limestone and used to replicate its displacement control behavior may be also effective in replicating its relaxation behavior. Such studies may open new avenues to simulate geophysical-scale problems known to undergo cycles of loading and relaxation such as investigating faults behavior during sequences of active and inactive tectonics.
- In this work, viscoplasticity was used as a regularization technique to suppress the ill-posedness of strain localization problems. In the future, such approach may be used in conjunction with other regularization techniques, such as non-local modeling or second-gradient plasticity, which may simplify the calibration efforts by providing new avenues to integrate micro-scale measurements linked to the characteristic length of the material behavior.
- Most of the numerical predictions discussed in this study are a direct emanation of the interplay between hardening upon pore compaction and softening upon loss of cementation embedded in the selected constitutive model. Despite the considerable insight provided by this hypothesis, the fundamental structure of the model remains phenomenological in nature. As a result, the link of its hardening variables (i.e., initial value and evolution) to measurable microscopic geometry (e.g., grain size, pore size, cement volume fraction) and mechanical properties (cement strength, grain strength) has not yet been unlocked. Expanding the model in this direction would offer further opportunities for integrating multi-scale testing and modeling. The incorporation of microscopic features into evolution laws also has potential to

enrich the resulting predictive capabilities, possibly offering further flexibility to improve the model performance also at the macroscale.

- The numerical analyses presented in this thesis were conducted by assuming mechanical isotropy of Maastricht Tuffeau. Available evidence indicates non-negligible mechanical anisotropy characterized by variation in terms of the initial yielding and deformation, while the inclination of the compaction bands are independent of loading-bedding direction. Appendix C provide a theoretical development of constitutive modeling of cross-anisotropy calibrated against the data of the limestone. Phenomenological tensorial operators were used to adjust the yield surface and the flaw rule. It is suggested that microstructural directional quantities such as grains, contacts, and pores orientation could form the bases for constructing physics based tensorial operators and help explaining the origin of observed anisotropy.

References

Alshibli, K., and A. Hasan (2008), Spatial variation of void ratio and shear band thickness in sand using x-ray computed tomography, *Géotechnique*, *58*(4), 249–257.

Ando, E. (2013), Experimental investigation of microstructural changes in deforming granular media using x-ray tomography, Ph.D. thesis.

Andrade, J. E., J. W. Baker, and K. C. Ellison (2008), Random porosity fields and their influence on the stability of granular media, *International Journal for Numerical and Analytical Methods in Geomechanics*, *32*(10), 1147–1172.

Andrade, J. E., C. Avila, S. A. Hall, N. Lenoir, and G. Viggiani (2011), Multiscale modeling and characterization of granular matter: from grain kinematics to continuum mechanics, *Journal of the Mechanics and Physics of Solids*, *59*(2), 237–250.

Andrade, J. E., I. Vlahinić, K.-W. Lim, and A. X. Jerves (2012), Multiscale tomography-to-simulation framework for granular matter: the road ahead, *Géotechnique Letters*, *2*(3), 135–139.

Arroyo, M., R. Castellanza, and R. Nova (2005), Compaction bands and oedometric testing in cemented soils, *Soils and foundations*, *45*(2), 181–194.

Atkinson, B. K. (1984), Subcritical crack growth in geological materials, *Journal of Geophysical Research: Solid Earth*, *89*(B6), 4077–4114.

Aydin, A., and R. Ahmadov (2009), Bed-parallel compaction bands in aeolian sandstone: their identification, characterization and implications, *Tectonophysics*, *479*(3-4), 277–284.

Aydin, A., R. I. Borja, and P. Eichhubl (2006), Geological and mathematical framework for failure modes in granular rock, *Journal of Structural Geology*, *28*(1), 83–98.

Ballas, G., R. Soliva, J.-P. Sizun, H. Fossen, A. Benedicto, and E. Skurtveit (2013), Shear-enhanced compaction bands formed at shallow burial conditions; implications for fluid flow (provence, france), *Journal of Structural Geology*, *47*, 3–15.

Ballas, G., H. Fossen, and R. Soliva (2015), Factors controlling permeability of cataclastic deformation bands and faults in porous sandstone reservoirs, *Journal of Structural Geology*, *76*, 1–21.

Barraclough, T. W., J. R. Blackford, S. Liebenstein, S. Sandfeld, T. J. Stratford, G. Weinländer, and M. Zaiser (2017), Propagating compaction bands in confined compression of snow, *Nature Physics*, *13*(3), 272.

Bastawros, A., H. Bart-Smith, and A. Evans (2000), Experimental analysis of deformation mechanisms in a closed-cell aluminum alloy foam, *Journal of the Mechanics and Physics of Solids*, *48*(2), 301–322.

Baud, P., E. Klein, and T.-f. Wong (2004), Compaction localization in porous sandstones: spatial evolution of damage and acoustic emission activity, *Journal of Structural Geology*, *26*(4), 603–624.

Baud, P., P. Meredith, and E. Townend (2012), Permeability evolution during triaxial compaction of an anisotropic porous sandstone, *Journal of Geophysical Research: Solid Earth*, *117*(B5).

Baud, P., T. Reuschlé, Y. Ji, C. S. Cheung, and T.-f. Wong (2015), Mechanical compaction and strain localization in bleurswiller sandstone, *Journal of Geophysical Research: Solid Earth*, *120*(9), 6501–6522.

Baud, P., A. Schubnel, M. Heap, and A. Rolland (2017), Inelastic compaction in high-porosity limestone monitored using acoustic emissions, *Journal of Geophysical Research: Solid Earth*, *122*(12), 9989.

Baxevanis, T., E. Papamichos, O. Flornes, and I. Larsen (2006), Compaction bands and induced permeability reduction in tuffeau de maastricht calcarenite, *Acta Geotechnica*, *1*(2), 123–135.

Bažant, Z. P., and M. Jirásek (2002), Nonlocal integral formulations of plasticity and damage: survey of progress, *Journal of Engineering Mechanics*, *128*(11), 1119–1149.

Belytschko, T., S. Loehnert, and J.-H. Song (2008), Multiscale aggregating discontinuities: a method for circumventing loss of material stability, *International Journal for Numerical Methods in Engineering*, *73*(6), 869–894.

Bennett, K. C., L. A. Berla, W. D. Nix, and R. I. Borja (2015), Instrumented nanoindentation and 3d mechanistic modeling of a shale at multiple scales, *Acta Geotechnica*, *10*(1), 1–14.

Bésuelle, P. (2001), Compacting and dilating shear bands in porous rock: theoretical and experimental conditions, *Journal of Geophysical Research: Solid Earth*, *106*(B7), 13,435–13,442.

Bésuelle, P., and J. W. Rudnicki (2004), Localization: shear bands and compaction bands, *International Geophysics Series.*, *89*, 219–322.

Boehler, J. (1970), Equilibre limite des sols anisotropes, *J. de Mecanique*, *9*(1), 5–33.

Boehler, J., and A. Sawczuk (1977), On yielding of oriented solids, *Acta Mechanica*, *27*(1-4), 185–204.

Bonet, J., and R. D. Wood (1997), *Nonlinear continuum mechanics for finite element analysis*, Cambridge university press.

Borja, R. I., X. Song, A. L. Rechenmacher, S. Abedi, and W. Wu (2013), Shear band in sand with spatially varying density, *Journal of the Mechanics and Physics of Solids*, *61*(1), 219–234.

Brace, W., and D. Kohlstedt (1980), Limits on lithospheric stress imposed by laboratory experiments, *Journal of Geophysical Research: Solid Earth*, *85*(B11), 6248–6252.

Bruchon, J.-F., J.-M. Pereira, M. Vandamme, N. Lenoir, P. Delage, and M. Bornert (2013a), Full 3d investigation and characterisation of capillary collapse of a loose unsaturated sand using x-ray ct, *Granular Matter*, *15*(6), 783–800.

Bruchon, J.-F., J.-M. Pereira, M. Vandamme, N. Lenoir, P. Delage, and M. Bornert (2013b), X-ray microtomography characterisation of the changes in statistical homogeneity of an unsaturated sand during imbibition, *Géotechnique Letters*, *3*(2), 84–88.

Buscarnera, G., and R. T. Laverack (2014), Path dependence of the potential for compaction banding: Theoretical predictions based on a plasticity model for porous rocks, *Journal of Geophysical Research: Solid Earth*, *119*(3), 1882–1903.

Buscarnera, G., and R. Nova (2011), Modelling instabilities in triaxial testing on unsaturated soil specimens, *International journal for numerical and analytical methods in geomechanics*, *35*(2), 179–200.

Buscarnera, G., G. Dattola, and C. di Prisco (2011), Controllability, uniqueness and existence of the incremental response: A mathematical criterion for elastoplastic constitutive laws, *International Journal of Solids and Structures*, *48*(13), 1867–1878.

Carroll, M. (1991), A critical state plasticity theory for porous reservoir rock, *Recent Advances in Mechanics of Structured Continua*, *117*, 1–8.

Castañeda, P. P. (2002), Second-order homogenization estimates for nonlinear composites incorporating field fluctuations: Itheory, *Journal of the Mechanics and Physics of Solids*, *50*(4), 737–757.

Castellanza, R., E. Gerolymatou, and R. Nova (2009), Experimental observations and modelling of compaction bands in oedometric tests on high porosity rocks, *Strain*, *45*(5), 410–423.

Cazacu, O., N. Cristescu, J. Shao, and J. Henry (1998), A new anisotropic failure criterion for transversely isotropic solids, *Mechanics of Cohesive-frictional Materials: An International Journal on Experiments, Modelling and Computation of Materials and Structures*, *3*(1), 89–103.

Challa, V., and K. A. Issen (2004), Conditions for compaction band formation in porous rock using a two-yield surface model, *Journal of engineering mechanics*, *130*(9), 1089–1097.

Chambon, R. (1986), Bifurcation par localisation en bande de cisaillement, une approche avec des lois incrementalement non linéaires, *Journal de Mécanique théorique et appliquée*, *5*(2), 277–298.

Charalampidou, E.-M., S. A. Hall, S. Stanchits, H. Lewis, and G. Viggiani (2011), Characterization of shear and compaction bands in a porous sandstone deformed under triaxial compression, *Tectonophysics*, *503*(1-2), 8–17.

Chemenda, A. (2009), The formation of tabular compaction-band arrays: theoretical and numerical analysis, *Journal of the Mechanics and Physics of Solids*, *57*(5), 851–868.

Chemenda, A. I., and D. Mas (2016), Dependence of rock properties on the lode angle: Experimental data, constitutive model, and bifurcation analysis, *Journal of the Mechanics and Physics of Solids*, *96*, 477–496.

Chemenda, A. I., G. Ballas, and R. Soliva (2014), Impact of a multilayer structure on initiation and evolution of strain localization in porous rocks: Field observations and numerical modeling, *Tectonophysics*, *631*, 29–36.

Chen, L., J.-F. Shao, and H. Huang (2010), Coupled elastoplastic damage modeling of anisotropic rocks, *Computers and Geotechnics*, *37*(1-2), 187–194.

Chen, Q., A. Seifried, J. E. Andrade, and J. W. Baker (2012), Characterization of random fields and their impact on the mechanics of geosystems at multiple scales, *International*

Journal for Numerical and Analytical Methods in Geomechanics, *36*(2), 140–165.

Cheung, C. S., P. Baud, and T.-f. Wong (2012), Effect of grain size distribution on the development of compaction localization in porous sandstone, *Geophysical Research Letters*, *39*(21).

Chiles, J.-P., and P. Delfiner (2009), Geostatistics: modeling spatial uncertainty, *497*.

Cil, M. B., M. Xie, A. I. Packman, and G. Buscarnera (2017), Solute mixing regulates heterogeneity of mineral precipitation in porous media, *Geophysical Research Letters*.

Cilona, A., P. Baud, E. Tondi, F. Agosta, S. Vinciguerra, A. Rustichelli, and C. J. Spiers (2012), Deformation bands in porous carbonate grainstones: Field and laboratory observations, *Journal of Structural Geology*, *45*, 137–157.

Cilona, A., D. R. Faulkner, E. Tondi, F. Agosta, L. Mancini, A. Rustichelli, P. Baud, and S. Vinciguerra (2014), The effects of rock heterogeneity on compaction localization in porous carbonates, *Journal of Structural Geology*, *67*, 75–93.

Company, U. S. (1997), F-50 unground silica product data sheet.

Croize, D., F. Renard, and J.-P. Gratier (2013), Compaction and porosity reduction in carbonates: A review of observations, theory, and experiments, in *Advances in Geophysics*, vol. 54, pp. 181–238, Elsevier.

Crook, A. J., J.-G. Yu, S. M. Willson, et al. (2002), Development of an orthotropic 3d elastoplastic material model for shale, in *SPE/ISRM Rock Mechanics Conference*, Society of Petroleum Engineers.

Cruz-Atienza, V. M., C. Villafuerte, and H. S. Bhat (2018), Rapid tremor migration and pore-pressure waves in subduction zones, *Nature communications*, *9*(1), 2900.

Cruz-Orive, L. M. (1997), Stereology of single objects, *Journal of microscopy*, *186*(2), 93–107.

Cuss, R., E. Rutter, and R. Holloway (2003), The application of critical state soil mechanics to the mechanical behaviour of porous sandstones, *International Journal of Rock Mechanics and Mining Sciences*, *40*(6), 847–862.

Dafalias, Y. F. (1986), Bounding surface plasticity. i: Mathematical foundation and hypoplasticity, *Journal of Engineering Mechanics*, *112*(9), 966–987.

Das, A., and G. Buscarnera (2014), Simulation of localized compaction in high-porosity calcarenite subjected to boundary constraints, *International Journal of Rock Mechanics and Mining Sciences*, *71*, 91–104.

Das, A., G. D. Nguyen, and I. Einav (2011), Compaction bands due to grain crushing in porous rocks: a theoretical approach based on breakage mechanics, *Journal of Geophysical Research: Solid Earth*, *116*(B8).

De Borst, R., and H.-B. Mühlhaus (1992), Gradient-dependent plasticity: formulation and algorithmic aspects, *International Journal for Numerical Methods in Engineering*, *35*(3), 521–539.

Deng, S., and A. Aydin (2012), Distribution of compaction bands in 3d in an aeolian sandstone: The role of cross-bed orientation, *Tectonophysics*, *574*, 204–218.

Deng, S., L. Zuo, A. Aydin, J. Dvorkin, and T. Mukerji (2015a), Permeability characterization of natural compaction bands using core flooding experiments and three-dimensional image-based analysis: Comparing and contrasting the results from two different methods, *AAPG Bulletin*, *99*(1), 27–49.

Deng, S., A. Cilona, C. Morrow, C. Mapeli, C. Liu, D. Lockner, M. Prasad, and A. Aydin (2015b), Cross-bedding related anisotropy and its interplay with various boundary conditions in the formation and orientation of joints in an aeolian sandstone, *Journal of Structural Geology*, *77*, 175–190.

Desrues, J., and G. Viggiani (2004), Strain localization in sand: an overview of the experimental results obtained in grenoble using stereophotogrammetry, *International Journal for Numerical and Analytical Methods in Geomechanics*, *28*(4), 279–321.

Desrues, J., R. Chambon, M. Mokni, and F. Mazerolle (1996), Void ratio evolution inside shear bands in triaxial sand specimens studied by computed tomography, *Géotechnique*, *46*(3), 529–546.

Dewers, T., P. Newell, S. Broome, J. Heath, and S. Bauer (2014), Geomechanical behavior of cambrian mount simon sandstone reservoir lithofacies, iowa shelf, usa, *International Journal of Greenhouse Gas Control*, *21*, 33–48.

Dewers, T. A., K. A. Issen, D. J. Holcomb, W. A. Olsson, and M. D. Ingraham (2017), Strain localization and elastic-plastic coupling during deformation of porous sandstone, *International Journal of Rock Mechanics and Mining Sciences*, *98*, 167–180.

di Prisco, C., S. Imposimato, and I. Vardoulakis (2000), Mechanical modelling of drained creep triaxial tests on loose sand, *Geotechnique*, *50*(1), 73–82.

DiGiovanni, A., J. Fredrich, D. Holcomb, and W. Olsson (2007), Microscale damage evolution in compacting sandstone, *Geological Society, London, Special Publications*, *289*(1), 89–103.

DiMaggio, F. L., and I. S. Sandler (1971), Material model for granular soils, *Journal of Engineering Mechanics*.

Drugan, W. J., and J. R. Willis (1996), A micromechanics-based nonlocal constitutive equation and estimates of representative volume element size for elastic composites, *Journal of the Mechanics and Physics of Solids*, *44*(4), 497–524.

FEI (2016), *Avizo 3D image analysis software, Version 9.2, edited.*, FEI Visualization Sciences Group.

Fortin, J., A. Schubnel, and Y. Guéguen (2005), Elastic wave velocities and permeability evolution during compaction of bleurswiller sandstone, *International Journal of Rock Mechanics and Mining Sciences*, *42*(7), 873–889.

Fortin, J., S. Stanchits, G. Dresen, and Y. Guéguen (2006), Acoustic emission and velocities associated with the formation of compaction bands in sandstone, *Journal of Geophysical Research: Solid Earth*, *111*(B10).

Fortin, J., S. Stanchits, G. Dresen, and Y. Gueguen (2009), Acoustic emissions monitoring during inelastic deformation of porous sandstone: comparison of three modes of deformation, *Pure and Applied Geophysics*, *166*(5-7), 823–841.

Fossen, H., and A. Bale (2007), Deformation bands and their influence on fluid flow, *AAPG bulletin*, *91*(12), 1685–1700.

Fossen, H., R. A. Schultz, Z. K. Shipton, and K. Mair (2007a), Deformation bands in sandstone: a review, *Journal of the Geological Society*, *164*(4), 755–769.

Fossen, H., R. A. Schultz, Z. K. Shipton, and K. Mair (2007b), Deformation bands in sandstone: a review, *Journal of the Geological Society*, *164*(4), 755–769.

Fossen, H., R. A. Schultz, and A. Torabi (2011), Conditions and implications for compaction band formation in the navajo sandstone, utah, *Journal of Structural Geology*, *33*(10), 1477–1490.

Fossum, A. F., J. T. Fredrich, et al. (2000), Cap plasticity models and compactive and dilatant pre-failure deformation, in *4th North American Rock Mechanics Symposium*, American Rock Mechanics Association.

Gajst, H., R. Weinberger, W. Zhu, V. Lyakhovsky, S. Marco, and E. Shalev (2018), Effects of pre-existing faults on compaction localization in porous sandstones, *Tectonophysics*, *747*, 1–15.

Gens, A., and R. Nova (1993), Conceptual bases for a constitutive model for bonded soils and weak rocks, *Geotechnical engineering of hard soils-soft rocks*, *1*(1), 485–494.

Gitman, I. M. (2006), Representative volumes and multi-scale modelling of quasi-brittle materials.

Griffiths, J., D. R. Faulkner, A. P. Edwards, and R. H. Worden (2018), Deformation band development as a function of intrinsic host-rock properties in triassic sherwood sandstone, *Geological Society, London, Special Publications*, *435*(1), 161–176.

Grueschow, E., and J. W. Rudnicki (2005), Elliptic yield cap constitutive modeling for high porosity sandstone, *International Journal of Solids and Structures*, *42*(16), 4574–4587.

Gudehus, G., and K. Nübel (2004), Evolution of shear bands in sand, *Geotechnique*, *54*(3), 187–201.

Guo, N., and J. Zhao (2014), A coupled fem/dem approach for hierarchical multiscale modelling of granular media, *International Journal for Numerical Methods in Engineering*, *99*(11), 789–818.

Haimson, B. (1978), The hydrofracturing stress measuring method and recent field results, in *International Journal of Rock Mechanics and Mining Sciences & Geomechanics Abstracts*, vol. 15, pp. 167–178, Elsevier.

Haimson, B., and A. Klaetsch (2007), Compaction bands and the formation of slot-shaped breakouts in st. peter sandstone, *Geological Society, London, Special Publications*, *284*(1), 89–105.

Hale, J. K., and H. Koçak (2012), *Dynamics and bifurcations*, vol. 3, Springer Science & Business Media.

Hall, S., M. Bornert, J. Desrues, Y. Pannier, N. Lenoir, G. Viggiani, and P. Bésuelle (2010), Discrete and continuum analysis of localised deformation in sand using x-ray μct and volumetric digital image correlation, *Géotechnique*, *60*(5), 315–322.

Hashin, Z., and S. Shtrikman (1963), A variational approach to the theory of the elastic behaviour of multiphase materials, *Journal of the Mechanics and Physics of Solids*, *11*(2), 127–140.

Hassani, B., and E. Hinton (1998), A review of homogenization and topology optimization ihomogenization theory for media with periodic structure, *Computers & Structures*, *69*(6), 707 – 717.

Heap, M. J., N. Brantut, P. Baud, and P. G. Meredith (2015), Time-dependent compaction band formation in sandstone, *Journal of Geophysical Research: Solid Earth*, *120*(7), 4808–4830.

Hettema, M., E. Papamichos, and P. Schutjens (2002), Subsidence delay: field observations and analysis, *Oil & Gas Science and Technology*, *57*(5), 443–458.

Hill, R. (1963), Elastic properties of reinforced solids: some theoretical principles, *Journal of the Mechanics and Physics of Solids*, *11*(5), 357–372.

Hill, R. E. (1989), Analysis of deformation bands in the aztec sandstone, valley of fire state park, nevada, Master's thesis, University of Nevada, Las Vegas.

Hol, S., A. van der Linden, S. Bierman, F. Marcelis, and A. Makurat (2018), Rock physical controls on production-induced compaction in the groningen field, *Scientific reports*, *8*(1), 7156.

Holcomb, D., and W. Olsson (2003), Compaction localization and fluid flow, *Journal of Geophysical Research: Solid Earth*, *108*(B6).

Holcomb, D., J. W. Rudnicki, K. A. Issen, and K. Sternlof (2007), Compaction localization in the earth and the laboratory: state of the research and research directions, *Acta Geotechnica*, *2*(1), 1–15.

Howard, V., and M. Reed (2004), *Unbiased stereology: three-dimensional measurement in microscopy*, Garland Science.

Huang, L., P. Baud, B. Cordonnier, F. Renard, L. Liu, and T.-f. Wong (2019), Synchrotron x-ray imaging in 4d: Multiscale failure and compaction localization in triaxially compressed porous limestone, *Earth and Planetary Science Letters*, *528*, 115,831.

Imposimato, S., and R. Nova (1998), An investigation on the uniqueness of the incremental response of elastoplastic models for virgin sand, *Mechanics of Cohesive-Frictional Materials*, *3*, 65–87.

Issen, K., and J. Rudnicki (2000), Conditions for compaction bands in porous rock, *Journal of Geophysical Research: Solid Earth*, *105*(B9), 21,529–21,536.

Issen, K. A. (2002), The influence of constitutive models on localization conditions for porous rock, *Engineering Fracture Mechanics*, *69*(17), 1891–1906.

Jin, Z., W. Li, C. Jin, J. Hambleton, and G. Cusatis (2018), Anisotropic elastic, strength, and fracture properties of marcellus shale, *International Journal of Rock Mechanics and Mining Sciences*, *109*, 124–137.

Kanit, T., S. Forest, I. Galliet, V. Mounoury, and D. Jeulin (2003), Determination of the size of the representative volume element for random composites: statistical and numerical approach, *International Journal of solids and structures*, *40*(13-14), 3647–3679.

Katsman, R., E. Aharonov, and H. Scher (2005), Numerical simulation of compaction bands in high-porosity sedimentary rock, *Mechanics of materials*, *37*(1), 143–162.

Kim, H.-K., and J. C. Santamarina (2006), The effect of spatial variability on soil behavior: Load-deformation response, in *GeoCongress 2006: Geotechnical Engineering in the Information Technology Age*, pp. 1–6.

Klein, E., P. Baud, T. Reuschlé, and T. Wong (2001), Mechanical behaviour and failure mode of bentheim sandstone under triaxial compression, *Physics and Chemistry of the*

Earth, Part A: Solid Earth and Geodesy, *26*(1-2), 21–25.

Klimczak, C., R. Soliva, R. A. Schultz, and J. Chéry (2011), Sequential growth of deformation bands in a multilayer sequence, *Journal of Geophysical Research: Solid Earth*, *116*(B9).

Labuz, J. F., and J. Bridell (1993), Reducing frictional constraint in compression testing through lubrication, in *International journal of rock mechanics and mining sciences & geomechanics abstracts*, vol. 30, pp. 451–455, Pergamon.

Lagioia, R., and R. Nova (1995), An experimental and theoretical study of the behaviour of a calcarenite in triaxial compression, *Géotechnique*, *45*(4), 633–648.

Lagioia, R., A. Puzrin, and D. Potts (1996), A new versatile expression for yield and plastic potential surfaces, *Computers and Geotechnics*, *19*(3), 171–191.

Lantuéjoul, C. (1991), Ergodicity and integral range, *Journal of Microscopy*, *161*(3), 387–403.

Lazari, M., L. Sanavia, C. di Prisco, and F. Pisan (2018), Predictive potential of perzyna viscoplastic modelling for granular geomaterials, *International Journal for Numerical and Analytical Methods in Geomechanics*.

Liu, W. K., and C. McVeigh (2008), Predictive multiscale theory for design of heterogeneous materials, *Computational Mechanics*, *42*(2), 147–170.

Liu, Y., W. Sun, Z. Yuan, and J. Fish (2016), A nonlocal multiscale discrete-continuum model for predicting mechanical behavior of granular materials, *International Journal for Numerical Methods in Engineering*, *106*(2), 129–160.

Louis, L., P. Baud, and T.-f. Wong (2009), Microstructural inhomogeneity and mechanical anisotropy associated with bedding in rothbach sandstone, *Pure and Applied Geophysics*, *166*(5-7), 1063–1087.

Ma, X., J. W. Rudnicki, and B. C. Haimson (2017), Failure characteristics of two porous sandstones subjected to true triaxial stresses: applied through a novel loading path, *Journal of Geophysical Research: Solid Earth*, *122*(4), 2525–2540.

Maier, G., and T. Hueckel (1979), Nonassociated and coupled flow rules of elastoplasticity for rock-like materials, in *International Journal of Rock Mechanics and Mining Sciences & Geomechanics Abstracts*, vol. 16, pp. 77–92, Elsevier.

Marinelli, F., and G. Buscarnera (2015), Parameter calibration for high-porosity sandstones deformed in the compaction banding regime, *International Journal of Rock Mechanics and Mining Sciences*, *78*, 240–252.

Marinelli, F., and G. Buscarnera (2018), Instability criteria for quasi-saturated viscous soils, *International Journal for Numerical and Analytical Methods in Geomechanics*, *42*(3), 379–400.

Marinelli, F., F. Pisanò, C. di Prisco, and G. Buscarnera (2017), Model-based interpretation of undrained creep instability in loose sands, *Géotechnique*, pp. 1–14.

Matheron, G. (1989), Estimating and choosing. an essay on probability in practice.

McGarr, A., and N. Gay (1978), State of stress in the earth's crust, *Annual Review of Earth and Planetary Sciences*, *6*(1), 405–436.

McLamore, R., and K. Gray (1967), The mechanical behavior of anisotropic sedimentary rocks, *Journal of Engineering for Industry*, *89*(1), 62–73.

Meier, H. A., P. Steinmann, and E. Kuhl (2008), Towards multiscale computation of confined granular media-contact forces, stresses and tangent operators, *Technische Mechanik*, *28*(1), 32–42.

Menéndez, B., W. Zhu, and T.-F. Wong (1996), Micromechanics of brittle faulting and cataclastic flow in berea sandstone, *Journal of structural geology*, *18*(1), 1–16.

Micarelli, L., A. Benedicto, and C. Wibberley (2006), Structural evolution and permeability of normal fault zones in highly porous carbonate rocks, *Journal of Structural Geology*, *28*(7), 1214–1227.

Miehe, C., J. Dettmar, and D. Zäh (2010), Homogenization and two-scale simulations of granular materials for different microstructural constraints, *International Journal for Numerical Methods in Engineering*, *83*(8-9), 1206–1236.

Mollema, P., and M. Antonellini (1996), Compaction bands: a structural analog for anti-mode i cracks in aeolian sandstone, *Tectonophysics*, *267*(1-4), 209–228.

Needleman, A. (1988), Material rate dependence and mesh sensitivity in localization problems, *Computer methods in applied mechanics and engineering*, *67*(1), 69–85.

Nicol, A., C. Childs, J. Walsh, and K. Schafer (2013), A geometric model for the formation of deformation band clusters, *Journal of Structural Geology*, *55*, 21–33.

Nitka, M., G. Combe, C. Dascalu, and J. Desrues (2011), Two-scale modeling of granular materials: a dem-fem approach, *Granular Matter*, *13*(3), 277–281.

Nova, R. (1980), The failure of transversely isotropic rocks in triaxial compression, in *International Journal of Rock Mechanics and Mining Sciences & Geomechanics Abstracts*, vol. 17, pp. 325–332, Elsevier.

Nova, R. (1994), Controllability of the incremental response of soil specimen subjected to arbitrary loading programmes., *Journal of the Mechanical Behavior of Materials*, *5*, 221–243.

Nova, R., and A. Zaninetti (1990), An investigation into the tensile behaviour of a schistose rock, in *International Journal of Rock Mechanics and Mining Sciences & Geomechanics Abstracts*, vol. 27, pp. 231–242, Elsevier.

Nova, R., R. Castellanza, and C. Tamagnini (2003), A constitutive model for bonded geomaterials subject to mechanical and/or chemical degradation, *International Journal for Numerical and Analytical Methods in Geomechanics*, *27*(9), 705–732.

Oka, F., T. Adachi, and A. Yashima (1994), Instability of an elasto-viscoplastic constitutive model for clay and strain localization, *Mechanics of materials*, *18*(2), 119–129.

Oka, F., S. Kimoto, H. Kobayashi, and T. Aadachi (2002), Anisotropic behavior of soft sedimentary rock and a constitutive model, *Soils and foundations*, *42*(5), 59–70.

Olsson, W., and D. Holcomb (2000), Compaction localization in porous rock, *Geophysical Research Letters*, *27*(21), 3537–3540.

Olsson, W., D. Holcomb, and J. Rudnicki (2002), Compaction localization in porous sandstone: Implications for reservoir mechanics, *Oil & Gas Science and Technology*, *57*(5), 591–599.

Olsson, W. A. (1999), Theoretical and experimental investigation of compaction bands in porous rock, *Journal of Geophysical Research: Solid Earth*, *104*(B4), 7219–7228.

Olsson, W. A. (2001), Quasistatic propagation of compaction fronts in porous rock, *Mechanics of Materials*, *33*(11), 659–668.

Papazoglou, A., G. Shahin, F. Marinelli, C. Dano, G. Buscarnera, and G. Viggiani (2017), Localized compaction in tuffeau de maastricht: Experiments and modeling, in *International Workshop on Bifurcation and Degradation in Geomaterials*, pp. 481–488, Springer.

Papazoglou, A., P. Bésuelle, C. Dano, and G. Viggiani (2019), Full 3d investigation of localized compaction in Tuffeau de Maastricht using x-ray computed tomography, *submitted*.

Papka, S. D., and S. Kyriakides (1998), In-plane crushing of a polycarbonate honeycomb, *International Journal of Solids and Structures*, *35*(3-4), 239–267.

Park, C., and S. Nutt (2001), Anisotropy and strain localization in steel foam, *Materials Science and Engineering: A*, *299*(1-2), 68–74.

Perzyna, P. (1966), Fundamental problems in viscoplasticity, *Advances in applied mechanics*, *9*, 243–377.

Pietruszczak, S., and Z. Mroz (2000), Formulation of anisotropic failure criteria incorporating a microstructure tensor, *Computers and Geotechnics*, *26*(2), 105–112.

Pietruszczak, S., D. Lydzba, and J.-F. Shao (2002), Modelling of inherent anisotropy in sedimentary rocks, *International Journal of Solids and Structures*, *39*(3), 637–648.

Pijnenburg, R., B. Verberne, S. Hangx, and C. Spiers (2018), Deformation behavior of sandstones from the seismogenic groningen gas field: Role of inelastic versus elastic mechanisms, *Journal of Geophysical Research: Solid Earth*, *123*(7), 5532–5558.

Pisanò, F., and C. di Prisco (2016), A stability criterion for elasto-viscoplastic constitutive relationships, *International Journal for Numerical and Analytical Methods in Geomechanics*, *40*(1), 141–156.

Rass, L., R. Y. Makhnenko, Y. Podladchikov, and L. Laloui (2017), Quantification of viscous creep influence on storage capacity of caprock, *Energy Procedia*, *114*, 3237 – 3246, 13th International Conference on Greenhouse Gas Control Technologies, GHGT-13, 14-18 November 2016, Lausanne, Switzerland.

Rath, A., U. Exner, C. Tschegg, B. Grasemann, R. Laner, and E. Draganits (2011), Diagenetic control of deformation mechanisms in deformation bands in a carbonate grainstone, *AAPG bulletin*, *95*(8), 1369–1381.

Robert, R., P. Robion, P. Souloumiac, C. David, and E. Saillet (2018), Deformation bands, early markers of tectonic activity in front of a fold-and-thrust belt: Example from the tremp-graus basin, southern pyrenees, spain, *Journal of Structural Geology*, *110*, 65–85.

Rotevatn, A., E. Thorsheim, E. Bastesen, H. S. Fossmark, A. Torabi, and G. Sælen (2016), Sequential growth of deformation bands in carbonate grainstones in the hangingwall of an active growth fault: implications for deformation mechanisms in different tectonic regimes, *Journal of Structural Geology*, *90*, 27–47.

Rotevatn, A., H. S. Fossmark, E. Bastesen, E. Thorsheim, and A. Torabi (2017), Do deformation bands matter for flow? insights from permeability measurements and flow simulations in porous carbonate rocks, *Petroleum Geoscience*, *23*(1), 104–119.

Rudnicki, J. W. (2002), Conditions for compaction and shear bands in a transversely isotropic material, *International Journal of Solids and Structures*, *39*(13-14), 3741–3756.

Rudnicki, J. W. (2004), Shear and compaction band formation on an elliptic yield cap, *Journal of Geophysical Research: Solid Earth*, *109*(B3).

Rudnicki, J. W., and J. Rice (1975), Conditions for the localization of deformation in pressure-sensitive dilatant materials, *Journal of the Mechanics and Physics of Solids*, *23*(6), 371–394.

Rustichelli, A., E. Tondi, F. Agosta, A. Cilona, and M. Giorgioni (2012), Development and distribution of bed-parallel compaction bands and pressure solution seams in carbonates (bolognano formation, majella mountain, italy), *Journal of Structural Geology*, *37*, 181–199.

Saillet, E., and C. A. Wibberley (2010), Evolution of cataclastic faulting in high-porosity sandstone, bassin du sud-est, provence, france, *Journal of Structural Geology*, *32*(11), 1590–1608.

Sari, M. (2019), A multi-physics visco-plasticity theory for porous sedimentary rocks.

Schultz, R., and R. Siddharthan (2005), A general framework for the occurrence and faulting of deformation bands in porous granular rocks, *Tectonophysics*, *411*(1-4), 1–18.

Schultz, R. A. (2009), Scaling and paleodepth of compaction bands, nevada and utah, *Journal of Geophysical Research: Solid Earth*, *114*(B3).

Schultz, R. A. (2011), Relationship of compaction bands in utah to laramide fault-related folding, *Earth and Planetary Science Letters*, *304*(1-2), 29–35.

Schultz, R. A., C. H. Okubo, and H. Fossen (2010), Porosity and grain size controls on compaction band formation in jurassic navajo sandstone, *Geophysical Research Letters*, *37*(22).

Schutjens, P. M. (1991), Experimental compaction of quartz sand at low effective stress and temperature conditions, *Journal of the Geological Society*, *148*(3), 527–539.

Semnani, S. J., J. A. White, and R. I. Borja (2016), Thermoplasticity and strain localization in transversely isotropic materials based on anisotropic critical state plasticity, *International Journal for Numerical and Analytical Methods in Geomechanics*, *40*(18), 2423–2449.

Shahin, G., J. Desrues, S. D. Pont, G. Combe, and A. Argilaga (2016), A study of the influence of rev variability in double-scale fem× dem analysis, *International Journal for Numerical Methods in Engineering*, *107*(10), 882–900.

Shipton, Z. K., and P. A. Cowie (2003), A conceptual model for the origin of fault damage zone structures in high-porosity sandstone, *Journal of Structural Geology*, *25*(3), 333–344.

Soliva, R., G. Ballas, H. Fossen, and S. Philit (2016), Tectonic regime controls clustering of deformation bands in porous sandstone, *Geology*, *44*(6), 423–426.

Sternlof, K., J. Chapin, D. Pollard, and L. Durlofsky (2004), Permeability effects of deformation band arrays in sandstone, *AAPG bulletin*, *88*(9), 1315–1329.

Sternlof, K. R., J. W. Rudnicki, and D. D. Pollard (2005), Anticrack inclusion model for compaction bands in sandstone, *Journal of Geophysical Research: Solid Earth*, *110*(B11).

Sternlof, K. R., M. Karimi-Fard, D. Pollard, and L. Durlofsky (2006), Flow and transport effects of compaction bands in sandstone at scales relevant to aquifer and reservoir management, *Water Resources Research*, *42*(7).

Sun, W., J. E. Andrade, J. W. Rudnicki, and P. Eichhubl (2011), Connecting microstructural attributes and permeability from 3d tomographic images of in situ shear-enhanced compaction bands using multiscale computations, *Geophysical Research Letters*, *38*(10).

Tadmor, E. B., M. Ortiz, and R. Phillips (1996), Quasicontinuum analysis of defects in solids, *Philosophical magazine A*, *73*(6), 1529–1563.

Tavani, S., P. Granado, F. Balsamo, M. Pizzati, I. Cantarero, A. Corradetti, and J. Muoz (2018), Shear-enhanced compaction-solution bands in quartz-rich calcarenites of the cotiella massif (spanish pyrenees), *Journal of Structural Geology*, *114*, 274 – 279.

Tembe, S., P. Baud, and T.-f. Wong (2008), Stress conditions for the propagation of discrete compaction bands in porous sandstone, *Journal of Geophysical Research: Solid Earth*, *113*(B9).

Tommasi, A., D. Mainprice, G. Canova, and Y. Chastel (2000), Viscoplastic self-consistent and equilibrium-based modeling of olivine lattice preferred orientations: Implications for the upper mantle seismic anisotropy, *Journal of Geophysical Research: Solid Earth*, *105*(B4), 7893–7908.

Tondi, E., M. Antonellini, A. Aydin, L. Marchegiani, and G. Cello (2006), The role of deformation bands, stylolites and sheared stylolites in fault development in carbonate grainstones of majella mountain, italy, *Journal of structural geology*, *28*(3), 376–391.

Torabi, A., and H. Fossen (2009), Spatial variation of microstructure and petrophysical properties along deformation bands in reservoir sandstones, *Aapg Bulletin*, *93*(7), 919–938.

Torabi, A., R. Gabrielsen, H. Fossen, P. Ringrose, E. Skurtveit, E. Ando, F. Marinelli, G. Viggiani, S. Dal pont, A. Braathen, A. Hovland, P. Bsuelle, R. Alikarami, H. Zalmstra, and S. D. (2015), Strain localization in sandstone and its implications for co2 storage, *First Break*, *33*(7), 81 – 92.

Townend, E., B. D. Thompson, P. M. Benson, P. G. Meredith, P. Baud, and R. P. Young (2008), Imaging compaction band propagation in diemelstadt sandstone using acoustic emission locations, *Geophysical Research Letters*, *35*(15).

Tsopela, A. (2014), Master's thesis, University Grenoble-Alpes.

Vajdova, V., P. Baud, and T.-f. Wong (2004), Compaction, dilatancy, and failure in porous carbonate rocks, *Journal of Geophysical Research: Solid Earth*, *109*(B5).

Valdes, J. R., F. L. Fernandes, and I. Einav (2012), Periodic propagation of localized compaction in a brittle granular material, *Granular Matter*, *14*(1), 71–76.

Van den Eijnden, A., P. Bésuelle, R. Chambon, and F. Collin (2016), A fe 2 modelling approach to hydromechanical coupling in cracking-induced localization problems, *International Journal of Solids and Structures*, *97*, 475–488.

Vernik, L., and M. D. Zoback (1992), Estimation of maximum horizontal principal stress magnitude from stress-induced well bore breakouts in the cajon pass scientific research borehole, *Journal of Geophysical Research: Solid Earth*, *97*(B4), 5109–5119.

Veveakis, E., and K. Regenauer-Lieb (2015), Cnoidal waves in solids, *Journal of the Mechanics and Physics of Solids*, *78*, 231–248.

Veveakis, E., K. Regenauer-Lieb, and R. Weinberg (2014), Ductile compaction of partially molten rocks: the effect of non-linear viscous rheology on instability and segregation, *Geophysical Journal International*, *200*(1), 519–523.

Wang, B., Y. Chen, and T.-f. Wong (2008), A discrete element model for the development of compaction localization in granular rock, *Journal of Geophysical Research: Solid Earth*, *113*(B3).

Wawersik, W. R., J. W. Rudnicki, P. Dove, J. Harris, J. M. Logan, L. Pyrak-Nolte, F. M. Orr Jr, P. J. Ortoleva, F. Richter, N. R. Warpinski, et al. (2001), Terrestrial sequestration of co2: An assessment of research needs, in *Advances in geophysics*, vol. 43, pp. 97–IX, Elsevier.

Wennberg, O. P., G. Casini, A. Jahanpanah, F. Lapponi, J. Ineson, B. G. Wall, and P. Gillespie (2013), Deformation bands in chalk, examples from the shetland group of the oseberg field, north sea, norway, *Journal of Structural Geology*, *56*, 103–117.

Wilkins, S. J., R. K. Davies, and S. J. Naruk (2019), Subsurface observations of deformation bands and their impact on hydrocarbon production within the holstein field, gulf of mexico, usa, *Geological Society, London, Special Publications*, *496*, SP496–2018.

Wong, T.-f., and P. Baud (2012), The brittle-ductile transition in porous rock: A review, *Journal of Structural Geology*, *44*, 25–53.

Wong, T.-f., C. David, and W. Zhu (1997), The transition from brittle faulting to cataclastic flow in porous sandstones: Mechanical deformation, *Journal of Geophysical Research: Solid Earth*, *102*(B2), 3009–3025.

Wong, T.-f., P. Baud, and E. Klein (2001), Localized failure modes in a compactant porous rock, *Geophysical Research Letters*, *28*(13), 2521–2524.

Wood, D. M. (1990), *Soil behaviour and critical state soil mechanics*, Cambridge university press.

Wu, H., A. Papazoglou, G. Viggiani, C. Dano, and J. Zhao (2020), Compaction bands in tuffeau de maastricht: insights from x-ray tomography and multiscale modeling, *Acta Geotechnica*, *15*(1), 39–55.

Yin, Z.-Y., C. S. Chang, M. Karstunen, and P.-Y. Hicher (2010), An anisotropic elastic–viscoplastic model for soft clays, *International Journal of Solids and Structures*, *47*(5), 665–677.

Zhang, F. (2006), *The Schur complement and its applications*, vol. 4, Springer Science & Business Media.

Zhou, X., M. Karimi-Fard, L. J. Durlofsky, and A. Aydin (2014), Fluid flow through porous sandstone with overprinting and intersecting geological structures of various types, *Geological Society, London, Special Publications*, *374*(1), 187–209.

Zuluaga, L. F., A. Rotevatn, E. Keilegavlen, and H. Fossen (2016), The effect of deformation bands on simulated fluid flow within fault-propagation fold trap types: Lessons from the san rafael monocline, utah, *AAPG Bulletin*, *100*(10), 1523–1540.

APPENDIX A

Mathematical Derivations of Instability Indices

To derive the ODE expressed in Equation 3, the rate-dependent response is recasted through the additive decomposition of elastic and viscoplastic strain (i.e., $\dot{\varepsilon} = \dot{\varepsilon}^{el} + \dot{\varepsilon}^{vp}$):

$$\begin{Bmatrix} \dot{\varepsilon}_a \\ \dot{\varepsilon}_r \end{Bmatrix} = \begin{bmatrix} \dfrac{1}{E} & \dfrac{-\nu}{E} \\ \dfrac{-\nu}{E} & \dfrac{1-\nu}{2E} \end{bmatrix} \begin{Bmatrix} \dot{\sigma}_a \\ 2\dot{\sigma}_r \end{Bmatrix} + \Phi \begin{Bmatrix} \dfrac{\partial g}{\partial \sigma_a} \\ \dfrac{\partial g}{\partial \sigma_r} \end{Bmatrix} \tag{A.1}$$

where the subscript a and r are referred to the axial and radial component of the corresponding variable. Equation A.1 can be rewritten as function of response and controlled variables, thus obtaining:

$$\begin{Bmatrix} \dot{\varepsilon}_a \\ 2\dot{\sigma}_r \end{Bmatrix} = \underbrace{\begin{bmatrix} \dfrac{1}{E}\left(\dfrac{1-\nu-2\nu^2}{1-\nu}\right) & -\dfrac{2\nu}{1-\nu} \\ \dfrac{2\nu}{1-\nu} & \dfrac{2E}{1-\nu} \end{bmatrix}}_{\mathbf{C}} \begin{Bmatrix} \dot{\Sigma}_a \\ \dot{E}_r \end{Bmatrix} + \Phi \underbrace{\begin{bmatrix} 1 & \dfrac{2\nu}{1-\nu} \\ 0 & -\dfrac{2E}{1-\nu} \end{bmatrix}}_{\mathbf{D}} \begin{Bmatrix} \dfrac{\partial g}{\partial \sigma_a} \\ \dfrac{\partial g}{\partial \sigma_r} \end{Bmatrix} \tag{A.2}$$

in which the controlled variables are indicated through capital letters (i.e., $\dot{\Sigma}_a \equiv \dot{\sigma}_a$ and $\dot{E}_r \equiv \dot{\varepsilon}_r$). The differential form of the viscoplastic response is obtained by further developing the acceleration of the axial strain and radial stress:

$$\ddot{\varepsilon}_a = \underbrace{\left(C_{11}\ddot{\Sigma}_a + C_{12}\ddot{E}_r\right)}_{F_{\varepsilon}^{a}} + \frac{d\Phi}{dt}\left[\frac{\partial g}{\partial \sigma_a} + D_{12}\frac{\partial g}{\partial \sigma_r}\right] + \Phi\left[\frac{d}{dt}\frac{\partial g}{\partial \sigma_a} + D_{12}\frac{d}{dt}\frac{\partial g}{\partial \sigma_r}\right] \tag{A.3}$$

$$\ddot{\sigma}_r = \underbrace{\left(C_{21}\ddot{\Sigma}_a + C_{22}\ddot{E}_r\right)}_{F_{\sigma}^{a}} + \frac{d\Phi}{dt}\left[D_{22}\frac{\partial g}{\partial \sigma_r}\right] + \Phi\left[D_{22}\frac{d}{dt}\frac{\partial g}{\partial \sigma_r}\right], \tag{A.4}$$

where the components F_ε^a and F_σ^a represent a first contribution to the forcing vector $\mathbf{F}$. The time derivatives of the viscous nucleus $\dot{\Phi}$ and the gradient of the plastic potential can be developed as follows:

$$\dot{\Phi} = \frac{\partial \Phi}{\partial f}\left[\frac{\partial f}{\partial \Sigma_a}\dot{\Sigma}_a + \frac{\partial f}{\partial \sigma_r}\left(2\dot{\sigma}_r\right) - H\Phi\right], \tag{A.5}$$

by using Equation A.2, it is possible to expand the radial stress $\dot{\sigma}_r$ and rearrange Equation A.5 as a function of the controllability index:

$$\dot{\Phi} = -\frac{\partial \Phi}{\partial f}\underbrace{\left[H - H_\chi - \frac{H_{\sigma\varepsilon}}{\Phi}\right]}_{H_{CB}}\Phi \longrightarrow \begin{cases} H_{\sigma\varepsilon} & = \dot{\Sigma}_a\left[\frac{\partial f}{\partial \sigma_a} + \frac{\partial f}{\partial \sigma_r}\left(\frac{2\nu}{1-\nu}\right)\right] + \dot{E}_r\frac{\partial f}{\partial \sigma_r}\left(\frac{2E}{1-\nu}\right) \\ H_\chi & = -\frac{\partial f}{\partial \sigma_r}\left(\frac{2E}{1-\nu}\right)\frac{\partial g}{\partial \sigma_r} \end{cases} \tag{A.6}$$

The time derivative of the plastic potential can be developed as follows:

$$\frac{d}{dt}\frac{\partial g}{\partial \sigma_a} + D_{12}\frac{d}{dt}\frac{\partial g}{\partial \sigma_r} = \left(\frac{\partial^2 g}{\partial \sigma_a^2}\dot{\Sigma}_a + \frac{\partial^2 g}{\partial \sigma_a \partial \sigma_r}\dot{\sigma}_r\right) + D_{12}\left(\frac{\partial^2 g}{\partial \sigma_a \partial \sigma_r}\dot{\Sigma}_a + \frac{\partial^2 g}{\partial \sigma_r^2}\dot{\sigma}_r\right) \tag{A.7}$$

$$D_{22}\frac{d}{dt}\frac{\partial g}{\partial \sigma_r} = D_{22}\left(\frac{\partial^2 g}{\partial \sigma_a \partial \sigma_r}\dot{\Sigma}_a + \frac{\partial^2 g}{\partial \sigma_r^2}\dot{\sigma}_r\right). \tag{A.8}$$

By collecting response and controlled variables, this equation is equivalent to:

$$\frac{d}{dt}\frac{\partial g}{\partial \sigma_a} + D_{12}\frac{d}{dt}\frac{\partial g}{\partial \sigma_r} = \underbrace{\dot{\Sigma}_a\left(\frac{\partial^2 g}{\partial \sigma_a^2} + D_{12}\frac{\partial^2 g}{\partial \sigma_a \partial \sigma_r}\right)}_{F_\varepsilon^b} + \dot{\sigma}_r\left(\frac{\partial^2 g}{\partial \sigma_a \partial \sigma_r} + D_{12}\frac{\partial^2 g}{\partial \sigma_r^2}\right) \tag{A.9}$$

$$D_{22}\frac{d}{dt}\frac{\partial g}{\partial \sigma_r} = \underbrace{\dot{\Sigma}_a\left(\frac{\partial^2 g}{\partial \sigma_a \partial \sigma_r}\right)D_{22}}_{F_\sigma^b} + \dot{\sigma}_r\frac{\partial^2 g}{\partial \sigma_r^2}D_{22} \tag{A.10}$$

By combining Equation A.6, Equation A.9 and A.10 with the system of equations A.3 and A.4, it is possible to rearrange the acceleration of the response variables as follows:

$$\begin{Bmatrix} \ddot{\varepsilon}_a \\ 2\ddot{\sigma}_r \end{Bmatrix} = H_{CB}\left(-\frac{\partial \Phi}{\partial f}\right)\mathbf{D}\begin{Bmatrix} \Phi\dfrac{\partial g}{\partial \sigma_a} \\ \Phi\dfrac{\partial g}{\partial \sigma_r} \end{Bmatrix} + \begin{Bmatrix} D_{12}\dfrac{\partial^2 g}{\partial \sigma_r^2} + \dfrac{\partial^2 g}{\partial \sigma_a \partial \sigma_r} \\ D_{22}\dfrac{\partial^2 g}{\partial \sigma_r^2} \end{Bmatrix}\Phi\dot{\sigma}_r + \mathbf{F} \tag{A.11}$$

The term $\mathbf{D}(\Phi\partial g/\partial\sigma)$ is equivalent to $\mathbf{D}\varepsilon^{vp}$ therefore Equation A.11 can be modified according to the following developments:

$$\begin{Bmatrix} \dot{\varepsilon}_a^{vp} \\ \dot{\varepsilon}_r^{vp} \end{Bmatrix} = \begin{Bmatrix} \dot{\varepsilon}_a - \dot{\varepsilon}_a^{el} \\ \dot{E}_r - \dot{\varepsilon}_r^{el} \end{Bmatrix} = \begin{Bmatrix} \dot{\varepsilon}_a - \frac{1}{E}\left(\dot{\Sigma}_1 - 2\nu\dot{\sigma}_r\right) \\ \dot{E}_r - \frac{1}{E}\left(\dot{\sigma}_r(1-\nu) - \nu\dot{\Sigma}_a\right) \end{Bmatrix} \tag{A.12}$$

By combining all the equations it is possible to obtain the differential system reported in section 3:

$$\begin{Bmatrix} \ddot{\varepsilon}_a \\ \\ 2\ddot{\sigma}_r \end{Bmatrix} = \begin{bmatrix} -\dfrac{\partial \Phi}{\partial f}H_{CB} & \dfrac{\nu}{1-\nu}\Phi\dfrac{\partial^2 g}{\partial \sigma_r^2} + \Phi\dfrac{\partial^2 g}{\partial \sigma_a \partial \sigma_r} \\ \\ 0 & -\dfrac{\partial \Phi}{\partial f}H_{CB} - \dfrac{2E}{(1-\nu)}\Phi\dfrac{\partial^2 g}{\partial \sigma_r^2} \end{bmatrix} \begin{Bmatrix} \dot{\varepsilon}_a \\ \\ 2\dot{\sigma}_r \end{Bmatrix} + \mathbf{F} \tag{A.13}$$

APPENDIX B

Conversion rules of porosity to constitutive-consistent-parameter

The constitutive model used in this work captures the mechanical effects of changes in porosity through the state variable P_{so}, which incorporates porosity hardening through a formalism typical of critical state models for geomaterials [*Wood*, 1990]. When porosity is the matter of concern, a conversion rule into an initial value of P_s may be employed. Such rule can be derived by integrating the evolution law of P_s (see Equation C.12 in the Appendix), from which it follows:

$$P_s = P_{so} \exp\left[\frac{1}{B_p}(\epsilon_v^p - \epsilon_{vo}^p)\right] \tag{B.1}$$

This equation can be further elaborated by assuming that the elastic strain increment is negligible during the plastic compaction stage, thus resulting into:

$$\Delta\epsilon_v = \epsilon_v - \epsilon_{vo} = -\Delta\phi = -\left(\phi - \phi_o\right) \tag{B.2}$$

in which ϕ_o is the averaged (i.e. mean) porosity over the whole specimen. Substituting Eq. (B.2) in Eq.(B.1) it follows:

$$P_s = P_{so} \exp\left[-\frac{1}{B_p}\left(\phi - \phi_o\right)\right] \tag{B.3}$$

This expression will be used hereafter to characterize the influence of the porosity field on the spatial fluctuations of the yielding strength of the simulated material. An illustration of

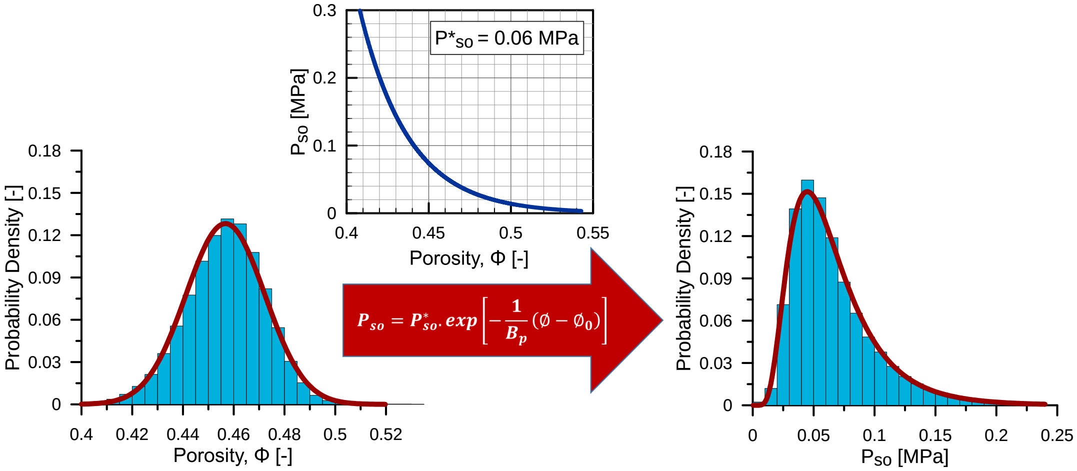

Figure B.1. Porosity conversion to model-specific internal variables (P_{so}). The figure on the left shows a Gaussian distribution of initial porosity, while the figure on the right illustrates the corresponding log-normal distribution of the hardening variable P_s resulting from the conversion scheme. The figure at the top is an illustration of the selected porosity-P_s relation.

this conversion is presented in Figure B.1, where a statistical distribution of porosity values across the sample characterized by normal distribution is converted into a corresponding distribution of P_{so} values here characterized by a log-normal distribution of the yield surface size.

APPENDIX C

Constitutive Modeling of Anisotropic Porous Rocks [*]

The experimental work conducted on Maastricht Tuffeau and discussed in Chapter 4 was expanded to examine the mechanical anisotropy [*Papazoglou et al.*, 2019]. The high-porosity rock displayed a marked dependence of the initial yielding on bedding-loading angle. Anisotropy signatures were also seen in the deformation behavior with post-yielding stress plateaus characterized by marked variation in elongation depending on the direction of loading (Fig. C.1). While classical studies of anisotropy focused on stiffness and strength (e.g., [*Pietruszczak and Mroz*, 2000; *Semnani et al.*, 2016]), the intriguing observations on anisotropic flow behavior in Maastricht Tuffeau compels the need for an integrated constitutive theory that allows for quantifying the characteristics of anisotropy not only in terms of elasticity and first yielding, but even in terms of the post-yielding deformation behavior.

1. Constitutive Theory of Cross-Anisotropic Materials

The origin of mechanical anisotropy in geomaterials is not yet fully understood. The literature, however, distinguishes between elastic anisotropy and inelastic anisotropy with elastic modulus and strength peaks that are dependent on bedding directions. The anisotropy in these two phases of behavior appear sometimes interconnected. Experimental studies disclosed concurrent trends of dependence on bedding direction [*Jin et al.*, 2018; *Louis et al.*,

---

[*] The content of this chapter is published in:

- Shahin, G., Papazoglou, A., Marinelli, F., Dano, C., Viggiani, G., and Buscarnera, G. Compaction Localization in Anisotropic Maastricht Tuffeau (in preparation)

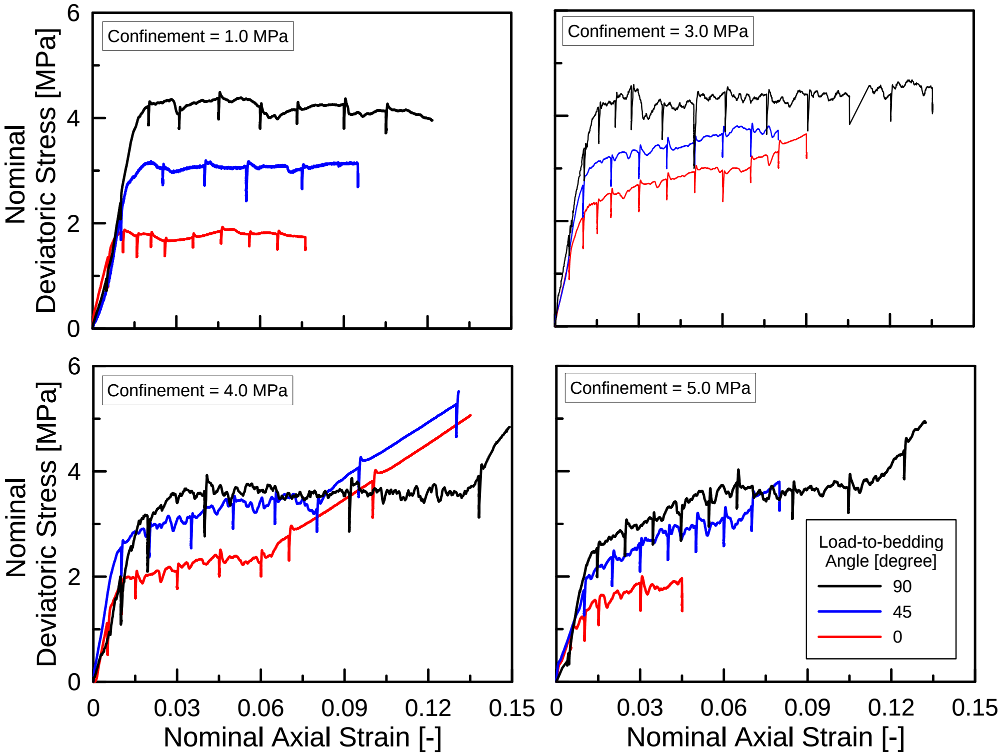

Figure C.1. Mechanical response of triaxial compression on Maastricht Tuffeau specimens cored in various directions with respect to bedding. The test was conducted under varying confining pressures.

2009; *Nova and Zaninetti*, 1990], which could be attributed to common microstructural unites, such as alignments in the granular structure and the microstructural cracks which form the bases for structural foliations and bedding planes in sedimentary rocks [*Bennett et al.*, 2015; *McLamore and Gray*, 1967]. The existence of structural fabrics has been reflected on the formation of plasticity models, where microstructural notions that utilize second order tensors to identify cross-anisotropy were used to formulate plasticity models [*Boehler and Sawczuk*, 1977; *Chen et al.*, 2010; *Oka et al.*, 2002; *Pietruszczak and Mroz*, 2000; *Pietruszczak et al.*, 2002]. Fourth order tensors that incorporates microstructural notions have also been used in the literature to project the stress space into alternative configurations, leading to the bedding dependent material strength [*Boehler*, 1970; *Cazacu et al.*, 1998; *Crook et al.*, 2002; *Nova*, 1980; *Semnani et al.*, 2016].

1.1. Constitutive Theory

A constitutive theory for modeling anisotropic materials is presented. The theory is based on the notion of fictitious isotropy where a tensorial operator is used to project the real Cauchy stress tensor, σ, onto an alternative stress configuration, $\boldsymbol{\sigma}^f$. For this purpose, a fourth order tensor, $\mathbb{P}^f$, is defined as:

$$\boldsymbol{\sigma}^f = \mathbb{P}^f \, \boldsymbol{\sigma} \tag{C.1}$$

The anisotropic yield surface in the real configuration is assumed equivalent to an isotropic yield surface in the alternative configuration. Based on this assumption, it is possible to utilize standard constitutive models to address cases of anisotropy by determining suitable projection operators. Yielding surface in the alternative configuration is defined by:

$$f = f(\boldsymbol{\sigma}^f, \Psi) \tag{C.2}$$

with, Ψ, are a vector of state variable. Equivalently, for the purpose of defining an anisotropic plastic potential, a tensorial operator, $\mathbb{P}^g$, is used to project again the real Cauchy stress tensor, σ, onto an alternative stress configuration, $\boldsymbol{\sigma}^g$, as following:

$$\boldsymbol{\sigma}^g = \mathbb{P}^g \, \boldsymbol{\sigma} \tag{C.3}$$

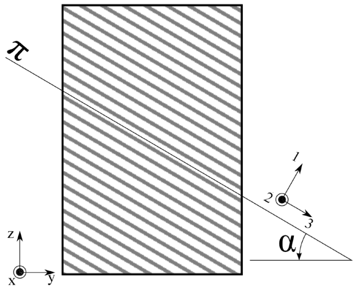

Figure C.2. Schematic of orthogonal basis for transversely isotropic material.

The plastic potentials in the alternative configuration is defined by:

$$g = g(\boldsymbol{\sigma}^g) \tag{C.4}$$

To determine these projectors, let's start by defining the three mutually orthogonal unit vectors n_1, n_2, and n_3 which identify a cross-anisotropic material whose response is invariant with respect to an arbitrary rotation around n_1, the normal to the bedding planes, (Fig. C.2). Based on this system, a second-order tensor, $\mathbf{F}$, that describes material's intrinsic characteristics of bedding orientation is defined by the dyadic product of the bedding plane identifier, $\boldsymbol{n}_1$:

$$\mathbf{F} = \boldsymbol{n}_1 \otimes \boldsymbol{n}_1 \tag{C.5}$$

In case of transverse isotropy, linear elastic materials can be characterized through the strain tensor, $\boldsymbol{\varepsilon}$, and the fabric tensor, $\mathbf{F}$:

$$\begin{aligned} \sigma_{ij} &= \mathbb{D}^{el}_{ijkl}\varepsilon_{kl} \\ &= \lambda \text{tr}(\epsilon)\delta_{ij} + \mu_{\perp}\varepsilon_{ij} + \alpha\left(\text{tr}(\epsilon)F_{ij} + F_{kl}\varepsilon_{kl}\delta_{ij}\right) + 2\left(\mu_{\parallel} - \mu_{\perp}\right)\left(F_{ik}\varepsilon_{kj} + \varepsilon_{ik}F_{kj}\right) + \beta\left(F_{kl}\varepsilon_{kl}\right)F_{ij} \end{aligned} \tag{C.6}$$

where $\mu_{\perp}$ and $\mu_{\parallel}$ are The elasticity tensor can be written as a function of the tensorial basis $\mathbb{T}_i$:

$$\begin{aligned}
\mathbb{D}^{el} &= +2\mu_{\parallel}\underbrace{(\mathbb{I})}_{\mathbb{T}_1} + \lambda\underbrace{(\mathbf{I}\otimes\mathbf{I})}_{\mathbb{T}_2} + \alpha\underbrace{(\mathbf{F}\otimes\mathbf{I}+\mathbf{I}\otimes\mathbf{F})}_{\mathbb{T}_3} + 2\left(\mu_{\parallel}-\mu_{\perp}\right)\underbrace{(\mathbf{F}\boxtimes\mathbf{I}+\mathbf{I}\boxtimes\mathbf{F})}_{\mathbb{T}_4} + \beta\underbrace{(\mathbf{F}\otimes\mathbf{F})}_{\mathbb{T}_5} \\
&= C_1^e\mathbb{T}_1 + C_2^e\mathbb{T}_2 + C_3^e\mathbb{T}_3 + C_4^e\mathbb{T}_4 + C_5^e\mathbb{T}_5 \\
&= \sum_{i=1}^{5} C_i^e\mathbb{T}_i
\end{aligned} \tag{C.7}$$

where $C_0^e = 2\mu_{\parallel}$, $C_1^e = \lambda$, $C_2^e = \alpha$, $C_3^e = 2\left(\mu_{\parallel}-\mu_{\perp}\right)$ and $C_4^e = \beta$, are elastic material coefficients. The symbol $\boxtimes$ satisfies the following properties: $\mathbf{A}\boxtimes\mathbf{B}\mathbf{C} := \mathbf{A}\mathbf{C}^{\intercal}\mathbf{B} = A_{ik}C_{lk}B_{lj}$. The bases of anisotropic elasticity, $\mathbb{T}_i$, are used in this work to construct the fourth order tensor $\mathbb{P}^h_{ijkl}$ as following:

$$\mathbb{P}^h = C_1^h\mathbb{T}_1 + C_2^h\mathbb{T}_2 + C_3^h\mathbb{T}_3 + C_4^h\mathbb{T}_4 + C_5^h\mathbb{T}_5 = \sum_{i=1}^{5} C_i^h\mathbb{T}_i \tag{C.8}$$

where the eigenvalues C_i^h, with $i = 1 \rightarrow 5$, are characteristics of the plastic anisotropy and can vary from the elastic parameters. The superscript h makes reference to either yield surface ($h = f$) or plastic potential ($h = g$). In the following section, this projector is applied on a particular case for modeling the anisotropy of Maastricht Tuffeau.

1.2. Continuum formulation

This theory is here applied on the constitutive law introduced in Section 2.4 [*Nova et al.*, 2003] by adjusting the expressions of the yield surface and the plastic potential as follow:

$$\left.\begin{array}{l} f \\ \\ g \end{array}\right\} = A_h^{K_{1h}/C_h} \times B_h^{-K_{2h}/C_h} \times p^h - P_c^* = 0 \tag{C.9a}$$

$$K_{1h/2h} = \frac{\mu_h\left(1-\alpha_h\right)}{2\left(1-\mu_h\right)}\left(1 \pm \sqrt{1-\frac{4\alpha_h\left(1-\mu_h\right)}{\mu_h\left(1-\alpha_h\right)^2}}\right) \tag{C.9b}$$

$$A_h = 1 + \frac{\eta^h}{K_{1h}M_h} \tag{C.9c}$$

$$B_h = 1 + \frac{\eta^h}{K_{2h}M_h} \tag{C.9d}$$

$$C_h = (1-\mu_h)(K_{1h}-K_{2h}) \tag{C.9e}$$

$$\tag{C.9f}$$

Where η^h, p^h, and q^h are defined as follows:

$$p^h = \frac{1}{3}\sigma_{ij}^h\delta_{ij} \quad q^h = \sqrt{\frac{3}{2}s_{ij}^h s_{ij}^h} \quad \eta^h = \frac{q^h}{p^h+p_t} \tag{C.10}$$

in which $s_{ij}^h = \sigma_{ij}^h - p\delta_{ij}$, δ_{ij} is Kronecker delta. Under axisymmetric stress conditions, p^h and q^h can be specified as:

$$p^h = \frac{\sigma_1^h + 2\sigma_3^h}{3} \quad q^h = \sigma_1^h - \sigma_3^h \tag{C.11}$$

where σ_1^h and σ_3^h are the maximum and minimum principal stress, respectively. The subscript/superscript h in the symbols above makes reference to either yield surface ($h = f$) or plastic potential ($h = g$).

These mechanisms are still introduced through hardening rules defined for both P_s and P_m, as follows:

$$\dot{P}_s = \frac{P_s}{B_p}\dot{\epsilon}_v^p \tag{C.12}$$

$$\dot{P}_m = -\rho_m P_m(|\dot{\epsilon}_v^p| + \xi_m \dot{\epsilon}_s^p) \tag{C.13}$$

While the plastic strains are obtained by substituting the constitutive functions in the plastic flow rule, as follows:

$$\dot{\epsilon}_{ij}^p = \Lambda \mathbb{P}^g \frac{\partial g(\sigma_{ij}^g)}{\partial \sigma_{ij}^g} \tag{C.14}$$

1.3. Parametric Analysis

1.3.1. Yield Surface. To illustrate the distortion of the yield surface resulting from the application of the new operator, $\mathbb{P}^f$, a sensitivity analysis has been conducted on its tensorial components. Fig. C.3a-b illustrate the effects of applying a transformation of the stress space through $\mathbb{T}_1$ solely. Here, $C_{2\rightarrow5}^f$ were set to zero while C_1^f was altered around the isotropic value (1.0) by ±0.1. Loading perpendicular to bedding is marked by a continuous-blue line, while loading parallel to bedding is marked by a dashed-red line. The isotropic yield surface ($C_1^f = 1.0$) is displayed in gray. This convention of color/line-type holds for the entire stud, unless otherwise is not specified. This analysis indicate the first basis has an isotropic effects over the yield surface, as changing C_1^f results in yield surfaces that are independent from loading direction. It can be seen that this basis has alter the yield surface in an isotropic fashion, as the resulting yield surfaces are coincident. The effects of altering the eigenvalue, however, is remarkably different. Increasing C_1^f from 1.0 to 1.1 (Fig. C.3a) leads to a non-homothetic variation in the yield surface characterized by a marked reduction in the hydrostatic yielding, an increase in the deviatoric strength at lower confinement pressures, and a decrease in the shear strength at relatively higher confinement pressures. By contrast, reducing C_1^f (Fig. C.3b) leads to an increase in the hydrostatic yielding along with an entire increase in the deviatoric strength.

Fig. C.3c-d display a sensitivity analysis of the effects of the second tensor, $\mathbb{T}_2$, on the yield surface. The eigenvalue, C_2^f, has been altered by ±0.1 around its isotropic value (0.0). C_1^f was set to 1.0, while the other eigenvalues, $C_{3\to5}^f$, were set to zero. It can be seen that the yield surface variations are qualitatively similar to those observed with the first basis. Specifically, the resulting distortions are isotropic, while increasing C_2^f leads to a reduction in the isotropic yield stress with an increase in the deviatoric yielding stresses in the range of a relatively low confinement pressure. An increase in the hydrostatic yielding pressure occurs by reducing C_2^f. Despite these similarities, differences can be seen, especially in the degree of changes in the yielding threshold under the same magnitude of alteration in the eigenvalue. With the second basis, stronger variations are seen particularly in the range of high confining pressure. For example, increasing C_2^f leads to a decrease in the hydrostatic yielding three times as much as the decrease observed with the first basis.

The analysis conducted on the third basis, $\mathbb{T}_3$, is presented in Fig. C.3e-f. While C_1^f has been set to 1.0, C_2^f and $C_{4,5}^f$have been set to 0.0, C_3^f has been altered by ±0.1 around the isotropy value (0.0). It can be readily seen that assigning positive values of C_3^f results in yield surfaces that are larger in the bedding direction. Negative values, by contrast, result in yield surfaces that are larger in the bedding-perpendecular direction. A similar effect with almost

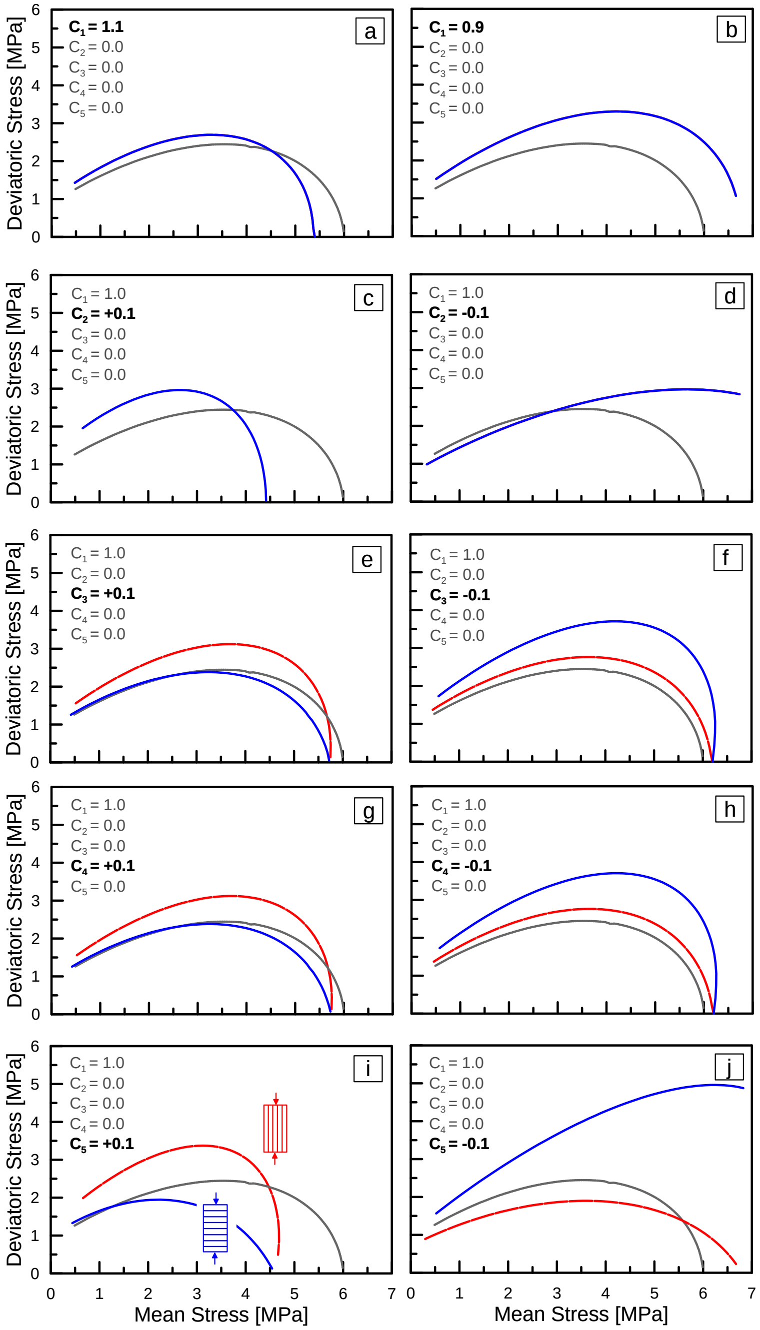

Figure C.3. Parametric analyses illustrating the transformations produced by each basis on the isotropic yield surface. (a-b) illustrate the effects of the first basis, (c-d) the second basis, (e-f) the third basis, (g-h) the fourth basis, and (i-j) the fifth basis.

the same intensity is observed with the fourth basis, $\mathbb{T}_4$, suggesting that one may use either bases to obtain the same effect on the yield surface, (Fig. C.3g-h). Finally, the sensitivity analysis conducted over the fifth basis is presented in Fig. C.3i-j, showing that the effect of this basis resembles the effects of the third and the fourth bases, i.e., positive alterations in C_5^f lead to higher strengths in bedding direction. Despite the qualitative similarities, the intensity of variations is remarkably different, in that, this basis leads to about three times stronger distortions.

This analysis suggests that a projection operator that consists of $\mathbb{T}_1$ (with $C_1^f = 1.0$) combined with another basis from the group of $\mathbb{T}_3$, $\mathbb{T}_4$ and $\mathbb{T}_5$ is adequate to reproduce the transformations required to capture the anisotropy effects on the yield surface. Here, $\mathbb{T}_1$ is combined with $\mathbb{T}_3$ to generate the operator used for the rest of this study:

$$\mathbb{P}^f = \mathbb{T}_1 + C_3^f\ \mathbb{T}_3 \tag{C.15}$$

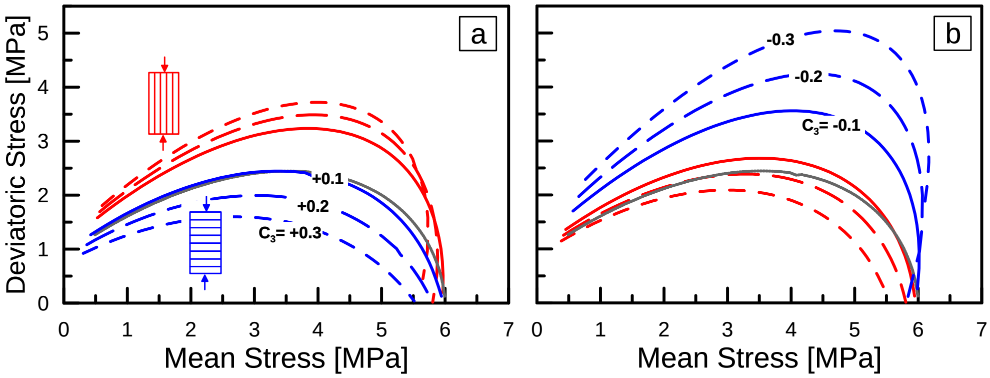

Figure C.4. Parametric analyses illustrating the transformations produced by the third basis on the isotropic yield surface, with the third eigenvalue ranging (a) from $+1 \rightarrow +3$, and (b) from $-3 \rightarrow -1$.

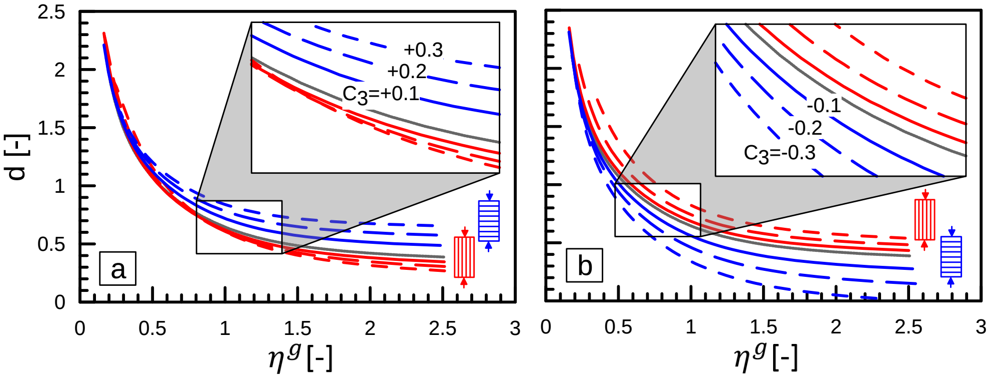

Figure C.5. Parametric analyses illustrating the dilatancy function transformations produced by the projection operator (displayed in the transformed configuration σ^f) with different values of C_3^f: (a) $+1 \rightarrow +3$, and (b) $-3 \rightarrow -1$.

It is worth mentioning that simulating the anisotropy in terms of the yielding surface has boiled down to a problem of a single free parameter (C_3^f). A more refined illustration of the performance of this projector is presented in Fig. C.4 showing the intensity of variation caused with different values of C_3^f (i.e., $-3 \rightarrow +3$). It can be noticed that switching the sign of the eigenvalue while maintaining magnitude results in remarkable differences in terms of the resulting distortions in the yield surface. For example, increasing C_3^f by $+0.1$ (Fig. C.4a) leads to small distortions if compared to those seen with $C_3^f = -0.1$ (Fig. C.4b).

1.3.2. Plastic Potential. The parameters of the plastic potential, M_g, μ_g, and α_g, can be defined on the basis of the underlying stress-dilatancy relationship, which in this model is given as follows:

$$d = \frac{\dot{\epsilon}_v^p}{\dot{\epsilon}_d^p} = \frac{\partial g/\partial p^g}{\partial g/\partial q^g} = \mu_g(M_g - \eta^g)(\frac{\alpha_g M_g}{\eta^g} + 1) \tag{C.16}$$

This function defines the ratio of volumetric and deviatoric plastic strains computed for a given imposed stress level (e.g., in correspondence of the plastic flow plateau). These ratios can be reported in the $\eta^g - d$ space. Starting from a projector based on a homotopic mapping ($\mathbb{P}^g = \mathbb{P}^f$), the variations in the dilatancy function resulting from different values of C_3^g are depicted in Fig. C.5. It can be seen that marked distortions in the dilatancy function occur, especially in the range of high η^g. Such variations result in different dilatancy angles depending on the loading direction. Similar to the yielding surface, the sign of the eigenvalue has a marked role in determining the direction of the larger/smaller dilatancy angle. For example, with a positive C_3^g, the dilatancy in bedding-perpendicular direction is larger than the dilatancy in bedding-parallel direction (Fig. C.5a), while with a negative C_3^g, the larger dilatancy angle corresponds to the bedding-parallel direction (Fig. C.5b).

2. Model Calibration and Mechanical Performance

The basic features of the constitutive framework discussed in previous sections are illustrated through a set of numerical examples. The model will be calibrated on the grounds of the macroscopic material rheology emerging from different stress probes on Maastricht Tuffeau. The capability of the model in capturing the anisotropic behavior of the material is then demonstrated through a set of numerical simulations.

The measurements presented in Section 2 provide considerable insight for a model calibration. The current procedure will benefit from the parameter calibration proposed for the same material by in Chapter 4.2.1 on the basis of an isotropy assumption. The wide range of confinement pressures covered by the triaxial tests, in both cases of bedding-parallel and bedding-perpendicular loading direction, in fact, readily allows for the determination of the yield surface in both directions. The yield threshold is depicted in the $p-q$ stress space. By adjusting the shape parameters, M_f, μ_f, and α_f, as well as the anisotropy eigenvalue C_3^f, the mathematical expression of the yield surfaces is defined, as shown in Fig. C.6a.

The parameters of the plastic potential, M_g, μ_g, and α_g, can instead be defined on the basis of the underlying stress-dilatancy relationship. These relationship can be reported in the $\eta^g - d$ space, as shown in Fig. C.6b, and are used to calibrate the shape parameters. Although this procedure relies on global measurements taken in the post-yielding regime (i.e., where the specimen exhibits a structural response with heterogeneous deformation patterns), since they are expressed in the form of a normalized strain ratio they can be regarded as representative of the material behavior inside the active zone, thus providing a first-order insight on the expected plastic flow characteristics, which will be later further assessed through full-field simulations. In fact, the displayed dilatancy functions in Fig. C.6b are based on $\mathbb{P}^g = \mathbb{P}^f$, where it can be seen that the dilatancy function in the bedding direction is in a good agreement with the experimental data. A clear mismatch, however, can be seen in the perpendicular direction (all dataset where above the plot of the yield surface, and the aim here is to bring it to the middle). As will be seen later, such mismatches will affect the robustness of the model predictions.

The hydrostatic compression behavior is used to calibrate the hardening behavior, i.e., ρ_m, B_p, and the initial values of the internal variables, P_{so} and P_{mo}. The yielding stress upon hydrostatic loading, $P_{co} = P_{so} + P_{mo}$, can be assumed to coincide with the stress at which the hydrostatic compressibility sharply increases. In fact, because of the rotations in the stress space caused by the projection operator, the point of intersection between the yield surface and the mean stress axis does not coincide with P_{co}, which had to be readjusted to capture the yielding point on the hydrostatic axis. The ratio P_{so}/P_{mo} governs the rate of destructuration occurs upon volumetric loading. This rate appears in the form of a magnified

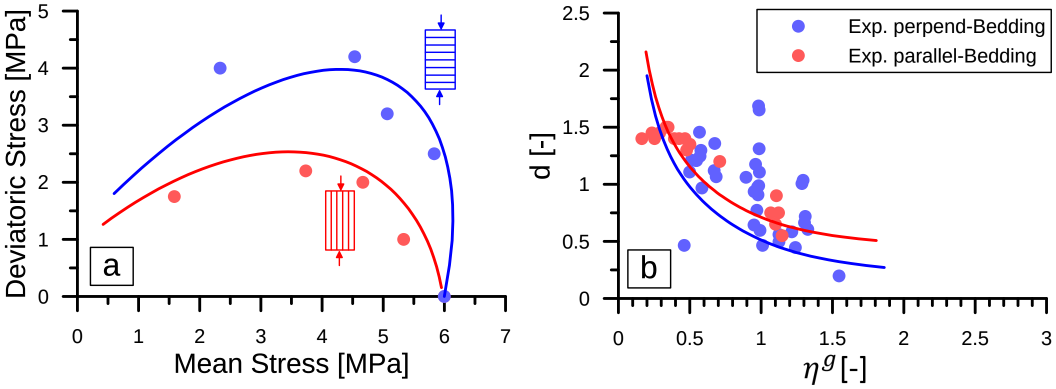

Figure C.6. Yield surface and dilatancy function calibrated for Maastricht Tuffeau with a projector based on a homotopic mapping.

plastic volumetric deformation taking place upon yielding. On the other hand, ρ_m controls the amount of softening during this stage of enhanced plastic deformation. B_p, in turn, defines the rate of plastic hardening in the post-plateau region, where inter-particle bonds have been fully destructured. As a result, this constant regulates the porosity hardening emerging upon volumetric deformation in a completely reconstituted material. The overall behavior under hydrostatic compression reproduced by the model is depicted in Fig. C.7, where it can be readily seen that the model satisfactorily reproduces the material behavior.

Fig. C.8 presents the responses reproduced by the model for triaxial compression under 1.0, 3.0, 4.0, and 5.0 MPa confining pressure reported along with the experimental counterpart. It can be seen that the model reproduces satisfactorily the yielding threshold and the post-yielding strength. Yet, it is clear that the model is unable to retain satisfactorily performance in terms of the plateau-elongation. In fact, while the limestone displays a shorter plateau in bedding-direction, the model predicts a longer plateau. For comparison, reference can be made to the case of 4.0MPa confining pressure where the test was extended to a deformation interval that allows for a clear characterization of the plateau.

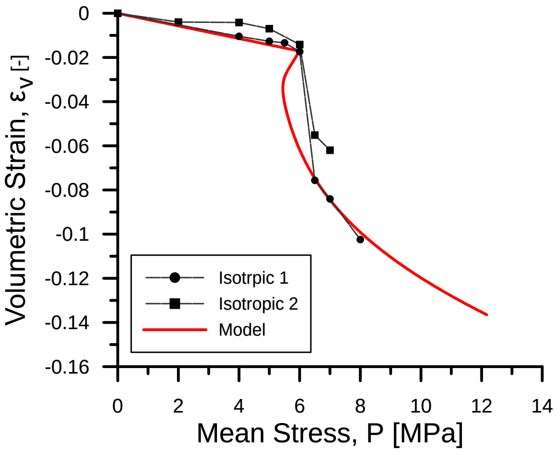

Figure C.7. Material response under isotropic loading predicted by the model. Computations are illustrated along with experimental data.

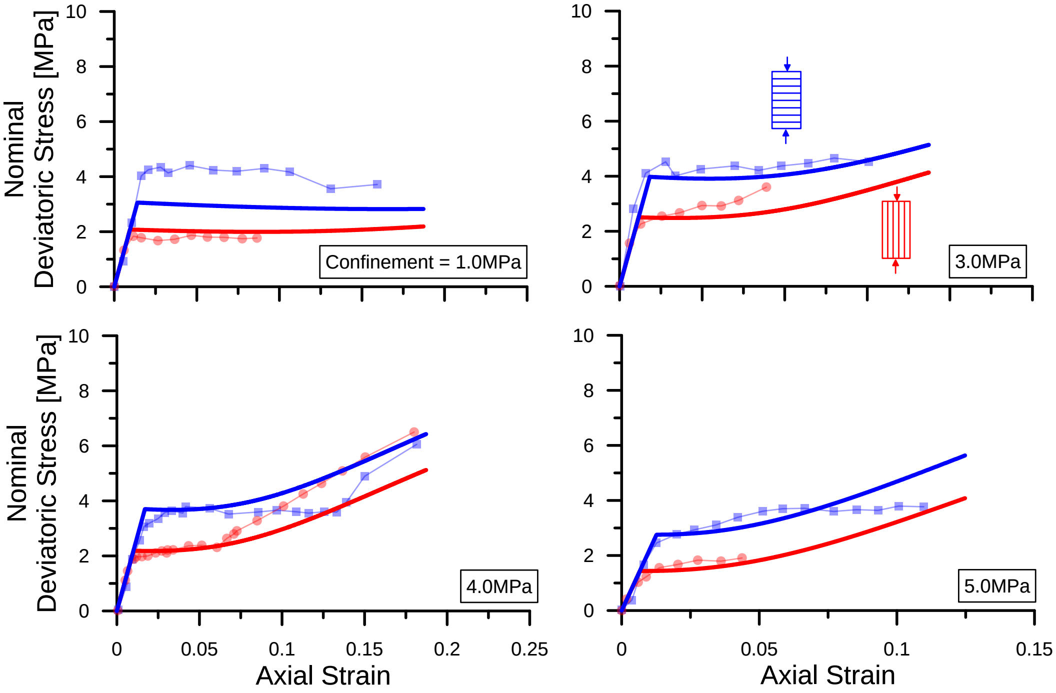

Figure C.8. Material responses predicted by the model with a projector based on a homotopic mapping, showing detectable mismatches in the elongation of the plateau.

3. Heterotopic Mapping of Stress Space

The stress mapping approach used in the previous section for the yield surface and plastic potential was characterized by the same projector (i.e., $\mathbb{P}^g = \mathbb{P}^f$). As a result, for both surfaces the mapping procedure brought the real stress state at the same location of a projected stress space (hence, "*homotopic mapping*"). By contrast, in this section the possible use of different projectors is explored (i.e., $\mathbb{P}^g \neq \mathbb{P}^f$). As a result, the mapping procedure would rely on two different projected stress spaces, thus possibly leading to different relative locations of the mapped stress state into the projected stress spaces (hence, hereafter referred to as "*heterotopic mapping*"). The same bases of $\mathbb{P}^f$, however, are used along with independent eigenvalues, C_i^g, to combine $\mathbb{P}^g$. Therefore, a projection operator based on the two bases, $\mathbb{T}_1$ and $\mathbb{T}_3$, has been adopted:

$$\mathbb{P}^g = C_1^g\ \mathbb{T}_1 + C_3^g\ \mathbb{T}_3 \tag{C.17}$$

It is worth noting that one can use any combinations of tensorial bases without making reference to the bases used for $\mathbb{P}^f$. Similar to $\mathbb{P}^f$, C_1^g has been fixed to 1.0, thus the anisotropy in the flaw rule boils down to a problem of a single parameter (C_3^g).

A parametric analysis has been conducted to explain the sensitivity of the dilatancy function to the variations of C_3^g. The outcomes are reported in Fig. C.9, where the dilatancy function is plotted versus η^g. It can be readily seen that by using a coefficient C_3^g having opposite sign compared to C_3^f, it is possible to adjust the dilatancy function for both directions (bedding-parallel and bedding-perpendicular direction) to be almost the same. Such readjustments are necessary to qualitatively match the experimental measurements of Maastricht Tuffeau. Subsequently, the following projector is proposed on the basis of a full re-calibration of the third eigenvalue C_3^g:

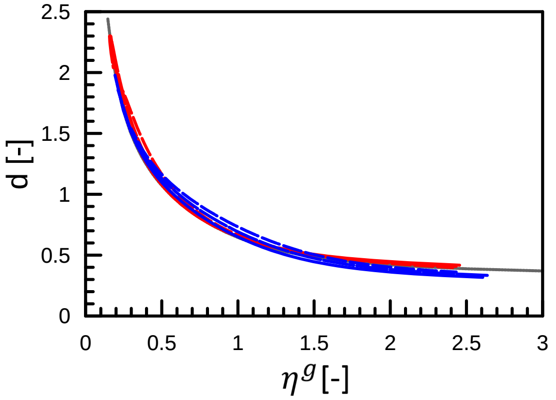

Figure C.9. Parametric analyses illustrating the transformations produced by the modified third basis on the dilatancy function, plotted in the transformed configuration (σ^g). The analysis was conducted with $C_1^g = 1.0$, $C_2^g = 0.0$, and $C_3^g =$ -1/-2/-3 $\times\, C_3^f$.

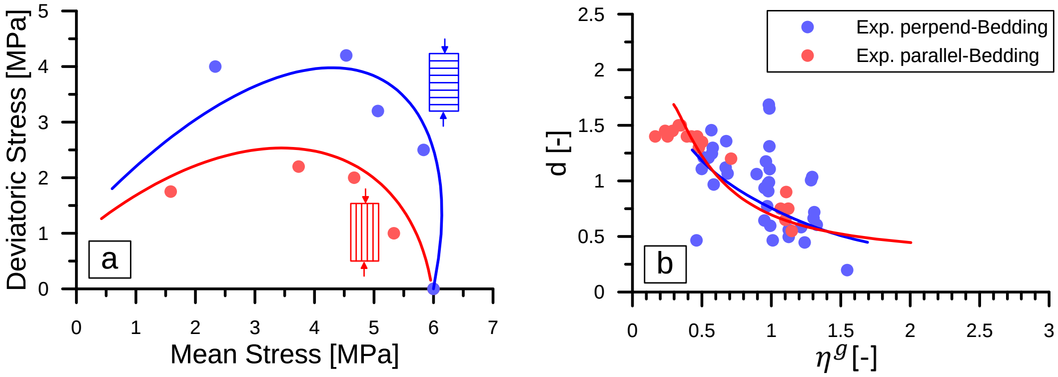

Figure C.10. Yield surface and dilatancy function calibrated for Maastricht Tuffeau with a projector based on a heterotopic mapping.

$$\mathbb{P}^g = \mathbb{T}_1 + (\mathbf{-1.5})\, C_3^f\, \mathbb{T}_3 \tag{C.18}$$

Fig. C.10 depicts the obtained dilatancy function plotted versus the projected stress ratio η^g computed based on the alternative stress configuration $\boldsymbol{\sigma}^g = \mathbb{P}^g\boldsymbol{\sigma}$. The third eigenvalue

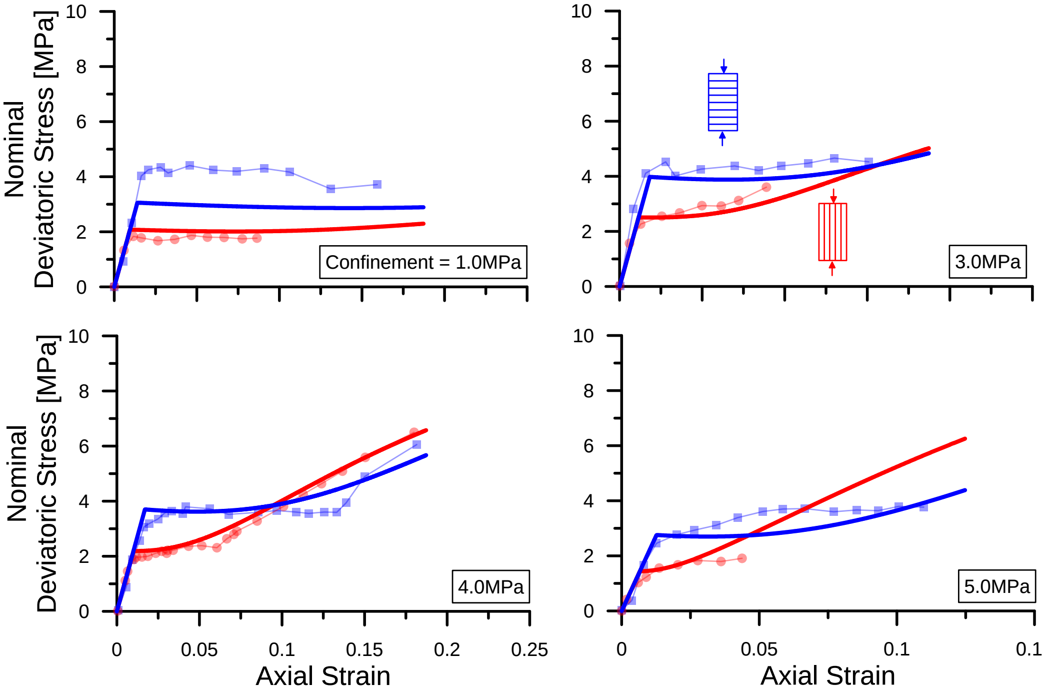

Figure C.11. Material responses predicted by the model with a projector based on a heterotopic mapping, showing adequate performance of the model in terms of the elongation of the plateau.

has been adjusted to match the dilatancy curve associated with the case of compression perpendicular to bedding. Despite the identical location of the two emerging plastic flow rules, the differences in mapping and yielding imply that the simulations at the same confinement will operate at very different points of the stress-dilatancy curve, thus resulting in different plastic behavior (and different plateau lengths). The stress-strain responses predicted based on the adjusted dilatancy function is illustrated in Fig. C.11. In this figure, it can be seen that the model has a better performance in the post-yielding regime, especially in terms of plateau elongation. In agreement with the experiments, the plateau elongation in bedding-perpendicular direction is longer than the plateau in bedding direction. In can also be seen that the model reproduces rates of post-plateau rehardening comparable with

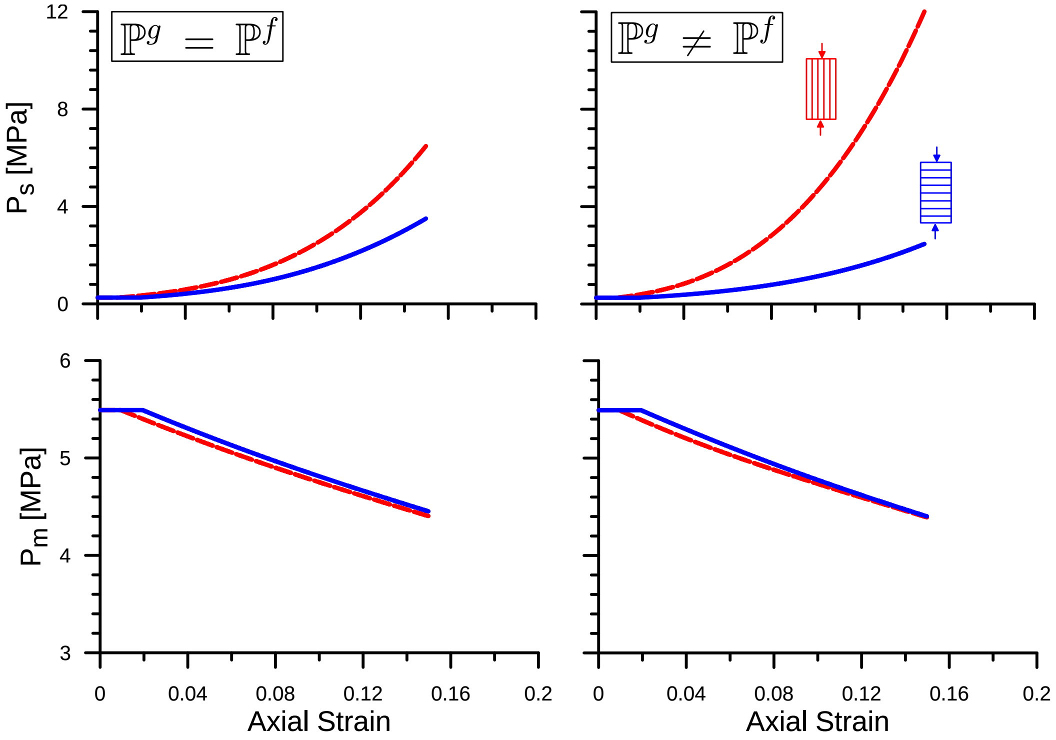

Figure C.12. Illustration of the hardening variables, P_s and P_m, evolution predicted with a projector based on homotopic mapping (left) and a projector based on a heterotopic mapping (right) showing marked differences in terms of the rate of hardening growth.

those measured in the experiments for each bedding orientation strength in both directions in consistency with the experimental observations. The model parameters and its anisotropy constants are summarized in Table C.1 and Table C.2.

Fig. C.12 illustrates the evolution of the state variables, P_s and P_m, under triaxial compression in both directions computed based on a homotopic and a heterotopic mapping. The responses are reported as a function of the imposed deformation. It can be noticed that the simulations based on heterotopic mapping involves higher rates of hardening in the bedding-parallel direction, versus a lower rate of hardening in the bedding-perpendicular

Table C.1. Constitutive parameters and internal variables for Maastricht Tuffeau.

	Definition	
K [MPa]	Bulk modulus	350
G [MPa]	Shear modulus	78
ρ_m	Parameter governing softening under volumetric deformation	0.2
ξ_m	Parameter governing softening under deviatoric deformation	5.0
B_p	Isotropic plastic compressibility	0.03
μ_f	Shape parameter of the yield surface	0.9
α_f	Shape parameter of the yield surface	2.0
M_f	Shape parameter of the yield surface	0.65
μ_g	Shape parameter of the plastic potential	0.6
α_g	Shape parameter of the plastic potential	0.14
M_g	Shape parameter of the plastic potential	1.60
κ	Expansion of the yield surface in the tensile stress domain	0.15
P_{so} [MPa]	Initial size of the elastic domain (cohesionless medium)	.25
P_{mo} [MPa]	Lithification-induced expansion of the initial elastic domain	5.5

Table C.2. Anisotropy parameters for Maastricht Tuffeau.

	C_1^f	C_2^f	C_3^f	C_4^f	C_5^f
Yield Surface	1.0	0.0	-0.2	0.0	0.0
	C_1^g	C_2^g	C_3^g	C_4^g	C_5^g
Plastic Potential	1.0	0.0	-1.5 × -0.2	0.0	0.0

direction. No differences in the softening behavior is observed in both cases. This differences in the rate of hardening explains the differences in the elongation of the plateau observed in the simulation based on various mapping methods.

4. Conclusions

A theory for the constitutive modeling of transversely anisotropic elastoplastic materials was presented in this chapter. The framework addressed the signatures of the anisotropy on both the yielding stresses and the deformation behavior. For this purpose, elastic anisotropy was incorporated in the model and its bases were used to construct a tensorial projectors to replicate the anisotropic plasticity. The proposed model appeared to fairly capture the overall anisotropic strength peaks. In this work, however, it was shown that it is necessary to use distinct tensorial projectors, which despite sharing the same elastic bases, involve markedly distinct eigenvalues. This is in order to enhance the model performance on replicating the post-yielding behavior, specifically the dependence of plateau-elongation on bedding direction. The tensorial projector used in this work involved five tensorial bases and eigenvalues. The Sensitivity analyses showed that it was possible to replicate most of the mechanical aspects of Maastricht Tuffeau and under various confining pressures by incorporating a projector constructed with only two tensorial bases. Material-point analyses based on triaxial test simulation were conducted under confining pressures of 1.0-, 2.0-, 4.0-, 5.0-MPa, and subjected to bedding-parallel and bedding-perpendicular compression. The analyses illustrated the satisfactory performance of the proposed model in replicating the yielding conditions, the post-yielding deformation and the post-plateau hardening behavior. Further work, however, is required to examine the model in light of the localization theory and calibrate its performance to reproduce the pressure dependence of the band inclination, as well as the full-field response of specimens of anisotropic Maastricht Tuffeau.

APPENDIX D

Assessment of Statistical Homogeneity in Granular Media*

One of the challenges of examining the spatial fluctuation of material properties in granular media is the inference of macroscopic quantities from microscopic observables. For this purpose, the concept of REV is typically employed, leading to the determination of a sample-volume that guarantees regularity and reproducibility (i.e., over which the considered material property can be homogenized). This procedure is conducted by means of statistical approaches, according to which the specimen is assumed to derive from an underlying random process (*Howard and Reed* [2004]; *Matheron* [1989]). A crucial element of defining an REV is that the random process fulfills the conditions of *stationarity* and *ergodicity* (*Cruz-Orive* [1997]). Stationarity implies that the statistics of the considered property (i.e. mean and standard deviation) is invariant over the specimen domain, while ergodicity is defined by the following expression (*Matheron* [1989]):

$$A = \lim_{|v| \to \infty} |v| var\{z(v)\} \tag{D.1}$$

in which $|v|$ is the size of the sample, $z(v)$ is the property of interest computed over the sample volume, $var\{z(v)\}$ is the variance of all samples at each specific size $|v|$, and A is a material constant associated with the length scale of fluctuation. Since homogeneous specimens exhibit a finite scale of fluctuation, Eq. D.1 requires that an increase of sample

---

*The content of this chapter was published in:

- Shahin, G., Cil, M., and Buscarnera, G. (2018). Assessment of statistical homogeneity in chemically treated granular materials. Gotechnique Letters, 8(1), 32-39.

volume induces a reduction of the variance as fast as the rate of the increase of sample size. In this regard, *Lantuéjoul* [1991] argued that the trends of variance evolution can be used to inspect homogeneity. In particular, the decay of the variance in samples of different size can be expressed as a function of the volume through the following relation:

$$var\{z(v)\} = \frac{A}{|v|^b} = \frac{a^b.P(1-P)}{|v|^b} \tag{D.2}$$

in which P indicates the property of interest averaged over the whole specimen, while a and b characterize the underlying random process, and are often referred to as stereological parameters (SPs). Parameter a primarily quantifies the scale of microscopic fluctuation, while b controls the rapidity of variance reduction as a function of the sample volume. According to *Lantuéjoul* [1991], homogeneous media exhibit an asymptotic decay of the variance characterized by $b \geq 1$. Instead, heterogeneous media display a lower rate of variance decay with $0 < b < 1$. For these reasons, hereafter parameter b will be used as a metric of homogeneity (*Bruchon et al.* [2013b]; *Kanit et al.* [2003]), with the goal to examine the microstructural properties of a granular soil subjected to mineral precipitation.

1. Materials and Experiments

To quantify the spatio-temporal progression of precipitation, the microstructure of a granular material subjected to a flow-through precipitation experiment was imaged in situ via synchrotron X-ray microtomography (SMT). F-50 Ottawa sand (*Company* [1997]) was used in the experiments. Particles of size smaller than 290 μm were removed via sieving to facilitate visualization. The remaining particles were rinsed with deionized water and dried in an oven for 24 h at 110°. The tested sand has a specific gravity $G_s = 2.65$ and a permeability of 51 μm^2 (*Cil et al.* [2017]). It is a fairly uniform sand with a median size $D_{50} = 375\ \mu m$,

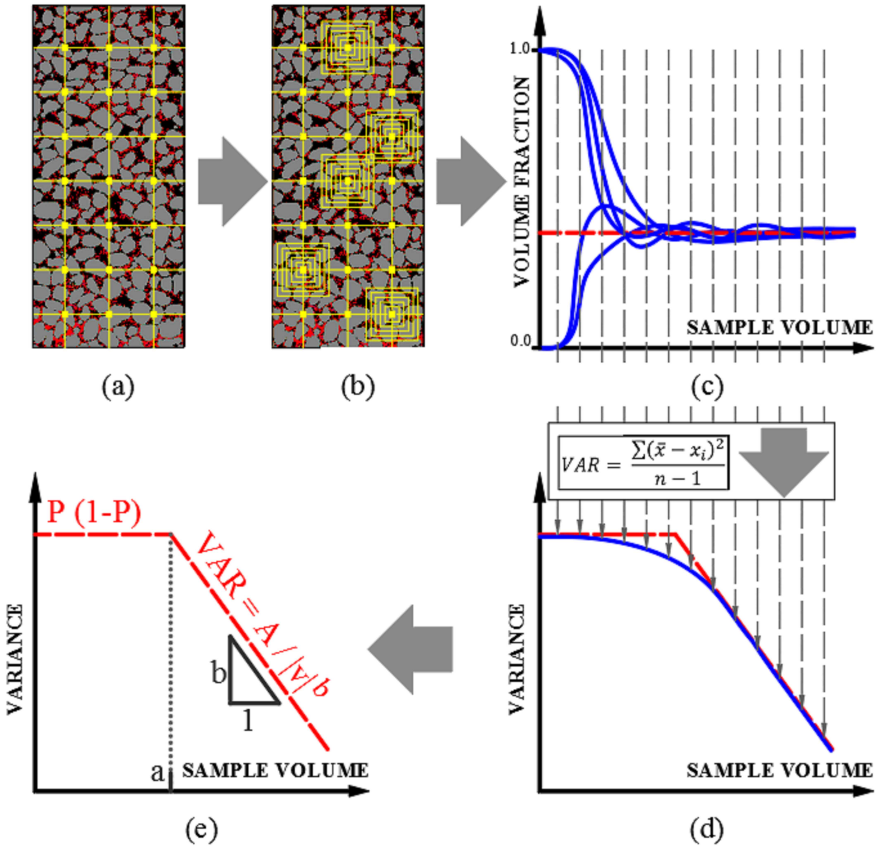

Figure D.1. Illustration of the approach used to define the stereological parameters, a and b. (a) Definition of the grid. (b) Sampling and gradually growth of the measurement cell, over which the property of interest is computed. (c) Matheron's granulometries: the computed property is plotted against the cell volume. (d) Variogram: the variance of the granulometries are plotted against the cell volume in logarithmic scale, (e) Fitting of Equation D.2 to define the stereological parameters that match the asymptotic trends of the variogram.

and a coefficient of uniformity $C_u = 1.3$, and a coefficient of curvature $C_c = 1.0$. The sand was packed within a cylindrical aluminum container through a wet pluviation method, which involved pouring the sand into the tubing filled with 1 mM $CaCl_2$ solution and densifying the assembly through tamping. The cylindrical specimen had a diameter of 4.2 mm and a height of 10.94 mm. 40 mM $CaCl_2$ and 80 mM $NaHCO_3$ solutions were injected into the specimen at a constant flow rate of 8.6×10^{-3} $l.h^{-1}$ via a Gilson Minipuls 2 peristaltic pump.

The two reactants were mixed in a chamber located upstream of the column (Figure 2.17a). The mixing of $CaCl_2$ and $NaHCO_3$ resulted in a supersaturated solution with respect to $CaCO_3$, which produced $CaCO_3$ precipitation within the pore space of the packed assembly (*Cil et al.* [2017]).

SMT scans were carried out in the Beamline $13 - BMD$ of the GeoSoilEnvironCARS at the Advanced Photon Source, Argonne National Laboratory in Lemont, IL, USA. The X-ray energy was set to 33 keV and 900 radiographs were acquired at 0.2° angular increments during each SMT scan. The pixel size of the SMT images is 3.18 μm. The specimen was scanned multiple times during the precipitation experiment (Figure 2.17c) and was flushed with 1mM $CaCl_2$ solution for 10 min before each scan to remove suspended precipitates. The specimen was subjected to 9048 pore volumes of influent solution until clogging of the inlet.

The SMT images were analyzed using Avizo (*FEI* [2016]). The sequential SMT images were initially registered and an anisotropic diffusion filter was applied to each image to reduce noise. Sand particles, $CaCO_3$ precipitates and pores were identified and labelled (i.e., trinarized) on the basis of the changes in registered images and the X-ray attenuation difference of the three phases. The evolution of the specimen during mineral precipitation is displayed in Figure 2.17, which illustrates the microscopic changes due to the accumulation of mineral deposits within the pores.

2. Analysis based on the Theory of Geostatistics

To examine the homogeneity of the specimen from a statistical standpoint, some assumptions have to be made. Specifically, each scan has been considered separately from the others as a realization of a distinct random process. With this assumption, the analysis is converted into the inspection of six individual random processes. The hypothetical temporal dimension of each of these processes carries a purely statistical meaning (i.e., it does not bear a physical relation with the underlying reaction-transport process), and it is therefore assumed stationary (*Chiles and Delfiner* [2009]). The inspection of homogeneity is, therefore, performed only over space.

The spatial homogeneity of each specimen can be assessed by quantifying the SPs (i.e., a and b). This procedure entails the computation of granulometries and their corresponding variogram. In soil mechanics, the primary interest is the solid matrix (in this case the combination of particles and precipitates). However, it is possible to show that the geometric duality of solids and pores implies the equivalence of their statistical attributes, thus generating identical variograms for solid and pore phases (see Appendix A). For this reason, hereafter the computations are primarily referred to the pore space, in that they are sufficient to assess the statistical homogeneity of the solid matrix.

2.1. Granulometries and variograms

To compute the Matheron's granulometry, a cubical cell is used as structuring element. A regular 3D grid is placed on the image (Figure D.1a), and samples are collected at each node through a cell centered on the selected location and gradually increasing in size.

The property of interest (e.g., the volume fraction of pores) is calculated for each sample size. This procedure is repeated for all the nodes of the grid (Figure D.1b-c), enabling the generation of variograms (i.e., plots of the variance associated with each sample size, (Figure D.1d). The stereological parameters are finally defined by fitting Equation D.2 to the asymptote of the variogram (Figure D.1e). Figure D.2 illustrates the outcome of this procedure at different stages of the precipitation process (i.e., until pore clogging).

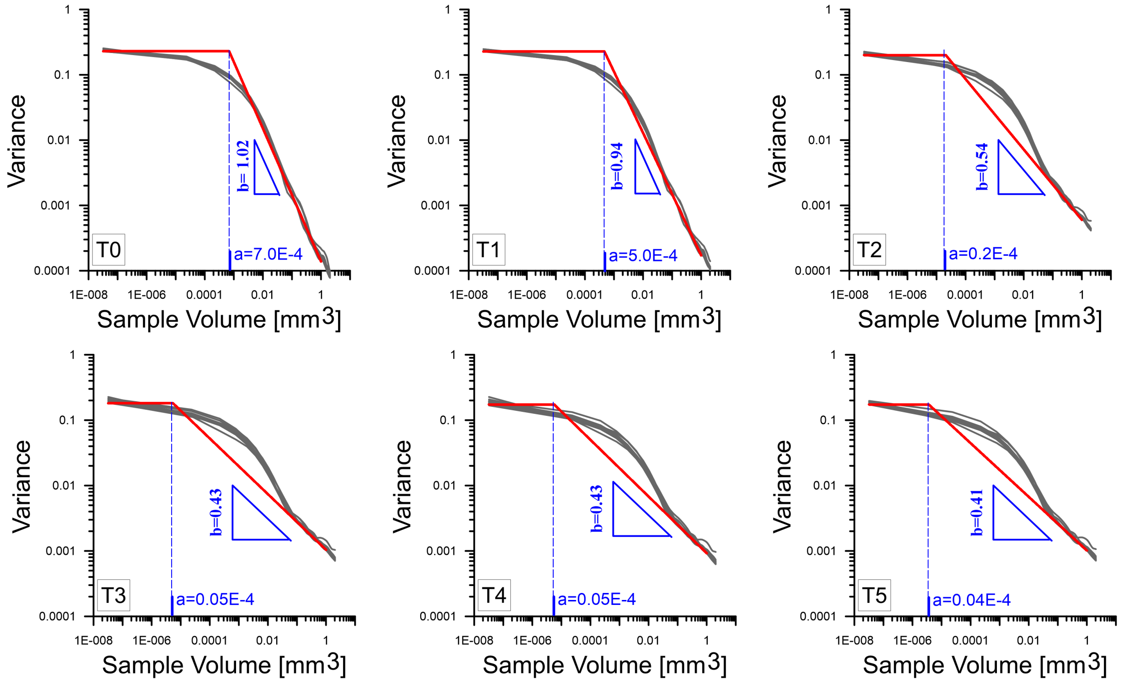

Figure D.2. Variograms of the pore phase computed for different sample-population sizes at each precipitation stage $T0-T5$. Computations performed through grids having a number of nodes varying from 28 to 11250. For each precipitation stage, the generated variograms are reported, along with the SPs (calibrated variogram plotted in red).

2.2. Evolution of the stereological parameters

Obtaining an unbiased estimate of the SPs requires an adequate sample population. Hence, a sensitivity analysis on the population size has been performed. Different grids with a number of nodes ranging from 28 to 11250 have been used to generate the granulometries. The corresponding variograms of the pore phase have been processed and the associated SPs have been determined through the asymptote fitting procedure described in the previous section. While such fitting procedure has been carried out manually, a qualitative assessment of its accuracy has been provided by computing the average error involved with it. The results

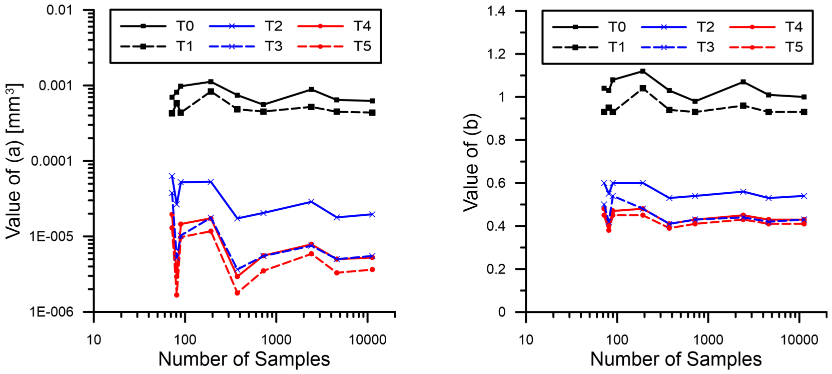

Figure D.3. Sensitivity of the SPs (a and b) to the sample-population size (i.e. the number of grid nodes). The SPs display stable trend for larger population size. The averaged value of the last 5 trials is adopted to derive an unbiased estimate of the SPs.

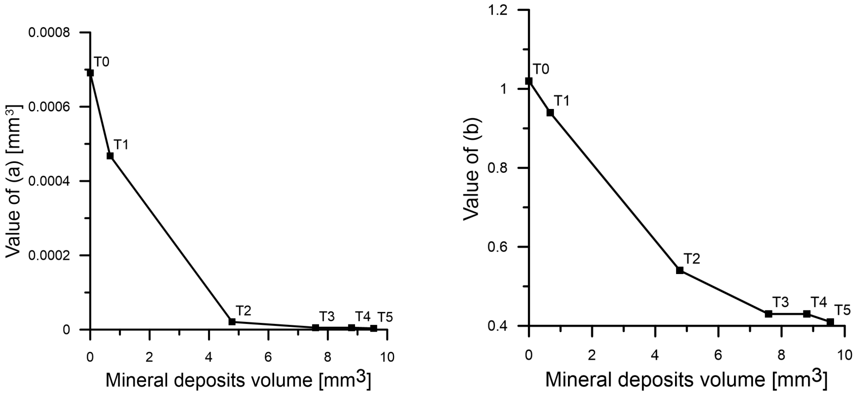

Figure D.4. Evolution of the SPs (a and b) of the pore phase during precipitation. The analysis shows that the unprecipitated matrix is homogeneous as ($b = 1.02$), while precipitation causes a sharp deterioration of homogeneity since the early stages of the process ($b < 1$).

are discussed in Appendix B, where, for a sufficient number of sample points, the error was always below 5%.

The variation of the SPs as a function of the population size is depicted in Figure D.3, which shows a remarkable fluctuation of both parameters at smaller population sizes. As the size of the population increases, the trends of variation of a and b become more stable, thus indicating a decrease of the underlying bias. Thus, the average of the last five trials has

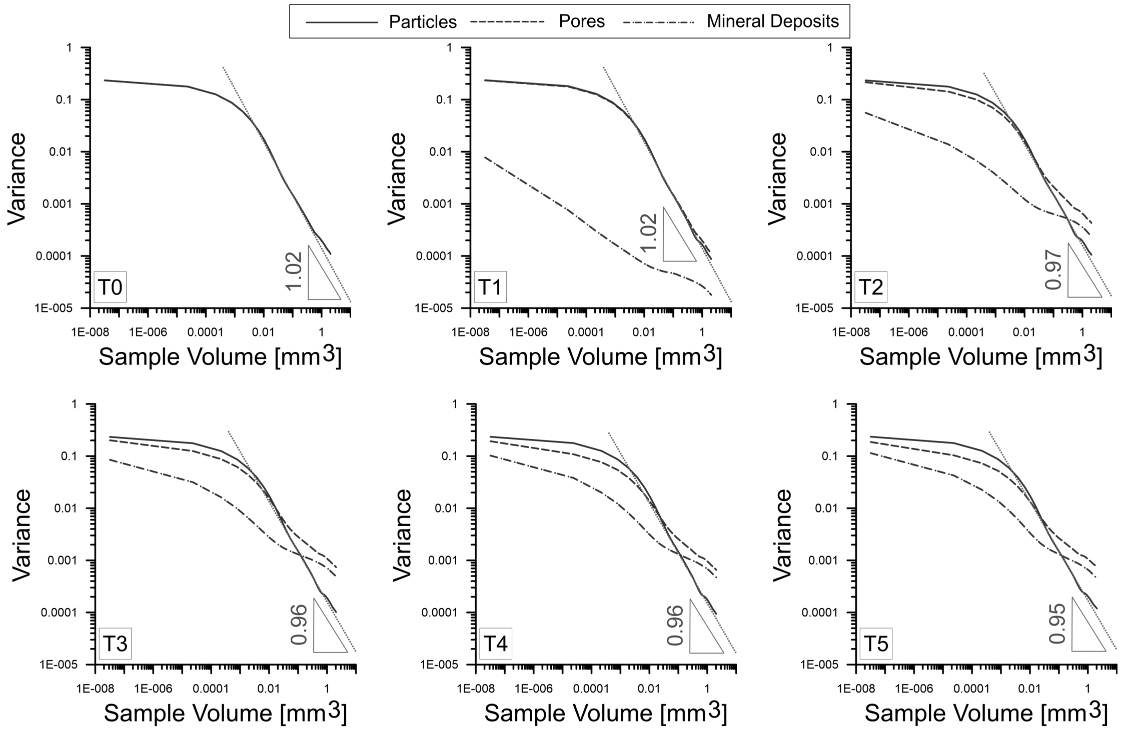

Figure D.5. Varigrams of the three phases, grains (continuous), pores (dashed), and mineral deposits (dash-dotted) for the various stages of the precipitation process. The value of b of the grains has is not affected by precipitation, while the other phases display deterioration of their homogeneity reflected by a slower rate of variance decay.

been used to quantify the SPs. These values are plotted against the mass of precipitation in Figure D.4 to illustrate the statistical implications of the reactive process.

This analysis shows that b is equal to 1.02 only at the initial state $T0$, thus indicating homogeneity of the unprecipitated skeleton. Precipitation, however, is found to induce a rapid deterioration of homogeneity, manifested by the sharp decline of b. The intensity of deterioration decreases after stage $T3$, when nearly constant values of b are attained. Similar trends can be observed also for parameter a, which controls the length scale of microstructural fluctuations (i.e., it also decays with increasing the mass of mineral deposits). Although these results refer to the pore phase, similar arguments can be derived from the other microstructural units. An example is illustrated in Figure D.5, where the variograms of granular skeleton, pore phase and mineral deposits are shown. It is readily apparent that, while the statistical features of the skeleton are unaltered by the precipitation process (i.e., $b \approx 1$ also after treatment), all the other units display heterogeneous properties.

Such results indicate that mineral deposits bridging the grains increase the heterogeneity up to a point that an REV cannot be rigorously defined. An examination of the relative error associated with the sampling procedure is illustrated in Figure D.6a, where the coefficient of variation (C_V) defined as the normalized standard deviation ($C_V = \sigma/m$) of the pore volume fraction is plotted for each stage of precipitation. The figure shows that much larger sample volumes would be necessary to reach a sufficiently low degree of statistical variability. In other words, if σ/m is limited to 10%, the presence of mineral deposits causes a rapid growth in sample size necessary to guarantee such requirement on the relative error (Figure D.6b).

2.3. Spatial analysis

The degradation of sample homogeneity reflects an uneven distribution of precipitation products. To ascertain this feature, the spatial variability of the precipitated mass has been inspected by plotting over the specimen the degree of clogging (i.e., the volume ratio between mineral deposits and inter-granular pores). For this purpose, the skeleton of sand particles is taken as reference frame. This choice was made because the skeleton is not altered by precipitation and is homogeneous throughout the process. Indeed, from the analysis of specimen $T0$, an REV of ($300 \times 300 \times 300$ voxels) can be defined (which involves a mean $m = 0.36$ and a standard deviation $\sigma = \sqrt{(A/|v|^b)} = 0.013$). This reference volume is used to inspect the spatial variability of the degree of pore clogging. Specifically, an observation cell with

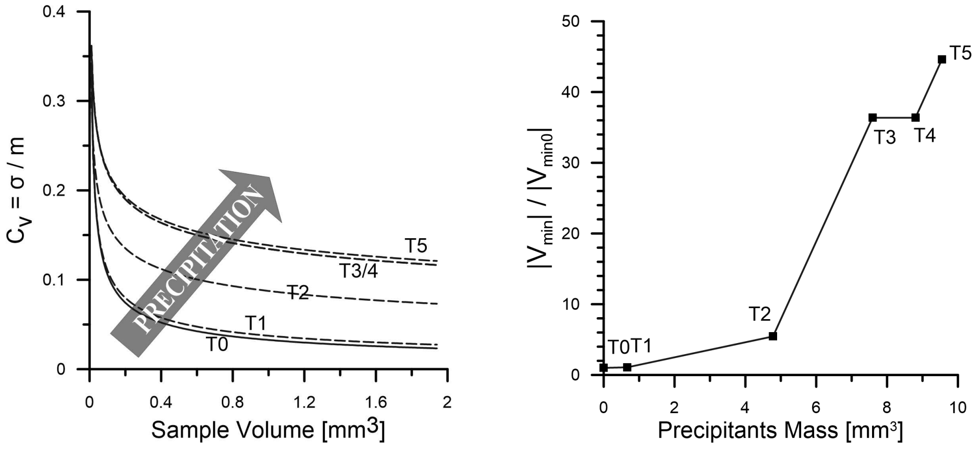

(a) (b)

Figure D.6. Volume-dependence of the normalized standard deviation of specimens with different amounts of mineral deposits. Trends predicted from Eq. D.2 calibrated on the basis of the variograms in Figure D.4. (a) Evolution of the relative error for various precipiation stages. (b) Sample volume associated with a 10% relative error (C_V). $|Vmin|$ indicates the minimum sample volume guaranteeing $\sigma/m \leq 10\%$, while $|V_{min0}|$ is the same volume computed for the initial (unprecipitated) skeleton.

the size of the selected REV is used to scan the sample along a vertical and a horizontal axis located at the center of the specimen (Figure D.7).

The analysis conducted along the vertical axis shows that the precipitant mass grows with similar patterns in the upper two-thirds of the specimen, while it shows significant deviations in the lower-third immediately after scan $T1$. This result reflects an increase of the local degree of clogging in proximity of the inlet (Figure D.7a). Similarly, the same analysis conducted along the transversal direction reveals asymmetric mass deposition at the center of the specimen (Figure D.7b-c), which can be interpreted as a result of uneven clogging at the inlet and a consequent non-uniform mineral growth downstream. These results suggest that boundary effects at the inlet and asymmetries developing along the specimen height are the main causes of the deterioration of the homogeneity.

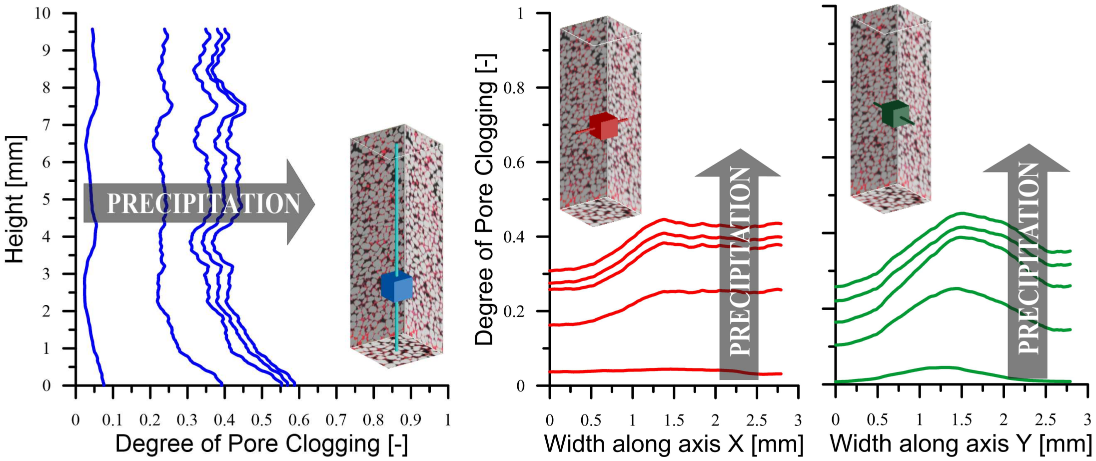

(a) (b) (c)

Figure D.7. Evolution of the degree of pore clogging along (a) a vertical axis located at the center, and (b-c) two horizontal axes located at the mid-height. The analysis reveals a steady evolution of precipitation over the upper two-thirds of the specimen, whereas faster mineral accumulation occurs at the lower third. Similarly, the inspection of the variation of pore clogging across a horizontal section located at the mid-height displays non-uniform precipitation.

3. Conclusions

A quantitative assessment of the homogeneity of a chemically altered granular soil has been conducted by means of a statistical analysis. The precipitation process is shown to cause a rapid deterioration of the homogeneity in an otherwise uniform sand. The quantitative metrics defining the length scale of fluctuation and the deviation from homogeneity have revealed that the accumulation of mineral deposits and the consequent clogging of the pores are responsible for this effect. By making reference to the REV size defined for the unprecipitated granular skeleton, it was shown that such loss of homogeneity was controlled by higher precipitation at the inlet and by a non-symmetric mineral growth along the transverse direction. This finding illustrates the benefits of a statistical assessment of the spatial heterogeneity of a sample. While it was shown that an REV cannot be rigorously defined even at the early stages of the precipitation process, the analysis pointed out that the length scale of fluctuation depends on the amount of precipitation and tends to decrease as the precipitation clog the pores. Similarly, it was shown that the accumulation of precipitation reduces the rate at which the standard deviation decreases upon an increase of sample size. Such observations suggest that, compared to unstructured granular materials, cemented and/or chemically-treated soils need stricter requirements to define the minimum size of the samples for laboratory testing.

APPENDIX E

Patterns of Compaction Band Propagation

The simulations presented in previous chapters displayed different forms of heterogeneous compaction, namely compaction front propagation in Maastricht Tuffeau and tabular compaction in Bleurswiller sandstone. The mechanical properties of these rocks are characterized by strain-softening in the former versus strain-hardening in the latter. This Appendix illustrates some aspects concerning the connection between the propagation patterns and the material constitutive properties, thus illustrating the resulting differences in the local responses and the overall mechanical field.

1. Stress Evolution in Hardening and Softening Materials

To illustrate the connection between the phenomenology of compaction banding and the pattern of bands propagation, the possible scenarios of stress path evolution upon activating inelastic compaction in predominantly hardening and predominantly softening materials is here discussed at the material-point level. First, the kinematic and static constraints associated with pure compaction banding are recalled. Equilibrium is enforced over the stress perpendicular to the band interface. incremental stress components contained within the plane of the band are not subjected to such constraints and a jump in their value may take place. Kinematically, the perpendicular strain includes a jump, while strain compatibility is enforced along the band (Fig. 2.18).

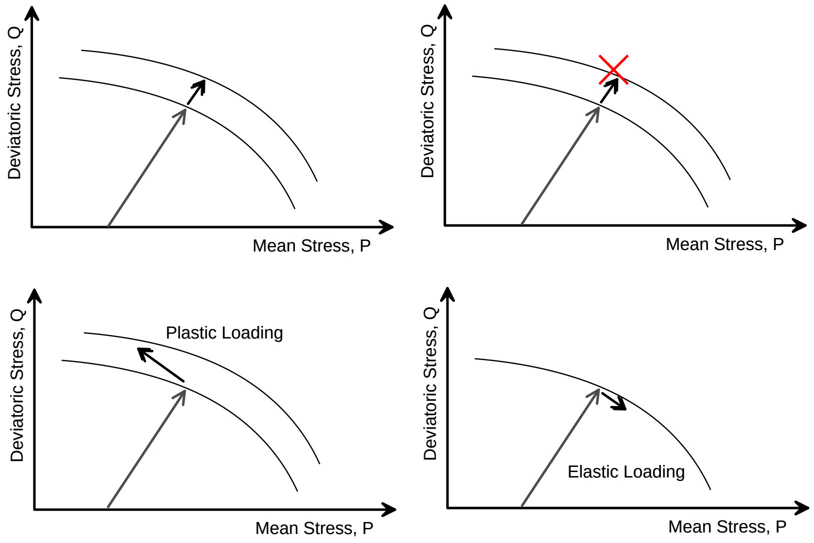

Figure E.1. Schematic illustration of the possible scenarios of stress evolution in a hardening material

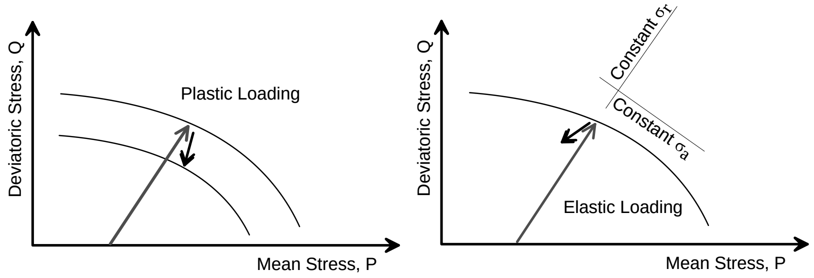

Figure E.2. Schematic illustration of the possible scenarios of stress evolution in a softening material

A triaxial compression path intersecting with the yield surface in a hardening regime with bifurcation involves an expansion of the yield surface. This expansion could occur following a constant-radial stress path (Fig. E.1a). In such scenario, however, equilibrium conditions at the band boundaries dictate that the stress path outside the band follows that same path and subsequently elastic unloading (as a result of bifurcation) is not possible (Fig. E.1b). However, other possible scenarios in which the axial stress equilibrium is maintained can be identified. Specifically, inside the band, the stress path could deviate from constant radial-stress and evolve with the same increments of axial stress (Fig. E.1c). In such case, the inelastic loading inside the band dictates a growth in the yield surface, while outside the band (Fig. E.1d) the stress path evolves in the opposite direction inside the elastic domain with the same incremental changes of the axial stress (unloading). It is worth mentioning that such scenario implies that the radial stress inside and outside the band evolves in opposite directions.

On the other hand, a triaxial compression path intersecting with the yield surface in a softening regime with bifurcation implies the contraction of the yield surface. The stress path could evolve inwards the yield surface with axial stress increments that maintain equilibrium (Fig. E.2). In such case, the radial stresses inside and outside the band evolve in any directions that maintain global equilibrium with the external lateral traction.

2. Stress Field of Different Propagation Patterns

Numerical analyses based on finite element simulations of triaxial compression are conducted. The model used in the thesis is retained for this purpose. Fig. E.4 displays the results of simulations performed for both rocks. By making reference to the sandstone simulation (upper part), it can be seen that the specimen exhibits compaction localization in a form of discrete bands which spread sequentially across the domain. At variance, the simulation of Maastricht Tuffeau (lower) displays compaction localization emerging in the middle of the specimen (at $L2$) and eventually spreading towards the ends of the specimen in a form of thickening band. In connection with different forms of bands propagation, marked differences in mechanical responses are observed, especially in terms of the deformation behavior that follows yielding. While softening is a marked feature of the post-yielding response in the Maastricht Tuffeau model, Bleurswiller sandstone displays stages of strain hardening in association with the nucleation of discrete bands, especially in the domain of compaction localization (Fig. E.3).

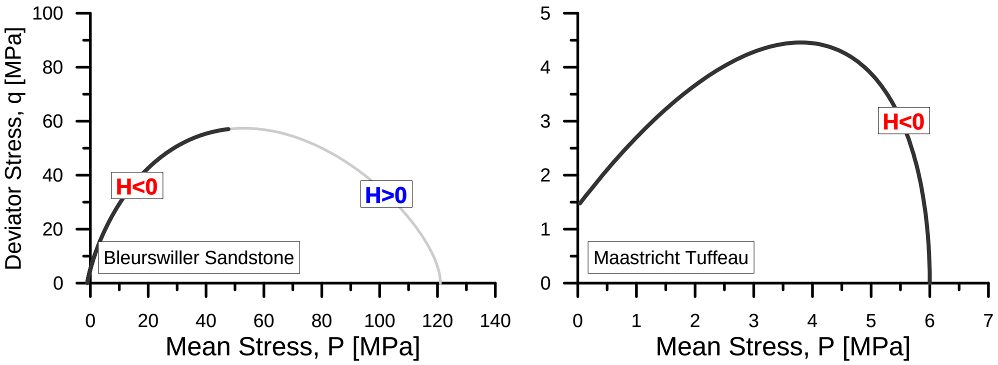

Figure E.3. Illustration of the hardening ($H > 0$) and softening domains ($H < 0$) on the yield surface of Bleurswiller sandstone (left) and Maastricht Tuffeau (right)

The local responses that accompany the different propagation patterns have been explored. The case of thickening band in Maastricht Tuffeau has been considered first. The computations at Gauss points located inside and outside the compacted zones are reported in Fig. E.5. It can be seen that the growth of compaction localization is accompanied by material softening, thus leading to a contraction of the yield surface along with a contraction in the extent of the domain of instability. The stress path includes a decay in the axial stress with minor alterations in the radial stresses. Away from the active localization zone, the material undergoes elastic unloading with a stress path characterized by a decrease in the axial stress along with unaltered radial stresses. It can be noticed that despite the discontinuities in the radial stresses, the equilibrium in the axial stresses has shaped the direction according to which the stress paths inside and outside the zone of active compaction evolve.

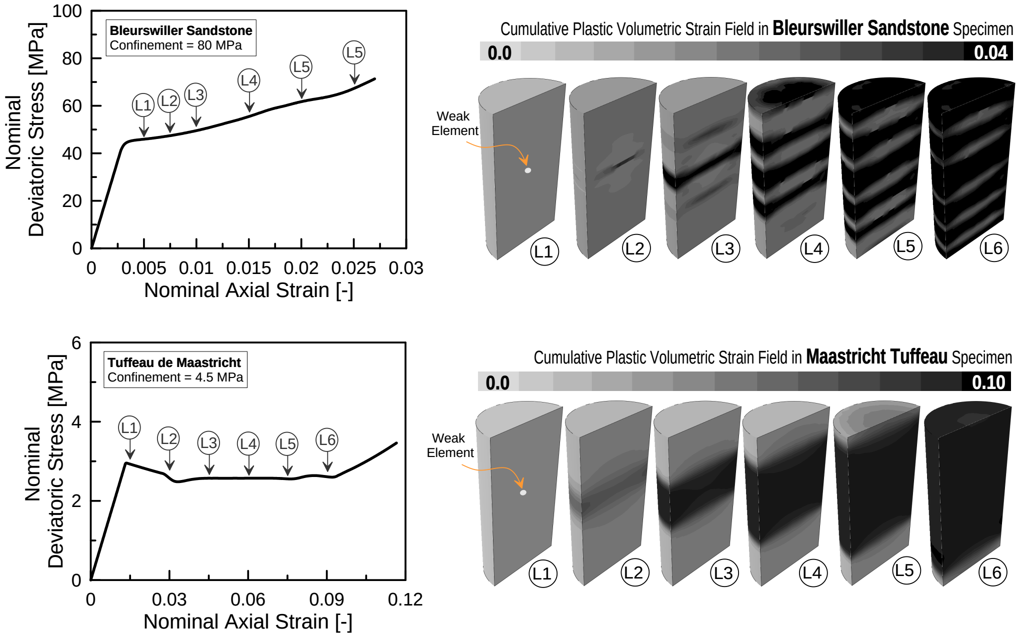

Figure E.4. Triaxial compression test conducted on specimens of Bleurswiller sandstone (upper) and Maastricht Tuffeau (lower), illustrating the overall mechanical responses and the evolution of the strain field at specific deformation intervals marked on the stress-strain response curve.

To examine the local responses associated with the sequential spread of discrete bands, Fig. E.6 displays the evolving responses at sequential deformation intervals, first, after the growth of the first band ($a1 \rightarrow d1$) and, second, after the growth of the second set of compaction bands ($a2 \rightarrow d2$). Material points inside the first band ($d1\&2$), the second band ($b1\&2$), in between ($c1\&2$) and away from the two bands ($a1\&2$) were selected. This illustration reveals specific features of local material responses. First, as the specimen undergoes yielding, the entire domain displays inelastic homogeneous deformation associated with an expansion of the yield surface, up to a point where heterogeneous deformation takes place.

The emergence of the first band carries specific distribution of local responses characterized by stress paths inside the active zone that are typical of axisymmetric deformation

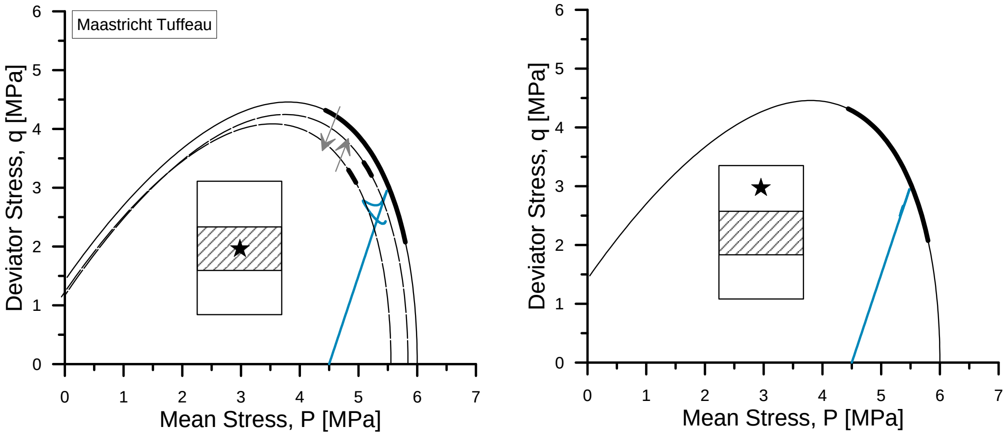

Figure E.5. Stress path evolution at Gauss points located inside (left) and outside (right) the compaction band in a simulation of triaxial compression on a Maastricht Tuffeau specimen.

under constant-traction ($d1$, 1 → 2). At the immediate proximity of the active zone, the material undergoes unloading in a direction that is opposite to loading inside the active band ($c1$, 1 → 2). The location at which the next compaction band emerges undergoes nearly negligible loading ($b1$, 1 → 2), while the far zones remain unaltered ($a1$, 1 → 2).

The second stage, i.e., the emergence of the second set of bands, is associated with the following evolution in stresses profile (in Fig. E.6$a2$-$d2$, marked by bold lines). The material inside the first compaction band undergoes oedometer-like unloading ($a2$, 2 → 3), while the material inside the emerging bands undergoes oedometer-like loading ($b2$, 2 → 3) in a fashion that resembles the emergence of the first band ($d1$, 1 → 2). The elastic zone inbetween the two bands continues to display elastic unloading ($c2$, 2 → 3). The zones away from the two bands undergo unloading ($d2$, 2 → 3) again in a direction that is opposite to the direction of loading inside the active zone.

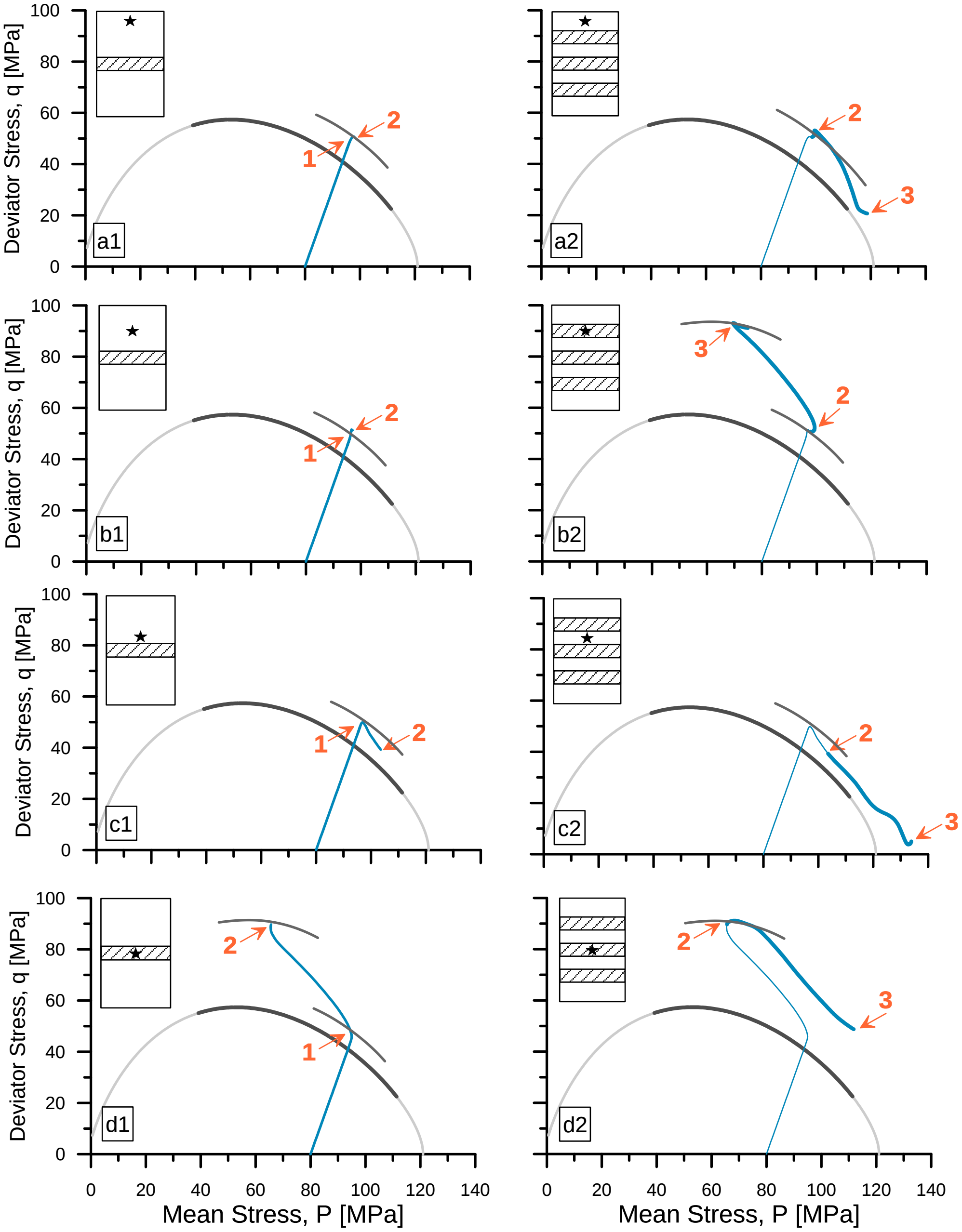

Figure E.6. Stress path evolution at Gauss points located throughout the domain after the emergence of the first band (left column, stage 1 → 2) and after the emergence of the following bands (right column, stage 2 → 3) in a simulation of triaxial compression on a simulated specimen of Bleurswiller sandstone.

3. Yielding Barrier Profile in Hardening and Softening Rocks

The following analyses provide a close look at the evolving *yielding barrier* profile at the initiation of localized compaction and its evolution as compaction banding propagates. A yielding barrier is the strain-energy input that is required to bring a material point from its current state to a first activation of plasticity, i.e., on the yield surface. In a viscoplastic modeling context, a proxy that can be useful to characterize this barrier is the value of the function, f. As this value is equal to zero when the stress state is exactly on the yield surface, negative values indicate states inside the elastic domain. To simplify the analysis, the value of the yield surface function, f, is normalized by the maximum absolute value, $|f|_{max}$. Negative values of $f/|f|_{max}$ indicate zones of yielding barriers (i.e., additional external loading is necessary to activate permanent deformation), while positive values indicate active plastic deformation (i.e., the external work input is being dissipated through viscoplastic strains)

The evolution of the profile of $f/|f|_{max}$ across the specimen of Maastricht Tuffeau is reported in Fig. E.7, elucidating the connection between compaction band propagation in form of a thickening band and the profile of the yielding barrier. (b) Shows the profile of $f/|f|_{max}$ at three sequential deformation intervals, i.e., I and II, also marked on the stress-strain curve in (a). The profile of $f/|f|_{max}$ upon the emergence of the first compaction band (at I) is characterized by a spike of active plastic deformation inside the portion of active compaction where material displays a mobilization of overstress as a result of viscosity (I, $1 \rightarrow 2$). A monotonic transition from active plastic deformation to zones of yielding barriers (I, $1 \rightarrow 3$ & $2 \rightarrow 4$) is observed, with transition points that appear to be located at the edges of the zone of active compaction (I, 1&2). Such transition dictates zones of higher potentials for the propagation of inelastic deformation, as the work-barrier that material in these locations needs to pass is minimal. This can be apparent from the profile of $f/|f|_{max}$ displayed in II, where it can be readily seen that the propagation of the compacted zones has taken place at the points of transition observed in I, new points of transition emerge (II, 1^* and 2^*) generating favorable locations for compaction propagation.

The evolution of the profile of $f/|f|_{max}$ across the specimen of Bleurswiller sandstone is reported in Fig. E.8, illustrating the patterns of yielding barrier profiles associated with compaction band propagation in the form of discrete bands. (b) Shows the profile of $f/|f|_{max}$ at three sequential deformation intervals, i.e., I and II, also marked on the stress-strain curve in (a). The profile of $f/|f|_{max}$ upon the emergence of the first compaction band (at I) is characterized by a spike of active plastic deformation inside the portion of active compaction where material displays a mobilization of overstress as a result of viscosity (I, $1 \rightarrow 2$). A transition from active plastic deformation to a yielding barrier takes place with the point of transition marked by (2). At variance with Maastricht Tuffeau, the yielding barrier profile in the simulation of Bleurswiller sandstone has a sharp dip in the specimen volume adjacent to the first activated band (I, $2 \rightarrow 4$ and $1 \rightarrow 3$), which non-monotonically decays at a finite distance generating zones of equal yielding barriers (I, $4 \rightarrow 6 \rightarrow 8$ and $3 \rightarrow 5 \rightarrow 7$). Such finite distance is linked with the formation of the next band.

It is, therefore apparent that different patterns of spatial compaction lead to different alterations of the stress field. Specifically, the response of Maastricht Tuffeau is controlled by softening-rich debonding processes, which lead to elastic stress relaxation outside the process zone. As a result, the portions of the domain most likely to generate further plastic compaction are confined to the layers adjacent to the active band, from which compaction propagates as a front. By contrast, the response of the sandstone is found controlled by pore collapse and plastic non-normality, which leads to a stress field characterized by an elastic

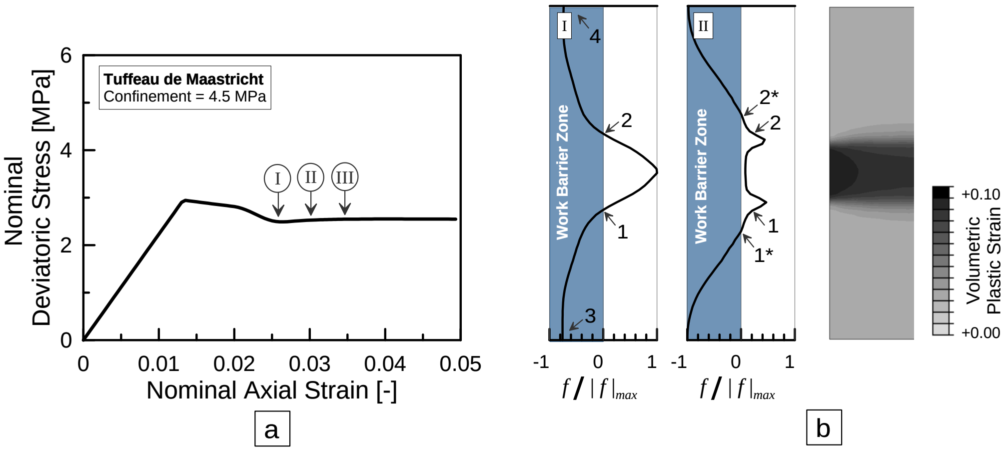

Figure E.7. Illustration of the evolution of overstress profile along a specimen of Maastricht Tuffeau subjected to triaxial compression, and showing a propagation of localized compaction in form of a thickening band.

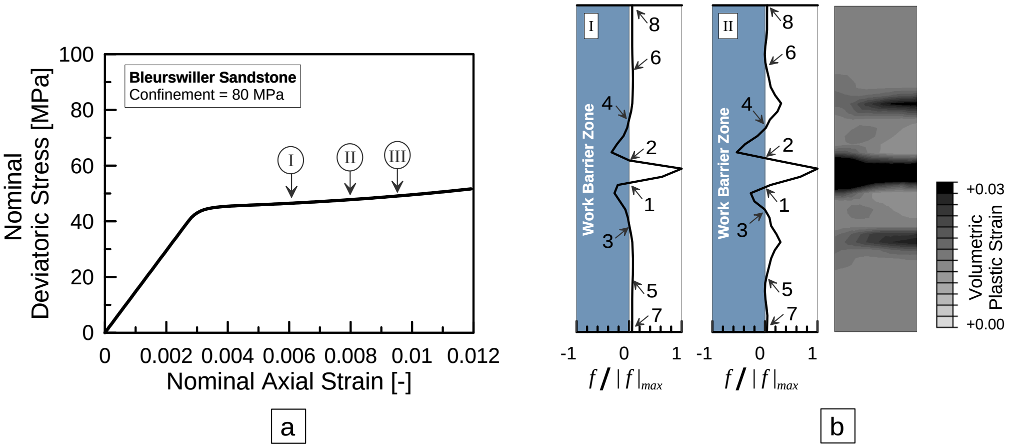

Figure E.8. Illustration of the evolution of overstress profile along a specimen of Bleurswiller sandstone subjected to triaxial compression, and showing a propagation of localized compaction in form of discrete bands.

buffer immediately adjacent to the active band. As a result, new band nucleation is more likely to occur at a finite distance from the active deformation site, eventually resulting in compaction bands with regular spacing. These findings give a possible insight on the role of the material properties in causing the competing modes and further studies taking into account the system dimensions and the global equilibrium/compatibility conditions are necessary for providing a mechanistic interpretation of the band-to-spacing ratio.

Ghassan Shahin

Ph.D. Candidate
Civil and Environmental Engineering
Northwestern University

Technology Institute
2145 Sheridan Avenue, A230
Evanston, IL, 60208, USA

Tel: +1 847-644-2473
gshahin@u.northwestern.edu

EDUCATION AND QUALIFICATION

2016-Present	**Doctor of Philosophy in Civil & Environmental Engineering** Northwestern University, USA Thesis title: *Geomechanical Modeling of Inception and Propagation of Compaction Bands in Porous Media*
2013-2015	**Master of Science in Earthquake Engineering** Erasmus Mundus Consortium:
	Institute for Advanced Study of Pavia (IUSS) — Italy
	University of Grenoble-Alpes (University of Grenoble-1) — France
	University of Patras — Greece
	Middle East Technical University — Turkey
2005-2010	**Bachelor of Science in Civil Engineering** Damascus University, Syria

PROFESSIONAL APPOINTMENTS

2020-2021	**Research Fellow, Experimental and Computational Grain Micromechanics** Johns Hopkins University, Baltimore, Maryland, USA
2017-2020	**Research Assistant, Geomechanics of Porous Rocks** Northwestern University, Evanston, Illinois, USA
2011-2012	**Junior Designer and Estimation Engineer, Steel Structures** Roots Steel Structures, Damascus Suburbs, Syria
2010-2011	**Site Engineer, Reinforced Concrete Structures** LAMA Construction, Damascus Governate, Syria

RESEARCH INTERESTS

Study of natural and man-made systems with an emphasis on the mechanics of granular and porous media. My research interests include Computational and Experimental Geomechanics, The theory of Material Instability, Constitutive and Multiscale Modelling, Mechanics and Physics of Granular Materials, Experimental and Theoretical Micromechanics, and their application to Energy Geotechnologies.

AWARDS

Walter P. Murphy Fellowship	Northwestern University	$65,747
Erasmus Mundus Scholarship, Ph.D.	European Commission	€100,000 (declined)
Erasmus Mundus Scholarship, M.Sc.	European Commission	€38,000

PUBLICATIONS

Peer-Reviewed Journal Articles

1. **Shahin, G.**, Desrues, J., Pont, S.D., Combe, G., Argilaga, A., (2016). *A study of the influence of REV variability in double-scale FEM× DEM analysis.* International Journal for Numerical Methods in Engineering, 107(10), 882-900.
2. **Shahin, G.**, Cil, M., Buscarnera, G. (2018). *Assessment of statistical homogeneity in chemically treated granular materials*, Géotechnique Letters, 8(1), 32-39.
3. **Shahin, G.**, Papazoglou, A., Marinelli, F., Buscarnera, G. (2019). *Calibration of a numerical model of Maastricht Tuffeau based on evidence of pressure-dependent compaction localization.* International Journal of Rock Mechanics and Mining Sciences, 121, 104039.
4. **Shahin, G.**, Marinelli, F., Buscarnera, G. (2019) *Theoretical Interpretation of Delayed Compaction Banding in Porous Rock.* Journal of Geophysical Research: Solid Earth, 124. https://doi.org/10.1029/2019JB017498

Journal Articles in Review

5. **Shahin, G.,** Viggiani, G., Buscarnera, G. *Simulating Rock Heterogeneities through a CT-FE Mapping Scheme Discloses Effects of Boundary Friction on Compaction Banding Onset.*
6. Shahin, G., Buscarnera, G. *Simulation of emergent compaction banding fronts caused by frictional boundaries.*

Journal Articles in Preparation

7. **Shahin, G.**, Rudnicki, J., Buscarnera, G., *Modeling of Propagation Patterns of Compaction Bands in Porous Rocks.*
8. **Shahin, G.**, Marinelli, F., Papazoglou, A., Viggiani, G., Buscarnera, G. *Compaction Localization of Anisotropic Maastricht Tuffeau.*
9. **Shahin, G.**, Rudnicki, J., Buscarnera, G. *Numerical Analyses of Compaction Bands Patterns in Geological Fields*
10. **Shahin, G.**, Buscarnera, G. *Micromechanics-based Hardening Rules for Cemented Granular Materials*

Referenced Conference Proceedings

1. Papazoglou, A., **Shahin, G.,** Marinelli, F., Dano, C., Buscarnera, G., Viggiani, G. *Localized Compaction in Tuffeau de Maastricht: Experiments and Modelling.* International Workshop on Bifurcation and Degradation in Geomaterials, Limassol, Cyprus (2017)
2. **Shahin G.**, Buscarnera, G. *Numerical Simulation of Localized Compaction Creep in Heterogeneous Porous Rock.* ARMA, New York, NY, USA (2019)
3. Buscarnera, G., Marinelli, F., **Shahin G.**. *Constitutive Modeling Approaches for Cross-Anisotropic Porous Rocks.* ARMA, Golden, CO, USA (2020)

International Conference Presentations

1. **Shahin, G.**, Cil, M., Buscarnera, G. *Statistical characterization of the heterogeneity of porous media subjected to reactive transport.* EMI, Boston, MA, USA (2018)
2. **Shahin, G.**, Viggiani, G., Buscarnera, G. *Simulation of Compaction Bands in Porous Rocks Based on X-ray CT Measurements.* EMI, Pasadena, CA, USA. (2019)
3. **Shahin, G.**, Marinelli, F., Buscarnera, G. *Numerical Simulation of Localized Compaction Creep in Heterogeneous Porous Rock.* ARMA, New York, NY, USA (2019)

REVIEWING ACTIVITIES

International Journal for Numerical and Analytical Methods for Geomechanics	1 paper
Géotechnique Letters	1 paper
PLOS ONE Journal	1 paper
Royal Society Open Science	1 paper
53rd U.S. Rock Mechanics Geomechanics Symposium, 2019, New York, NY, USA	6 papers
Geotechnical Earthquake Engineering and Soil Dynamics, 2018, Austin, TX, USA	2 papers
Geo-Congress, 2020, Minneapolis, MN, USA	2 papers

MENTORSHIP

Ritaja Ray (Ph.D. student): Breakage Mechanics-based Modeling of Strain Localization
Dawei Xue (Ph.D. student): Compaction Bands in Field-Scale Problems

TEACHING ACTIVITIES

GEN-ENG 205-2 (ENGINEERING ANALYSIS II): Introduction to statics and dynamics of objects and structural systems for first-year undergraduate engineering students.

CIV-ENV 302-0 (ENGINEERING LAW): The American legal system from an engineer's perspective. Contract, patent, corporation, antitrust, property, and environmental law. Torts, product liability, and arbitration.

CIV-ENV 417-0 (MECHANICS OF CONTINUA): Basic understanding of tensors and tensor calculus, stress as a tensor, the difference between material and spatial descriptions of motion, the measures of strain and deformation and deformation rate, balance of mass, momentum and energy, and Introduction to constitutive behavior. (served as grader twice)

OTHER ACTIVITIES

NASA's 3D-PRINTED MARTIAN HABITAT CHALLENGE Collaboration on the design of printing formwork and the system of granular material transportation.